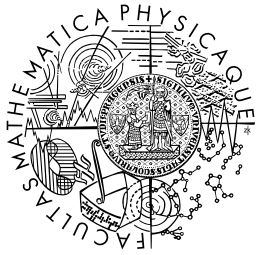

FACULTY
OF MATHEMATICS
AND PHYSICS
Charles University

DOCTORAL THESIS

Jindřich Žižka

Yarkovsky and YORP Effects in Dynamics of Small Bodies of the Solar System

Astronomical Institute, Charles University, Prague

Supervisor of the doctoral thesis:	Prof. RNDr. David Vokrouhlický, DrSc.
Study programme:	Physics
Study branch:	Theoretical Physics, Astronomy and Astrophysics

Prague 2018

I declare that I carried out this doctoral thesis independently, and only with the cited sources, literature and other professional sources.

I understand that my work relates to the rights and obligations under the Act No. 121/2000 Sb., the Copyright Act, as amended, in particular the fact that the Charles University has the right to conclude a license agreement on the use of this work as a school work pursuant to Section 60 subsection 1 of the Copyright Act.

In Jevíčko date ..... signature of the author

Title: Yarkovsky and YORP Effects in Dynamics of Small Bodies of the Solar System

Author: Jindřich Žižka

Department: Astronomical Institute, Charles University, Prague

Supervisor: Prof. RNDr. David Vokrouhlický, DrSc., Astronomical Institute, Charles University, Prague

Abstract: In this thesis, we study the influence of non-gravitational perturbations induced by the Yarkovsky/YORP effect and solar radiation pressure (SRP) on the orbital evolution of selected asteroids, asteroid families and pairs. These perturbations are of great importance if one wants to perform precise and long-term propagation of meter-sized and kilometer-sized bodies. Although they have found many applications in the Solar System, here, we particularly investigated how they influence the orbit of near-Earth asteroid (99942) Apophis and what is their role in the age determination of asteroid families and pairs. Our numerical simulations showed that the perturbations of Apophis' orbit caused by the SRP are orders of magnitude smaller than those produced by the Yarkovsky effect. The age determination of asteroid families and pairs was another pillar of this work. Over the past decade it turned out that the Yarkovsky effect must be taken into account for backward propagation of pair/family members. We modified the current method for estimating the age of asteroid pairs to be suitable for weakly convergent cases and discovered 7 young pairs with similar-sized components, which is in contradiction with the current theory of pair formation. In addition, we focused on an interesting pair of asteroids - (87887) 2000 SS286 and (415992) 2002 AT49. This pair had ambiguous solution of its age. Nevertheless, using numerical experiments with synthetic pairs, we were able to determine its correct age and found that it is currently the youngest known system. Last but not least we constrained the age of the well-known pair (6070) Rheinland – (54827) 2001 NQ8 and determined the most probable rotational sense of (54827) 2001 NQ8.

Keywords: celestial mechanics, non-gravitational perturbations, young asteroid families and pairs

I would very much like to thank my supervisor, Prof. RNDr. David Vokrouhlický, DrSc., who guided me through my PhD studies, provided me with valuable advice and encouraged me to solve interesting tasks in the field of celestial mechanics. I would also like to thank the president of the company Georadis s.r.o. in Brno, Ing. Tomáš Brunclík, who helped me and supported me during my studies.

I thank my wife, children, parents, my extended family and close friends for helping me to overcome a number of challenges I had to deal with during my studies. I would also like to thank Ing. Jana Hegerová (Vrážné u Jevíčka), Mgr. Adam Obrusník (Brno), RNDr. Jan Janík, Ph.D. (Brno), Mgr. Štěpán Ledvinka, Ph.D. (Brno) and Mgr. Tomáš Záležák, Ph.D. (Brno) for reading and reviewing parts of the dissertation and for their technical assistance. I also thank my excellent teachers at Jevíčko Gymnasium - Ing. Bohuslav Vacek (Moravská Třebová) and Mgr. Petr Němec (Olomouc), who sparked my interest in physics.

I dedicate this work to my sons Hyneček and Jindříšek and to my physics teachers Ing. Bohuslav Vacek and Mgr. Petr Němec.

Contents

Introduction

This dissertation deals with the dynamics of small bodies of the Solar System considering the influence of non-gravitational perturbations such as the Yarkovsky and YORP effects and the solar radiation pressure. More than a century has passed since Ivan Yarkovsky, a Russian of Polish origin, described the phenomenon that now bears his name. However, it was not until 20 years ago when the non-gravitational perturbations induced by the Yarkovsky and YORP effects became a major interest of the scientific community. Since then, both phenomena have not only been analytically described but also confirmed on selected asteroids in the Solar System. Although these perturbations are several orders of magnitude weaker in comparison to the gravitational influence of planets, they play a significant role in long-term orbital evolution of meter-sized and kilometer-sized bodies.

Due to the rotation and non-zero value of the thermal inertia of an asteroid, there is an asymmetric temperature distribution on its surface and a time lag between the irradiation and emission of thermal photons. The resulting, relatively small, reaction force changes the heliocentric orbit of the body, namely its semi-major axis. As a result, the body spirals either toward or away from the Sun (Yarkovsky effect). The photons also affect the body by torque (YORP effect), which leads to acceleration or deceleration of its rotation and a change in the orientation of the spin axis. Note that the reorientation of the spin axis induced by the YORP effect also retroactively affects the strength of the Yarkovsky effect.

Both effects have a wide range of applications. In particular, they are considered in situations where we study long-term orbital history of separate asteroids or asteroid families and pairs. The deeper we want to delve into the past, the more important is the accuracy of the Yarkovsky and YORP model that we use on our journey back in time. An interesting task is, for example, the reconstruction of post-disintegration evolution of asteroid families and pairs. Assuming that a certain set of bodies in the Solar System has a common origin, it is necessary to prove such a hypothesis. For this reason we propagate their orbits back in time with the view that all of them once meet in a certain space volume. It is therefore necessary to model, as accurately as possible, the gravitational and non-gravitational perturbations. These models then contribute to the overall view of the orbital history of our Solar System.

If turned around, they can also give us an insight into the future. In this respect, the most interesting for us are near-Earth asteroids (NEAs). It is because they are under a stronger influence of the Yarkovsky and YORP effects and also because for some NEAs, both of the effects have already been predicted, measured, and finally confronted with the theory. Modeling of the Yarkovsky and YORP effects has also provided for more accurate calculations of future impact probabilities of near-Earth asteroids.

This thesis deals with some of these applications of non-gravitational perturbations in the Solar System. The following is a brief overview of its structure and the content of individual chapters.

Chapter 1 focuses on the theoretical background of the Yarkovsky and YORP effects, which are the central concepts of the dissertation, and discusses their major applications in the Solar System. It also introduces important photometric quantities that are often referred to throughout the dissertation.

Chapter 2 presents our research into the influence of solar radiation pressure on the orbital evolution of the near-Earth asteroid (99942) Apophis until 2029, when it will experience a close encounter with the Earth. We used two scattering models in our study - the Hapke model and the classic Lambert model. We also compared the influence of the solar radiation pressure on the Apophis' orbit with the Yarkovsky effect.

Chapter 3 deals with young asteroid families and pairs, especially with methods of their identification and age determination. We modified the current method of age determination to be more suitable for weakly convergent (suspect) cases. Using our modification we were able to discover 7 asteroid pairs whose members are similar in size. This finding is, however, in contradiction with the current theory of pair formation and is discussed in more detail. The end of this chapter is dedicated to the best studied pair (6070) Rheinland – (54728) 2001 NQ8. We examined its age and also modeled different rotational senses of both components, seeking the most likely realization. Finally, we reviewed the role of the Yarkovsky effect in the orbital evolution of (6070) Rheinland – (54728) 2001 NQ8.

In Chapter 4, we study an extraordinary pair of asteroids (87887) 2000 SS286 and (415992) 2002 AT49. Our simulations revealed that there are two possible solutions of its age - either it is older than 50 kyr or younger than 10 kyr, which would be a record among the well-documented pairs. The question of the real age of this pair is the main subject of this chapter. We developed a numerical method by which we were able to decide whether this pair is extremely young or older than 50 kyr.

As the Yarkovsky and YORP effects can give us an insight into the past, we also wanted to look back - to the history of understanding of our Solar System. Appendix B provides a chronological overview of some significant historical moments in the research of the Solar System since Pre-Antiquity until the present day. Within this context, we introduce key concepts of the perturbation theory.

Appendix A includes reprints of the author's articles.

I believe that this dissertation will be of further use to those interested in non-gravitational perturbations in the Solar System.

Author

In Jevíčko, on 25$^{\text{th}}$ May 2018

1. Yarkovsky and YORP effects in the Solar System

The motion of bodies in the Solar System is primarily determined by gravity of the Sun and planets, where the interaction with planets is considered only as a minor perturbation.

However, smaller bodies ($D < 10$ km) are also influenced by non-gravitational perturbations. On long time scales, these can have a major influence on the orbital motion. Non-gravitational perturbations include *the Yarkovsky effect*, *YORP (Yarkovsky – O'Keefe – Radzievskii – Paddack) effect*, *Radiation pressure* and *the Poynting-Robertson effect*. In this chapter, we focus on the former two.

1.1 Yarkovsky effect

The Yarkovsky effect produces a continuous drift da/dt of the semi-major axis of the orbiting body. It is caused by the delay between the incidence of the solar radiation on the surface and the subsequent re-radiation to a different direction. The drift of the semi-major axis has major implications on the long-term orbital evolution of small Solar System bodies with the size ranging from ≈ 10 cm to $\approx$ 10 km.

It is rather surprising that the Yarkovsky effect was introduced into the hall of fame of major Solar System discoveries as late as the 1990s - almost 100 years after it had first been published by Ivan Yarkovsky.

1.1.1 Ivan Osipovich Yarkovsky (1844 - 1902)

Ivan Osipovich Yarkovsky was born on 24 May, 1844 in a small military outpost close to lake Osveya at Belarussia's northern border. His father, Osip Janovic, died when Ivan was 3 years old. After death of his father, little Ivan and his mother left for Moscow, where his mother started working as a governess. He received elementary education at a parish school and later frequented a military school for orphans. He was, however, not admitted to a military technical college - most likely due to his Polish national minority status. Nonetheless, in 1868, he was admitted to the Institute of Practical Technology (nowadays called Technological Institute) in St. Petersburg and graduated as a civil engineer in 1872. Subsequently, he married Elena Alexandrovna Sendzikovskaya.

Yarkovsky was travelling extensively after his studies, visiting construction machine producers in Germany, Belgium and France. He got employed in the Kiev-Brest railway company and then in Alexandrovsk railway company Moscow-Brest, for which he worked at different positions for over 20 years. Apart from that, he became the president of the Russian Technological Society - an organization supporting technology development in Russia. Yarkovsky was not just interested in railway technology but also by airfoil aerodynamics[1], designed a ship powered by wave energy, was involved in the development of a rotary printer,

[1] He passed his interest in aircraft to his son, Vitold, who became a pilot with Ilya Muromec in St. Petersburg.

jackscrew, combustion furnace and other devices. His curiosity eventually brought him to the natural sciences.

In his time, it was still believed that ether existed - an omnipresent substance believed to be the transport medium for gravitational and electromagnetic interaction. He believed that an increase in the density of ether could be related to increasing complexity of matter - probably implying the presence of more complex elements. He was further assured in his opinion after Dmitri Mendeleev discovered the periodic trends. According to Yarkovsky, the periodic trends illustrated that although each atom was created in its "stable form", the diversity of atoms that is observed could be a consequence of transitions between atoms and coupling of ether with matter.

However, Yarkovsky correctly assumed that atoms can be divided into smaller units and can undergo changes. He exchanged letters about this with Mendeleev himself, who tended to be of the opposite persuasion. Yarkovsky's ideas proved to be correct only after natural radioactivity was discovered, by Henri Bequerel in 1896.

The discovery of different kinds of stellar spectra in the second half of the 19th century supported his thoughts about the creation, development and destruction of stars. He thought that stars grew by attracting ether which can be converted to matter in their core. According to him, not just stars, but also Earth and other planets were to grow in size. Yarkovsky was, for a long time, studying matter, radiation and gravity and he was looking for a complete theory that would capture these phenomena. Unfortunately, he was wrong in many of these assumptions and his ideas did not get the interest of the physics community.

However, his work of outstanding importance was published in French in 1888 and is called *Kinetic Theory of Universal Gravitation in Relation to the Formation of the Chemical Elements*. In this publication, he not only summarized his thoughts on ether and the structure of matter but also mentioned an effect nowadays called the Yarkovsky effect. Motivated by the thought of omnipresent ether, he argued that planets are being slowed down by ether as they orbit the Sun. To prevent them from spiraling towards the Sun, Yarkovsky argued, there had to be an effect acting against the decceleration of planets by ether. According to him, this effect was heating up the compressed ether in front of the body that would then expand on the opposite side of the planet, thereby giving the planet the necessary acceleration. He supported this idea by the observation of the Great Comet of 1882 (1882 II) which did not exhibit any decceleration along its orbit.

Due to health problems and family complications, he left the Alexandrovsk railway company in 1894 and moved with all his 6 children to St. Petersburg. There, he worked shortly for the Nevsky mechanical and shipbuilding plant before moving to a smaller town of Dyatkovo and becoming a vice-manager of the Maltsovov railway engine company.

In 1901, he got ill and started taking treatment abroad - first in Badenweiler, then Heidelberg. He died of sarcoma in Heidelberg's faculty hospital in 1902. During the Russian Revolution of 1917 Yarkovsky's work got back to Poland, to the hands of his grandson - Hendryk. The whole archive, however, disappeared during World War II. The work of Yarkovsky was then re-discovered in a sequence of coincidences.

An Estonian astronomer **Ernst Öpik** (1893 – 1984), who studied the motion of small bodies in the Solar System, published a paper, where he noted that a similar effect of spiraling towards or away from the Sun was earlier suggested by a Russian civil engineer Yarkovsky around 1900 (see Öpik, 1951). Ernst Öpik was referring to a pamphlet published in St. Petersburgh that he vaguely remembered while reading it in Estonia in 1909. Independent of Yarkovsky, a similar effect was discovered and published in 1952 by a Soviet astronomer Viktor Vladimir Radzievskii (Radzievskii, 1952). Though the effect was extensively studied in the following years, the details about his discoverer have for long remained obscure.

There had been short mentions of Yarkovsky before his lost pamphlet was discovered, in publications of a Soviet geologist Vladimir B. Neiman (Neiman et al., 1965) and an american astronomer Joseph A. Burns (Burns et al., 1979). Yarkovsky's original writing was discovered as late as 2003 by an amateur Dutch astronomer George Beekman. It was in the library of Sternberg's Institute in Moscow. A great deal of information about Ivan Osipovich Yarkovsky can then be found in Beekman (2006).

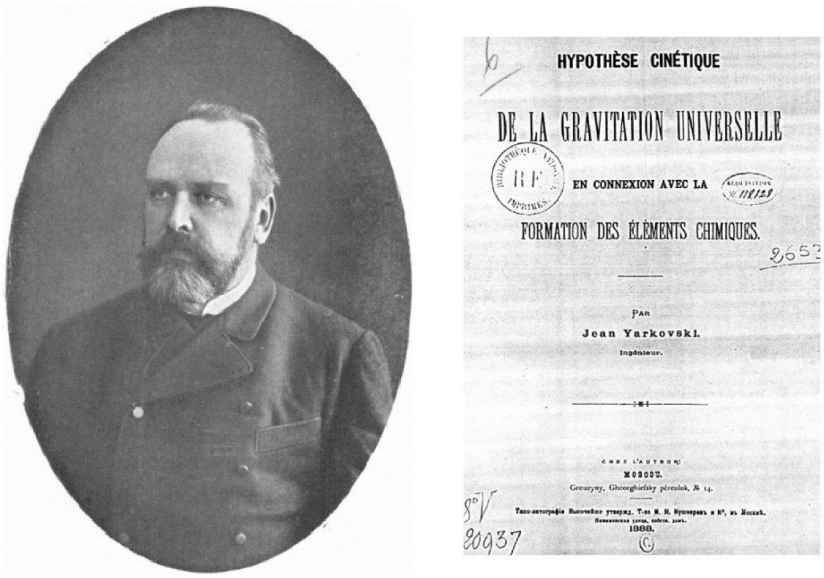

Figure 1.1: Ivan Osipovich Yarkovsky on an undated photograph and the front page of his pamphlet. Source: Beekman (2006).

1.1.2 The mechanism and the mathematical description

The Yarkovsky effect is a consequence of thermal re-radiatiation of the energy received from the Sun. This re-radiation causes a relatively small reaction force. Over a long period, the action of this force changes the heliocentric trajectory of the body, especially its semi-major axis. Depending on the rotation of an asteroid, this force then induces Yarkovsky drift either towards or away from the Sun (Fig. 1.2).

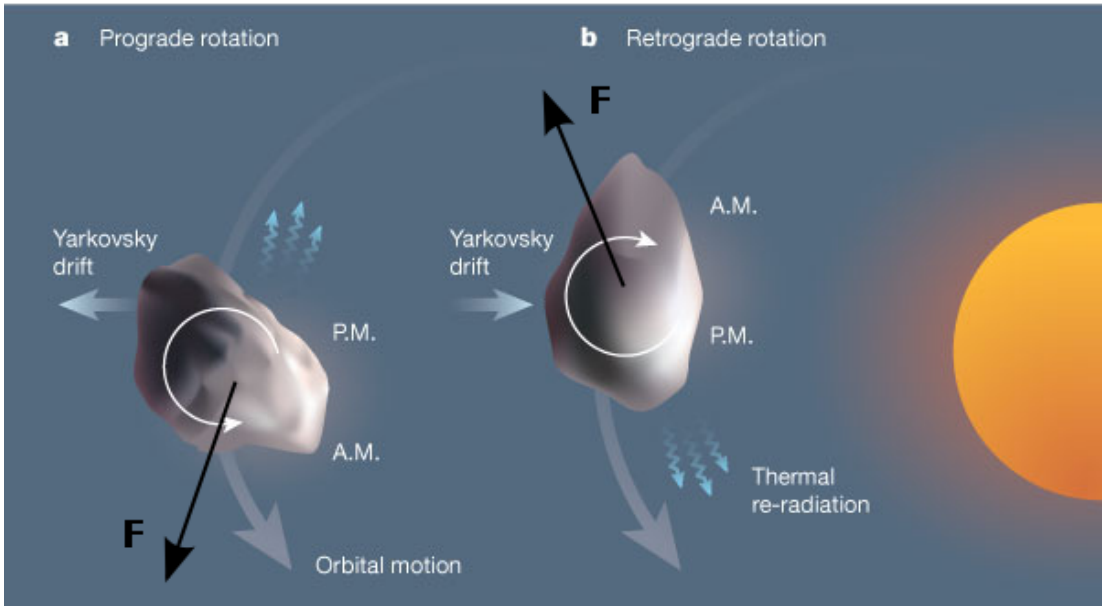

Figure 1.2: The origin of the reaction forces **F** for the case of prograde rotation (a) and retrograde rotation (b). In both cases, the infrared radiation is emitted from the afternoon side. Source: Binzel (2003).

The Yarkovsky effect is formally divided into its *diurnal* and *seasonal* variant. Fig. 1.2 illustrates the diurnal Yarkovsky effect depending on the two directions of rotation. In Fig. 1.3, we can see both the variants in the course of the orbital cycle. The extent of the Yarkovsky effect certainly depends on many factors such as the size of the body, its composition and thermal properties, the distance from the Sun, the orientation of its spin axis, etc.

To calculate the Yarkovsky force, we first have to find the temperature distribution on the surface of the body. We consider a suitable coordinate system connected to the body. In general, the scalar field of the temperature $T(\mathbf{r}, t)$ in point $\mathbf{r}$ and time t is given by the *heat diffusion equation*

$$\rho C_P \frac{\partial T}{\partial t} - \nabla \cdot (K \nabla T) = \dot{q}_V, \tag{1.1}$$

where K is the thermal conductivity, C_P the heat capacity at constant pressure, ρ the mass density and $\dot{q}_V$ the rate of heating per unit volume[2]. The energy conservation equation for the surface layer of the body, which then also provides the boundary condition for the heat equation, takes the form

$$\epsilon(\mu_0)\sigma T^4 + K\mathbf{n}_\perp \cdot \nabla T = (1 - A_h(\mu_0))\mu_0 F, \tag{1.2}$$

[2]Typically not considered and set $\dot{q}_V = 0$.

where $\mathbf{n}_\perp$ is the unit vector normal to a given surface element dS, $\mu_0 = \mathbf{n}_\perp \cdot \mathbf{n_0}$ is the cosine of the zenith distance of the Sun (the unit vector $\mathbf{n}_0$ is pointing towards the Sun), σ is the Stefan-Boltzmann constant, $\epsilon(\mu_0)$ is the *hemispherical emissivity*, $A_h(\mu_0)$ the *hemispheric albedo*, F the collimated flux of Sun's radiation and $\mu_0 F dS$ the radiant energy absorbed by the surface element dS.

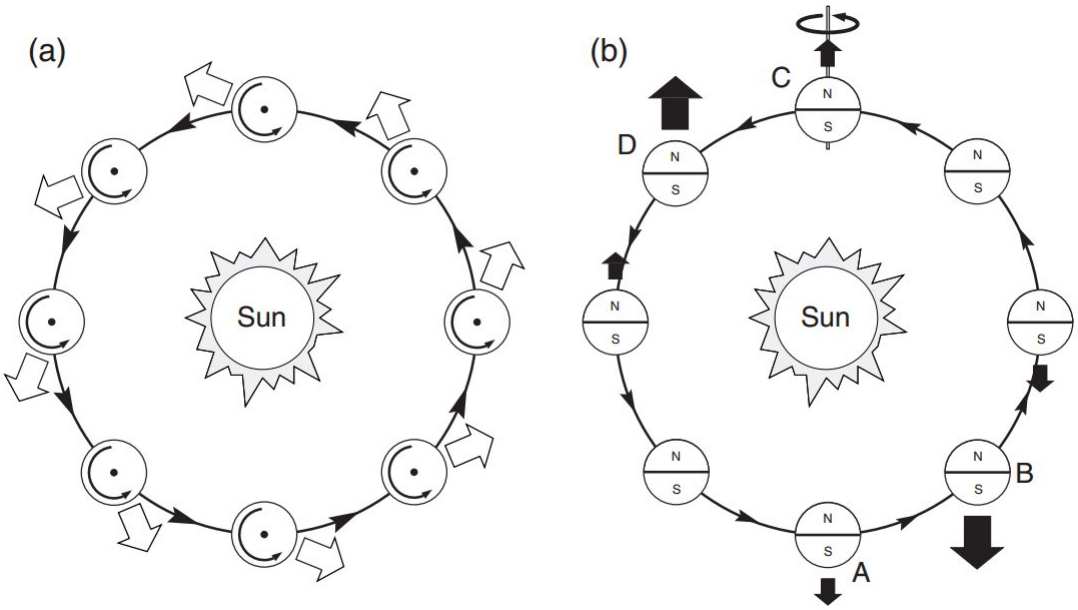

Figure 1.3: An illustration of the *diurnal* and *seasonal* Yarkovsky effect. Figure (a) demonstrates the origin of the reaction force for the case of prograde rotation with the axis of rotation perpendicular to the orbital plane. For this diurnal variant, prograde rotation leads to the body spiraling away from the Sun. The seasonal Yarkovsky effect is shown in figure (b), where the axis of rotation lies in the orbital plane. The magnitude of the reaction force varies with the orientation of the northern and southern hemispheres towards the Sun. The thermal inertia in this illustration was chosen so that the heat delay corresponds to the displacement in the orbit of 45°. If the radiation illuminates the hemispheres in points A and C, then the reaction force takes the maximum action in points B and D. For the seasonal Yarkovsky effect, the body always spirals towards the Sun, regardless of the rotation direction. Figure adapted from Bottke et al. (2006).

Numerical solution for a wire model of an asteroid

In practice we model the Yarkovsky effect by using a wire model of an asteroid with its surface being composed of many surface elements. In this paragraph we introduce the local set of coordinates and necessary photometrical quantities. We also derive and discuss the physical meaning of the terms in the heat equation (1.1) and provide equations, which are needed for calculating the Yarkovsky force.

Let us now define a local set of coordinates (local solar frame) with the origin in the center of a surface element dS, the base vector $\mathbf{e}_z$ pointing in the direction of $\mathbf{n}_\perp$ and a vector $\mathbf{e}_x \parallel \mathbf{M}$, where $\mathbf{M} = (\mathbf{n}_0 - \mu_0 \mathbf{n}_\perp)/\sqrt{1-\mu_0^2}$ is pointing towards the intersection of the horizon and the meridian passing through the Sun.

The last base vector $\mathbf{e}_y$ is then chosen so that an orthogonal coordinate system is obtained (Fig. 1.4).

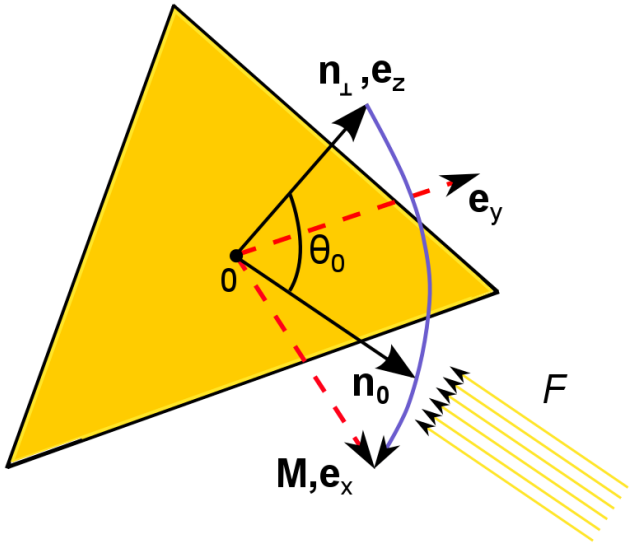

Figure 1.4: Local orthogonal coordinate system $(\mathbf{e}_x, \mathbf{e}_y, \mathbf{e}_z)$ for a selected surface element in a wire model of the body. Vector $\mathbf{e}_z$ is identical with the normal unit vector $\mathbf{n}_\perp$, vector $\mathbf{e}_x$ has the direction of $\mathbf{M} = (\mathbf{n}_0 - \mu_0\mathbf{n}_\perp)/\sqrt{1-\mu_0^2}$ and $\mathbf{e}_y$ is chosen so that a right-handed orthogonal system is formed. The surface element is illuminated by a collimated radiant flux F from the direction $\mathbf{n}_0$.

Let $I(\mathbf{n}, \mathbf{n}_0) = I(\mu, \mu_0, \mathbf{n}\cdot\mathbf{n}_0)$ be the *radiation intensity* in the direction $\mathbf{n}$, which was originally coming from the direction $\mathbf{n}_0$, while $\mu = \cos\theta = \mathbf{n}\cdot\mathbf{n}_\perp$ and $\mu_0 = \cos\theta_0 = \mathbf{n}_0\cdot\mathbf{n}_\perp$. Then, in the coordinate system defined, it must certainly hold that

$$\mathbf{n}_0 = \begin{pmatrix} \sqrt{1-\mu_0^2} \\ 0 \\ \mu_0 \end{pmatrix} \qquad \mathbf{n} = \begin{pmatrix} \sqrt{1-\mu^2}\cos\phi \\ \sqrt{1-\mu^2}\sin\phi \\ \mu \end{pmatrix}, \tag{1.3}$$

where (θ, ϕ) are the usual spherical coordinates.

The amount of radiant energy scattered by the surface element dS per unit time into the upper hemisphere Ω_+ is given by the expression[3]

$$d\mathcal{E}_{\mathrm{sca}} = dS \int_{\Omega_+} \mu I(\mu, \mu_0, \phi)\, d\Omega, \tag{1.4}$$

where $I(\mu, \mu_0, \phi)$ is the intensity of the scattered radiation. The ratio between the radiant energy scattered by the surface element dS to the upper hemisphere Ω_+ per unit time, and the energy of perpendicular incident radiation to the surface element dS per unit time is referred to as *hemispheric albedo*

$$A_h(\mu_0) = \frac{1}{F\mu_0} \int_{\Omega_+} \mu I(\mu, \mu_0, \phi)\, d\Omega. \tag{1.5}$$

[3] $dE_\nu = I_\nu(x, y, z, \varphi, \theta, t)\cos\theta\, d\nu\, ds\, d\Omega$ is the energy emitted in the frequency range $[\nu, \nu+d\nu]$ by an infinitesimal surface element ds in the direction (φ, θ) to a solid angle $d\Omega$ in a time interval dt (Mihalas, 1978).

Further, we can define the *Bidirectional scattering function* $r_{\text{sca}}(\mu, \mu_0, \phi)$ using the expression

$$I(\mu, \mu_0, \phi) = F r_{\text{sca}}(\mu, \mu_0, \phi). \tag{1.6}$$

The hemispheric albedo then takes the form

$$A_h(\mu_0) = \frac{1}{\mu_0} \int_{\Omega_+} \mu r_{\text{sca}}(\mu, \mu_0, \phi)\, d\Omega. \tag{1.7}$$

Now we will describe the physical meaning of the terms in the heat equation (1.1). The thermal energy corresponding to the portion of radiation that is absorbed by the surface element dS per unit time is given by

$$d\mathcal{E}_{\text{abs}} = F\mu_0\, dS - dS \int_{\Omega_+} \mu I(\mu, \mu_0, \phi) d\Omega = F\mu_0(1 - A_h(\mu_0))\, dS, \tag{1.8}$$

where, in the case of $\mu_0 \leq 0$, we set $d\mathcal{E}_{\text{abs}} = 0$.

Let us now define the *total directional emissivity* ϵ as the ratio of the total flux emitted in a given direction to the solid angle $\Delta\Omega$ to the total flux emitted in the same direction by an ideal blackbody using the expression (Brewster, 1992)

$$\epsilon = \frac{I(\mu, \mu_0, \phi) \cos\theta \Delta\Omega}{I_b \cos\theta \Delta\Omega}, \tag{1.9}$$

where I_b is the blackbody radiation intensity. In analogy, the *total hemispherical emissivity* ϵ_h is defined as the ratio of the total flux radiated to the upper hemisphere to the total flux radiated by an ideal blackbody. This quantity fulfills the following condition

$$\epsilon_h(\mu_0) = \frac{\int_{\Omega_+} I(\mu, \mu_0, \phi) \cos\theta\, d\Omega}{\pi I_b} = \frac{1}{\pi} \int_{\Omega^+} \mu r_{\text{th}}(\mu, \mu_0, \phi)\, d\Omega, \tag{1.10}$$

where $r_{\text{th}}(\mu, \mu_0, \phi)$ is the *Bidirectional emissivity function*. By substituting (1.9) to (1.10), we get the following formula for the total hemispherical emissivity

$$\epsilon_h(\mu_0) = \frac{1}{\pi} \int_{\Omega_+} \epsilon \cos\theta\, d\Omega = \frac{1}{\pi} \int_{\Omega_+} \epsilon\mu\, d\Omega. \tag{1.11}$$

Using (1.10) and the Stefan-Boltzmann law, the energy *radiated* by an element dS to upper hemisphere Ω_+ per unit time can be expressed as[4]

$$dS \int_{\Omega_+} I(\mu, \mu_0, \phi) \cos\theta\, d\Omega = \epsilon_h(\mu_0)\sigma T^4\, dS, \tag{1.12}$$

where $\sigma \approx 5.67 \cdot 10^{-8}$ $\text{Wm}^{-2}\text{K}^{-4}$ is the Stefan-Boltzmann constant. The physical meaning of the terms in the boundary condition (1.2) is then described by expressions (1.8), (1.12) and the *Fourier's law* in the form

$$dQ = K\mathbf{n}_\perp \cdot \nabla T\, dS, \tag{1.13}$$

which expresses the amount of heat dQ passing through the surface element dS in the direction $-\mathbf{n}_\perp$ per unit time.

[4] $\pi I_b = \sigma T^4$.

In practical simulation, it is often necessary to make an appropriate choice to the function $r(\mu, \mu_0, \phi)$. There are simple empirical models and also more sophisticated models motivated by the physics of the problem. With the simplified empirical models, separation of variables is usually assumed for $r(\mu, \mu_0, g)$

$$r(\mu, \mu_0, g) \simeq d(\mu, \mu_0) f(g), \tag{1.14}$$

where $\cos g = \mathbf{n} \cdot \mathbf{n}_0$ is the phase angle, $f(g)$ the *surface phase function* and $d(\mu, \mu_0)$ the *limb-darkening function*.

For example, the traditional Lambert model assumes that the scattering of the radiation has uniform probability in all directions (Lambert, 1759). This makes the function $r(\mu, \mu_0, \phi)$ proportional to the cosine of the zenith distance of the Sun. Thus (1.7) leads to

$$r_L(\mu, \mu_0, \phi) = r_L(\mu_0) = \mu_0 \frac{A}{\pi}, \tag{1.15}$$

where A is the plain albedo[5].

Other frequently used empirical models include, for example, the Lommel-Seeliger model (Seeliger, 1887), the Minnaert model (Minnaert, 1941) or the Lunar-Lambert model (e.g. Buratti and Veverka, 1983). These models capture the reflective properties of surfaces for different albedos. For example, highly reflective surfaces with the albedo of ≈ 1 can be described very well using the Lambert model. In the case of asteroids with typical albedo of < 0.5, on the other hand, the Lambert model can serve as a first approximation. For bodies with the geometric albedo of < 0.20, the Lommel-Seeliger model is more suitable.

The second group, which is more motivated by the physics, includes the class of Hapke models (Hapke, 1981, 1984, 1986, 2002, 2008, 2012). Moreover, Hapke models have been recently improved and made more accurate. This includes, for example, considering multiple scattering (Hapke, 2002) on grains with an anisotropic phase function and considering the *coherent backscatter opposition effect (CBOE)* on particles larger than the wavelength of the incident radiation. Other improvements, especially with regard to the influence of the porosity of the planetary regolith were presented in Hapke (2008) and Helfenstein and Shepard (2011). Other analytical models used both in photometry and spectroscopy include the Shkuratov model (Shkuratov et al., 1999) or the Lumme-Bowell model (Lumme and Bowell, 1981). An exhaustive overview of all the models used is provided in Li et al. (2015). In the next chapter, the widely-used Hapke's *single-scattering approximation* is discussed in relation to the perturbation of the orbit of the asteroid (99942) Apophis.

Let us calculate the non-gravitational perturbation forces. The photons of incident radiation are either scattered from the surface of the body but a part of them is also re-radiated in the thermal spectrum. Following from the third Newton law, both the effects must contribute to the change of momentum of the body.

[5]Which is equal to hemispheric albedo.

After some algebra, it can be shown that the infinitesimal non-gravitational forces acting on the surface element dS are given by

$$\mathrm{d}\mathbf{f}_{\mathrm{sca}} = -\frac{F}{c}(K_1^{\mathrm{sca}}\mathbf{n}_\perp + K_2^{\mathrm{sca}}\mathbf{M})\,dS, \tag{1.16}$$

$$\mathrm{d}\mathbf{f}_{\mathrm{th}} = -\frac{\sigma T^4}{c}(K_1^{\mathrm{th}}\mathbf{n}_\perp + K_2^{\mathrm{th}}\mathbf{M})\,dS, \tag{1.17}$$

while

$$K_1^{\mathrm{sca}}(\mu_0) = \int_{\Omega^+} \mu^2 r_{\mathrm{sca}}(\mu,\mu_0,\phi)\,d\Omega, \tag{1.18}$$

$$K_2^{\mathrm{sca}}(\mu_0) = \int_{\Omega^+} \mu\sqrt{1-\mu^2}\cos\phi\, r_{\mathrm{sca}}(\mu,\mu_0,\phi)\,d\Omega, \tag{1.19}$$

and

$$K_1^{\mathrm{th}}(\mu_0) = \frac{1}{\pi}\int_{\Omega^+} \mu^2 r_{\mathrm{th}}(\mu,\mu_0,\phi)\,d\Omega, \tag{1.20}$$

$$K_2^{\mathrm{th}}(\mu_0) = \frac{1}{\pi}\int_{\Omega^+} \mu\sqrt{1-\mu^2}\cos\phi\, r_{\mathrm{th}}(\mu,\mu_0,\phi)\,d\Omega. \tag{1.21}$$

In the case of the Lambert model, $K_1^{\mathrm{sca}}(\mu_0) = \frac{2}{3}\mu_0 A$, $K_1^{\mathrm{th}}(\mu_0) = \frac{2}{3}\epsilon$, $K_2^{\mathrm{sca}}(\mu_0) = 0$, $K_2^{\mathrm{th}}(\mu_0) = 0$. The resulting dynamical effects are, in complete, given by integral summations

$$\mathbf{f}_{\mathrm{sca}} = \int_S \mathrm{d}\mathbf{f}_{\mathrm{sca}} \qquad \mathbf{f}_{\mathrm{th}} = \int_{S'} \mathrm{d}\mathbf{f}_{\mathrm{th}}, \tag{1.22}$$

where we either integrate over the illuminated area S or over the whole surface S'. Similarly, for the non-gravitational torques (the YORP effect), it formally holds that

$$\mathbf{T}_{\mathrm{sca}} = \int_S \mathbf{r}\times\mathrm{d}\mathbf{f}_{\mathrm{sca}} \qquad \mathbf{T}_{\mathrm{th}} = \int_{S'} \mathbf{r}\times\mathrm{d}\mathbf{f}_{\mathrm{th}}, \tag{1.23}$$

where $\mathbf{r}$ is the position vector of the surface element dS.

Let us note that the perturbation effects of the radiation forces in the visible range are very small and even vanish in the case of circular orbits. However, the perturbations induced by thermal forces $\mathbf{f}_{\mathrm{th}}$ are of application interest, especially in relation to the changes of the semi-major axis. The Gaussian perturbation equation for the semi-major axis takes, in the approximation $e \to 0$, the form (Bertotti et al., 2003)

$$\frac{da}{dt} = \frac{2}{mn}(\mathbf{f}\cdot\mathbf{e}_\tau + \mathcal{O}(e)), \tag{1.24}$$

where n is the mean motion and $\mathbf{f}$ the perturbing force. The unit vector $\mathbf{e}_\tau = \mathbf{e}_h \times \mathbf{e}_r$ lies in the osculating plane of the trajectory. Here, $\mathbf{e}_h$ is the unit vector pointing along the angular momentum vector and $\mathbf{e}_r$ the unit vector in the radial direction[6].

[6]From figure (Fig. 1.5), it is apparent that $\mathbf{f}\cdot\mathbf{e}_\tau = -f_Y$.

Linear model for finding the surface temperature $T(0,t)$

To investigate the influence of the Yarkovsky effect, it is first necessary to determine the temperature distribution on the surface of the body. In general, this is achieved by solving the heat equation (1.1) in a coordinate system connected with the moving body in the form

$$\frac{\partial T}{\partial t} - \kappa \nabla^2 T = 0, \tag{1.25}$$

where $\kappa = \frac{K}{\rho C_P}$ is the so-called *thermal diffusivity*. This simplified formulation of the heat equation holds, as long as we disregard the dependence of ρ, C_P and K on temperature. If we assume small temperature fluctuations ΔT within the volume of the body, we can introduce constant values of these quantities, taken at an average temperature T_{av}.

Let us first consider a 1D case, i.e. $T(\mathbf{r},t) \to T(x,t)$, where x is the depth. To simplify the subsequent calculations, especially equation (1.25), it is advantageous to introduce the following coordinate scaling: $x \to x' = x/l_s$ (Spencer et al., 1989; Lagerros, 1996b), $t \to \zeta = \mathrm{e}^{i\omega(t\,-\,t_0)}$ (Vokrouhlický, 1998a). The imaginary unit fulfills $i = \sqrt{-1}$ and $\omega = 2\pi f$, where f is the rotational frequency of the body. The physical meaning of l_s is the *penetration depth* of the thermal wave, as shown further. Using this new set of coordinates, it must then hold that

$$i\zeta \frac{\partial T(x',\zeta)}{\partial \zeta} = \frac{\kappa}{\omega l_s^2} \frac{\partial^2 T(x',\zeta)}{\partial x'^2}, \tag{1.26}$$

and, therefore,

$$i\zeta \frac{\partial T(x',\zeta)}{\partial \zeta} = \frac{\partial^2 T(x',\zeta)}{\partial x'^2}, \tag{1.27}$$

as long as the scale parameter is $l_s = \sqrt{\frac{\kappa}{\omega}}$.

Owing to the periodic nature of the incident radiant flux, we can assume that the temperature will also vary periodically in a given point. For this reason, it is reasonable to assume the expression for $T(x',\zeta)$ (and $\Delta T(x',\zeta)$) in the separated form of the Fourier series

$$T(x',\zeta) = T_{\mathrm{av}} + \Delta T(x',\zeta) = T_{\mathrm{av}} + \sum_{\substack{n=-\infty \\ n\neq 0}}^{+\infty} T_n(x')\zeta^n, \tag{1.28}$$

where $i = \sqrt{-1}$ is the imaginary unit and T_n respective Fourier coefficients. Substituting to (1.27) yields the differential equation

$$i\zeta \frac{\partial \Delta T(x',\zeta)}{\partial \zeta} = \frac{\partial^2 \Delta T(x',\zeta)}{\partial x'^2}, \tag{1.29}$$

which transforms to the equation for the n-th Fourier coefficient

$$\frac{d^2 T_n(x')}{dx'^2} - inT_n(x') = 0. \tag{1.30}$$

If we consider the boundary condition $T_n(\infty) = 0$, the solution is

$$T_n(x') = T_n(0)\mathrm{e}^{-\sqrt{in}x'}. \tag{1.31}$$

Consequently, by taking equations (1.31) and (1.28), we obtain[7]

$$T(x',t) = T_{\text{av}} + \sum_{\substack{n=-\infty \\ n\neq 0}}^{+\infty} T_n(0)\mathrm{e}^{-\sqrt{\frac{n}{2}}x'}\mathrm{e}^{i(n\omega t-\sqrt{\frac{n}{2}}x'+\phi_n)}, \tag{1.32}$$

the real part of which is

$$T(x',t) = T_{\text{av}} + \sum_{n=1}^{+\infty} T_n(0)\mathrm{e}^{-\sqrt{\frac{n}{2}}x'}\cos\left(n\omega t - \sqrt{\frac{n}{2}}x' + \phi_n\right), \tag{1.33}$$

where $\phi_n = -n\omega t_0$ is the corresponding phase angle (Lagerros, 1996b). In the original coordinates (x,t), we obtain the real part in the form

$$T(x,t) = T_{\text{av}} + \sum_{n=1}^{+\infty} T_n(0)\mathrm{e}^{-\sqrt{\frac{n}{2}}\frac{x}{l_s}}\cos\left(n\omega t - \sqrt{\frac{n}{2}}\frac{x}{l_s} + \phi_n\right). \tag{1.34}$$

Looking at the expression above, it is apparent that the penetration depth of the thermal wave l_s is a measure of the exponential attenuation of temperature.

To obtain the Fourier coefficients $T_n(0)$, a boundary condition for the heat equation is necessary. Therefore, we re-formulate the equation (1.2), so that[8]

$$\epsilon(\mu_0)\sigma T^4(0,t) - K\left(\frac{\partial T(x,t)}{\partial x}\right)_0 = [1-A_h(\mu_0)]\mathcal{E}(\mu_0,t), \tag{1.35}$$

while we assume the energy flux to a surface element also in the form of a Fourier series

$$\mathcal{E}(\mu_0,\zeta) = \sum_{n=-\infty}^{+\infty}\mathcal{E}_n(\mu_0)\zeta^n = \mathcal{E}_{\text{av}} + \Delta\mathcal{E}(\mu_0,\zeta) = \mathcal{E}_{\text{av}} + \sum_{\substack{n=-\infty \\ n\neq 0}}^{+\infty}\mathcal{E}_n(\mu_0)\zeta^n. \tag{1.36}$$

In the following expressions, for brevity, we do not explicitly specify the dependency on μ_0. If we use the linear approximation $T^4 \approx T_{\text{av}}^4 + 4T_{\text{av}}^3\Delta T$, the equation (1.35) takes the form

$$\epsilon\sigma T_{\text{av}}^4 + 4\epsilon\sigma T_{\text{av}}^3\Delta T(0,t) - K\left(\frac{\partial T(x,t)}{\partial x}\right)_0 = [1-A]\mathcal{E}_{\text{av}} + [1-A]\Delta\mathcal{E}. \tag{1.37}$$

The first two terms at both sides of the equation are equal, which gives

$$4\epsilon\sigma T_{\text{av}}^3\Delta T(0,t) - K\left(\frac{\partial T(x,t)}{\partial x}\right)_0 = [1-A]\Delta\mathcal{E}. \tag{1.38}$$

A simple calculation reveals that it holds

$$\left(\frac{\partial T(x,t)}{\partial x}\right)_0 = -(1+i)\frac{1}{l_s}\sum_{\substack{n=-\infty \\ n\neq 0}}^{+\infty} T_n(0)\sqrt{\frac{n}{2}}\,\mathrm{e}^{in\omega(t-t_0)}, \tag{1.39}$$

$$\Delta T(0,t) = \sum_{\substack{n=-\infty \\ n\neq 0}}^{+\infty} T_n(0)\mathrm{e}^{in\omega(t-t_0)}.$$

[7] $i = \mathrm{e}^{i\pi/2}$ and $\sqrt{in} = \mathrm{e}^{(i\pi/4)}\sqrt{n} = (1/\sqrt{2})(1+i)\sqrt{n}$

[8] The sign with the term $K\left(\frac{\partial T}{\partial x}\right)_0$ changed with regard to the equation (1.2) because in this case the coordinate x is the depth.

Substituting (1.39) to (1.38), we obtain the expression for the Fourier coefficient $T_n(0)$ and after using $T_n(0)$ in (1.34) we get the solution for $T(x,t)$.

Let us briefly demonstrate, for instance, the complete solution of the 1D problem for the eigenfrequency (n = 1). Even though we use just one frequency, this simple solution provides a basic insight into major qualitative characteristics of the Yarkovsky effect. In this case it holds that

$$\mathcal{E}(t) = \mathcal{E}_{\rm av} + \mathcal{E}_1 \mathrm{e}^{i\omega(t-t_0)}, \tag{1.40}$$

and

$$T_1(0) = \frac{(1-A)\mathcal{E}_1}{4\epsilon\sigma T_{\rm av}^3 + (1+i)K\sqrt{\frac{1}{2}\frac{1}{l_s}}}. \tag{1.41}$$

After some algebra we get

$$T_1(0) = \frac{(1-A)\mathcal{E}_1}{4\epsilon\sigma T_{\rm av}^3}\frac{1}{1+S+iS} = \frac{(1-A)\mathcal{E}_1}{4\epsilon\sigma T_{\rm av}^3}\frac{1}{\sqrt{1+2S+2S^2}}\mathrm{e}^{i\psi}, \tag{1.42}$$

where $\tan\psi = -\frac{S}{1+S}$ and $S = \sqrt{\frac{\rho\omega KC}{32}}\frac{1}{\epsilon\sigma T_{\rm av}^3}$. Here, ψ is the contribution to the total phase. Substituting (1.42) to (1.32) it holds for the surface layer that

$$T(0,t) = T_{\rm av} + \frac{(1-A)\mathcal{E}_1}{4\epsilon\sigma T_{\rm av}^3}\frac{1}{\sqrt{1+2S+2S^2}}\mathrm{e}^{i\omega(t-t_0+\frac{\psi}{\omega})}. \tag{1.43}$$

From this result it is easy to see that the non-zero value of the thermal conductivity K results in the phase shift ψ/ω which causes a delay between the irradiation and the corresponding increase of the surface temperature (see Fig. 1.2). The solution containing all the $T_n(0)$ terms can be found in Čapek (2007).

In many cases, a 1D model is sufficient for solving the dynamical action of the Yarkovsky effect. Especially with numerical simulation, we often use 3D wireframe models of the body, whereupon the body's surface is divided into a large number of triangular surface elements, e.g. using the Delaunay triangulation method. For each of these elements, we solve the contribution to the total Yarkovsky drift of the body using the 1D approximation. For small Solar System objects, it is reasonable to expect that the solar radiation is the only source of energy. Then we can imagine that the body consists of a practically isothermal core and the temperature fluctuations happen exclusively in a relatively thin surface layer. If the penetration depth of the heat wave l_s is much smaller than the dimensions of the body, then this approximation is well-justified. This criterion is usually met for bodies larger than $\approx$ 20 m, unless they exhibit large thermal inertia $\Gamma = \sqrt{\rho CK}$. Thus, for each surface element of the body, we numerically solve the 1D heat equation. Then we obtain the resulting Yarkovsky force as the superposition over all the surface elements (Čapek and Vokrouhlický, 2005).

Linear spherical 3D model of the Yarkovsky effect

The ideal solution of the problem would certainly be a complete 3D analytical theory, which would reliably determine the temperature distribution inside a body and calculate the resulting Yarkovsky force. Unfortunately, the complexity of some of the calculations require certain simplifications regarding the shape of the body.

On the other hand, there are works that capture, to a varying extent, some special cases for solid spherical bodies. They typically consider two classical variants of the Yarkovsky effect - the diurnal and seasonal (Fig. 1.3), which were first discussed in Rubincam (1995, 1998) and Farinella et al. (1998). For instance, Vokrouhlický (1998a) provides an analytical theory valid for the diurnal variant of the Yarkovsky effect using the linear approximation on a spherically rotating body[9], which is further extended in Vokrouhlický (1998b) to an oblate spheroid.

The most general self-consistent linear theory of Vokrouhlický (1999) considers both the rotation of the body with the angular frequency $\omega_{\rm rot}$ and its revolution around the Sun with the angular frequency $\omega_{\rm rev}$. According to this theory, the drift of the semi-major axis da/dt depends both on $\omega_{\rm rot}$ and $\omega_{\rm rev}$. The diurnal and seasonal variants of the Yarkovsky effect then appear only in the limiting case of $\frac{\omega_{\rm rot}}{\omega_{\rm rev}} >> 1$. This limit is fulfilled for most cases in the Solar System. It can also be shown that the relative contribution of the newly appearing terms dependent both on $\omega_{\rm rot}$ and $\omega_{\rm rev}$ to the diurnal Yarkovsky drift is smaller than 10^{-3}. This conclusion then justifies the use of traditional limit variants of the Yarkovsky effect for most problems in the Solar System.

In this paragraph, we are going to derive the form of Yarkovsky force and its consequence on semi-major axis perturbation. Before we do that we will derive the thermal parameter Θ, an important quantity needed for calculating the Yarkovsky force. Let us to introduce additional variable scaling in the heat equation (Spencer et al., 1989). Let $T' = T/T_*$, $\mathcal{E}' = \mathcal{E}/\mathcal{E}_*$ and $\alpha = 1 - A$, where T_* is given by the expression $\epsilon\sigma T_*^4 = \alpha\mathcal{E}_*$. It also holds that $\Delta T' = \Delta T/T_*$ and $T_* = \sqrt{2}T_{\rm av}$ (see Rubincam, 1995, 1998). The flux $\mathcal{E}_*$ corresponds to the solar radiation flux at the current location of the body. We have

$$\sqrt{2}\epsilon\sigma T_*^3 \Delta T(0,\zeta) - K\left(\frac{\partial \Delta T(x,\zeta)}{\partial x}\right)_0 = \alpha\Delta\mathcal{E}. \tag{1.44}$$

By simple calculation, we obtain

$$\sqrt{2}\Delta T(0,\zeta) - \frac{K}{\epsilon\sigma T_*^3}\left(\frac{\partial \Delta T(x,\zeta)}{\partial x}\right)_0 = \frac{\alpha\Delta\mathcal{E}'\mathcal{E}_*}{\epsilon\sigma T_*^3}. \tag{1.45}$$

The final form of the boundary condition for the heat equation, this time in the scaled variables, is then given by

$$\sqrt{2}\Delta T'(0,\zeta) - \Theta\left(\frac{\partial \Delta T'(x',\zeta)}{\partial x'}\right)_0 = \Delta\mathcal{E}', \tag{1.46}$$

where $\Theta = \frac{\Gamma\sqrt{\omega}}{\epsilon\sigma T_*^3}$ is the so-called *thermal parameter*.

[9]For an axis of rotation preceding around the angular momentum vector, Vokrouhlický (1998b) applies a numerical solution.

We also assume constant angular distance θ_0 of the Sun from the axis of rotation. This practically means considering only the diurnal variant of the Yarkovsky effect because this angle changes due to orbiting around the Sun. An extended solution, which includes also the seasonal Yarkovsky effect or a combination of both can be found either in Vokrouhlický (1999) or Spitale (2001).

It is advantageous to introduce two coordinate systems: (a) a system co-rotating with the body and (b) a non-rotating system fixed with respect to the position of the Sun (Fig. 1.5). The system (a) is defined in such a manner that the axis z points along the axis of rotation of the body. The x-axis is chosen so that in $t = 0$, the Sun lies in the xz plane. The y-axis is then perpendicular to x and z. In this system of coordinates, we define the usual spherical coordinates (r, θ, ϕ), where $r = 0$ in the centre of the body, the angle θ points away from the spin axis and the angle ϕ points from the x axis in the positive direction.

The non-rotating system (b) points with its Z-axis also along the body's axis of rotation. However, the X axis merges with the x axis only at $t = 0$. The choice of Y-axis again forms an orthogonal system. Let the spherical coordinates be (r, ϑ, φ). It is then apparent that $(\vartheta,\ \varphi) = (\theta,\ \phi + \omega\ t)$.

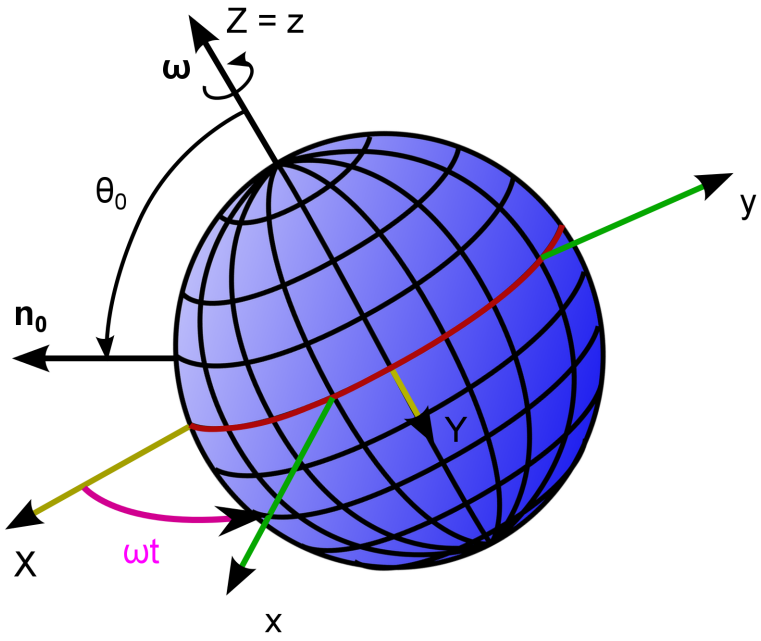

Figure 1.5: An illustration of the co-rotating system xyz as opposed to the XYZ system. Direction to the Sun is denoted $\mathbf{n}_0$. We assume that the body rotates around the principal axis of the inertia tensor with the angular velocity $\boldsymbol{\omega}$. The angle between $\boldsymbol{\omega}$ and $\mathbf{n}_0$ is θ_0.

The normal vector $\mathbf{n}_\perp$ in the point (θ, ϕ) is given by the expression[10]

$$\mathbf{n}_\perp(\theta, \phi) = (\sin\theta\cos\phi, \sin\theta\sin\phi, \cos\theta)^T, \tag{1.47}$$

and for $\mathbf{n}_0$ it holds that

$$\mathbf{n}_0(\theta_0, t) = (\sin\theta_0\cos\omega t, -\sin\theta_0\sin\omega t, \cos\theta_0), \tag{1.48}$$

[10]In the co-rotating system.

which can be expressed as follows, using the complex notation

$$\mathbf{n}_0 = \begin{pmatrix} \frac{1}{2}\zeta \sin\theta_0 \\ \frac{i}{2}\zeta \sin\theta_0 \\ \cos\theta_0 \end{pmatrix} + \begin{pmatrix} \frac{1}{2}\zeta \sin\theta_0 \\ \frac{i}{2}\zeta \sin\theta_0 \\ \cos\theta_0 \end{pmatrix}^* , \tag{1.49}$$

while $*$ denotes a complex conjugate vector. The dot product of these vectors then expresses the energy flux $\mathcal{E}'$ to a surface element at the position (θ, ϕ) in time ζ

$$\mathcal{E}' = \mathbf{n}_\perp(\theta, \phi) \cdot \mathbf{n}_0(\theta_0, \zeta), \tag{1.50}$$

where we assume the shadowing condition $\mathcal{E}' = 0$ if $\mathbf{n}_\perp \cdot \mathbf{n}_0 < 0$.

Similar to the 1D case, it is necessary to solve the heat equation. However, now we do so in spherical coordinates. Let $r' = r/l_s$ and $\zeta = \mathrm{e}^{i\omega t}$. It can be shown that (1.25) takes the form

$$i\zeta \frac{\partial \Delta T'(r', \theta, \phi, \zeta)}{\partial \zeta} = \frac{1}{r'^2} \left\{ \frac{\partial}{\partial r'} \left(r'^2 \frac{\partial}{\partial r'} \right) + \Lambda(\theta, \phi) \right\} \Delta T'(r', \theta, \phi, \zeta), \tag{1.51}$$

where

$$\Lambda(\theta, \phi) = \frac{1}{\sin\theta} \left[\frac{\partial}{\partial \theta} \left(\sin\theta \frac{\partial}{\partial \theta} \right) + \frac{1}{\sin\theta} \frac{\partial^2}{\partial \phi^2} \right]. \tag{1.52}$$

The boundary condition is, in the linear approximation

$$\sqrt{2}\Delta T'(R', \theta, \phi, \zeta) + \Theta \left(\frac{\partial \Delta T'(r', \theta, \phi, \zeta)}{\partial r'} \right)_{R'} = \Delta \mathcal{E}'. \tag{1.53}$$

As often in mathematical physics, where fundamental equations are solved in spherical coordinates, we express $\mathcal{E}'(\theta_0, \theta, \phi, \zeta)$ and $\Delta T'(r', \theta, \phi, \zeta)$ in the form of spherical harmonics.

$$\mathcal{E}' = \sum_{n \geq 0} \sum_{k=-n}^{n} a_{nk}(\theta_0, \zeta) Y_{nk}(\theta, \phi) = \mathcal{E}'_{\mathrm{av}} + \Delta \mathcal{E}', \tag{1.54}$$

where $\Delta \mathcal{E}' = \sum\limits_{n \geq 1} \sum\limits_{k=-n}^{n} a_{nk}(\theta_0, \zeta) Y_{nk}(\theta, \phi)$. It follows from the orthogonality of spherical harmonics that

$$a_{nk} = \int_\Omega \mathcal{E}'(\theta_0, \theta, \phi, \zeta) Y^*_{nk}(\theta, \phi) d\Omega, \tag{1.55}$$

while it is necessary to keep in mind that we integrate only across the illuminated part Ω. This is because obviously $\mathcal{E}' = 0$ in the non-illuminated region. For a general angle θ_0, it is problematic to find the integration area Ω.

However, we can benefit from Wigner's D-matrices which enable rotation of spherical harmonics by angles α, β, γ and take the form $D^j_{m'm}(\alpha, \beta, \gamma) = \mathrm{e}^{-im'\alpha} d^j_{m'm}(\beta) \mathrm{e}^{-im\gamma}$. Here, $d^j_{m'm}$ presents minor Wigner d-matrices, usually specified in classical literature[11] (e.g. Wigner, 1959).

[11] The strategy for calculating the a_{nk} coefficients is to perform the integration across the hemisphere for the case of $\theta_0 = 0$ and apply Wigner's D-operator on the spherical function $Y_{nk}(\theta, \phi)$ where the corresponding Euler angles are $\alpha = 0, \beta = \theta_0, \gamma = 0$. Therefore $a_{nk} = \int_{\Omega^+} \mathcal{E}'(0, \theta, \phi, \zeta) \sum\limits_{m'=-n}^{n} D^n_{m'k}(\theta_0) Y^*_{nm'}(\theta, \phi)\, d\Omega$.

Let us highlight that in our problem, the coefficients $a_{nk}(\theta_0, \zeta)$ can further be separated to the form $a_{nk}(\theta_0, \zeta) = b_{nk}(\theta_0)\zeta^k$. The meaningful terms correspond to $n = 0$ (monopole) and $n = 1$ (dipole terms). It holds that

$$b_{00} = a_{00} = \frac{\sqrt{\pi}}{2}, \qquad b_{10} = \sqrt{\frac{\pi}{3}}\cos\theta_0, \qquad b_{1\pm1} = \mp\sqrt{\frac{\pi}{6}}\sin\theta_0. \tag{1.56}$$

Since $a_{00}Y_{00} = \frac{\sqrt{\pi}}{2} \cdot \frac{1}{2\sqrt{\pi}} = \frac{1}{4}$, it is apparent that this monopole term corresponds to $\mathcal{E}'_{\mathrm{av}}$ because it must hold that $\mathcal{E}' = \frac{1}{4} + \Delta\mathcal{E}'$.

Similar to the source terms $\mathcal{E}'$, $\Delta\mathcal{E}'$ respectively, the $\Delta T'(r', \theta, \phi, \zeta)$ term can also be expressed using spherical harmonics. Let

$$\Delta T'(r', \theta, \phi, \zeta) = \sum_{n\geq1}\sum_{k=-n}^{n} t'_{nk}(r', \zeta)Y_{nk}(\theta, \phi), \tag{1.57}$$

where we can perform an additional separation $t'_{nk}(r', \zeta) = \tau'_{nk}(r')\zeta^k$. The subsequent procedure would again be based on solving the heat equation (1.51) with the corresponding boundary conditions (1.53) and it is discussed in Vokrouhlický (1998a). It can be shown that in a first approximation, it holds that

$$\Delta T'(R', \theta, \phi, \zeta) = \frac{1}{\sqrt{2}(1+\lambda)}\left\{b_{10}(\theta_0)Y_{10}(\theta, \phi) + \frac{b_{11}(\theta_0)\zeta}{1 + \frac{\lambda}{1+\lambda}\psi(\sqrt{-i}R')}Y_{11}(\theta, \phi) + C.C.\right\}, \tag{1.58}$$

where $C.C.$ denotes a complex conjugate expression and $\lambda \equiv \Theta/\sqrt{2}R'$. Similarly in the system fixed with regard to the Sun, where we do not expect an explicit temporal dependence ζ

$$\Delta T'(R', \vartheta, \varphi) = \frac{1}{\sqrt{2}(1+\lambda)}\left\{b_{10}(\theta_0)Y_{10}(\vartheta, \varphi) + \frac{b_{11}(\theta_0)}{1 + \frac{\lambda}{1+\lambda}\psi(\sqrt{-i}R')}Y_{11}(\vartheta, \varphi) + C.C.\right\}. \tag{1.59}$$

The fraction in the second term of this expression can be assumed to take the form

$$\frac{1}{1 + \frac{\lambda}{1+\lambda}\psi(z)} = \frac{A(x) + iB(x)}{C(x) + iD(x)} = E(x)\mathrm{e}^{i\delta(x)}, \tag{1.60}$$

where $z = \sqrt{-i}R'$ and $x = \sqrt{2}R'$. It then certainly holds that $z = \frac{1}{2}(1-i)x$.

Let us now specify the intermediate steps leading to the explicit forms of functions $A(x), B(x), C(x)$ and $D(x)$. It can be shown that the complex function $\psi(z)$ is related to the spherical Bessel function of the first order $j_1(z)$ by the expression (Vokrouhlický, 1998a)

$$\psi(z) = \frac{z}{j_1(z)}\frac{d}{dz}j_1(z) - 1. \tag{1.61}$$

If $j_1(z) = \frac{\sin z}{z^2} - \frac{\cos z}{z}$, then

$$\psi(z) = \frac{(z^2-3)\sin z + 3z\cos z}{\sin z - z\cos z}. \tag{1.62}$$

After a brief calculation, it turns out that

$$\frac{1}{1+\frac{\lambda}{1+\lambda}\psi(z)} = \frac{P(z)}{P(z)+Q(z)}, \tag{1.63}$$

where

$$\begin{aligned} P(z) &= (\mathrm{e}^{2iz}-1) - iz(\mathrm{e}^{2iz}+1), \\ Q(z) &= \frac{\lambda}{1+\lambda} \times \left[(z^2-3)(\mathrm{e}^{2iz}-1) + 3iz(\mathrm{e}^{2iz}+1)\right]. \end{aligned} \tag{1.64}$$

It is easy to show[12] that $P(z) = A(x) + iB(x)$, $C(x) = A(x) + \mathrm{Re}\{Q(z)\}$ and $D(x) = B(x) + \mathrm{Im}\{Q(z)\}$. Then

$$A(x) = -(x+2) - \mathrm{e}^x[(x-2)\cos x - x\sin x], \tag{1.65}$$

$$B(x) = -x - \mathrm{e}^x[x\cos x + (x-2)\sin x], \tag{1.66}$$

$$C(x) = A(x) + \frac{\lambda}{1+\lambda}\{3(x+2) + \mathrm{e}^x[3(x-2)\cos x + x(x-3)\sin x]\}, \tag{1.67}$$

$$D(x) = B(x) + \frac{\lambda}{1+\lambda}\{x(x+3) - \mathrm{e}^x[x(x-3)\cos x - 3(x-2)\sin x]\}. \tag{1.68}$$

1.1.3 Consequences on the dynamics

It is apparent that the Yarkovsky effect acts on the osculating orbit of the body through additional perturbing acceleration. For a quantitative description of the Yarkovsky force, it is necessary to know the form of the function $r_{\mathrm{th}}(\mu, \mu_0, \phi)$ (1.10). Our further considerations are based on Lambert's model. We start with the known relation between the energy and the momentum of a photon $E = pc$, where c is the speed of light.

Let us imagine the situation (Fig. 1.4), when the surface element dS radiates in time dt a packet of radiation dE in the direction $\mathbf{n}$ to the solid angle $d\Omega$. The corresponding change of momentum of the body is then $\frac{d\mathbf{p}}{dt} = -\frac{1}{c}\frac{dE}{dt}\mathbf{n}$. It certainly holds that

$$\frac{d\mathbf{p}}{dt} = -\frac{1}{c} I(\theta, \theta_0, \phi)\cos\theta \, dS \, d\Omega \, \mathbf{n} \tag{1.69}$$

or, analogously

$$\frac{d\mathbf{p}}{dt} = -\frac{1}{c} I(\mu, \mu_0, \phi)\mu^2 \, dS \, d\Omega \, \mathbf{n}_\perp. \tag{1.70}$$

The change of the momentum of the body after radiating in all the directions from the surface element dS is then

$$\frac{d\mathbf{p}}{dt} = -\frac{1}{c} dS \, \mathbf{n}_\perp \int_{\Omega^+} I(\mu, \mu_0, \phi)\mu^2 \, d\Omega = -dS \, \mathbf{n}_\perp \frac{I_b}{c} \int_{\Omega^+} r_{\mathrm{th}}(\mu, \mu_0, \phi)\mu^2 \, d\Omega, \tag{1.71}$$

while we expect that it holds in the Lambert model that $r_{\mathrm{th}} = \epsilon = const$. The Yarkovsky acceleration $\mathrm{d}\mathbf{a}_Y$ is then

$$\mathrm{d}\mathbf{a}_Y = -\frac{2}{3}\frac{\epsilon\sigma T^4(R, \theta, \phi, \zeta)}{mc} \, dS \, \mathbf{n}_\perp(\theta, \phi). \tag{1.72}$$

[12] We remind that $\sin z = \frac{1}{2i}(\mathrm{e}^{iz} - \mathrm{e}^{-iz})$ and $\cos z = \frac{1}{2}(\mathrm{e}^{iz} + \mathrm{e}^{-iz})$.

The complete contribution from all the surface elements is obtained by integration over the whole surface of the body[13]

$$\begin{aligned}\mathbf{a}_Y &= -\frac{2}{3}\frac{\epsilon\sigma}{mc}\int_S T^4(R,\theta,\phi,\zeta)\mathbf{n}_\perp(\theta,\phi)\,dS \\ &\approx -\frac{8}{3}\frac{\epsilon\sigma}{mc}T_{\mathrm{av}}^3\int_S \Delta T(R,\theta,\phi,\zeta)\mathbf{n}_\perp(\theta,\phi)\,dS. \end{aligned} \tag{1.73}$$

For illustration, we will now calculate the Z-coordinate of the Yarkovsky force f_Z acting on the unit mass of the body in the XYZ coordinate system. We will use (1.73) and the result of (1.59). It, therefore, holds that

$$\begin{aligned} f_Z &= -\frac{2}{3}\frac{\epsilon\sigma}{mc}\int_S T^4(R,\vartheta,\varphi)\mathrm{n}_{\perp z}(\vartheta,\varphi)\,dS \\ &\approx -\frac{8}{3}\frac{\epsilon\sigma}{mc}T_{\mathrm{av}}^3\int_S \Delta T(R,\vartheta,\varphi)\mathrm{n}_{\perp z}(\vartheta,\varphi)\,dS = \\ &= -\frac{4}{3}\frac{\epsilon\sigma}{mc}T_{\mathrm{av}}^3 T_*\frac{\cos\theta_0}{\sqrt{2}(1+\lambda)}\int_S \cos^2\vartheta\,dS = \\ &= -\frac{1}{3}\frac{\epsilon\sigma}{mc}T_*^4R^2\frac{\cos\theta_0}{1+\lambda}\int_S \cos^2\vartheta\,d\Omega = \\ &= -\frac{4\alpha}{9}\Phi\frac{\cos\theta_0}{1+\lambda}, \end{aligned} \tag{1.74}$$

while $\Phi \equiv \pi R^2\mathcal{E}_*/mc$. In a similar manner, it can be shown that

$$f_X + if_Y = -\frac{4\alpha}{9}\Phi\frac{\sin\theta_0}{1+\lambda}E_{R'}\mathrm{e}^{-i\delta_{R'}}, \tag{1.75}$$

where $E_{R'} \equiv E(\sqrt{2}R')$ a $\delta_{R'} = \delta(\sqrt{2}R')$. Considering that f_X and f_Y are functions of λ, they must depend on Θ and R'. The equations for f_X and f_Y can be derived in a rather complicated manner, whereupon

$$f_X = -\frac{4\alpha}{9}\Phi\sin\theta_0\frac{1+\kappa_1\Theta}{1+2\kappa_1\Theta+\kappa_2\Theta^2}, \tag{1.76}$$

and

$$f_Y = -\frac{4\alpha}{9}\Phi\sin\theta_0\frac{\kappa_3\Theta}{1+2\kappa_1\Theta+\kappa_2\Theta^2}. \tag{1.77}$$

The coefficients κ_1, κ_2 and κ_3 are the functions of R'. Let us outline the derivation of these functions. We first compare (1.76) and (1.77) with the equation (1.75) which yields

$$\mathrm{Re}\left\{\frac{1}{1+\lambda}E(x)\mathrm{e}^{-i\delta(x)}\right\} = \frac{1+\kappa_1\Theta}{1+2\kappa_1\Theta+\kappa_2\Theta^2}, \tag{1.78}$$

$$\mathrm{Im}\left\{\frac{1}{1+\lambda}E(x)\mathrm{e}^{-i\delta(x)}\right\} = \frac{\kappa_3\Theta}{1+2\kappa_1\Theta+\kappa_2\Theta^2}. \tag{1.79}$$

From (1.60), it follows that

$$\left(\frac{AC+BD}{C^2+D^2}\right) + i\left(\frac{BC-AD}{C^2+D^2}\right) = G(x) + iH(x) = E(x)\mathrm{e}^{i\delta(x)}, \tag{1.80}$$

[13]The term T_{av}^4 provides a zero contribution after integrating over the whole surface of the body and, therefore, does not contribute to the overall Yarkovsky effect.

and, therefore

$$\frac{x}{x+\Theta}\left(\frac{AC+BD}{C^2+D^2}\right)=\frac{1+\kappa_1\Theta}{1+2\kappa_1\Theta+\kappa_2\Theta^2}, \tag{1.81}$$

$$\frac{x}{x+\Theta}\left(\frac{AD-BC}{C^2+D^2}\right)=\frac{\kappa_3\Theta}{1+2\kappa_1\Theta+\kappa_2\Theta^2}. \tag{1.82}$$

Let us now turn our attention to equations (1.65)-(1.68) and define functions $C'(x)$ and $D'(x)$ so that

$$C=A+\frac{\Theta}{x+\Theta}C', \qquad D=B+\frac{\Theta}{x+\Theta}D', \tag{1.83}$$

while it apparently holds that

$$C'(x)=3(x+2)+\mathrm{e}^x[3(x-2)\cos x+x(x-3)\sin x], \tag{1.84}$$

$$D'(x)=x(x+3)-\mathrm{e}^x[x(x-3)\cos x-3(x-2)\sin x]. \tag{1.85}$$

Substituting (1.83) to (1.81) and (1.82) we obtain

$$\kappa_1(x)=\frac{A^2(x)+B^2(x)+A(x)C'(x)+B(x)D'(x)}{x[A^2(x)+B^2(x)]}, \tag{1.86}$$

$$\kappa_2(x)=\frac{A^2(x)+B^2(x)+C'^2(x)+D'^2(x)+2A(x)C'(x)+2B(x)D'(x)}{x^2[A^2(x)+B^2(x)]}, \tag{1.87}$$

$$\kappa_3(x)=\frac{A(x)D'(x)-B(x)C'(x)}{x[A^2(x)+B^2(x)]}, \tag{1.88}$$

also keeping in mind that $x=\sqrt{2}R'$. Applying (1.76) and (1.77) in (1.24) we easily show that the diurnal Yarkovsky drift is

$$\left(\frac{da}{dt}\right)_d=-\frac{8\alpha}{9}\frac{\Phi}{n}\frac{E_{R'}\sin\delta_{R'}}{1+\lambda}\cos\gamma+\mathcal{O}(e) \tag{1.89}$$

or

$$\left(\frac{da}{dt}\right)_d=\frac{8\alpha}{9}\frac{\Phi}{n}\frac{\kappa_3\Theta}{1+2\kappa_1\Theta+\kappa_2\Theta^2}\cos\gamma+\mathcal{O}(e), \tag{1.90}$$

where γ is the obliquity.
Let us also mention the seasonal Yarkovsky drift (Vokrouhlický, 1999)

$$\left(\frac{da}{dt}\right)_s=\frac{4\alpha}{9}\frac{\Phi}{n}\frac{E_{R'}\sin\delta_{R'}}{1+\lambda}\sin^2\gamma+\mathcal{O}(e) \tag{1.91}$$

or

$$\left(\frac{da}{dt}\right)_s = -\frac{4\alpha}{9}\frac{\Phi}{n}\frac{\kappa_3\Theta_n}{1+2\kappa_1\Theta_n+\kappa_2\Theta_n^2}\sin^2\gamma + \mathcal{O}(e), \tag{1.92}$$

where n is the mean motion and $\Theta_n = \frac{\Gamma\sqrt{n}}{\epsilon\sigma T_*^3}$.

Thus, the Yarkovsky drift depends on the composition of the body or the composition of the surface layer, the distance from the Sun, the obliquity, the diameter of the body and other thermophysical parameters. It is then technically impossible to graphically illustrate the complete general characteristic of the Yarkovsky effect. However, if we limit ourselves to a smaller set of input parameters, we can plot the values of the Yarkovsky drift for selected cases (Fig. 1.7).

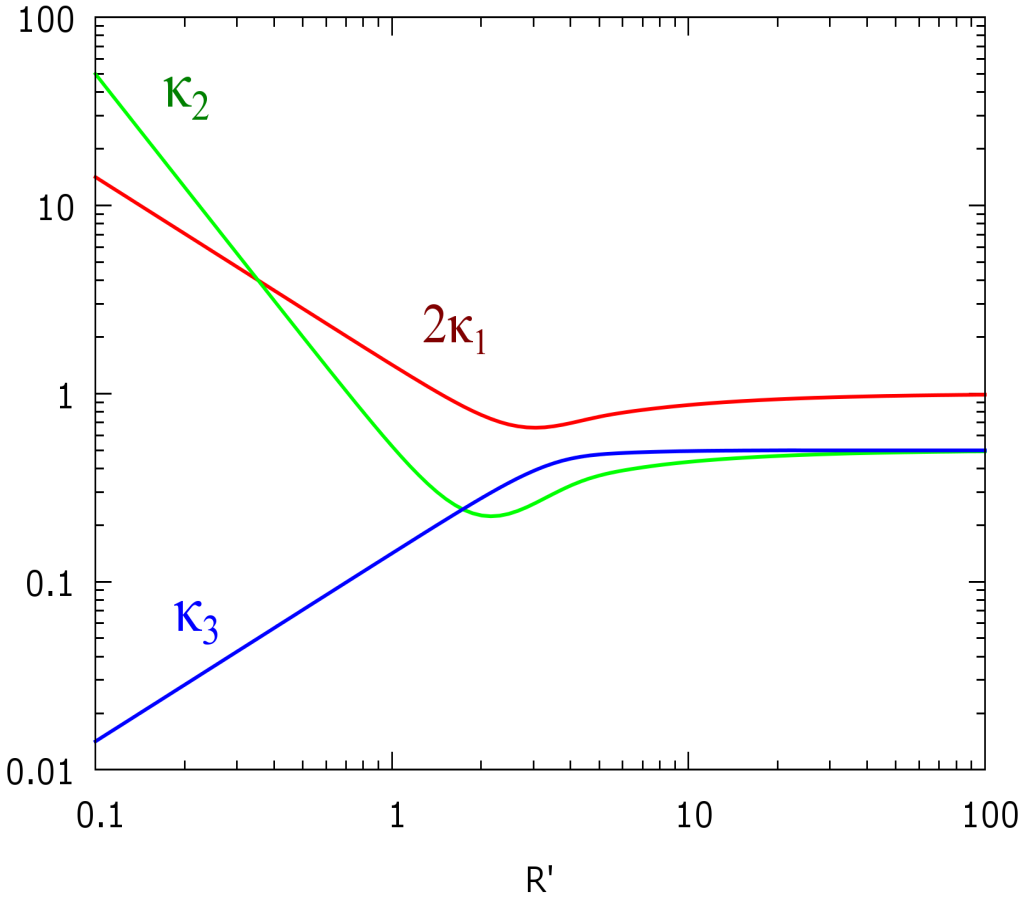

Figure 1.6: The dependence of the functions $\kappa_1, \kappa_2, \kappa_3$ on R' according to expressions (1.86) - (1.88).

The dependence on obliquity γ

For the sake of further considerations, let us note that thanks to $R' > 0$, the values of functions $\kappa_1(x), \kappa_2(x)$ and $\kappa_3(x)$ are positive. It is then apparent from the dependence of the semi-major axis drift on the obliquity γ that (a) for the

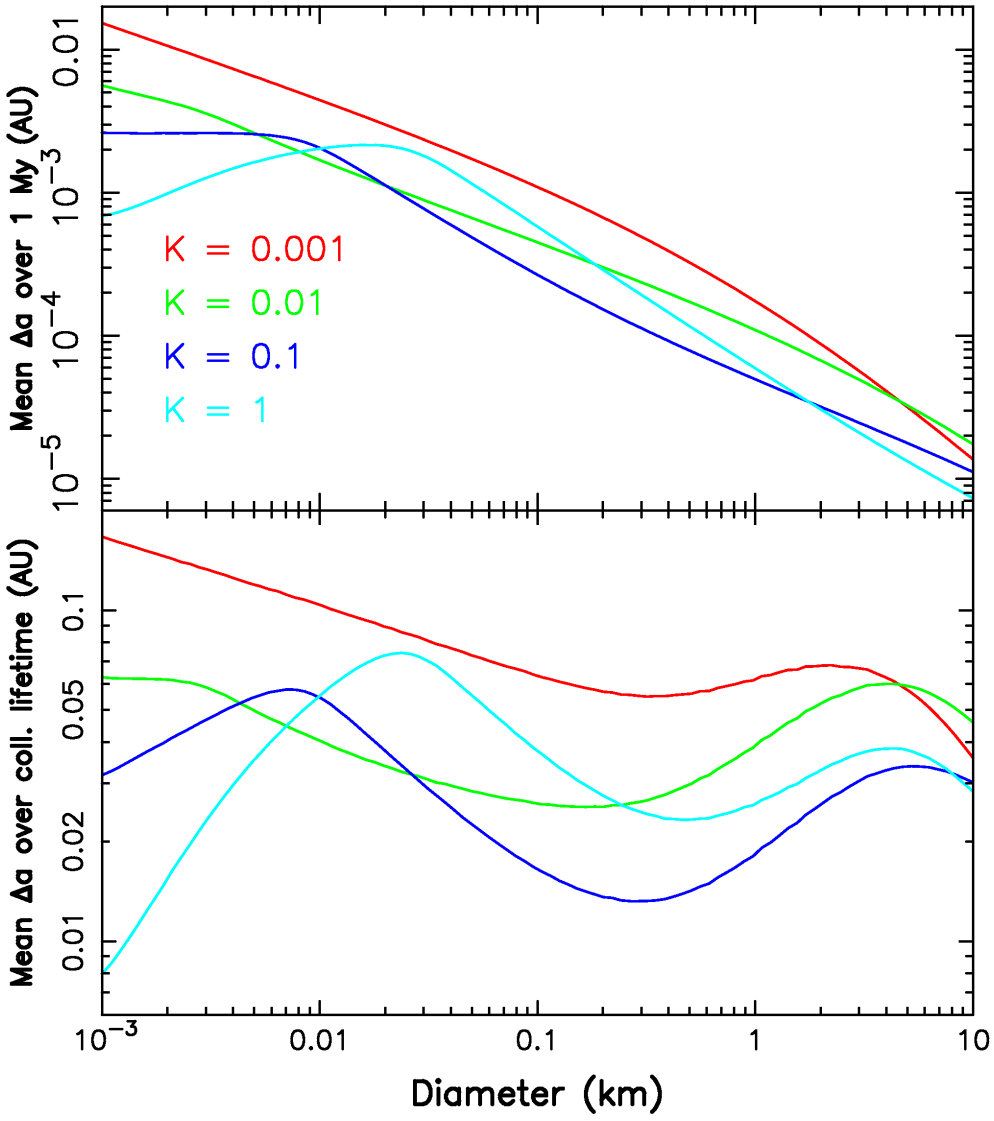

Figure 1.7: The upper figure shows the mean change of the semi-major axis Δa for asteroids in the inner main belt in the period 1 Myr. Both variants of the Yarkovsky effect were considered. The heat capacity was, in this case, $C_p = 680$ J kg^{-1} K^{-1}. The density of the surface layer and the bulk density were 1.7 g cm^{-3} and 2.5 g cm^{-3}, respectively. The period of rotation was for the chosen asteroid diameter D [m] calculated from the expression $P = 5(D/2)$ s (Farinella et al., 1998), which well captures the observed distribution of rotation periods of fragments formed by laboratory disintegration of smaller bodies (≈ 20 cm) and it is also in good agreement with observations of actual asteroids. Plotted are the cases of different thermal conductivities $K = 0.001, 0.01, 0.1$ and 1.0 W m^{-1} K^{-1}. Let us note that at lower values of thermal conductivity $K \approx 0.001$ m^{-1} K^{-1}, corresponding to regolith-covered bodies, the diurnal variant of the Yarkovsky effect is dominant. At higher values of K, the seasonal variant is dominant (Farinella et al., 1998). The lower figure demonstrates the mean change of the semi-major axis during the estimated collisional lifetime of the asteroids (Bottke et al., 2005).

diurnal variant, prograde rotation implies $da/dt > 0$, while retrograde rotation implies $da/dt < 0$ and (b) for the seasonal variant, $da/dt < 0$ is valid for both the prograde and retrograde rotation. The diurnal Yarkovsky drift takes extremal values if the spin axis lies ($\gamma = 90°$) or is perpendicular ($\gamma = 0° \vee \gamma = 180°$) to the orbital plane. The seasonal Yarkovsky drift is zero if $\gamma = 0°$ and maximum if $\gamma = 90°$.

The dependence on size R

Let us first consider the limit case of large bodies $R' >> 1$ (bodies larger than units of meters) with the corresponding penetration depth l_s. If $R' \to \infty$ then $\kappa_1 \to 1$, $\kappa_2 \to 1/2$ and $\kappa_3 \to 1/2$. In this limit, the dependence of the semi-major axis drift on the size R can only originate from the term $\Phi \equiv \pi R^2 \mathcal{E}_*/mc$ where $m \sim R^3$ and, therefore, $da/dt \sim 1/R$ (cf. Fig. 1.7). If $R' << 1$, then $\kappa_1 \sim 1/R'$, $\kappa_2 \sim 1/R'^2$ and $\kappa_3 \sim R'$ in the limit of $R' \to 0$. Consequently, it is evident that $da/dt \sim R^2$ which is consistent with the expected result, whereupon the Yarkovsky effect should vanish for very small bodies. The maximum drift is achieved for $R' \approx 1$.

The dependence on heliocentric distance d

Let us independently analyze the diurnal and seasonal variant of the effect. For the diurnal variant, we assume the usual situation of large Θ and R'. We then easily see that $da/dt \sim \Phi/(n\Theta)$. The power of four of the subsolar temperature T_*^4 depends on the sunlight flux E_* which decreases with the square of distance d^2. From this, it immediately follows that $T_* \sim 1/d^{1/2}$. From the dependence of the thermal parameter on the subsolar temperature $\Theta \sim 1/T_*^3$, it follows that $\Theta \sim d^{3/2}$. The product $n\Theta$ is then virtually independent of the distance d and the term where the distance has the main impact is $\Phi \sim 1/d^2$. Finally, we can say that for the diurnal variant, it approximately holds that $da/dt \sim 1/d^2$.

For the seasonal variant, one has to take more caution. Firstly, an approximation similar to the previous case (i.e. $da/dt \sim \Phi/(n\Theta_n)$) is not justified in all cases. For example, for the Kuiper belt bodies, the penetration depths of the thermal wave can reach up to $l_s \approx 0.1$ km, which prevents us from using the limit $R' \to \infty$. The da/dt drift for the seasonal variant is, therefore, rather flat and corresponds approximately to $\sim d$.

	ρ [kg/m^3]	K [W/m/K]	C [J/kg/K]
Basalt	3500	2.65	680
Iron-rich	8000	40	500
Regolith-covered	1500	0.0015	680

Table 1.1: Thermal parameters of some materials. Source: Farinella et al. (1998).

1.1.4 Detection and selected applications

Let us first mention some key information about the detection of the Yarkovsky effect. It is apparent from the previous section that the Yarkovsky effect

has long-term influence on the semi-major axis of the body. The effect causes both radial and transversal shift in the body's orbit. Consider the perturbation equation (e.g. Danby, 1992)

$$\frac{dn}{dt} = -\frac{3}{2}\frac{n}{a}\frac{da}{dt}, \tag{1.93}$$

where n is the mean motion. The change of the mean anomaly ΔM during a time interval Δt is given by

$$\Delta M = -\frac{3}{4}\frac{n}{a}\frac{da}{dt}(\Delta t)^2. \tag{1.94}$$

The Yarkovsky drift da/dt then induces transversal and radial shifts in the orbit $\Delta\tau \approx a\eta\Delta M$ and $\Delta r \approx ae\Delta M/\eta$, where $\eta = \sqrt{1-e^2}$. Let us note that the observations do not allow us to directly measure the secular changes of the semi-major axis. However, it is possible to measure a shift in its trajectory. The first body, for which the Yarkovsky effect was predicted and then measured was the near-Earth asteroid (6489) Golevka. Vokrouhlický et al. (2000) predicted, from the then-available radar and astrometric data, the positions of Golevka during its close approach to Earth in 2003. They made the prediction in two versions - one without and one with considering the Yarkovsky effect. Radar observations and the subsequent analysis of Golevka's orbit (Chesley et al., 2003) showed very good agreement with the prediction involving the Yarkovsky effect and a significant deviation between real trajectory and the trajectory calculated from the purely gravitational model.

Another body, for which the Yarkovsky effect was detected using a range of optical methods is (152563) 1992 BF (Vokrouhlický et al., 2008). There were optical observations available from years 1992-2005 and 4 observations from 1953. The whole data set could not be, however, fitted by a purely gravitational model, unless the Yarkovsky effect was included.

With time, the number of successful detections grew, as well as the number of suspected cases, for which it might be possible to detect the Yarkovsky effect in future (Chesley et al., 2008; Nugent et al., 2012; Farnocchia et al., 2013b). These works are clearly a big motivation for observational astronomy. Note that the most accurate measurement was achieved for the asteroid (101955) Bennu. The smallest body, for which the Yarkovsky effect was detected is 2009 BD ($D \approx 4$ m), among the largest are (2100) Ra-Shalom and (4179) Toutatis (Nugent et al., 2012; Farnocchia et al., 2013b). A more comprehensive list can be found in Vokrouhlický et al. (2015a) and Chesley et al. (2016).

To make a preliminary test if and to what extent the Yarkovsky effect influences the orbital evolution of an asteroid, its available astrometric data is fitted using an additional transversal component of acceleration $a_T = A_2/r^2$, where r is the heliocentric distance (Farnocchia et al., 2013b). This method is very advantageous because it allows us to detect the Yarkovsky effect and the semi-major axis drift without knowing the exact thermophysical parameters of the object.

Transport of meteoroids and NEAs from the main belt

The first studies that considered the Yarkovsky effect as the possible cause of meteoroid transport from the main belt towards the Earth are Öpik (1951) and

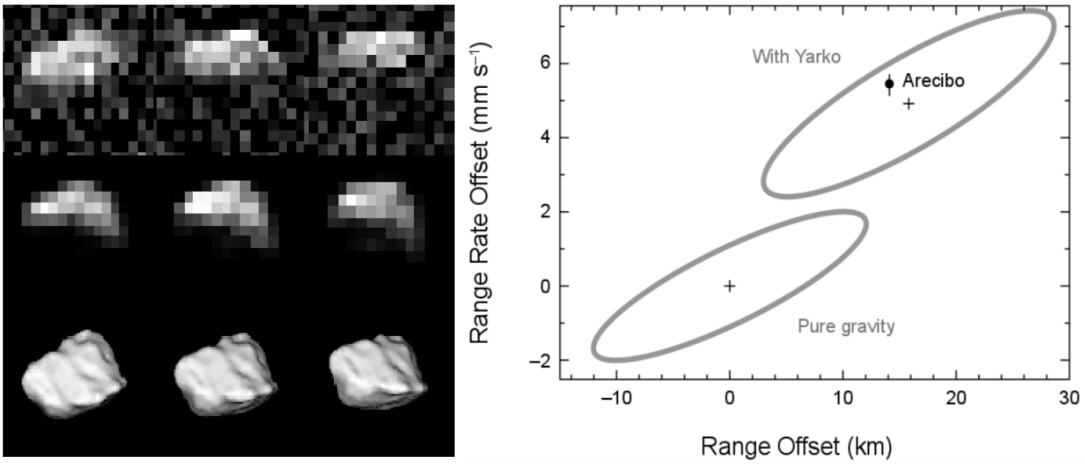

Figure 1.8: On the left are the radar observations and the computer model of the near-Earth asteroid (6489) Golevka (Source: NASA). On the right is the radar measurement of Golevka's position from the Arecibo Observatory in comparison to the prediction of a purely gravitational model and the model including the Yarkovsky effect. Plotted are also the corresponding confidence bands (3σ) for each of these models. Source: Chesley et al. (2003).

Peterson (1976). Today's view on the transport mechanisms due to the Yarkovsky effect, however, originates from more recent analyses by Farinella et al. (1998), Vokrouhlický and Farinella (2000) and Bottke et al. (2000b).

If we considered direct transport of meteoroids by spiraling towards the Sun as a consequence of the Yarkovsky effect, it would appear that e.g. for meter-sized objects, this effect would happen at non-realistic time scales. The bodies would, furthermore, have to have uncommon thermophysical parameters. On the first sight, it could then seem that the Yarkovsky effect cannot be responsible for migration of main belt objects towards the Sun.

Let us consider a rather different mechanism, i.e. transport of meteoroids to orbital resonant regions. The capture of objects by strong resonances, such as the J3/1 resonance or the secular resonance ν_6 leads to significant perturbations to their orbits. Vokrouhlický and Farinella (2000) have shown that meteoroids and asteroidal fragments which have been created from collisions in the inner or central parts of the main belt could have been, due to the Yarkovsky effect, transported to these orbital resonance regions. The capture of an object in a resonance leads to an increase in the eccentricity of its orbit, which can intersect the orbits of the inner planets. In most cases, the eccentricity grows to such an extent ($e \to 1$) that the object either finishes its journey in the Sun or is scattered by the planets. Approximately 1% of these bodies collide with the Earth or the Moon.

The transport model mentioned above can also effectively explain the distribution of CRE (cosmic ray exposure) values of meteorites (Fig. 1.9). It is also capable of explaining, why the measured CRE values are larger than the expected residence time of the bodies in the resonances. This is because the fragments are already under the influence of the cosmic radiation when they are being transported to the resonance. Using this model, we can also explain why the exposure times are almost an order of magnitude higher for iron meteorites compared to

stony meteorites.

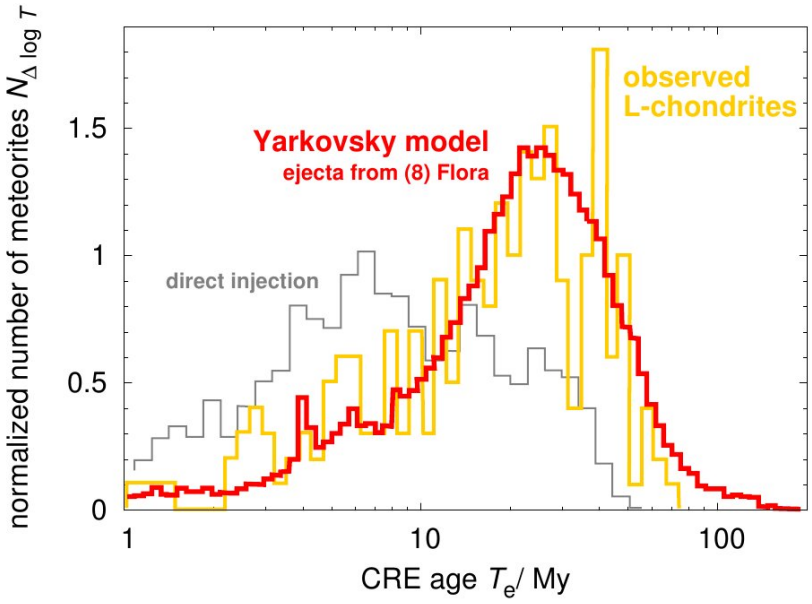

Figure 1.9: Measurements of the exposure times of L-chondrites (yellow histogram). The red line illustrates the results from the numerical propagation of fragments escaping the parent asteroid (8) Flora, considering the Yarkovsky force (Vokrouhlický and Farinella, 2000). The gray line illustrates the same but without taking into account the Yarkovsky effect. It is apparent that the model (red) well describes the real data (yellow). Taken from: Brož (2006).

Collisions in the main belt produce a number of fragments which are exposed to cosmic radiation during four stages. They (I) travel from the point of their origin to the resonance, (II) remain in the resonance for some time[14], (III) gradually change their orbits which start intersecting Earth's orbit, (IV) take collision course with the Earth and collide with it. The Yarkovsky effect then not only increases the number of NEAs but also maintains the flux of meteoroids to the collision course with Earth.

Morbidelli and Vokrouhlický (2003) simulated the origin of kilometer-sized NEAs due to the influence of Yarkovsky and YORP effects on the main belt objects. To address this task, one has to know the cumulative distribution of absolute magnitudes of NEAs and MBAs. The cumulative distribution of the main belt objects fulfills $N(< H) \simeq 10^{\gamma H}$ where $\gamma = 0.25$ and $15.5 < H < 18$ (Morbidelli and Vokrouhlický, 2003; Jedicke and Metcalfe, 1998). For NEAs in the same range of H, it holds that $\gamma = 0.35$ (Rabinowitz et al., 2000; Bottke et al., 2000a; Stuart, 2001). Morbidelli and Vokrouhlický (2003) found that the flux of new fragments to the resonant regions J3/1 and ν_6 is $150 - 200$ objects in 1 Myr. The model that the authors used gives for the NEAs $\gamma = 0.33$, which is a very good agreement.

Let us note that the Yarkovsky effect influences the overall structure of the main belt and the orbital evolution of individual populations. It can also supply the non-stable parts of the resonance regions with new bodies. Let us, for instance, mention the 2/1 resonance with Jupiter ($a \approx 3.27$ au). In this resonance,

[14]Up to 50% of smaller ($\approx$ 1 m) regolith bodies can even jump over the 3/1 resonance.

no objects were originally expected. In 1935, however, a minor planet (1362) Griqua was discovered in this region, being the first in tens and hundreds of newly discovered objects. In the present day, we distinguish 3 fundamental populations in the J2/1 resonance, classified according to their lifetimes. They are (a) the stable population (Zhongguo), (b) marginally stable population (Griqua) and (c) unstable population (Zulu). While the stable populations exhibit lifetimes of up to $\approx$ 4 Gyr (Chrenko et al., 2015), the objects on the unstable trajectories within this resonance are being gradually supplied by the Yarkovsky effect from Themis family (Brož et al., 2005). Brož and Vokrouhlický (2008) have shown that potential collision families would be, in the 2/1 resonance with Jupiter, scattered in no more than 1 Gyr. It would not then be possible to identify the older of these objects as clusters in the space of orbital elements. At present, however, 370 bodies in 2/1 resonance with Jupiter are known (Chrenko et al., 2015). Brož and Vokrouhlický (2008) have also studied the action of the Yarkovsky effect in the resonances. They found that a systematic increase of eccentricity in resonances helps objects with $D < 20$ km escape the resonance, rather than the semi-major axis drift.

At this point, however, let us keep in mind that the strong coupling between the Yarkovsky and YORP effects can, in future, reveal several weak points in these considerations. These would be primarily situations, when the obliquities would change rapidly or when there would be tumblers among the mentioned populations. It is also not unambiguously decided, where the L-chondrites, LL-chondrites and H-chondrites originated. It is expected that the LL-chondrites come from the Flora family (or directly the (8) Flora), L-chondrites from the Gefion family and H-chondrites from the asteroid (6) Hebe.

Physical properties of asteroids

Let us, for a moment, disregard the dependence of the Yarkovsky drift on the distance from the Sun. In that situation, it is evident that the semi-major axis drift da/dt depends on a number of thermophysical properties of the object, such as its diameter, mass, obliquity, angular velocity, thermal conductivity, etc. If only da/dt is known, we can use the expression (1.90), limit the value of $\cos\gamma$ and decide whether the object rotates in the prograde or retrograde direction.

The situation is, of course, better if the pole orientation or the angular frequency of rotation ω is known. Knowing $\cos\gamma$ and the diameter D, we can constrain other physical properties of the object, especially the thermal parameter Θ. The diameter of the body can be obtained either directly, from radar observations or derived from the taxonomic type or albedo measurements. Consequently, the space of free parameters comprises the volumetric mass density ρ and the thermal inertia Γ. This situation was investigated by Chesley et al. (2014) for the case of (101955) Bennu asteroid.

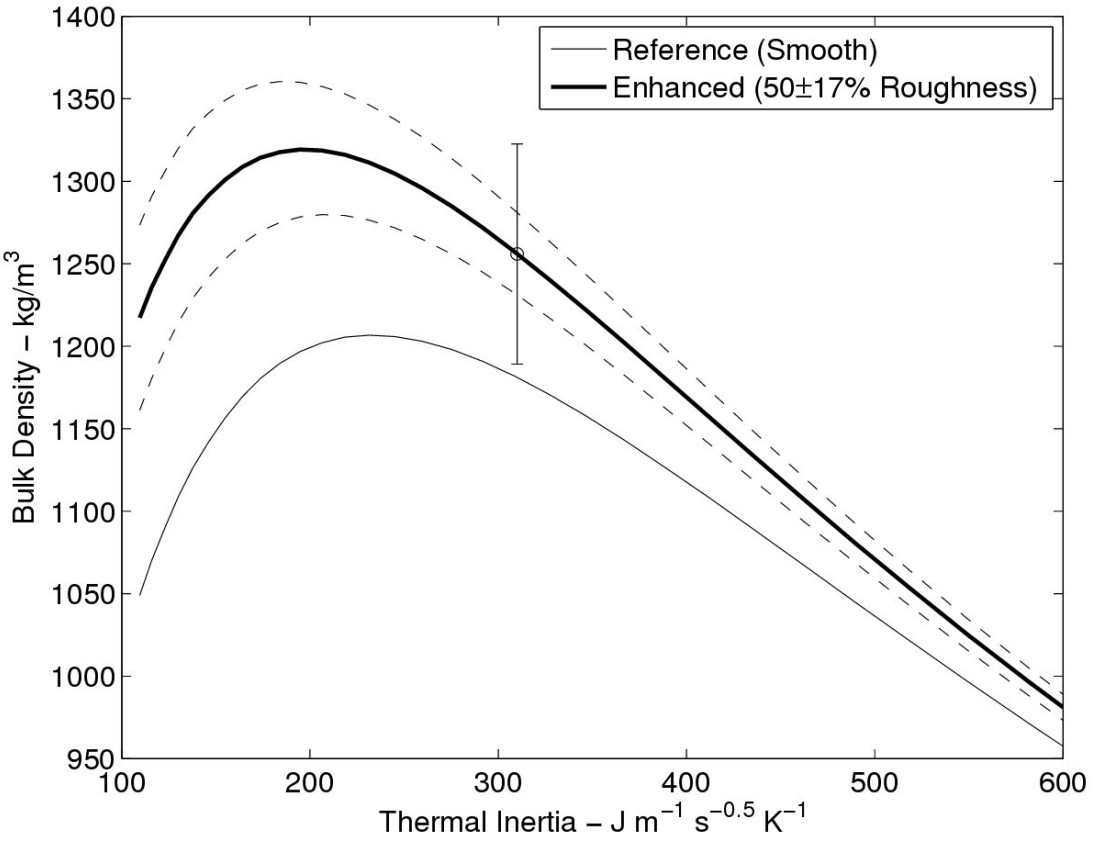

Figure 1.10: The dependence of the volumetric mass density of (101955) Bennu on the value of thermal inertia Γ. The full gray line denotes the solution for ρ and Γ with $da/dt = const.$, assuming a smooth surface and detailed information about the object's shape. The full black line denotes the solution for a rough surface. The dashed lines mark the uncertainty of this solution. Note that Chesley et al. (2014) found $\rho = 1180$ kg m^{-3} for the smooth surface and $\rho = 1260 \pm 70$ kg m^{-3} for the rough surface. The uncertainty of these values includes the uncertainty in the diameter of the body, the obliquity and the thermal intertia. Taken from: Chesley et al. (2014).

Let us mention that the asteroid (101955) Bennu is the target destination of the OSIRIS-REx probe, which was launched in 2016 and is aiming to collect samples from the surface and bring them back to Earth. The expected duration of the mission is 7 years. Other bodies, for which the mass density ρ was obtained using the model of Yarkovsky effect and radar thermophysical measurements are (1862) Apollo (Rozitis et al., 2013), (1620) Geographos (Rozitis and Green, 2014) and (29075) 1950 DA (Rozitis et al., 2014)[15].

The Yarkovsky effect also explains the excess of retrograde rotators among NEAs (La Spina et al., 2004). This observation probably originates in the location of the ν_6 resonance in the inner part of the main belt. Objects that drift towards this resonance come predominantly from the outer parts, which implies $da/dt < 0$ and, therefore, $\cos\gamma < 0$ (Morbidelli and Vokrouhlický, 2003).

[15]In the case of the rubble-pile asteroid (29075) 1950 DA, the influence of cohesive forces acting among individual grains was also studied. These forces apparently act against the centrifugal force and prevent the object from disintegrating.

Asteroid families and pairs

Members of asteroid families and pairs exhibit similar spectral properties and values of orbital elements. In the space of orbital elements, they form more or less numerous clusters. It is thought that they are remnants of catastrophic collisions or disintegration of parent asteroids in the past. Since their formation, the fragments have been under the influence of both the gravitational and non-gravitational perturbations. However, within the last few years it has become possible to constrain the age of a number of asteroid families and pairs using the modeling of the Yarkovsky/YORP effect. Formally, we can divide the families into young ones ($t_{\rm age} < 10$ Myr) and old ones ($t_{\rm age} > 10$ Myr). Very young asteroid families and pairs are discussed in detail in Chapter 3. In this paragraph, we only mention some applications of the Yarkovsky effect when studying the older asteroid families.

As opposed to methods used for determining the age of very young asteroid families (see Chapter 3), it is not possible to reconstruct secular angles (ϖ, Ω) of members of old families, due to deterministic chaos. At the very least, we can build on the proper elements a_p, e_p, i_p which can be understood as quasi-integrals of motion (Knežević et al., 2002). Even though deterministic chaos also gradually perturbs the proper elements, the element a_p for kilometer-sized asteroids is governed primarily by the Yarkovsky effect.

The role of the Yarkovsky effect in the age determination and orbital evolution of asteroid families was first studied for the families Koronis (Bottke et al., 2001) and Eos (Vokrouhlický et al., 2006b). The Koronis family occupies two principal regions in the proper elements space with two different values of e_p, but similar values of i_p (Fig. 1.11). It turns out that the border correponds to the position of the secular resonance $g+2g_5-3g_6$. Numerical propagation of synthetic fragments of the Koronis family spanning over 700 Myr and including the Yarkovsky effect was done by Bottke et al. (2001). Note that Bottke et al. (2001) scaled their size to be ≈ 3 times smaller than the current values to reduce the computational time[16]. This allowed him to reach the expected age of $T_{\rm age} \in [2.5, 3.0]$ Gyr (Marzari et al., 1999; Greenberg et al., 1996) and analyze the post-disintegration evolution of the family members (Fig. 1.11). Bottke et al. (2001) showed that drifting fragments of the Koronis family pass through the resonance $g+2g_5-3g_6$ and their eccentricities increase almost by a step-function (by the value ≈ 0.025), while the values of their inclinations remain unchanged.

The Eos family (> 4000 members) is located in the range $a_p \in [2.99, 3.03]$ au, $e_p \in [0.01, 0.13]$ and $i_p \in [8^\circ, 12^\circ]$. The majority of the fragments is located between the resonances J7/3, J9/4 and the secular resonance $z_1 = g - g_6 + s - s_6$. The strong resonance J7/3 bounds the family from the inside, the weaker resonance J9/4 from the outside[17]. After the disruption of the parent body[18], the family took a rather compact shape in the space of orbital elements. With time, some of the asteroids drifted towards the J7/3, others towards the J9/4 resonance.

[16]The fragments then drift ≈ 3 times faster.

[17]Though some of the bodies did pass this bound during the evolution of the family.

[18]After an impact, the fragments typically spread at velocities in the range of tens m/s.

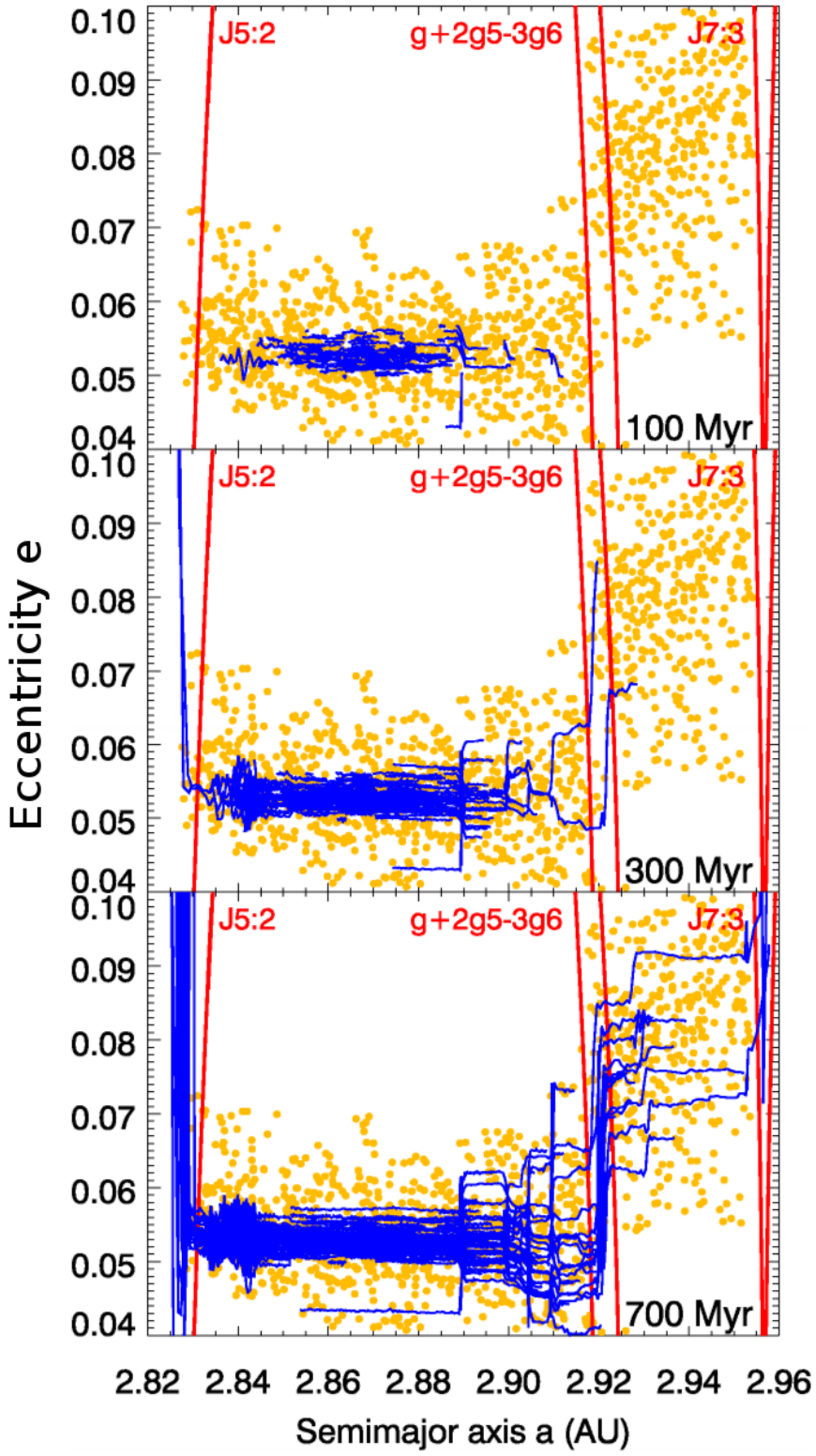

Figure 1.11: Koronis family in proper elements space. Blue lines denote the simulated post-disintegration evolution of 210 synthetic fragments influenced by the Yarkovsky effect. The current distribution of the Koronis family members is marked by yellow points. The resonant regions J5/2, J7/3 and $g + 2g_5 - 3g_6$ are shown. When passing through the resonance $g + 2g_5 - 3g_6$ ($\approx$ 2.92 au), a marked increase in eccentricities is observed. We see a good agreement between the simulated evolution and the current state. Taken from Bottke et al. (2001).

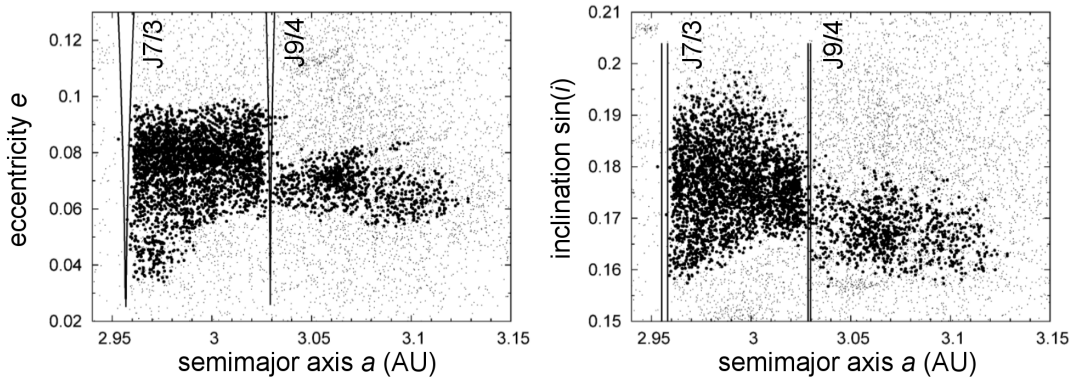

Figure 1.12: Distribution of the Eos family members as obtained from the Hierarchical clustering method (HCM) for $V_c < 50$ m s^{-1} (Bendjoya and Zappalà, 2002). Resonance regions J7/3 and J9/4 are shown. Adapted from Vokrouhlický et al. (2006b).

Upon entering the J7/3 resonance, marked perturbations to the eccentricities and inclinations were introduced and trajectories of some of the members were driven to cross the trajectories of the inner planets. For this reason, we do not observe any large group of Eos family members below this resonance region. Asteroids drifting towards J9/4 are also being scattered but to a much smaller extent than J7/3. This means that a certain percentage got beyond this resonance. Apart from that, some of the Eos family members are trapped in secular resonance z_1. Vokrouhlický et al. (2006b) estimated the age of the Eos family to be $1.3^{+0.15}_{-0.2}$ Gyr by analyzing the distribution of (a_p, H). Let us note that many families exhibit a V-shaped relation between a_p and H, because smaller fragments drift further away from the parent body (Fig. 1.13). This effect can be interpreted by the action of the Yarkovsky force on their post-disintegration evolution. Immediately after the impact, it can be expected that smaller fragments escape at higher velocities and also that they are under stronger influence of the Yarkovsky/YORP effect. The model of Vokrouhlický et al. (2006b) assumes isotropic distribution of the disintegration velocities of the fragments and gradual re-orientation of their spin axes as a consequence of collisions. The input parameters of the model are: (i) the initial velocity of 5 km sized fragments ($V(D) = V \cdot \frac{5\text{km}}{D}$), (ii) the age $T_{\text{age}} \in [0.2, 2.0]$ Gyr, (iii) the extent of the YORP effect c_{YORP} and (iv) the thermal conductivity K. The results of a number of repeated simulations with different input parameters are then compared with the current distribution (a_p, H). Eventually, cases exhibiting the best agreement are recorded. Brož and Morbidelli (2013) made a small correction in the age of the Eos family and found $T_{\text{age}} \in [1.5, 1.9]$ Gyr. They also found that the halo around this family is formed mostly by the scattering of objects which get to the J9/4 resonance due to the Yarkovsky effect.

Other families that have been studied are the Agnia (≈ 2.79 au) and Padua (≈ 2.75 au) families (Vokrouhlický et al., 2006a; Carruba, 2009), located in the central parts of the main belt and close to the z_1 resonance, as well as the Tina family (≈ 2.79 au) close to the secular resonance ν_6 (Carruba and Morbidelli, 2011). In the outer part of the main belt, we can find, for instance, the Sylvia family located in a rather less dense Cybele zone (Vokrouhlický et al., 2010).

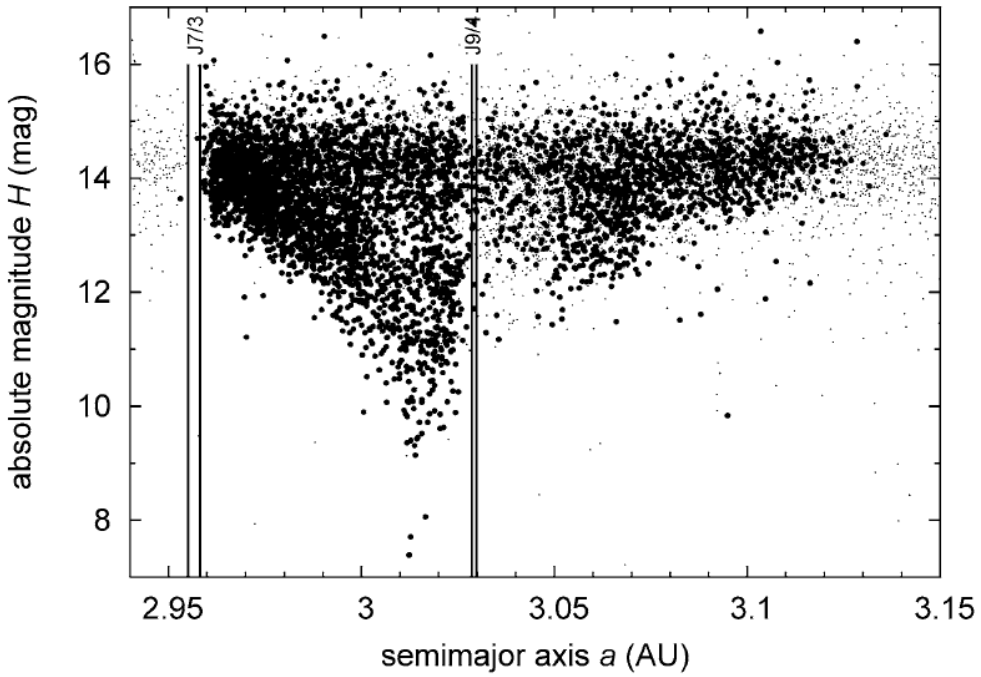

Figure 1.13: The distribution of the Eos family members (black points) in the (a_p, H) space according to the HCM method ($V_c < 50$ m s^{-1}). Grey points denote background asteroids. The lowered concentration of objects in the middle can be a consequence of the YORP effect which, upon disintegration, changes the obliquities towards extremal values. This, in turn, leads to a larger value of the Yarkovsky drift da/dt and the escape of the bodies towards the wings. The limiting $H \approx 17$ corresponds to 1-2 km sized fragments. Source: Vokrouhlický et al. (2006b).

From the interdisciplinary perspective, the Baptistina family ($\approx$ 2.26 au) is certainly of interest. Its age was estimated by Bottke et al. (2007) to be $T_{\rm age} = 160^{+30}_{-20}$ Myr. Bottke et al. (2007) found that the fragments of this family approached the J7/2 and M5/9 resonances due to the influence of the Yarkovsky/YORP effect. These resonances increased their eccentricities to such an extent, that they could intersect the orbits of terrestrial planets. One of the fragments of this family could have impacted the Earth, creating the Chicxulub crater[19] (P $\approx$ 90 %), later another could have created the Tycho crater on the Moon ($P \approx 70\%$). A more recent study of Masiero et al. (2012) discusses a rather broader interval of ages. Considering the volumetric mass density of $\approx$ 1.3 g cm^{-3}, it seems probable that the age is around $\approx$ 80 Myr while for $\rho \in [1.6, 2.8]$ g cm^{-3}, the range of possible ages is 140-320 Myr. However, if the age were indeed close to 80 Myr, it would be complicated to make the fragments intersect the Earth's orbit within 15 Myr after the family formation. This controversial topic is discussed in Delbo' et al. (2012).

[19]Slightly less than 65 million years ago.

1.2 YORP effect

1.2.1 Initial remarks

The YORP abbreviation (*Yarkovsky–O'Keefe–Radzievskii–Paddack*) was first introduced in Rubincam (2000) and corresponds to the initials of the names of notable astronomers who established the basics of the modern theory of Yarkovsky and YORP effect (Radzievskii, 1952; Paddack, 1969, 1973; Paddack and Rhee, 1975; O'Keefe, 1976). In the section about the Yarkovsky effect, we discussed not only the theory but also the orbital implications. The main emphasis was put on studying the perturbations to the semi-major axis. To construct a linear analytical theory of the Yarkovsky effect, we assumed the asteroids to be spherical.

The assumption of a smooth spherical body, however, excludes the existence of a torque caused by radiation leaving the body's surface. The situation does change markedly if we use a more realistic irregular shape.

Asymmetric radiation from the surface then causes a weak torque, which affects the rotation of the body and, therefore, obviously influences the Yarkovsky effect. The long-term non-gravitational perturbations then result from the coupling between the Yarkovsky and YORP effect.

1.2.2 The mechanism and the mathematical description

Let us consider an infinitesimal surface element of an arbitrary asymmetrical body. If radiation leaves this surface element, either by scattering or thermal emission, a reaction force $\mathrm{d}\mathbf{f}$ appears. This force acts, in the case of an isotropic model ($r_{\mathrm{sca}}(\mu_0)$, $r_{\mathrm{th}}(\mu_0)$) in the direction opposite to the normal $\mathbf{n}_\perp$. If $\mathrm{d}\mathbf{f}$ has a non-zero angle with the position vector $\mathbf{r}$ of the surface element, then it contributes to the total torque. Let us remind the formal relations (1.23)

$$\mathbf{T}_{\mathrm{sca}} = \int_S \mathbf{r} \times \mathrm{d}\mathbf{f}_{\mathrm{sca}} \qquad \mathbf{T}_{\mathrm{th}} = \int_{S'} \mathbf{r} \times \mathrm{d}\mathbf{f}_{\mathrm{th}}, \tag{1.95}$$

where S is the illuminated surface and S' the total surface area of the body. Note that $\mathrm{d}\mathbf{f}_{\mathrm{sca}}$ and $\mathrm{d}\mathbf{f}_{\mathrm{th}}$ are given by the expressions (1.16) and (1.17).

Let ω be the angular rotation frequency of the asteroid and $\mathbf{e}$ the unit vector pointing along the axis of rotation. Let us assume that the asteroid rotates around the shortest axis of the inertia tensor $\hat{\mathbf{I}}$ with respect to which it has the moment of inertia C. We can then write for the angular momentum $\mathbf{L}$

$$\mathbf{L} = C\omega\mathbf{e}. \tag{1.96}$$

The rate of change of the angular momentum equals the total torque

$$\frac{d\mathbf{L}}{dt} = \mathbf{T}. \tag{1.97}$$

Let us define the projection $T_s \equiv \mathbf{T} \cdot \mathbf{e}$ of the torque $\mathbf{T}$ to the direction of the spin axis $\mathbf{e}$. By a straightforward calculation (Rubincam, 2000), we can see that

$$\frac{d\omega}{dt} = \frac{T_s}{C}, \tag{1.98}$$

$$\frac{d\mathbf{e}}{dt} = \frac{\mathbf{T} - (\mathbf{T} \cdot \mathbf{e})\mathbf{e}}{C\omega}. \tag{1.99}$$

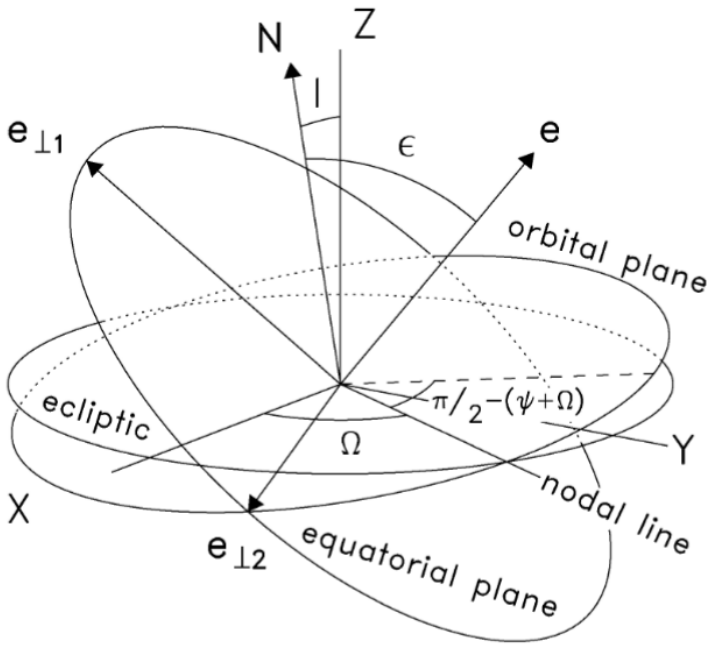

Figure 1.14: An illustration of vector **e** pointing along the axis of rotation and the definition of base vectors $\mathbf{e}_{\perp 1}, \mathbf{e}_{\perp 2}$ in the equatorial plane of the asteroid. The angle between the projection of vector **e** to the plane of orbit and the nodal line is $\pi/2 - (\psi + \Omega)$. Source: Čapek and Vokrouhlický (2004).

The orientation of vector **e** can be expressed using angles (ϵ, ψ, Ω) where ϵ is the angle between vector **e** and the normal unit vector to the orbital plane **N**, ψ is axial precession and Ω is the longitude of the ascending node. We can easily see that in the orbital plane with x-coordinate along the nodal line, vecor **e** is given by

$$\mathbf{e} = (\sin\epsilon \sin(\psi + \Omega), \sin\epsilon \cos(\psi + \Omega), \cos\epsilon), \tag{1.100}$$

from which it follows, according to (1.99), that

$$\frac{d\epsilon}{dt} = \frac{\mathbf{T} \cdot \mathbf{e}_{\perp 1}}{C\omega} \equiv \frac{T_\epsilon}{C\omega}, \tag{1.101}$$

$$\frac{d\psi}{dt} = \frac{\mathbf{T} \cdot \mathbf{e}_{\perp 2}}{C\omega} \equiv \frac{T_\psi}{C\omega}, \tag{1.102}$$

where

$$\mathbf{e}_{\perp 1} = \frac{(\mathbf{N} \cdot \mathbf{e})\mathbf{e} - \mathbf{N}}{\sin\epsilon}, \tag{1.103}$$

$$\mathbf{e}_{\perp 2} = \frac{\mathbf{e} \times \mathbf{N}}{\sin\epsilon}. \tag{1.104}$$

Let us note that the total torque **T** is influenced, apart from the YORP effect itself, also by the gravitational interaction and inertial forces which are a consequence of the motion of the reference system (Vokrouhlický and Čapek, 2002). It turns out that the gravitational and inertial terms dominate in the perturbations of the precession length ψ and have a decisive influence on the projection T_ψ. Their long-time contribution to T_s and T_ϵ is, however, negligible compared to the YORP effect. The YORP effect makes a major contribution to the secular changes of the angular velocity ω and obliquity ϵ.

1.2.3 Detection and selected applications

Although the YORP effect is a relatively weak perturbation, it has been detected for a number of asteroids in the past years. This has been achieved mainly by optical photometry and radar observations.

In general, we want to obtain the dependence of the sidereal period (or sidereal angular velocity) on time from the observations. There is a straightforward expression for the angular velocity

$$\omega(t) = \omega_0 + \dot{\omega}t, \tag{1.105}$$

where ω_0 is constant in time. Phase φ then fulfills $\varphi = \varphi_0 + \omega_0 t + (1/2)\dot{\omega}t^2$. The quadratic term is then fitted (Fig. 1.15).

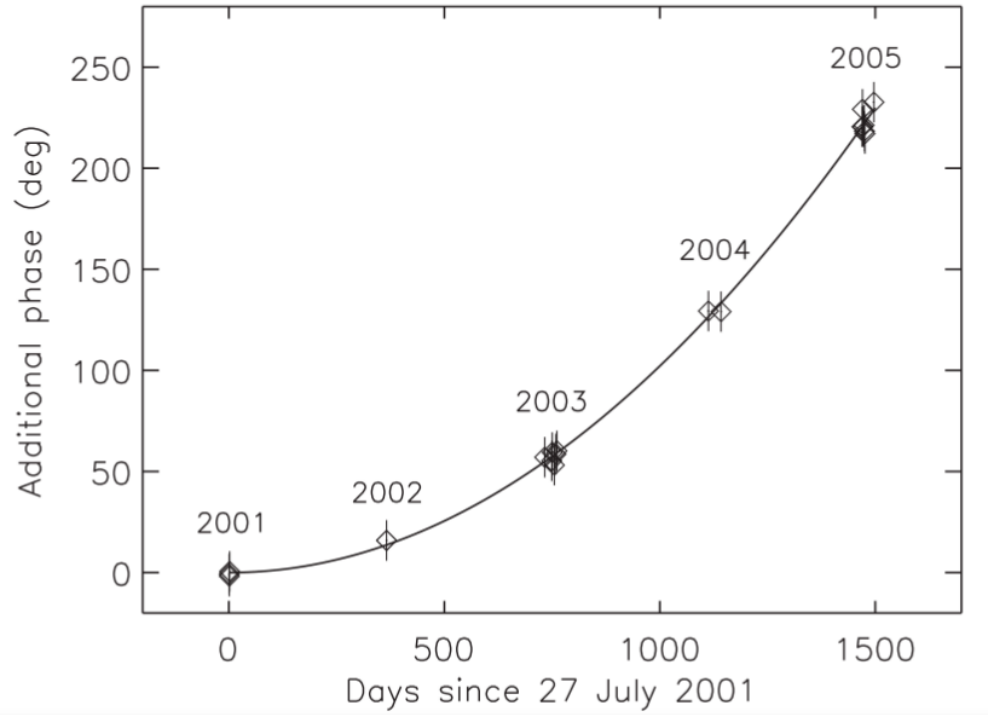

Figure 1.15: Additional phase $\Delta\phi = (1/2)(d\omega/dt)\Delta T^2$ according to measurements taking place from July 2001 to august 2005 for the asteroid (54509) YORP. Source: Taylor et al. (2007).

The first conclusive observation of the YORP effect was performed on a near-Earth co-orbiting asteroid (54509) YORP (Taylor et al., 2007; Lowry et al., 2007). The measurements revealed the pole orientation to be $(180°, -85°)$ in the ecliptic longitude and latitude and sidereal angular velocity $\omega_0 = 42582.41 \pm 0.02$ deg/day at the initial epoch 0^h UT, 27 July 2001. The measurements from several consecutive years have shown that the asteroid's rotation is accelerating. More specifically, from the quadratic fit of the measured data (Fig. 1.15), it was found that $d\omega/dt = (2.0 \pm 0.2) \times 10^{-4}$ deg/day^2.

Other successful cases of detection of the YORP effect include the asteroids (1862) Apollo (Kaasalainen et al., 2007; Ďurech et al., 2008b), (1620) Geographos (Ďurech et al., 2008a), (1865) Cerberus, (3103) Eger (Ďurech et al., 2012), (25143) Itokawa (Lowry et al., 2014) and more.

The very first numerical model of the YORP effect was the Rubincam's model (Rubincam, 2000) which took several approximations. It considered only Lambertian thermal emission, neglected scattering and assumed $K = 0$. The tested objects were placed on circular orbits and were rotating around the shortest principal axis of the inertia tensor. Rubincam's model was later extended in Vokrouhlický and Čapek (2002) and Čapek and Vokrouhlický (2004). Čapek and Vokrouhlický (2004) already included solutions of the heat equation for different values of the thermal conductivity. The heat equation was solved in a 1D approximation for each triangular facet of the body composed of many tetrahedrons.

Relatively recently, both analytical and semi-analytical theories of the YORP effect were formulated (Nesvorný and Vokrouhlický, 2007, 2008; Breiter and Michalska, 2008). These were, for some time, in a good agreement with the numerical models mentioned above and modeled the shapes of the bodies using spherical harmonics. Nesvorný and Vokrouhlický (2007) developed an analytical theory of the YORP effect for close-to-spherical bodies, with which they could explain some of the observations.

The theories of the YORP effect showed that[20] $\bar{T}_s = 0$ for the obliquities $\epsilon \approx 55°$ and $\epsilon \approx 125°$. In agreement with the above, let us for instance mention the results of Slivan (2002) and Slivan et al. (2003) who revealed 4 members of the Koronis family (out of 10 chosen candidates) with obliquities $\epsilon \approx 55°$. Their observations can be explained by the coupling of the YORP effect and the spin-orbit resonance s_6 (Vokrouhlický et al., 2003). The value $\epsilon \approx 55°$ is even a consequence of the balance between gravitational moments and moments caused by the YORP effect.

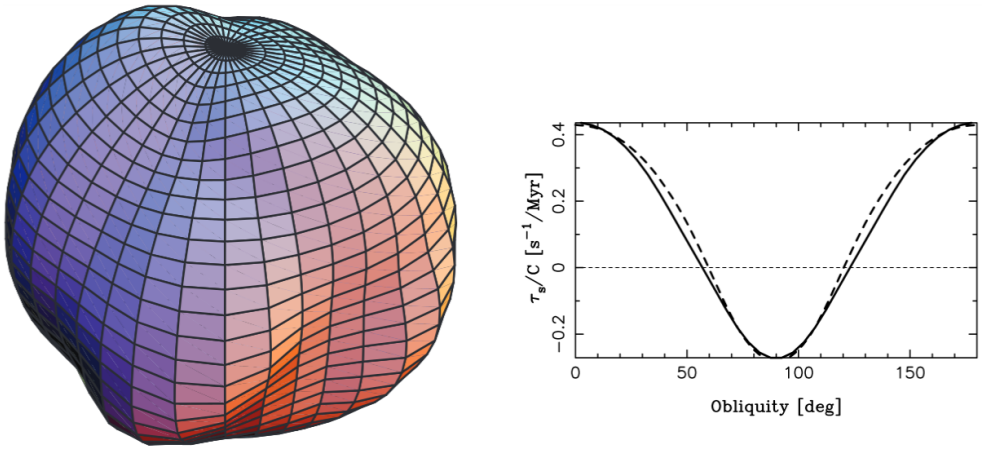

Figure 1.16: An example application of the analytical YORP effect theory according to Nesvorný and Vokrouhlický (2007) to a near-Earth asteroid 1998 KY_{26}. Left: The shape according to the work - contours denote constant longtitude and latitude values and meet on the poles. Right: The dependence of $\bar{T}_s$ on the obliquity ϵ. The full line is the analytical solution, the dashed line the numerical model of Čapek and Vokrouhlický (2004). It is apparent from the plot that the analytical and numerical solutions show good agreement and also that the value $\bar{T}_s$ is zero at $\epsilon \approx 55°$. In this case, C is the principal moment of inertia, $\rho = 2.8$ g cm^{-3} and $a = 1.23$ au. Source: Nesvorný and Vokrouhlický (2007).

[20]Here, we refer to averaging over the rotational and orbital period.

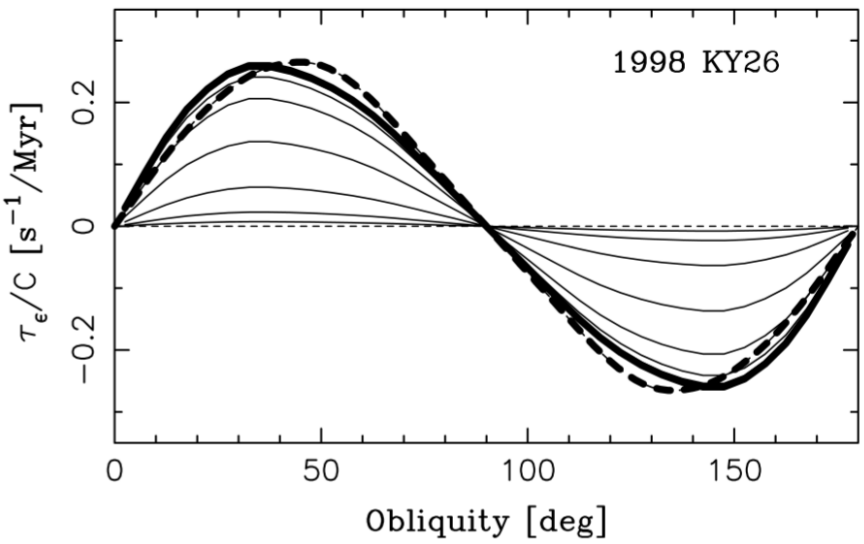

Figure 1.17: An application of the analytical theory of the YORP effect according to Nesvorný and Vokrouhlický (2008) to the near-Earth asteroid 1998 KY_{26}. Plotted is the dependence of $\bar{T}_\epsilon$ on the obliquity ϵ for different values of the thermal conductivity K. The full highlighted line corresponds to $K = 0$, the other full lines correspond to K from 10^{-9} to 1 W m^{-1} K^{-1}. The dotted line comes from the numerical solution for $K = 0$ (Čapek and Vokrouhlický, 2004). Compare with Fig. 1.16. Source: Nesvorný and Vokrouhlický (2008).

The work of Nesvorný and Vokrouhlický (2007) was extended by their following work Nesvorný and Vokrouhlický (2008) which studied the influence of the YORP effect on the obliquity, again for the case of close-to-spherical bodies. Breiter et al. (2010) expanded the class of analytical models of the YORP effect by a solution of the heat equation for close-to-spherical bodies in the limit of radii R comparable to the penetration depth l_ω. They concluded that the YORP effect is, for small objects, proportional to the inverse radius $\sim 1/R$ which is in contrast to the earlier models ($\sim 1/R^2$). The most recent semi-analytical model which includes both the YORP effect and the diurnal Yarkovsky effect[21] was developed by Golubov et al. (2016).

Let us note that at the same time, other semi-analytical models of the YORP effect were developed (Scheeres, 2007b; Scheeres and Mirrahimi, 2008). They also assumed rotation around the principal axis of the inertia tensor and took into account non-zero values of thermal inertia. None of the models mentioned above, however, included surface inhomogeneities such as craters, boulders, slopes, etc.

Overall, it is apparent that the whole issue is rather complicated and a number of effects influencing the rotation of small Solar System bodies have to be considered. For this reason, numerical models currently seem more fitting, as they allow to capture a plethora of effects. In this regard, the work of Statler (2009) is of importance, because it discusses the influence of craters, boulders and other surface irregularities. Statler (2009) concluded that the YORP effect is strongly dependent on the character and the positions of surface structures and cannot be calculated correctly unless the detailed topography is known.

[21]So far for convex objects.

The YORP effect certainly also depends on the chosen scattering model. This was investigated by Breiter and Vokrouhlický (2011). They studied the role of anisotropically scattered and anisotropically emitted thermal radiation in contrast to the isotropic Lambert model. For larger values of albedo, they discovered that the non-isotropic (Hapke) model gives, with regard to the Lambert model, rather different values in the change of obliquity and comparable values in the change of the rotation frequency.

Very sophisticated numerical models were constructed, for instance, by Rozitis and Green (Rozitis and Green, 2012, 2013). They discovered that rough surfaces reduce the efficiency of the YORP effect for any value of obliquity. In their works, they also included the role of self-heating, whereupon the surface elements can absorb not only solar radiation but also radiation from other surface elements. The authors also gave some attention to shielding effects and concluded that self-heating and shielding have substantial influence on the resulting YORP effect. Their work also presents a concise summary of the history and basic characteristics of earlier models.

Other recent models (Golubov and Krugly, 2012; Golubov et al., 2014) discuss the so-called TYORP effect (T stands for tangential). This refers to sideways radiation of meter-sized objects. These objects were approximated by walls placed on the asteroid surface (Golubov and Krugly, 2012). By using the 1D approximation of the heat equation, they revealed that the thermal radiation from the western wall exceeds the radiation from the eastern wall. This asymmetry also contributes to the total torque. Transition from the 1D model to a 3D model with a more realistic shape (spherical boulders) was achieved in Golubov et al. (2014). In the past few years, it seems very promising to model the thermophysical properties of asteroids using the finite element method also for realistically-shaped boulders (Ševeček et al., 2015, 2016). According to contemporary knowledge we can conclude that the YORP effect tends to slightly speed up the rotation of asteroids.

With time, the research also started focusing on more complex cases - the so-called tumblers - i.e. asteroids which do not rotate around any principal axis of the inertia tensor. Their rotation is, generally, composed of two (or more) rotation periods and it can be described by 2-dimensional Fourier series (Pravec et al., 2005).

The rotation of tumblers is, however, an energetically inefficient excited state of rotation with higher energy. It results in periodical loading of the body, internal friction, heating up and, therefore, energy dissipation. Gradual energy dissipation leads to damping of the rotation and transitioning to a lower energy state in which the object eventually rotates only around the shortest principal axis c of the inertia tensor. With respect to this axis, the object takes the maximum value of the moment of inertia I_c. The mentioned effect occurs on the time scale τ [Gyr], which is given by (see Harris, 1994)

$$\tau = \frac{P^3}{K^3 D^2}, \tag{1.106}$$

where P is the period of rotation in hours, D is the mean diameter in km and $K = 17 \pm 2.5$ is an empirical constant[22].

[22]More recent models provide $K \approx 38$ (see Pravec et al., 2005; Breiter et al., 2012).

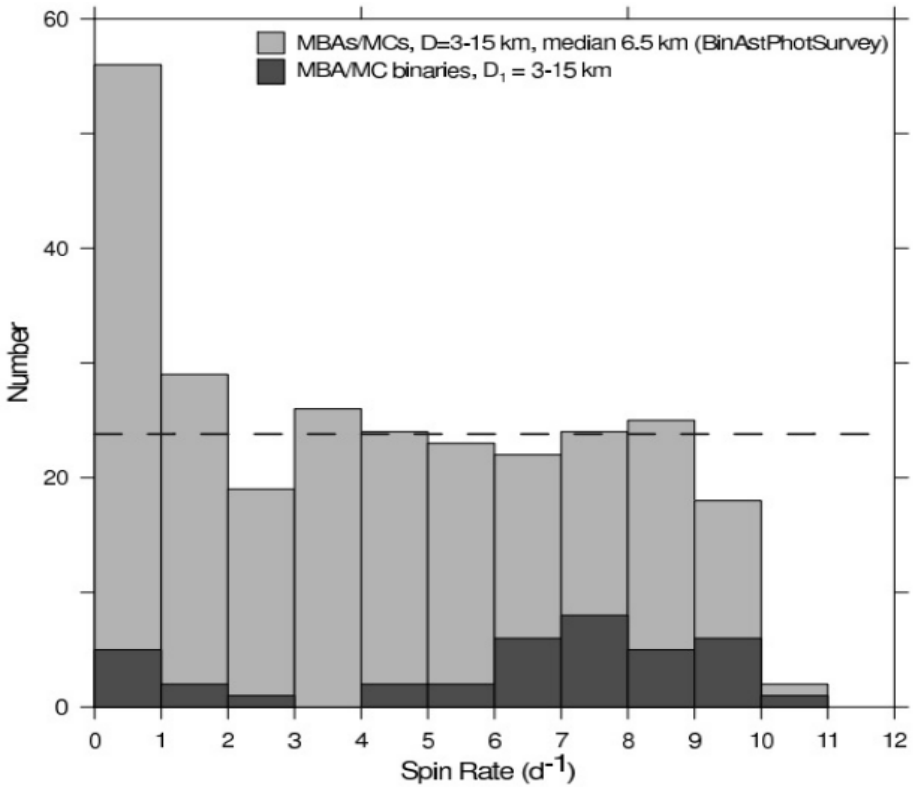

Figure 1.18: Distribution of rotation frequencies for MBA/MC with diameters 3 - 15 km. The dashed line corresponds to the average value in the range $f \in [1, 9.5]$ d^{-1}. For $f < 1$ d^{-1} and $f > 9.5$ d^{-1}, we observe a deviation from the uniform distribution. Source: Pravec et al. (2008).

Asteroids with a diameter larger than 40 km exhibit approximately Maxwellian distribution of rotational speeds (Pravec et al., 2008) which is rather intuitive because their rotational states are mostly governed by collisions. The YORP effect is, in this case, negligible. Observation data however show that the distribution of rotational speeds for smaller bodies is no longer Maxwellian. Pravec et al. (2008) found that for the main belt asteroids (MBA) and Mars-crossing asteroids (MC) with $D \in [3, 15]$ km, one observes (a) uniform distribution for the frequencies $f \in [1, 9.5]$ d^{-1}, (b) an increase in the number of asteroids for $f < 1$ d^{-1}, and (c) a decrease for $f > 9.5$ d^{-1}.

The question remains, how to interpret the cases (a), (b) and (c). Regarding (a): It turns out that the uniform distribution is a consequence of the YORP effect. From Čapek and Vokrouhlický (2004), it is apparent that the time derivative of the frequency is not a function of frequency for a body which rotates around the principal axis of the inertia tensor. This means that for any initial distribution of frequencies, the YORP effect smears this distribution towards a uniform one. A detailed description can be found in Pravec et al. (2008). Regarding (b): the explanation here is more complicated and takes into account different scenarios. An increase in the number of slow rotating bodies is probably caused by the fact that asteroids are created more often or remain for a longer time in the mode of slow rotators. It is also possible, that for slower rotation, the time derivative of the frequency is no longer independent of frequency and the YORP effect is weakened. This could lead to a longer residence in this rotational mode.

Regarding (c): The loss of fast rotating bodies can be explained by rotational fission of some of them.

The YORP effect also plays an important role in the distribution of obliquities of asteroids. According to the theory of Čapek and Vokrouhlický (2004), obliquity converges to 0° or 180°, when the thermal conductivity is non-zero. Hanuš et al. (2013) have analyzed more than 300 selected light curves and found that the ecliptical latitudes of the main belt objects statistically prefer values closer to 90° or −90°. Thus, in this case, the YORP theory is consistent with observations.

Let us note that the research is also shifting towards binary asteroids. If the secondary rotates synchronously with regard to its orbit around the primary, the thermal radiation from its surface should cause an acceleration or deceleration of its rotation (see Ćuk and Burns, 2005). Owing to tidal forces, this leads to an increase or decrease of the orbital radius. A recent analytical theory of the BY-ORP effect was developed by McMahon and Scheeres (2010). From their work, we can conclude that knowing the shape of the secondary and the obliquity of the binary, the BYORP effect is described by a single parameter B (BYORP coefficient). The sign of this parameter indicates whether the primary and secondary are approaching each other or getting further away[23]. At present, however, the main obstacle in modeling the BYORP effect is the lack of information about the shape of the secondary asteroid.

Let us mention that the YORP effect has also a major influence on the origin and orbital evolution of asteroid pairs and families. In this regard, we would like to direct the reader to Chapter 3. The state of the art of the Yarkovsky and YORP effects can then be found in Vokrouhlický et al. (2015a).

1.3 Conclusion

In this chapter, we provided a basic introduction to the theory of the Yarkovsky and YORP effects which play a significant role in the long-term orbital evolution of meter-sized and kilometer-sized bodies. Non-gravitational perturbations induced by the Yarkovsky effect are mainly caused by (i) asymmetric temperature distribution on the surface of an asteroid and (ii) by a time lag between the irradiation and emission of thermal photons, resulting in a relatively small reaction force which changes the heliocentric orbit of the body, namely its semi-major axis. An asteroid which is mainly under the influence of diurnal variant of the Yarkovsky effect spirals either toward or away from the Sun, depending on the obliquity. In case of the seasonal variant of the Yarkovsky effect, we always expect spiralling toward the Sun.

The incident, emitted and scattered radiation cause a torque that leads to an acceleration or deceleration of the rotation and a change in the orientation of the spin axis. The YORP effect is responsible for the creation of binary asteroids, young asteroid families and asteroid pairs and also for long-term preference of asteroid obliquities towards 0° and 180°.

However, for a precise modeling of both effects, the thermophysical properties, shape and detailed topography of the body are of great importance.

[23]The conditions for establishing a possible stable orbit are discussed in Jacobson and Scheeres (2011b).

2. Non-gravitational perturbations of the asteroid (99942) Apophis

In this chapter, we discuss the influence of non-gravitational perturbations on the orbital evolution of near-Earth asteroid (99942) Apophis. We also present, to a great extent, results of the publication by Žižka and Vokrouhlický (2011b), in which we studied perturbations of the orbit as a consequence of solar radiation pressure (see Paper 1 in the Appendix A). Numerous works have been published since the discovery of Apophis in 2004. They mostly focused on the detailed thermophysical description and corresponding radiation-based perturbations. We, therefore, aim to provide a broader interpretation of the current research related to this uncommon body.

2.1 The discovery and basic properties

Apophis was discovered on 19 June 2004 by the astronomers Roy A. Tucker, David J. Tholen and Fabrizio Bernardi in the Kitt Peak, Arizona, National Observatory.

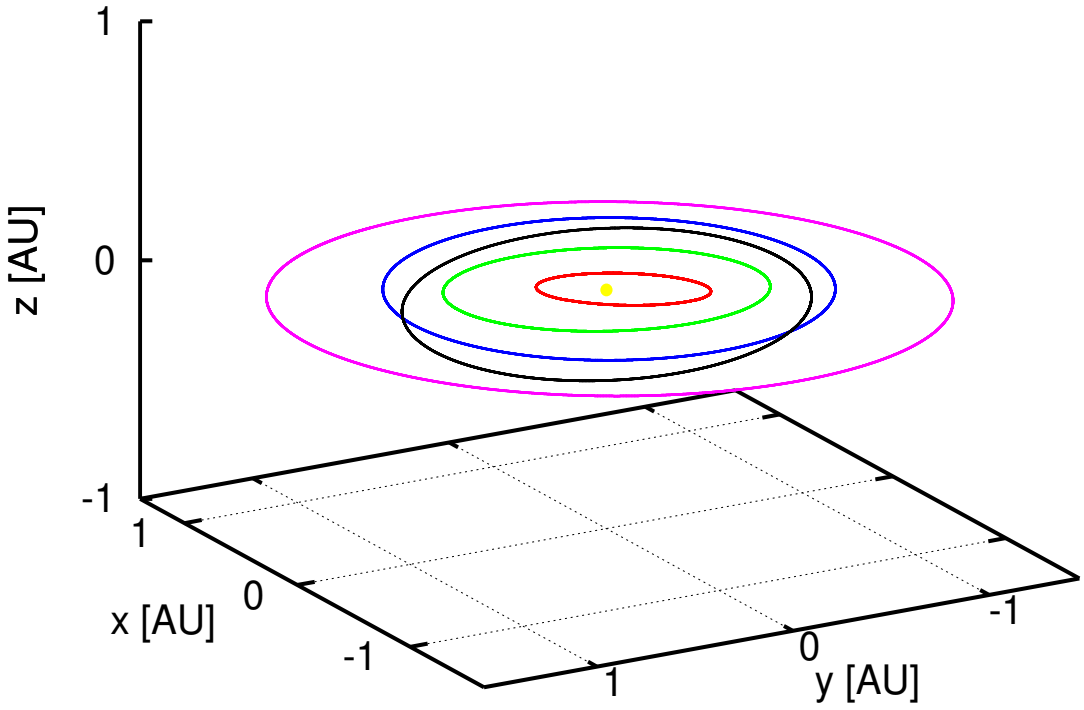

Figure 2.1: A schematic illustration of the orbit of near-Earth asteroid (99942) Apophis (black trajectory) in the heliocentric coordinate system. Pictured are also trajectories of Mercury (red), Venus, Earth and Mars (purple).

The motivation behind the naming of the asteroid comes from the discoverers' favorite TV series - Stargate SG-1. In this series, Apophis is a powerful Goa'uld with an overwhelming desire to destroy the Earth. The origin of the name Apophis itself, however, comes from an Egyptian mythological figure - Apep.

a [au]	h	k	p	q	λ [deg]
0.9226169083	-0.093583093	0.167083513	-0.011874844	-0.026596914	186.603144
			Uncertainty		
δa	δh	δk	δp	δq	$\delta\lambda$
$2.3 \cdot 10^{-10}$	$5.3 \cdot 10^{-9}$	$6.3 \cdot 10^{-9}$	$9.1 \cdot 10^{-9}$	$7.1 \cdot 10^{-9}$	$9.3 \cdot 10^{-7}$

Table 2.1: Non-singular orbital elements (MJD 58000.0) of Apophis' nominal orbit according to `AstDyS (http://hamilton.dm.unipi.it/astdys/)`. Let us note that a is the semi-major axis, $(h,k) = e(\sin\varpi, \cos\varpi)$ and $(p,q) = \tan(i/2)(\sin\Omega, \cos\Omega)$. Further, $\lambda = \varpi + M$ is the mean longitude, M is the mean anomaly, Ω is the longitude of the ascending node, ϖ is the longitude of the pericenter, e is the eccentricity and i is the inclination.

Immediately after the first observations, it was apparent that the object is of great interest and it was further observed the very next day - 20 June 2004. Further observations were, however, prevented by technical difficulties and poor weather conditions. In the meantime, the elongation was decreasing until Apophis got out of sight for several months. It was re-discovered in December 2004 by a team of astronomers from the australian Siding Spring Observatory (Gilmore et al., 2004). Their observations have shown that Apophis is a potentially dangerous asteroid with the impact probability of $\approx 2.7\%$ in April 2029. After the archive images of Apophis were published (Gleason et al., 2004) and the trajectory was made more accurate, the chance of an impact in 2029 was ruled out. The trajectory was made more accurate, among other data, also by using the Arecibo observatory radar measurements in 2005, 2006 and 2012-2013.

The distance between the Earth's centre and Apophis was, for the closest approach in 2029, determined to be $D_{\mathrm{enc}} \approx 6R_{\mathrm{Earth}}$ (Giorgini et al., 2008). However, despite the rather accurately established trajectory, an uncertainty remained with regard to Apophis' next close approach in 2036. New astrometric measurements considered by Chesley et al. (2009) have reduced this uncertainty by as much as 50% and provided new values of impact probabilities. Even so, they did not conclusively rule out the possibility of an impact in 2036.

Let us note that, apart from the gravitational perturbations, the future impact probabilities also depend on weak non-gravitational perturbations, which can manifest as large orbital uncertainties after the close approach in 2029. In this regard, the Yarkovsky effect is of key importance (see Chesley, 2006). Its influence was also discussed by Bancelin et al. (2012), who have not, however, included it in their calculations.

Farnocchia et al. (2013a) used the Monte Carlo method to model the possible orbital evolutions of Apophis, considering both the nominal-orbit uncertainty and the Yarkovsky effect. The gravitational part of their model included interactions with the Sun, planets, Moon, Pluto and 25 chosen asteroids. The test particles were propagated until 2029 and then projected to the corresponding b - plane.

By looking at the positions of the keyholes[1], Farnocchia et al. (2013a) analyzed the impact probabilities after 2029. Let us remind that the b - plane intersects the centre of the Earth and is perpendicular to the vector of the geocentric velocity of the projectile $\mathbf{V}_\infty$ (see Öpik, 1976). In the b-plane, we define the coordinates (ξ, η, ζ), where ξ increases along $\mathbf{T}$, η along $\mathbf{S}$, and ζ along $-\mathbf{R}$ (see Fig. 2.2).

In order to find the keyholes in the b-plane for 2029, Farnocchia et al. (2013a) propagated the trajectories of virtual asteroids densely covering the LOV[2] until the year 2113 and recorded very close approaches and collisions with the Earth. In total, they found 20 significant keyholes for which they calculated the impact probabilities. Most significant was the keyhole related to a possible impact in 2068, which could happen with the probability[3] IP $\approx 2 \cdot 10^{-6}$. The probability of an impact in 2036 was estimated by Farnocchia et al. (2013a) to be IP $\approx 7 \cdot 10^{-9}$, which is orders of magnitude less than the one in 2068.

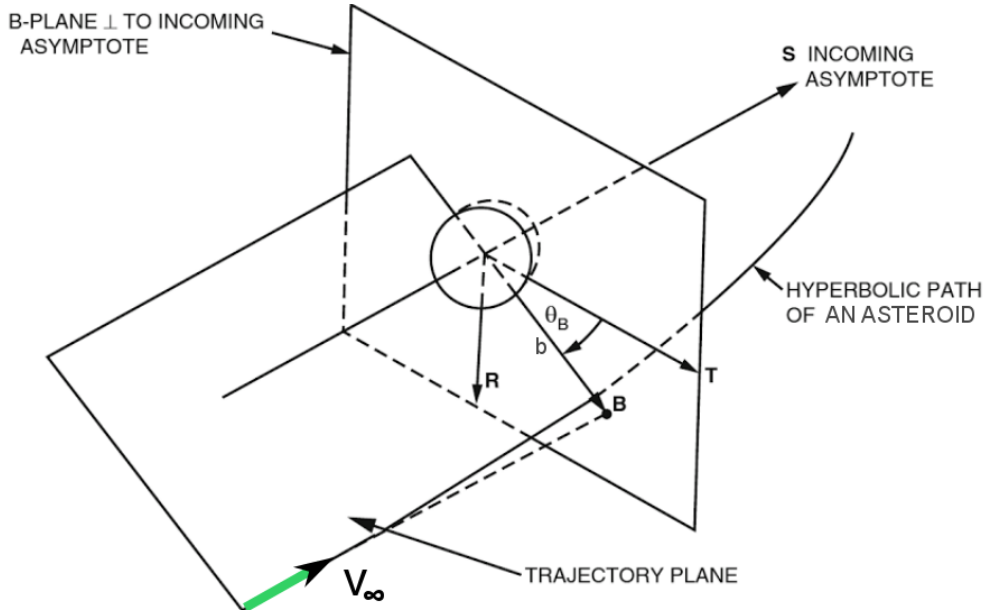

Figure 2.2: An illustration of the reference b-plane, which goes through the scattering body. The b-plane is perpendicular to the asymptotic trajectory and intersects it in point B. We define a local base $\{\mathbf{R}, \mathbf{S}, \mathbf{T}\}$ with the origin in the Earth's center, where $\mathbf{S} \parallel \mathbf{V}_\infty$, $\mathbf{T}$ lies in the ecliptic plane and $\mathbf{R}$ is perpendicular to $\mathbf{S}$ and $\mathbf{T}$. Vector $\mathbf{B}$ lies in the plane of the projectile's trajectory and it holds that $\mathbf{B} \perp \mathbf{S}$. The distance of B from the center is the so-called impact parameter b. Adapted from Doody (2009).

We have seen in the previous chapter, that the Yarkovsky drift da/dt strongly depends on thermophysical properties of the body. However, for almost 10 years after Apophis was discovered, some of the key properties necessary for precise modeling of the Yarkovsky effect were not known. Most importantly, the orientation of the pole and the shape of the body were still uncertain. This missing information has been filled by Pravec et al. (2014) and Müller et al. (2014).

[1]The term keyhole was first used by Chodas (1999). If a projectile passes through this small region in the b-plane, it is put on a future impact trajectory.

[2]= Line of Variation. LOV characterizes the orbital uncertainty (Milani et al., 2005).

[3]We mention nominal impact probabilities according to Farnocchia et al. (2013a).

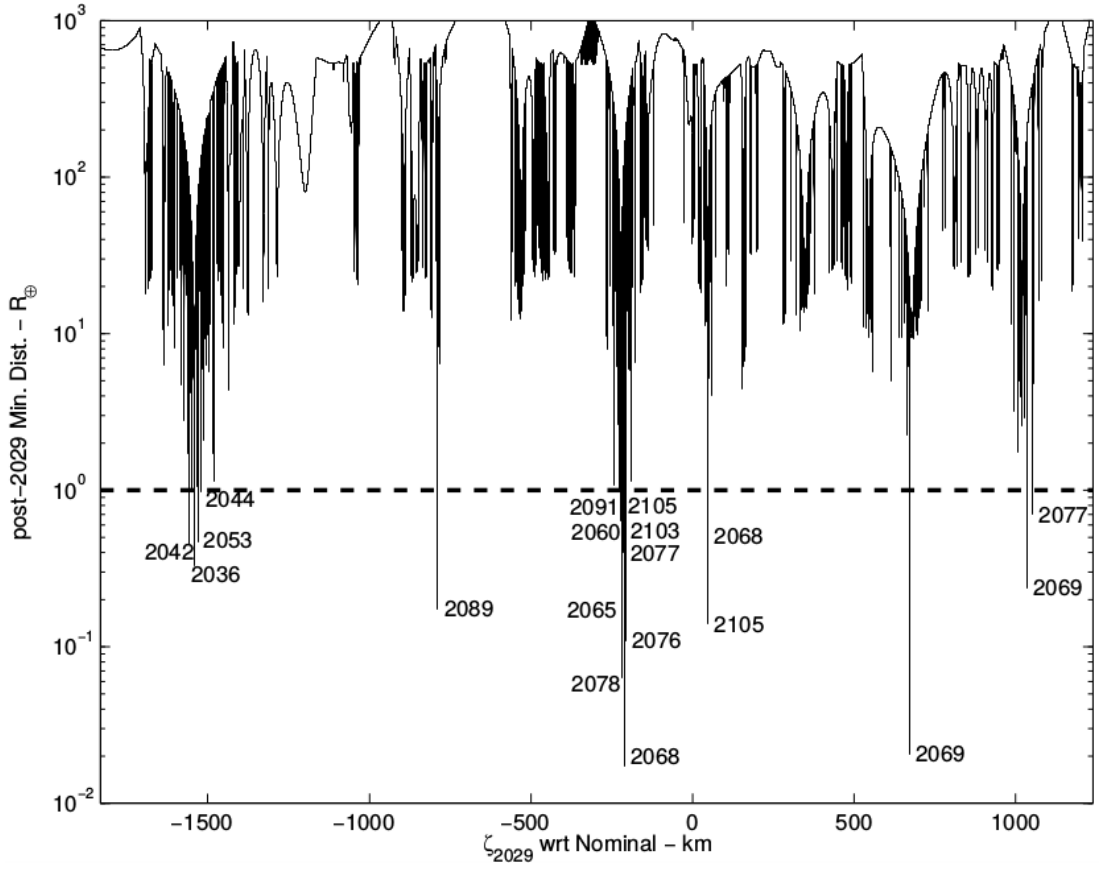

Figure 2.3: An overview of the keyholes found in the b-plane for 2029 according to Farnocchia et al. (2013a). The horizontal axis is the coordinate ζ and the y axis corresponds to the distance of the closest approach for a specific date, expressed in Earth's diameters $R_\oplus$. The reason why only the ζ coordinate is plotted is that the orbit uncertainty of Apophis projected into the 2029 b-plane is orders of magnitude larger in the ζ coordinate than in the other coordinates.

Pravec et al. (2014) found that Apophis does not rotate exclusively along the shortest axis of the inertia tensor, as assumed in the earlier models, but it exhibits a weak tumbling. At the same time, the authors used photometric measurements made between December 2012 and April 2013 to find its shape, which is close to an elongated ellipsoid (see Fig. 2.4 and 2.5). They have also shown that the rotational state of (99942) Apophis can be characterized by the rotational period $P_\psi = 263 \pm 6$ h and the precession period $P_\varphi = 27.38 \pm 0.07$ h. According to Pravec et al. (2014), Apophis rotates in a retrograde direction with the angular momentum oriented towards $(250°, -75°)$[4] in the ecliptic coordinates. The absolute magnitude was found to be $H = 19.09 \pm 0.19$ mag.

Since the discovery of Apophis, rather different values of its effective diameter[5] have been mentioned in literature. The most recent studies are, however, providing increasingly accurate data with smaller relative errors. From the first estimations, the diameter of Apophis was expected in the range $320 - 970$ m.

[4]The confidence band with regard to the nominal orientation of the angular momentum is approximately elliptical with the semimajor axis $\approx 27°$ and the semiminor axis of $\approx 14°$.

[5]The diameter of a volume-equivalent sphere.

Delbo' et al. (2007a) used polarimetric observations and found the geometric albedo to be $p_V = 0.33 \pm 0.08$. They also determined the absolute magnitude as $H = 19.7 \pm 0.4$ mag, which corresponds to the diameter of 270 ± 60 m. A few years later, Farnocchia et al. (2013a) carried out simulations while taking into account the observations from the Herschel Space Observatory and used $D_{\text{eff}} = 325 \pm 15$ m. Similar value was obtained by Müller et al. (2014) who determined the effective diameter of Apophis as 375^{+14}_{-10} m and constrained the thermal inertia Γ so that $\Gamma \in [250,\ 800]$ J m^{-2} s$^{-0.5}$ K^{-1}. They also calculated the most probable value $\Gamma \approx 600$ J m^{-2} s$^{-0.5}$ K^{-1} which approximately corresponds to a regolith layer with lower thermal conductivity interspersed with cliffs and boulders. Note that Müller et al. (2014) discussed the striking similarity in the size and thermal inertia of (99942) Apophis with (25143) Itokawa, which could be evidence of Apophis having the rubble-pile structure. These authors found $p_V = 0.30^{+0.05}_{-0.06}$.

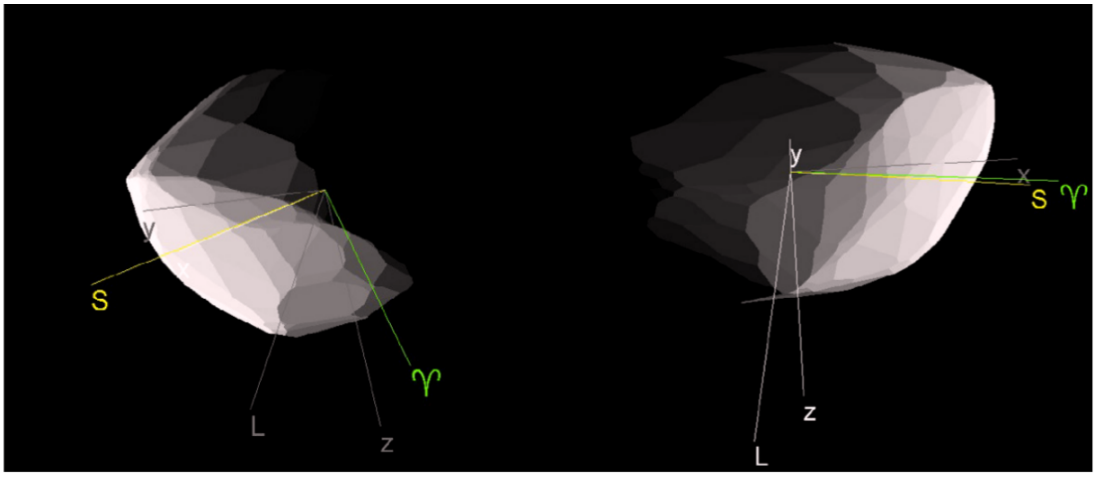

Figure 2.4: The shape of near-Earth asteroid (99942) Apophis according to Pravec et al. (2014). Shown is the situation in January (left) and March (right) of 2013 when Apophis was observed by the PACS photometer and spectrometer at the Herschel Space Observatory. The situation on the left and on the right corresponds to the phase angle of 60° before and after opposition, respectively. The x, y, z axes indicate the co-rotating coordinate system. The yellow line points towards the Sun, the green line towards the Vernal equinox.

Let us note that lower values of thermal inertia were recently obtained by Licandro et al. (2016) who found the following parameters of (99942) Apophis: $D_{\text{eff}} \in [380, 393]$ m, $p_V \in [0.27, 0.29]$ and $\Gamma \in [50, 500]$ J m^{-2} s$^{-0.5}$ K^{-1} and determined more up-to-date values of the Yarkovsky drift. Later, Yu et al. (2017) published comparable results of the thermal inertia $\Gamma = 100^{+240}_{-100}$ J m^{-2} s$^{-0.5}$ K^{-1}. According to Yu et al. (2017), the surface of Apophis is covered by coarse-grained regolith. They also came up with the hypothesis that Apophis may be one of Vesta's fragments, which has been delivered from the main belt by the Yarkovsky effect. The new information about the rotational state and the thermophysical properties (Pravec et al., 2014; Müller et al., 2014) were adopted by Vokrouhlický et al. (2015b) who modeled the orbital evolution of Apophis under the influence of the Yarkovsky effect. This topic is discussed in the last paragraph of this chapter.

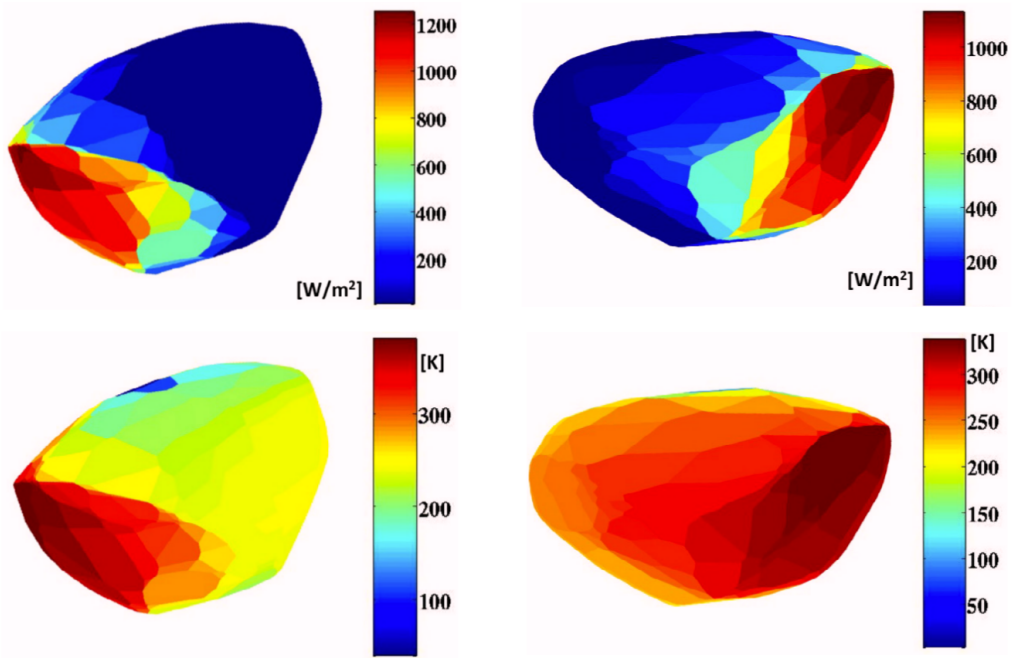

Figure 2.5: The same geometrical situation as in figure 2.4. The upper pair shows the solar flux to individual surface elements of the asteroid. The lower pair demonstrates the temperature distribution on the surface obtained by Müller et al. (2014) using a thermophysical model `TPM` (Lagerros, 1996a, 1997, 1998). Adapted from Müller et al. (2014).

2.2 The influence of solar radiation pressure

The asteroid (99942) Apophis still remains in the interest of astronomers, even though the collisions with Earth in 2029 and 2036 have been practically ruled out. It is, beyond doubt, a unique body which has been consistently receiving attention since it was discovered. In this paragraph, we provide a more detailed account of our results related to the influence of the solar radiation pressure (SRP) on the orbital evolution of (99942) Apophis until its close approach to Earth in 2029 ($\approx$ 38000 km). It is largely based on the publication by Žižka and Vokrouhlický (2011b) which can be found in Appendix A (Paper 1). Note that in our case we studied only the influence of incident and reflected radiation. Nonetheless, all gravitational and non-gravitational perturbations manifest in the orbital uncertainties in the 2029 b-plane.

Giorgini et al. (2008) studied the influence of SRP in a zeroth-order approximation and found that this type of non-gravitational perturbation is several times smaller than perturbations caused by the Yarkovsky effect. On the other hand, Rubincam (2007) obtained a different result by analytically calculating the orbital YORP effect for a non-symmetrical hemisphere-shaped object, taking the approximation of zero thermal inertia. He derived an expression for the change in along-track position Δd due to orbital YORP effect and showed that $\Delta d = 0.61325 \sin\beta [T(\mathrm{yr})]^2$ km. Here, T is the time in years and β the angle between the spin axis and the principal axis of the elliptical orbit (see Fig. 2.6).

In the extreme case ($T = 20$ yr, $\sin\beta \to 1$), Rubincam obtained $\Delta d \approx \pm 245$ km which is comparable with the Yarkovsky effect-induced perturbation ($\approx \pm 250$ km) (Chesley, 2006). Let us, however, stress that Rubincam's work includes a small mistake in the equation (33), which is given in the form

$$\overline{\frac{da}{dt}} = -\frac{2(3\pi - 8)F_{\mathrm{E}}e}{3\pi c\rho R_{\mathrm{A}}n}\left(\frac{a_{\mathrm{E}}}{a}\right)^2 \sin\beta, \tag{2.1}$$

while the square of π in the denominator is omitted. The equation should then take the form (see Žižka and Vokrouhlický, 2011b)

$$\overline{\frac{da}{dt}} = -\frac{2(3\pi - 8)F_{\mathrm{E}}e}{3\pi^2 c\rho R_{\mathrm{A}}n}\left(\frac{a_{\mathrm{E}}}{a}\right)^2 \sin\beta. \tag{2.2}$$

The change in along-track position $\Delta d = 0.61325 \sin\beta[T(\mathrm{yr})]^2$ km then reduces to $\Delta d = 0.19520 \sin\beta[T(\mathrm{yr})]^2$. This gives a maximum shift of $\approx \pm 78$ km. Be as it may, the discrepancy between Giorgini et al. (2008) and Rubincam (2007) motivated us to study the SRP effect on Apophis more thoroughly.

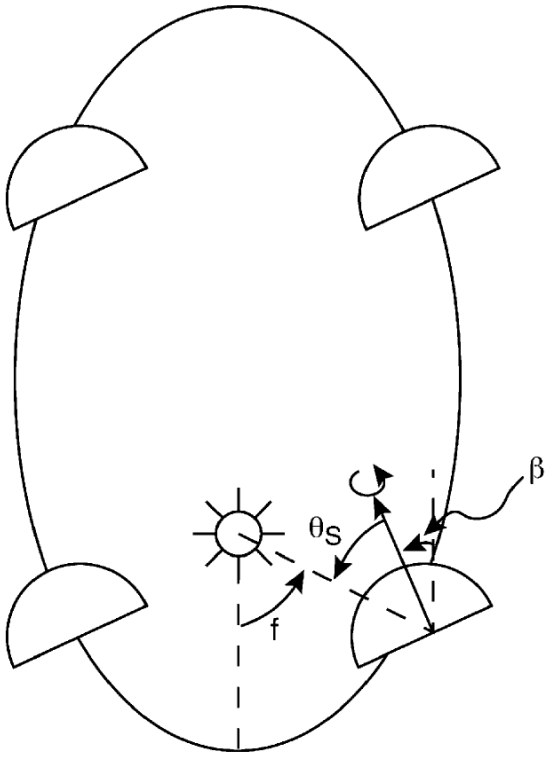

Figure 2.6: A hemispherical asteroid orbiting the Sun. The spin axis lies in the orbital plane. The angle between the principal axis of the osculating ellipse and the spin axis is β. The variable f is the true anomaly. Source: Rubincam (2007).

Solar radiation pressure (SRP)

The solar radiation incident on the asteroid surface is (i) partially scattered (mostly in the visible part of the spectrum) and (ii) partially absorbed and re-radiated in the infrared part of the spectrum. Both these effects lead to a change

in the object's momentum. Let us remind of the expressions (1.16) and (1.22), which describe the perturbation forces as a consequence of the scattered radiation

$$\mathbf{f}_{\mathrm{sca}} = \int_S \mathrm{d}\mathbf{f}_{\mathrm{sca}}, \tag{2.3}$$

$$\mathrm{d}\mathbf{f}_{\mathrm{sca}} = -\Sigma \frac{F}{c}(K_1^{\mathrm{sca}}\mathbf{n}_\perp + K_2^{\mathrm{sca}}\mathbf{M})\, dS, \tag{2.4}$$

where

$$K_1^{\mathrm{sca}}(\mu_0) = \int_{\Omega^+} \mu^2 r_{\mathrm{sca}}(\mu, \mu_0, \phi)\, d\Omega, \tag{2.5}$$

$$K_2^{\mathrm{sca}}(\mu_0) = \int_{\Omega^+} \mu\sqrt{1-\mu^2}\cos\phi\, r_{\mathrm{sca}}(\mu, \mu_0, \phi)\, d\Omega. \tag{2.6}$$

Here c is the speed of light and F is the solar radiation flux at the heliocentric distance r of Apophis. We also include the shadow function Σ which is equal to 1 if a surface element is illuminated and equal to 0 if not. The form of the function $r_{\mathrm{sca}}(\mu, \mu_0, \phi)$ defined in (1.6) depends on the radiation model used. We included the perturbation force $\mathbf{f}_{\mathrm{sca}}$ of the scattered radiation and also the perturbation force $\mathbf{f}_{\mathrm{inc}}$ of the incident radiation in our model. It holds for the resultant force $\mathbf{f}_{\mathrm{SRP}}$ that

$$\mathbf{f}_{\mathrm{SRP}} = \mathbf{f}_{\mathrm{sca}} + \mathbf{f}_{\mathrm{inc}}, \tag{2.7}$$

where

$$\mathbf{f}_{\mathrm{inc}} = -\frac{FS_\perp}{c}\mathbf{n}_0, \tag{2.8}$$

and $S_\perp$ is the cross-section of the object in the direction $\mathbf{n}_0$ towards the Sun. Since Apophis moves along an eccentric orbit, it is found at different heliocentric distances along its trajectory. From the dependence $F \approx r^{-2}$, it is evident that the magnitude of the perturbation force $|\mathbf{f}_{\mathrm{SRP}}|$ changes during one revolution about the Sun. In addition, short-term changes in the perturbation force $|\mathbf{f}_{\mathrm{SRP}}|$ are caused by the rotation of the asteroid, because the cross-section $S_\perp$ periodically varies in time. These effects have to be captured and evaluated in each integration step. Formally, we can write

$$S_\perp = \int_{S_0} (d\mathbf{S}\cdot\mathbf{n}_0)\Sigma(\mathbf{R}, \mathbf{n}_0), \tag{2.9}$$

where we integrate over the illuminated area S_0. The vector $d\mathbf{S} = \mathbf{n}_\perp dS$ points outwards from the surface element dS. In our simulation, the shape of the body was represented by a wire-frame polyhedron and the integration was substituted by summation over the corresponding surface elements[6].

The shadow function $\Sigma(\mathbf{R}, \mathbf{n}_0)$ depends on the overall shape of the body, on vector $\mathbf{n}_0$ and matrix $\mathbf{R}$. Matrix $\mathbf{R}$ is a transformation matrix between the inertial ecliptic system and the body-frame system. The shadowing effect was also included in our simulations - we investigated to what extent the shadowing influences the result.

[6]The area S_0 is a set of surface elements, for which the necessary illumination condition ($d\mathbf{S}\cdot\mathbf{n}_0 > 0$) is met. However, meeting this condition does not exclude elements which are in the shadow. The shadowing effect is captured by function Σ.

We used an algorithm described in Appendix 2 in Čapek (2007)[7]. Its complexity is $O(N^2)$ because we iterate through N surface elements and for each of them, we search $N-1$ elements to find those which are in the shadow[8].

Our simulations are, however, not only limited to a narrow set of simple geometrical shapes of Apophis (sphere, ellipsoid) but they also capture the orbital evolution of a number of convex and non-convex bodies with different pole orientations. Apart from the classical Lambert scattering model, we also consider a more sophisticated Hapke model. Finally, we will compare and discuss the results obtained using these two models.

Radiation models

When modeling the influence of SRP on the orbital evolution of Apophis, we numerically propagated the whole class of convex and non-convex bodies and considered both the classical Lambert model

$$r_{\mathrm{sca}}(\mu,\mu_0,\phi)=\frac{\mu_0}{\pi}A \Rightarrow K_1^{\mathrm{sca}}(\mu_0)=\frac{2}{3}\mu_0 A \wedge K_2^{\mathrm{sca}}=0, \tag{2.10}$$

and the Hapke bi-directional scattering model in the single-scattering approximation (e.g., Hapke, 1981, 2002)

$$r_{\mathrm{sca}}(\mu,\mu_0,\phi)=\frac{w}{4\pi}\frac{\mu_0}{\mu+\mu_0}\left[(1+B_0B_S(\alpha))P(\alpha)+H(\mu)H(\mu_0)-1\right], \tag{2.11}$$

where $B_S(\alpha)$ is the backscatter function, $H(x)$ is the Chandrasekhar H-function, w is the single-scattering albedo and $P(\alpha)$ is the Henyey-Greenstein phase function which describes the angular scattering properties of an average surface particle. The phase angle α is the angle between $\mathbf{n}_0$ and the direction of the scattered sunlight $\mathbf{n}$. Finally, the B_0 is the so-called opposition surge amplitude parameter, which is the ratio of the light scattered by an average regolith grain particle, divided by the total light backscattered at zero phase angle[9]. Note that the backscatter function $B_S(\alpha)$ captures the so-called opposition effect. This effect is observed as an increase of the brightness of those parts of the surface that have the phase angle approaching zero (see Fig. 2.7). The backscatter function takes the form

$$B_S(\alpha)=\left[1+(1/h_S)\tan(\alpha/2)\right]^{-1}, \tag{2.12}$$

where h_S is the backscatter width. The Chandrasekhar H-function is approximated in our calculations by the expression

$$H(x)=\frac{1+2x}{1+2\gamma x}, \tag{2.13}$$

where γ is given by $\gamma=\sqrt{1-w}$. For our purposes, we assume $P(\alpha)$ to take the form of the Henyey-Greenstein phase function

$$P(\alpha)=\frac{1-g^2}{(1+2g\cos\alpha+g^2)^{3/2}}, \tag{2.14}$$

[7]Available at `http://sirrah.troja.mff.cuni.cz/~davok/`.

[8]Some optimization has been achieved in the preprocessing phase. The algorithm can be sped up e.g. by pre-calculating and identifying shadowed elements in advance for different orientations of the $\mathbf{n}_0$ vector.

[9]For a fully opaque particle, $B_0=1$.

where g is an anisotropy parameter ($g \in [-1, 1]$). It holds that (a) $g < 0$ as long as backscattering dominates, (b) $g = 0$ as long as the scattering is isotropic and (c) $g > 0$ when forward scattering dominates. The presented Hapke model, therefore, has four free parameters (w, B_0, h_S, g). These can be found, in some cases, from high-quality photometry or their mean values can be deduced from the asteroid's spectral class (Helfenstein and Veverka, 1989).

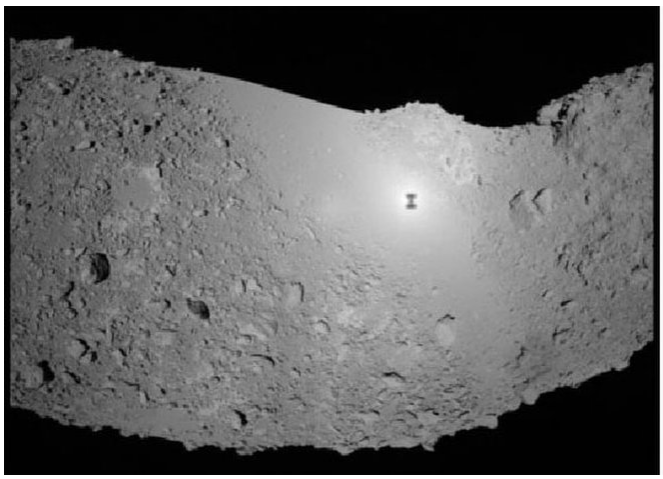

Figure 2.7: Opposition effect observable on the surface of (25143) Itokawa, which was visited by the Japanese Hayabusa probe. Source: JAXA.

The geometric (physical) albedo A_g is another widely-used photometric property. It expresses the ratio of the actual brightness of the body to the brightness of a Lambertian disc with the same cross-section and distance[10]. Let us consider a Cartesian system of coordinates $Oxyz$ with the origin in a sphere with radius R. Let us then illuminate and observe the sphere from direction z. An infinitesimal surface element on the sphere fulfills $dS = R^2 \sin\theta \, d\theta \, d\phi$. The amount of radiant energy E_{sph} reflected from the illuminated hemisphere to a unit solid angle in the direction of z is

$$E_{\text{sph}} = \int_{S^+} F r_{\text{sca}}(\mu_0, \mu_0, 0) \cos\theta \, dS, \tag{2.15}$$

where we integrate over a hemisphere. After a short manipulation, we obtain

$$E_{\text{sph}} = 2\pi R^2 F \int_0^1 r_{\text{sca}}(\mu_0, \mu_0, 0) \mu_0 \, d\mu_0. \tag{2.16}$$

Similarly, we express E_{Lam} for the Lambert disc ($\mu_0 = 1, A = 1$)

$$E_{\text{Lam}} = \pi R^2 F r_L(\mu_0) = \pi R^2 F \frac{\mu_0}{\pi} A = R^2 F. \tag{2.17}$$

The geometric albedo can then be calculated as

$$A_{\text{g}} = 2\pi \int_0^1 r_{\text{sca}}(\mu_0, \mu_0, 0) \mu_0 \, d\mu_0. \tag{2.18}$$

[10]We assume that both the body and the Lambertian disc are observed at zero phase angle (corresponds to opposition).

Let us further define the Bond albedo

$$A_B = 2 \int_0^1 \mu_0 A_h(\mu_0)\, d\mu_0, \tag{2.19}$$

where A_h is the hemispheric albedo (1.5). The Bond albedo expresses the ratio between the energy of radiation scattered by a spherical object in all directions and the energy of the incident radiation (e.g. Hapke, 2012).

In our simulation, we used $A_g = 0.33 \pm 0.08$ (Delbo' et al., 2007a). By substituting (2.11) to (2.18) one would obtain

$$A_g = \frac{1}{2} r_0 (1 + \frac{1}{3} r_0) + \frac{w}{8} \left[(1 + B_0) P(0) - 1 \right], \tag{2.20}$$

where $r_0 = (1 - \gamma)/(1 + \gamma)$. This relation then constrains the values of Hapke parameters (w, B_0, h_S, g).

When studying the orbital evolution of Apophis until 2029, we used two radiation models: (a) the Lambert model with the albedo $A = 0.2$ and (b) the Hapke model with the set of parameters $w = 0.5$, $g = -0.35$, $h_s = 0.02$ and $B_0 = 0.97$ which lead to $A_g = 0.34$. Let us note that the choice of Hapke's variables is not unambiguous. Our values correspond to a rather higher slope parameter G in the IAU $H - G$ system. The transformation relations between the slope parameter G and the Hapke parameters can be found in Verbiscer and Veverka (1995). For a typical value of $G \approx 0.15$, we could also use $w = 0.34, g = -0.27, h_s = 0.05$ and $B_0 = 1.98$ which leads to a practically identical value of the geometric albedo A_g. The described choice does not, however, have a statistically significant influence on our simulation results, as opposed to the previous set.

The functions $K_1^{\rm sca}(\mu_0)$ and $K_2^{\rm sca}(\mu_0)$ that appear in the expression for the perturbation force (2.4) depend on the zenith distance of the Sun and should be evaluated in each integration step. In the case of the Hapke model, we precomputed $K_1^{\rm sca}(\mu_0)$ and $K_2^{\rm sca}(\mu_0)$ to speed up the whole calculation (see Fig. 2.8). We chose a sufficiently dense mesh[11] of discrete values and obtained the $K_1^{\rm sca}(\mu_0)$ and $K_2^{\rm sca}(\mu_0)$ by linear interpolation. Let us remind that, in the case of the Lambertian model, $K_1^{\rm sca}(\mu_0) = \frac{2}{3}\mu_0 A \wedge K_2^{\rm sca} = 0$ where the albedo was chosen as[12] $A = 0.2$.

Used shape models for Apophis

Pravec et al. (2014) used photometric observations to deduce the shape of the asteroid (99942) Apophis (see Fig. 2.4). However, at the time of our study, its actual shape had not been known yet. In addition, the information about the pole orientation and the rotation speed were lacking. Our calculations were, therefore, based on a set of synthetically generated bodies - random Gaussian spheres (see Muinonen, 1998; Muinonen and Lagerros, 1998; Vokrouhlický and Čapek, 2002) which well reflect the real shapes of asteroids in the main belt. We also assumed that Apophis rotates around the shortest axis of the inertia tensor with the rotational period $T_{\rm rot} = 30.5$ h (Behrend et al., 2005). The direction of the spin axis was chosen randomly for each of the many repeated simulations.

[11] The μ_0 was sampled in the $[0, 1]$ interval.

[12] Equal to Bond albedo A_B as well as the hemispheric albedo A_h.

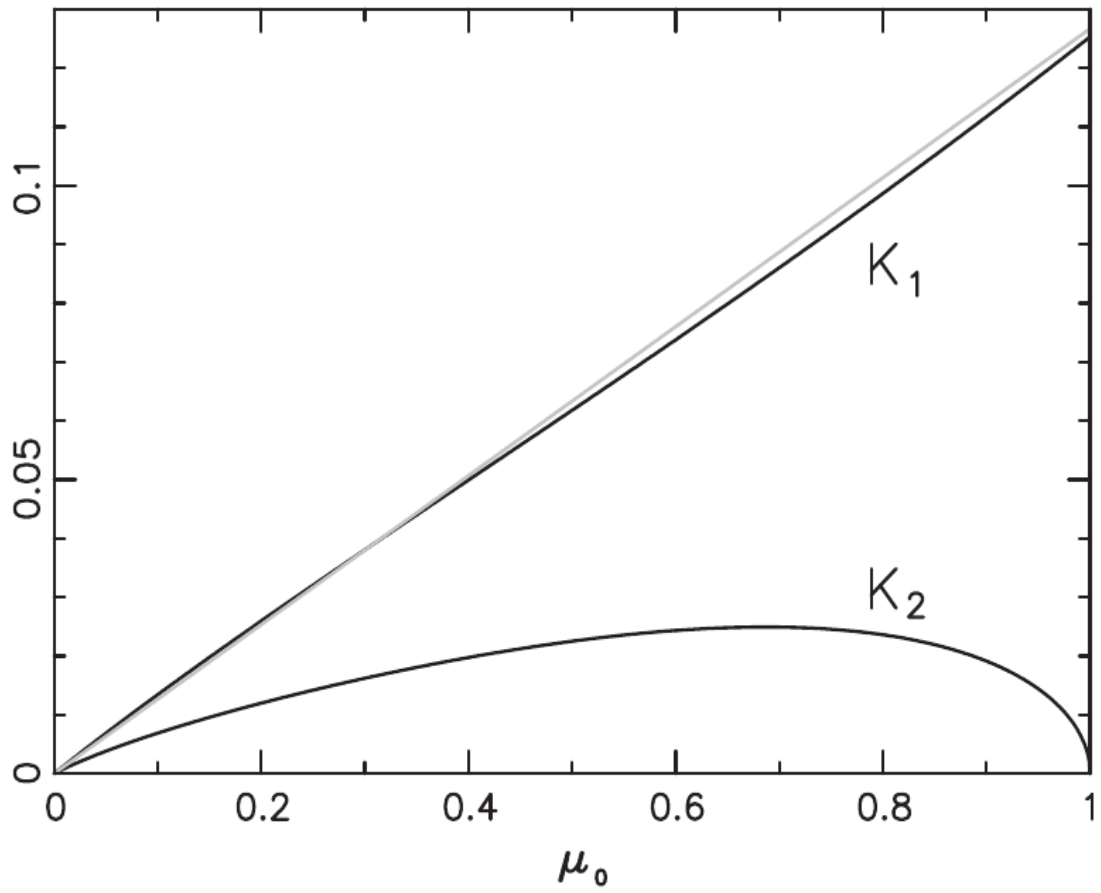

Figure 2.8: Functions $K_1(\mu_0)$ and $K_2(\mu_0)$ for a set of Hapke parameters $w = 0.5, g = -0.35, h_s = 0.02$ and $B_0 = 0.97$. The gray linear function with the slope $(2/3)A_B$ approximates very well ($A_B \approx 0.2$) the function $K_1(\mu_0)$. Source: Žižka and Vokrouhlický (2011b).

Specifically, we propagated 200 random Gaussian spheres created according to Vokrouhlický and Čapek (2002) and Čapek and Vokrouhlický (2004). Each sphere had 10 randomly chosen values of obliquity. Altogether, we numerically integrated 2000 bodies from March 2010 to April 2029. Note that our synthetic bodies had the density of[13] $\rho = 2$ g cm^{-3}. The size of each Gaussian sphere was scaled so that its volume was equal to that of a sphere with 270 m in diameter. Thus our results are statistical in nature since the rotational state and the shape of Apophis were not known at the time. Nonetheless, the results are significant because they capture the influence of SRP on the orbital evolution of Apophis until 2029 and also provide a relative comparison of the influence of SRP and the Yarkovsky effect. They also constrain possible values of the close-approach (CA) distance of Apophis when only SRP is taken into account. In addition, the actual shape of Apophis should follow our statistical results.

Since the Gaussian spheres are represented by polyhedrons, it is necessary to use a mathematical tool for finding their fundamental characteristics (see Dobrovolskis, 1996; Čapek, 2007).

[13]Since the density of Apophis was not known, we used the density of the asteroid (25143) Itokawa (Abe et al., 2006).

Each polyhedron can be divided into a set of partial tetrahedrons with the origin in point O and vertices $\mathbf{E}_i, \mathbf{F}_i, \mathbf{G}_i$. These vertices form the i-th triangular surface element on its surface (see Fig. 2.9). Let us now mention some of the key expressions. The center of mass $\mathbf{t}_i$ of the i-th surface element and the center of mass $\mathbf{r}_i$ of the i-th tetrahedron are given by

$$\mathbf{t}_i = \frac{1}{3}(\mathbf{E}_i + \mathbf{F}_i + \mathbf{G}_i), \tag{2.21}$$

$$\mathbf{r}_i = \frac{1}{4}(\mathbf{E}_i + \mathbf{F}_i + \mathbf{G}_i). \tag{2.22}$$

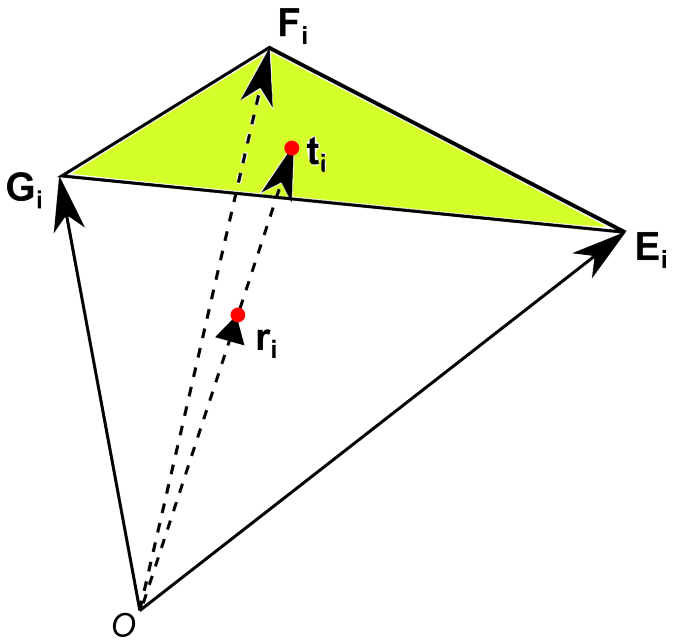

Figure 2.9: A tetrahedron with vertices $O, \mathbf{E}_i, \mathbf{F}_i, \mathbf{G}_i$, the center of mass $\mathbf{t}_i$ of the triangular facet and the center of mass $\mathbf{r}_i$ of the tetrahedron.

For the normal vector pointing outwards from the i-th surface element, it holds that

$$\mathbf{n}_i = \frac{1}{2}(\mathbf{F}_i - \mathbf{E}_i) \times (\mathbf{G}_i - \mathbf{E}_i), \tag{2.23}$$

while the total surface area of the body S is given by $S = \sum_i S_i = \sum_i |\mathbf{n}_i|$.

Let us define the parameter ν_i which denotes the number of surface elements with the index $j \neq i$ intersected by a line in the direction of $\mathbf{t}_i$. If we solve a linear equation for the j-th surface element

$$\mathbf{t}_i = a\mathbf{E}_j + b\mathbf{F}_j + c\mathbf{G}_j, \tag{2.24}$$

which gives the result $a > 0 \wedge b > 0 \wedge c > 0$, then vector $\mathbf{t}_i$ does, indeed, intersect the surface element. For convex bodies, it certainly holds that $\nu_i = 1$. A contribution of i-th tetrahedron to the total volume can be calculated using the expression

$$V_i = \frac{1}{3}(-1)^{\nu_i - 1}|\mathbf{E}_i \cdot \mathbf{n}_i|. \tag{2.25}$$

The total volume of the body is then obtained by a straightforward summation $V = \sum_i V_i$. The center of mass of the whole body at the assumption of uniform bulk density is

$$\mathbf{r} = \frac{1}{V} \sum_i V_i \mathbf{r}_i. \tag{2.26}$$

To define a coordinate system co-rotating with the body, it is beneficial to find the principal axes of the inertia tensor $\mathbf{I}$. It is also convenient to comupute the vectors $\mathbf{E}_i, \mathbf{F}_i, \mathbf{G}_i$ with respect to the center of mass of the body. We then have $\mathbf{E_i} \to \mathbf{E_i} - \mathbf{r}$, $\mathbf{F_i} \to \mathbf{F_i} - \mathbf{r}$, $\mathbf{G_i} \to \mathbf{G_i} - \mathbf{r}$. The components of the inertia tensor $\mathbf{I}_i$ of the i-th tetrahedron are given by (see Dobrovolskis, 1996)

$$I_{ixx} = P_{iyy} + P_{izz} \qquad I_{iyz} = -P_{iyz}, \tag{2.27}$$

$$I_{iyy} = P_{izz} + P_{ixx} \qquad I_{ixz} = -P_{ixz}, \tag{2.28}$$

$$I_{izz} = P_{ixx} + P_{iyy} \qquad I_{ixy} = -P_{ixy}, \tag{2.29}$$

where

$$P_{ijk} = \frac{\rho V_i}{20}(2E_jE_k + 2F_jF_k + 2G_jG_k + E_jF_k + E_kF_j + E_jG_k + E_kG_j + F_jG_k + F_kG_j). \tag{2.30}$$

The overall inertia tensor is then obtained by summation over all tetrahedrons

$$\mathbf{I} = \sum_i \mathbf{I}_i. \tag{2.31}$$

Once the inertia tensor $\mathbf{I}$ is known, it is no longer difficult to find its principal axes and the corresponding moments of inertia.

Apart from the Gaussian spheres, we also repeated our simulations for 16 actual shapes of near-Earth asteroids[14]. Each of the real shapes was propagated 50 times with a different pole orientation. Thus, we modeled the orbital evolution of 800 bodies in total, again from March 2010 to April 2029. It is important to mention that the results did not differ notably from the results obtained by using Gaussian spheres only.

Numerical simulation strategy

We used an open source package `OrbFit`[15] which includes a highly accurate Radau-Everhart integrator of the 15th order. In this package we implemented our numerical model of the radiation pressure. Let us now summarize the key points of our numerical simulation.

1. For each Gaussian sphere we pre-calculated all the important parameters, such as the total surface area S, the volume V and the position of the center of mass $\mathbf{r}$.

2. We expressed the vertices coordinates $\mathbf{E_i}, \mathbf{F_i}, \mathbf{G_i}$ relative to the center of mass $\mathbf{r}$. After determining the inertia tensor $\mathbf{I}$ including the principal axes $\mathbf{e}_x, \mathbf{e}_y, \mathbf{e}_z$ we transformed the normal vectors $\mathbf{n}_i$ and the vertices into the basis $\{\mathbf{e}_x, \mathbf{e}_y, \mathbf{e}_z\}$.

[14] Available at `http://echo.jpl.nasa.gov/links.html`.
[15] Available at `http://adams.dm.unipi.it/orbfit/`.

3. After a random choice of the angular velocity vector $\boldsymbol{\omega}$, we defined orthonormal bases $\mathcal{B} = \{\boldsymbol{\xi}, \boldsymbol{\eta}, \boldsymbol{\zeta}\}$ and $\mathcal{B}' = \{\boldsymbol{\xi'}, \boldsymbol{\eta'}, \boldsymbol{\zeta'}\}$ where $\boldsymbol{\omega} \parallel \boldsymbol{\zeta} \parallel \boldsymbol{\zeta'}$ and let the basis $\mathcal{B}'$ rotate at the angular frequency of $\omega = \frac{2\pi}{P_{\mathrm{rot}}}$ relative to the basis $\mathcal{B}$ with $P_{\mathrm{rot}} \approx 30.5$ h. It then holds that

$$\boldsymbol{\xi'} = \cos(\omega t)\boldsymbol{\xi} + \sin(\omega t)\boldsymbol{\eta}, \tag{2.32}$$

$$\boldsymbol{\eta'} = -\sin(\omega t)\boldsymbol{\xi} + \cos(\omega t)\boldsymbol{\eta}, \tag{2.33}$$

$$\boldsymbol{\zeta'} = \boldsymbol{\zeta}. \tag{2.34}$$

4. The position of Apophis is given by a heliocentric vector $\boldsymbol{x} = (x_1, x_2, x_3)$, which naturally points in the opposite direction than vector $\mathbf{n}_0$ pointing from Apophis towards the Sun. We expressed the components of $\boldsymbol{x}$ in the $\mathcal{B}'$ basis as

$$x'_1 = x_1\xi'_x + x_2\xi'_y + x_3\xi'_z, \tag{2.35}$$

$$x'_2 = x_1\eta'_x + x_2\eta'_y + x_3\eta'_z, \tag{2.36}$$

$$x'_3 = x_1\zeta'_x + x_2\zeta'_y + x_3\zeta'_z \tag{2.37}$$

and calculated the unit vector $\boldsymbol{n}_0$ which is in the co-rotating frame $\mathcal{B}'$ given by

$$\boldsymbol{n}_0 = -(x'_1, x'_2, x'_3)/\sqrt{(x'_1)^2 + (x'_2)^2 + (x'_3)^2}. \tag{2.38}$$

5. In each time step we determined the flux $F = F_{1\mathrm{au}}/x^2$ and decided which of the surface elements met the necessary condition of illumination $\boldsymbol{n}_i \cdot \boldsymbol{n}_0 > 0$. Consequently, we chose only those that were not shadowed.

6. Then either Lambertian or Hapke radiation model was used. For the i-th illuminated surface element, we found the contribution $(\mathrm{d}\mathbf{f}_{\mathrm{sca}})_i$ to the resulting force $\mathbf{f}_{\mathrm{sca}}$ and calculated $\mathbf{f}_{\mathrm{sca}} = \sum_{i=1}^{N}(\mathrm{d}\mathbf{f}_{\mathrm{sca}})_i$.

7. In each time step we calculated the cross-section of the body $S_\perp$, the force $\mathbf{f}_{\mathrm{inc}}$ and the resulting perturbation force $\mathbf{f} = \mathbf{f}_{\mathrm{sca}} + \mathbf{f}_{\mathrm{inc}}$ caused by both incident and scattered radiation.

8. The perturbation acceleration $\mathbf{a}$ has, in the original basis, the components

$$a_x = \frac{1}{\rho V}(f_x\xi'_x + f_y\eta'_x + f_z\zeta'_x), \tag{2.39}$$

$$a_y = \frac{1}{\rho V}(f_x\xi'_y + f_y\eta'_y + f_z\zeta'_y), \tag{2.40}$$

$$a_z = \frac{1}{\rho V}(f_x\xi'_z + f_y\eta'_z + f_z\zeta'_z). \tag{2.41}$$

9. Finally, the resulting perturbing acceleration $\mathbf{a}_{\mathrm{tot}}$ is given by the sum of gravitational interaction and SRP

$$\mathbf{a}_{\mathrm{tot}} = \mathbf{a}_{\mathrm{g}} + \mathbf{a}. \tag{2.42}$$

At this point, we summarize the statistical results that were obtained by propagation of the Gaussian spheres up to the point of the closest approach to Earth on April 13, 2029. We also briefly studied the hypothetical case of Apophis having a spherical shape. It can be shown that, for a spherical body and the Lambertian scattering, it holds that (see Vokrouhlický and Milani, 2000)

$$\mathbf{f}_{\mathrm{SRP}} = -\frac{FS_{\perp}}{c}\left(1+\frac{4}{9}A\right)\mathbf{n}_0. \tag{2.43}$$

As a control test, we carried out two sets of numerical integrations. First, we calculated the force $\mathbf{f}_{\mathrm{SRP}}$ analytically in each integration step using (2.43). Then, we constructed a wire-frame model of a sphere with 7200 surface elements, repeated the propagation and calculated $\mathbf{f}_{\mathrm{SRP}}$ numerically using the procedure described above. We also tried various orientations of the spin axis and in both approaches, we obtained identical distributions of recorded close approach (CA) distances in 2029. This simple test assured us that our algorithm should be implemented properly. In parts (a) to the figures below, we show the results that consider both the incident and scattered radiation. Parts (b) include the results caused exclusively by scattering. Note that without taking the SRP into account, Apophis will encounter Earth at a minimum nominal distance of 38046.825 km. The CA distances of Gaussian spheres are therefore given relative to this nominal value. We also compare the results obtained by the Lambertian and Hapke models. Finally, Fig. 2.12 shows the CA distances for real asteroid shapes.

The results

We studied the influence of incident and scattered radiation on the orbital evolution of (99942) Apophis from March 2010 to April 2029. We focused our attention especially on the distribution of close-approach distances between the Gaussian spheres and the Earth. The outcome of our study clearly shows that the role of the incident and scattered radiation in the orbital evolution of Apophis is more than an order of magnitude lower than the perturbations caused by the Yarkovsky effect (see Giorgini et al., 2008; Vokrouhlický et al., 2015b).

Furthermore, we did not observe any significant difference between applying the Lambert and Hapke model. The results also did not change when including the shadowing of individual surface elements - either in the case of Gaussian spheres or in the case of radar observation-based models. Note that if only scattering is considered, the CA distribution is symmetrical around zero. However, after taking the incident radiation into account, the encounter distances are increased by approximately 4 km.

Let us note that if we modeled the orbital evolution of Apophis using its actual shape and rotational state, the result should lie within the set of solutions obtained.

We are also convinced that the more recent value of the effective diameter of 375 m (Pravec et al., 2014) would lead to an even narrower CA distribution. It is also important to bear in mind that the year 2029 is now only 11 years away, as opposed to the original 19 years, meaning that the SRP will simply act for a shorter period.

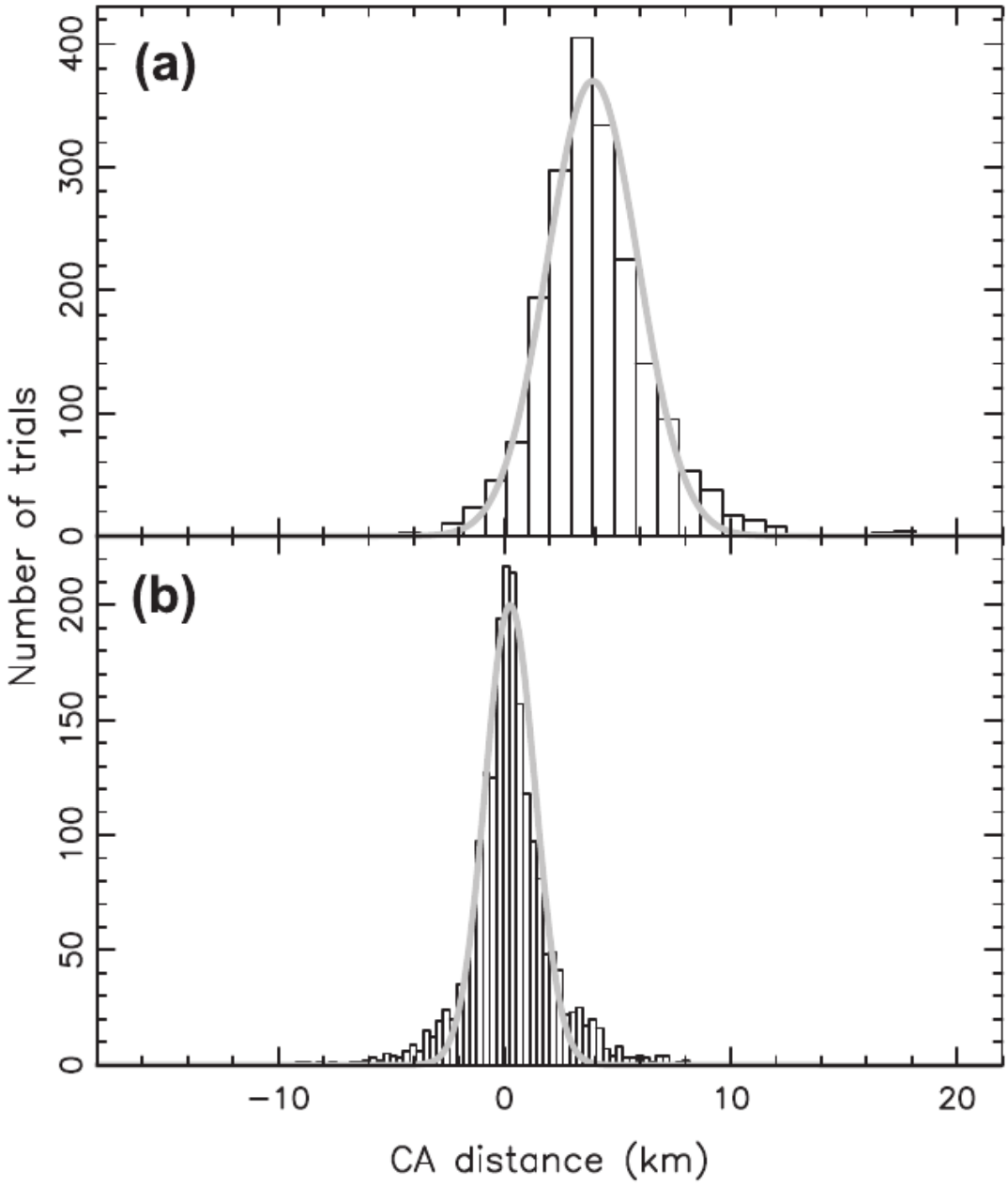

Figure 2.10: The distribution of close-approach (CA) distances between 2000 propagated Gaussian spheres and the Earth on 13 April 2029. The CA distances are related to the nominal trajectory of Apophis (see the text). Part (a) shows the results obtained when including both incident and scattered radiation, part (b) shows results obtained by considering only the scattered radiation. We used the Lambertian model with the albedo of 0.2. The effective diameter of all the bodies was equal to 270 m and the density was set to 2 g cm^{-3}. In part (a), the mean CA distance is $\approx$ 4 km with the standard deviation of $\approx$ 2 km. In part (b), the mean CA distance is $\approx$ 0 km and the standard deviation is $\approx$ 1.1 km. Source: Žižka and Vokrouhlický (2011b).

Pravec et al. (2014) have shown that Apophis does not rotate around any of the principal axes of the inertia tensor. This is rather different from our assumption. However, we still assume that tumbling will not have any significant influence on the results obtained.

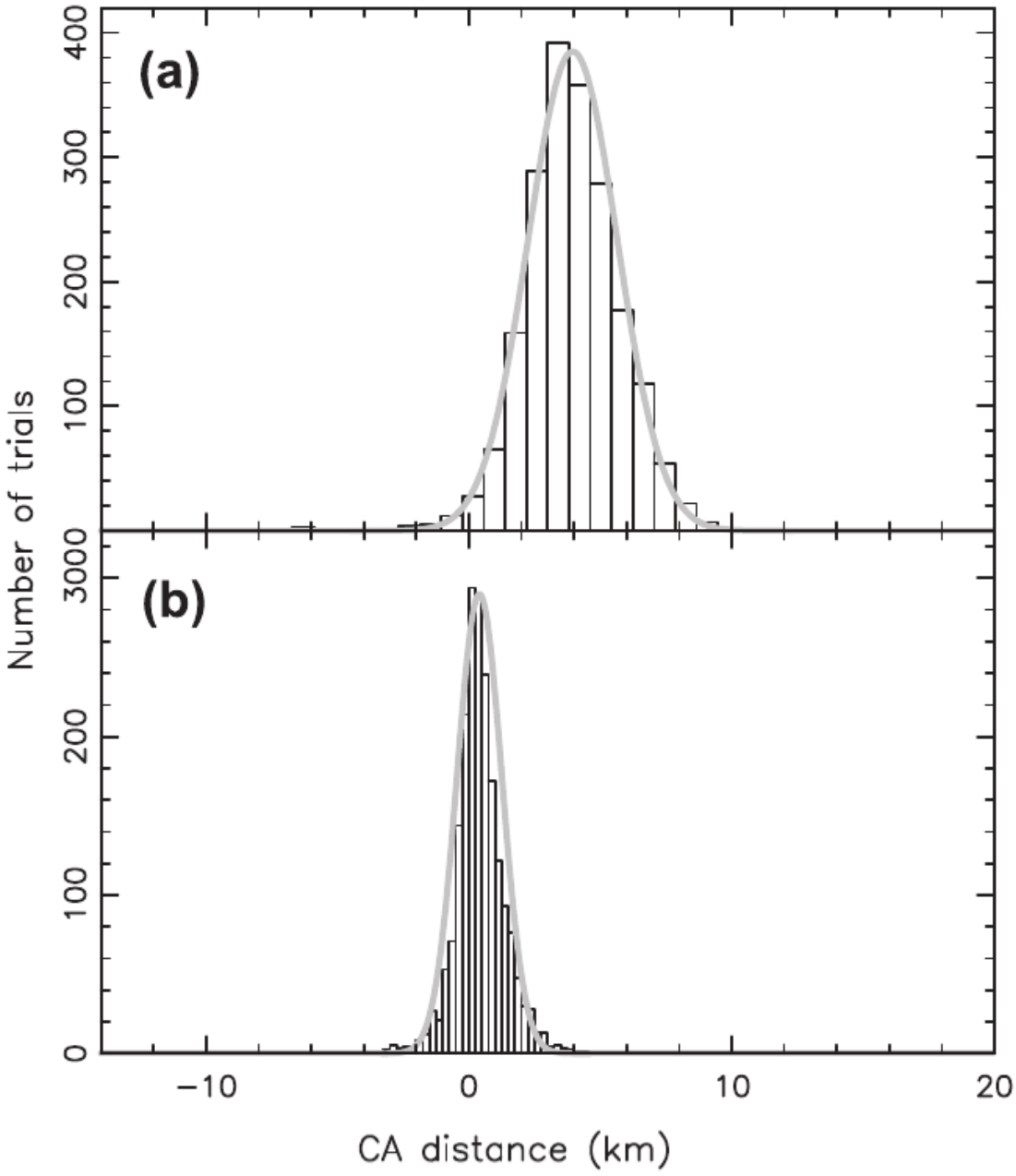

Figure 2.11: Similar to Fig. 2.10. Instead of the Lambertian model, the Hapke model was used. The parameters of the Hapke model are $w = 0.5$, $g = -0.35$, $h_s = 0.02$ and $B_0 = 0.97$. In part (a), the mean CA distance is ≈ 4 km with the standard deviation of ≈ 1.7 km. Part (b) gives the mean CA distance of ≈ 0 km with the standard deviation of ≈ 0.9 km. Source: Žižka and Vokrouhlický (2011b).

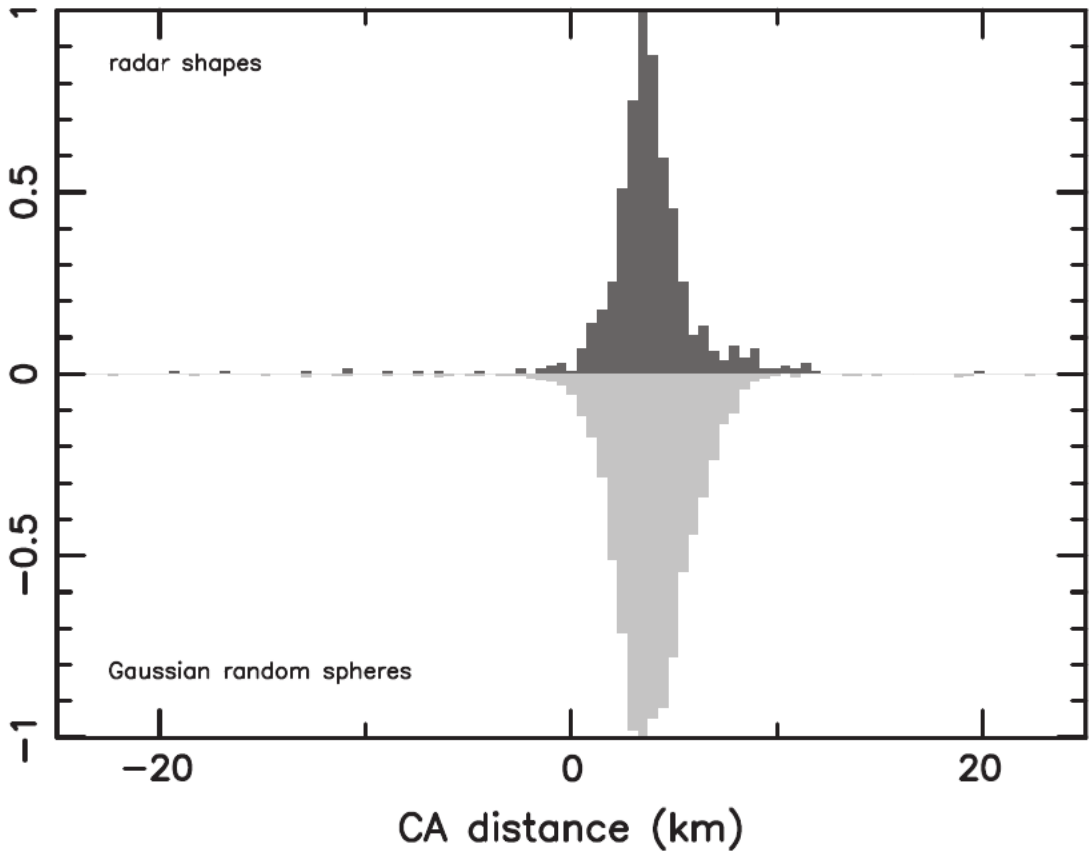

Figure 2.12: The distribution of CA distances with respect to the nominal orbit on 13 April 2029. We used 16 actual asteroid shapes derived from radar observations (top) and each of them propagated for 50 random pole orientations. The data is, therefore, based on 800 different configurations. We used the Hapke model and included the influence of incident and scattered radiation. The lower part of the figure shows, for reference, mirrored data from the upper part of Fig. 2.11. Note that the mean CA distance in the upper part is again ≈ 4.0 km with standard deviation of ≈ 1.3 km which is somewhat lower than 1.7 km. The distribution is normalized to the most occupied bin. Source: Žižka and Vokrouhlický (2011b).

To conclude, we expect that the perturbations in the orbital evolution of Apophis caused by incident and scattered radiation will play an important role primarily in future sophisticated models which should be able first to precisely capture the influence of the Yarkovsky and YORP effects. In the first approximation, it is, therefore, possible to neglect the effect of SRP. On the other hand, kilometer-sized uncertainties of the CA distance are still significant with respect to the keyhole sizes. This might be a very good motivation for re-calculating the whole problem for the actual shape of Apophis and its updated rotational state.

2.3 The influence of the Yarkovsky effect

Although the collision with Earth has been practically ruled out for the next few decades, there still exists a non-zero impact probability after the year 2060. In the previous paragraph, we mentioned that the Yarkovsky effect significantly participates in the perturbations of the Apophis' orbit. Note that it produces an order of magnitude larger orbital perturbations than the solar radiation pressure (Žižka and Vokrouhlický, 2011b). With time, Yarkovsky-induced perturbations manifest in the orbital uncertainties that are larger than those caused by observational uncertainties (see Chesley, 2006; Farnocchia et al., 2013a; Vokrouhlický et al., 2015b).

Chesley (2006) and Farnocchia et al. (2013a) studied the fingerprints of all possible orbital realizations of Apophis in the 2029 b-plane due to the Yarkovsky effect. They neglected the effect of SRP and carried out a number of repeated propagations with the thermophysical parameters (obliquity, effective diameter, etc.) chosen from the respective intervals of their limit values. A few years later, Vokrouhlický et al. (2015b) used a new solution of the shape and rotational state of Apophis (Pravec et al., 2014; Müller et al., 2014) and provided a more up-to-date model of its dynamical evolution. Their results also revised the impact probabilities after 2029. We will briefly outline how they modeled the Yarkovsky effect and what are its major consequences on the values of future impact probabilities.

Finding that Apophis does not rotate around any of the principal axes of the inertia tensor (NPA rotator = Non Principal Axis rotator) and that it exhibits weak tumbling, brought a major turnaround to the previous studies. The solutions in which we assume a body rotating around the shortest axis of the inertia tensor, therefore, do not correspond to the actual rotational state.

Let us remind that in the case of NPA rotators, we typically use Euler angles ϕ, θ, ψ to indicate the direction of the angular velocity vector $\boldsymbol{\omega}$ (see Fig. 2.13). These angles capture the transformation between the inertial system (X, Y, Z) and the non-inertial body-frame system[16] (x', y', z'). In principle, the motion of a NPA rotator can be described using 8 parameters. First, knowing the initial conditions is important - it is necessary to know the values of angles φ_0 and ψ_0 for an epoch t_0. The Euler angle θ depends on other parameters (see Kaasalainen, 2001). We place the moment of inertia vector $\mathbf{L}$ along the Z axis and describe its direction by the ecliptic longitude λ_L and the ecliptic latitude β_L. Other parameters that need to be known are $I_a = A/C$ and $I_b = B/C$, where (A, B, C) are the principal moments of inertia. Let us also note that the shortest axis c precedes around the vector $\mathbf{L}$. Finally, we also need to know the period of rotation P_ψ and the period of precession P_φ. The specified parameters can be determined from photometric measurements using inversion methods (see Kaasalainen, 2001; Pravec et al., 2005). In the case of Apophis, Pravec et al. (2014) found that $\beta_L = -75°$, $\lambda_L = 250°$, $P_\varphi = 27.38 \pm 0.07$ h, $P_\psi = 263 \pm 6$ h, $I_a = 0.61^{+0.11}_{-0.08}$ and $I_b = 0.965^{+0.009}_{-0.015}$.

Vokrouhlický et al. (2015b), however, considered another fundamental period P_{orb}, which corresponds to the period of Apophis' revolution around the Sun (assuming undisturbed trajectory).

[16] Basis vectors of this system correspond to the eigenvectors of the inertia tensor.

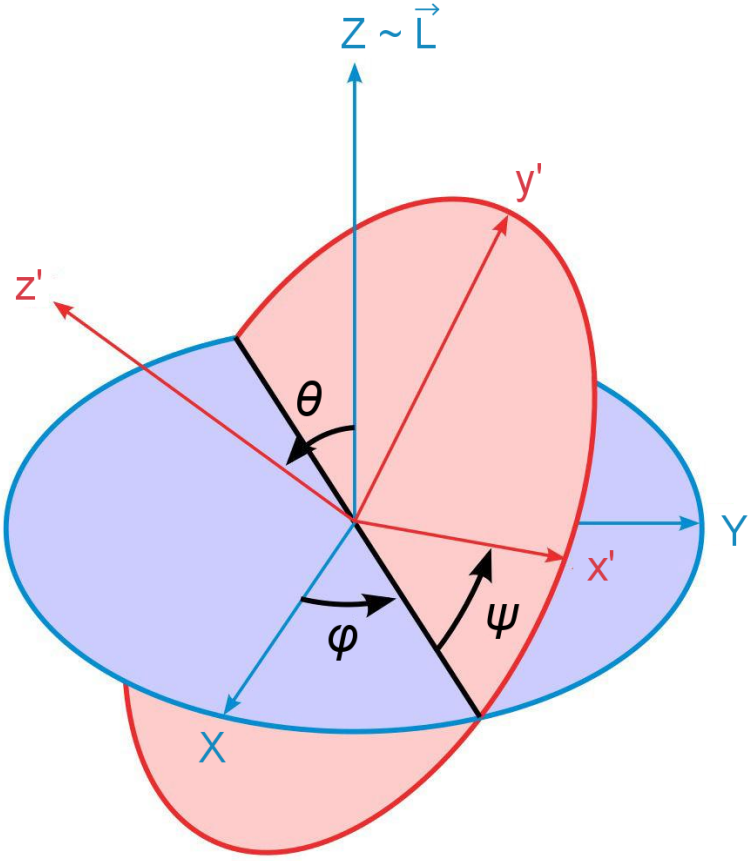

Figure 2.13: The coordinate system (x', y', z') connected with the rotating body. It is constructed from the initial state $x' \equiv X$, $y' \equiv Y$, $z' \equiv Z$ by applying a sequence of three operations: (I) rotation around the axis z' by the precession angle φ in the clockwise direction, (II) rotation around the tilted axis x' by the nutation angle θ and (III) rotation around the tilted axis z' by the spin angle ψ. The inertial system (X, Y, Z) can be connected with the moment of inertia vector $\mathbf{L}$. Vector $\mathbf{L}$ does not change its orientation as long as the total torque acting on the body is zero. The vector pointing towards the vernal equinox then lies in the XZ plane.

The periods P_φ and P_ψ can be formally included in the diurnal variant of the Yarkovsky effect while the P_{orb} would correspond to the seasonal variant (see Section 1.1.2). Even though analyzing the influence of the Yarkovsky effect on the orbital evolution of Apophis is, practically, a numerical task, the method of solving the heat equation requires[17] the period P_{orb} to be divisible by both P_ψ and P_ϕ. Vokrouhlický et al. (2015b) achieved this by slightly varying the semi-major axis of Apophis and by a small change of parameters specifying P_ψ and P_φ.

In their study, the model of Apophis is represented by a polyhedron with a total of 2024 surface elements (Pravec et al., 2014). For each of these elements, classical numerical methods (see Čapek and Vokrouhlický, 2005; Čapek, 2007) were applied to solve the heat equation. Note that Vokrouhlický et al. (2015b) neglected the heat transfer between the surface elements as well as the effect of mutual irradiation.

[17] A periodical solution of the heat equation is expected.

The heat equation was solved in 1D approximation with a single spatial coordinate z pointing from the surface element inside the body. Assuming a periodical solution with the period P_{orb}, we are interested in the domain $\mathcal{D} = (0, Z)\times(0, P_{\mathrm{orb}})$ where Z is the maximum depth considered, which was chosen as 15 times the penetration depth $h_{\mathrm{orb}} = \sqrt{KP_{\mathrm{orb}}/2\pi\rho C}$. Let us remind that K is the thermal conductivity, ρ the bulk density and C the heat capacity of the surface layer (see Section 1.1.2). The boundary conditions are: (i) $T(0, z) = T(P_{\mathrm{orb}}, z)$, (ii) the Neumann condition $(\partial T/\partial z)_{z=Z} = 0$ expressing the existence of an isothermal core at the depth of $z > Z$ and (iii) Robin boundary condition for the surface element $\epsilon\sigma T^4_{(z=0)} - K(\partial T/\partial z)_{z=0} = E(t)$ where $E(t)$ is the absorbed radiant energy (see Eq. 1.2). Vokrouhlický et al. (2015b) took the thermal conductivity from the range $K \in [0.01, 1]$ W m^{-1} K^{-1} and set the integration step size dt to 3 s. The depth was divided into $dz_j \simeq dze^{0.1j}$ segments, where j and $dz = 3 \times 10^{-3}\sqrt{K}$ m denote the j-th grid point and the initial step at the surface. For smaller values of the thermal conductivity K, the interval dz was further reduced because of the small penetration depth h_ϕ. Specifically, the initial step dz in that case corresponded to $(1/100)h_\phi$.

The effect of shadowing was also studied. Although the model of Apophis is convex, Vokrouhlický et al. (2015b) slightly modified its shape to make it a little non-convex. Then by direct tracing of solar rays, they identified the shadowed facets for which they set $E(t) = 0$. An important result of their study is that the shadowing effect changes the semi-major axis drift only in the order of a few percent, as opposed to the situation without shadowing. The heat equation was solved using the Finite Difference Method. Vokrouhlický et al. (2015b) used the discretization scheme for the region $\mathcal{D}$ with constant time step dt and exponentially growing step in the z coordinate. The numerical iterative solution was stopped if the relative temperature difference was less than $\simeq 0.1\%$ in all the points within the grid $\mathcal{D}$. The result of the whole process is the surface distribution of temperature. Next, they chose the Lambertian model and for each surface element they calculated the contribution to the overall Yarkovsky force. Let us outline the main steps in their computational strategy.

The perturbation force caused by the thermal emission from the i-th surface element takes the well-known form $\mathbf{\Delta f}_i = -(2/3)(\epsilon\sigma T_i^4/c)\mathbf{\Delta S}_i$ where ϵ is the emissivity and $\mathbf{\Delta S}_i$ the normal oriented outwards from the facet. The resulting perturbation force at time t is the sum of contributions from all the surface elements and it holds that $\mathbf{f}(t) = \sum \mathbf{\Delta f}_i$. By using the Gaussian perturbation equation, we then find the time derivative of the semi-major axis $\frac{da}{dt}$. It is also useful to average the $\frac{da}{dt}$ over one orbital period P_{orb} as follows

$$\left\langle \frac{da}{dt} \right\rangle = \frac{1}{P_{\mathrm{orb}}} \int_0^{P_{\mathrm{orb}}} (da/dt)dt. \tag{2.44}$$

Note that Vokrouhlický et al. (2015b) neglected the existence of shape irregularities with characteristic dimensions smaller than the size of surface elements (i.e. boulders, craters, slopes, etc.).

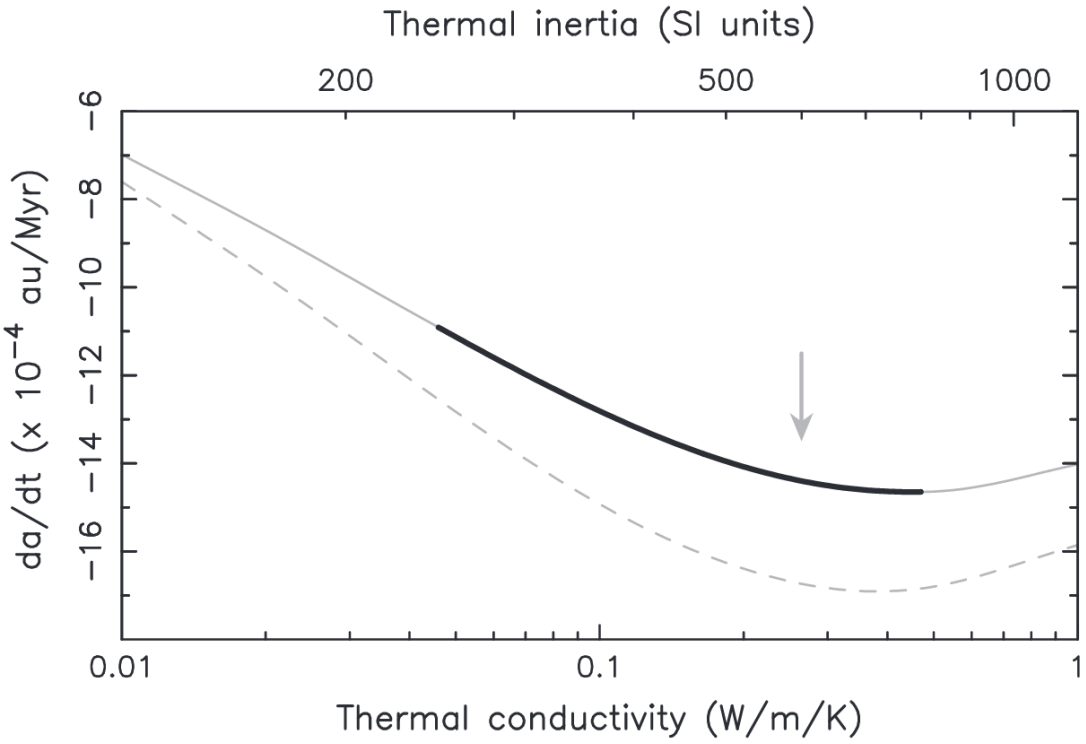

Figure 2.14: Secular drift of the semi-major axis $\left\langle \frac{da}{dt} \right\rangle$ of the asteroid (99942) Apophis caused by the Yarkovsky effect. The dependence covers the thermal conductivity values from the range $K \in [0.01, 1]$ W m^{-1} K^{-1} with other thermophysical parameters being *constant* (see the text). The full line presents the solution of both the A and B versions which are not distinguishable in the presented scale. The full black highlighted section captures the interval of expected thermal conductivities (Müller et al., 2014). The gray arrow corresponds to the surface thermal inertia of $\Gamma = 600$ (SI). The dashed curve shows the analytical solution for a spherical body with 375 m in diameter and the rotational period of 30.56 hours (see Vokrouhlický, 1999) which is on a circular orbit with pole orientation fixed at ecliptic coordinates of (250°, -75°). Source: Vokrouhlický et al. (2015b).

Vokrouhlický et al. (2015b) used two models to simulate the Yarkovsky effect, denoting them A and B. In model A, they set $I_a = 0.61042$ and in model B $I_a = 0.60710$. In both cases, they maintained the nominal value $I_b = 0.965$ (Pravec et al., 2014). These values were chosen so that the following ratios are integers: $P_{\rm orb}/P_\phi = 280$ and $P_{\rm orb}/P_\psi = 29$ for $P_{\rm orb} = 319.5972$ days for model A and $P_{\rm orb}/P_\phi = 288$ for model B. The solution A then corresponds to a smaller semi-major axis and the solution B to a larger semi-major axis. For this reason, it was necessary to re-calibrate the value of the Solar constant to be consistent with the actual heliocentric distance of Apophis. The shape model of Apophis (Pravec et al., 2014) was scaled so that its total volume equals to the volume of a sphere with diameter $D = 375$ m (Müller et al., 2014). Other nominal parameters used in the work by Vokrouhlický et al. (2015b) are the thermal capacity $C = 680$ J kg^{-1} K^{-1}, the surface and volume density 2 g cm^{-3}, the Bond albedo $A = 0.14$ and the emissivity $\epsilon = 1 - A = 0.86$. All of them are based on the mean values of distributions presented in Farnocchia et al. (2013a).

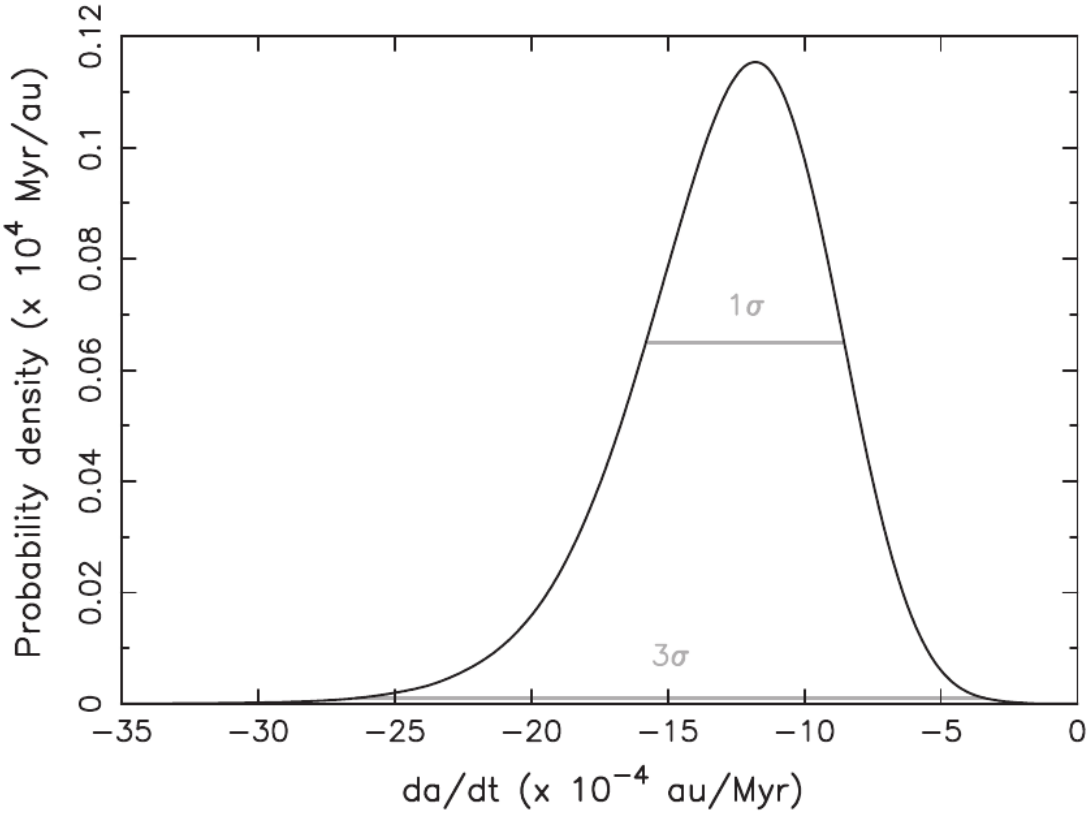

Figure 2.15: Statistical distribution of the mean semi-major axis drift $\left\langle \frac{da}{dt} \right\rangle$ according to Vokrouhlický et al. (2015b). The horizontal lines are 1σ and 3σ confidence levels. Let us note that the distribution is non-symmetrical with the peak at -11.8×10^{-4} au/Myr, the mean value of -12.8×10^{-4} au/Myr, the 1σ confidence interval of $[-15.7, -8.6] \times 10^{-4}$ au/Myr and the 3σ confidence interval of $[-26.4, -3.4] \times 10^{-4}$ au/Myr.

Vokrouhlický et al. (2015b) found (see Fig. 2.14) that the secular drift of the semi-major axis $\left\langle \frac{da}{dt} \right\rangle$ for the thermal conductivities $K \in [0.01, 1]$ W m^{-1} K^{-1} is in the range from -15×10^{-4} au/Myr to -11×10^{-4} au/Myr. Note that the difference with regard to the analytical solution is approximately 15% which proves that the analytical theory according to Vokrouhlický (1999) is a good zeroth approximation also for realistic bodies. In other words, the numerically found drift of Apophis $\left\langle \frac{da}{dt} \right\rangle$ is 0.85-times the result of the analytical solution. However, note that owing to a number of uncertain or limited thermophysical parameters of the asteroid, it is practically impossible to find the exact value of $\left\langle \frac{da}{dt} \right\rangle$. On the other hand, the study of Apophis' orbital evolution can still provide results of statistical/probabilistic nature. By using the analytical theory of the Yarkovsky effect (see Vokrouhlický, 1999), Vokrouhlický et al. (2015b) calculated the probability distribution of the $\left\langle \frac{da}{dt} \right\rangle$ values for *all* acceptable thermophysical parameters of Apophis (Müller et al., 2014; Pravec et al., 2014). The conclusions of this analysis are summarized in Fig. 2.15 which also includes the role of surface roughness in the enhancement of the Yarkovsky effect. In the next section, we briefly demonstrate how these results affected the future impact probabilities.

Future impact probabilities of Apophis

As already mentioned at the beginning of this chapter, the Yarkovsky effect is the dominant non-gravitational perturbation of the Apophis orbit. Let us note that all plausible gravity-only solutions manifest as only ≈ 1 s in the uncertainty of the closest approach time in 2029[18], while the uncertainty due to the Yarkovsky effect is roughly tens of seconds. The perturbations caused by incident and scattered radiation are rather insignificant (Žižka and Vokrouhlický, 2011b). In order to see if the available astrometric data of Apophis reveal the Yarkovsky effect, Vokrouhlický et al. (2015b) modelled this perturbation by additional tangential acceleration a_T in the form $a_T = A_2/r^2$ where r is the heliocentric distance in au (see Marsden et al., 1973; Farnocchia et al., 2013a,b). They fitted the relevant astrometric and radar observations and limited the value of A_2 so that $A_2 = (-51 \pm 28) \times 10^{-15}$ au d^{-2}. Let us now consider the Gaussian equation for the semi-major axis drift (see Murray and Dermott, 1999)

$$\frac{da}{dt} = \frac{2}{n\sqrt{1-e^2}}[\hat{R}e\sin f + \hat{T}(1+e\cos f)], \tag{2.45}$$

where n is the mean motion, e the eccentricity, f the true anomaly, $\hat{R}$ the radial and $\hat{T}$ the tangential component of the perturbation acceleration. The expression can be rewritten in the form[19]

$$\frac{da}{dt} = \frac{2}{n\sqrt{1-e^2}}\left[\hat{T}\frac{a(1-e^2)}{r}\right]. \tag{2.46}$$

By substituting $\hat{T}$, we obtain

$$\frac{da}{dt} = \frac{2a\sqrt{1-e^2}}{nr}A_2 g(r), \tag{2.47}$$

where $g(r) = 1/r^2$. Let us further follow the approach presented in Farnocchia et al. (2013b) and average the drift da/dt over the orbital period

$$\left\langle \frac{da}{dt} \right\rangle = \frac{1}{P_{\rm orb}}\int_0^{P_{\rm orb}} (da/dt)\,dt = \frac{a\sqrt{1-e^2}}{\pi}A_2\int_0^{P_{\rm orb}} \frac{g(r)}{r}\,dt. \tag{2.48}$$

If we employ the following relation between the differentials dt and df (see Murray and Dermott, 1999)

$$\frac{df}{dt} = \frac{na}{r\sqrt{1-e^2}}(1+e\cos f), \tag{2.49}$$

we obtain

$$\left\langle \frac{da}{dt} \right\rangle = \frac{(1-e^2)}{n\pi}A_2\int_0^{2\pi} g(r)(1+e\cos f)^{-1}\,df \tag{2.50}$$

$$= \frac{(1-e^2)}{n\pi}A_2\int_0^{2\pi} \frac{1}{r^2}(1+e\cos f)^{-1}\,df \tag{2.51}$$

$$= \frac{2(1-e^2)A_2}{np^2}, \tag{2.52}$$

[18] At the confidence level of 3σ.

[19] Considering only the tangential component $\hat{T}$ of the perturbation acceleration. Furthermore, we used the equation of an ellipse in the polar form $r = a(1-e^2)/(1+e\cos f)$.

while $p = a(1 - e^2)$ is the semilatus rectum. Therefore, it holds for the A_2 parameter

$$A_2 = \frac{1}{2} n \left(\frac{a}{1\text{au}} \right)^2 (1 - e^2) \left(\frac{da}{dt} \right). \tag{2.53}$$

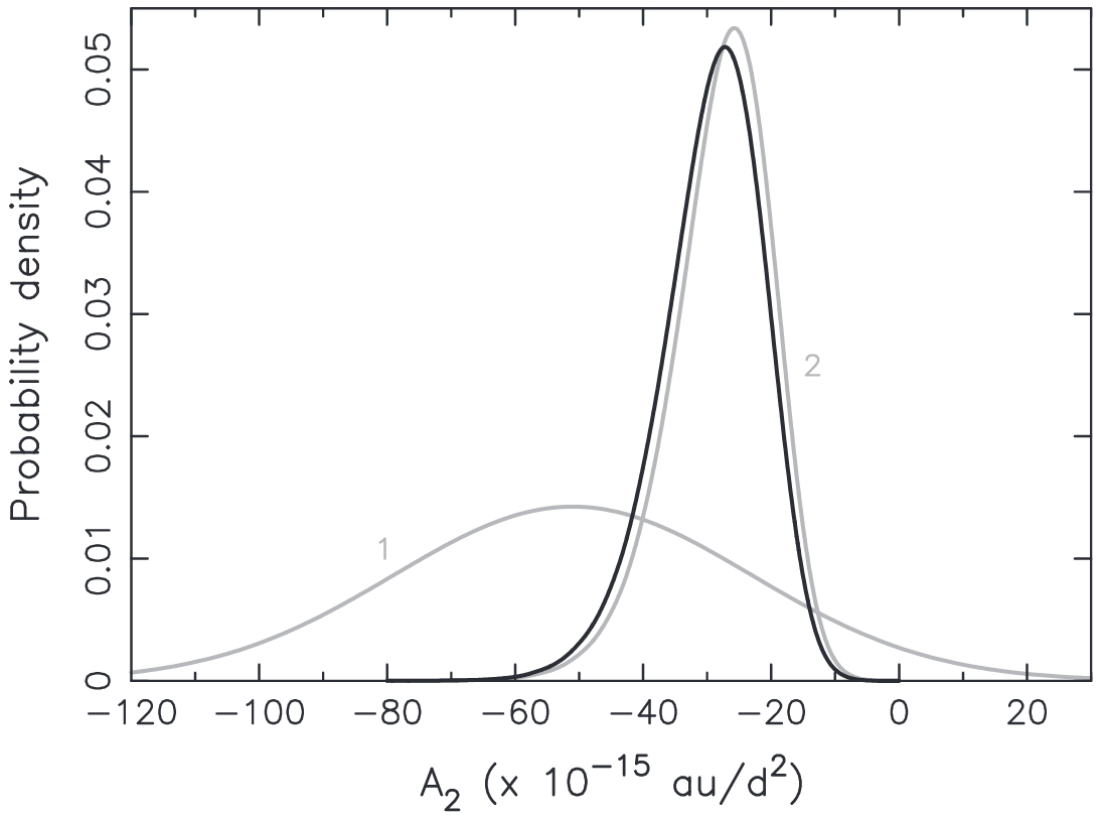

Figure 2.16: Probability density function of the A_2 parameter (see Eq. 2.53). The gray curve denoted (1) captures the statistical results obtained by fitting the observation data. The curve (2) was obtained by semi-analytical modeling (see the text). The full curve is a combination of both methods. Source: Vokrouhlický et al. (2015b).

Employing the statistical distribution of the semi-major axis drift (see Fig. 2.15) in the equation (2.53) practically provides a semi-analytical probabilistic distribution of the A_2 parameter. The resulting probability distributions of the A_2 obtained by fitting the astrometric data and by the semi-analytical method described above are compared in Fig. 2.16. Vokrouhlický et al. (2015b) used a combined distribution of the A_2 parameter to calculate the ephemerides of Apophis and also to revise the future impact probabilities.

The analysis of impact probabilities was, again, performed in the b-plane with the coordinates $(\xi_{2029}, \zeta_{2029})$ (see Section 2.1). The emphasis was put especially on the ζ_{2029} coordinate which is affected by the Yarkovsky-induced[20] perturbations most strongly.

[20]Above all, the clones generated within the uncertainty ellipsoid of Apophis orbit disperse along the orbit due to the Yarkovsky effect which is reflected in the uncertainty of the close approach moment.

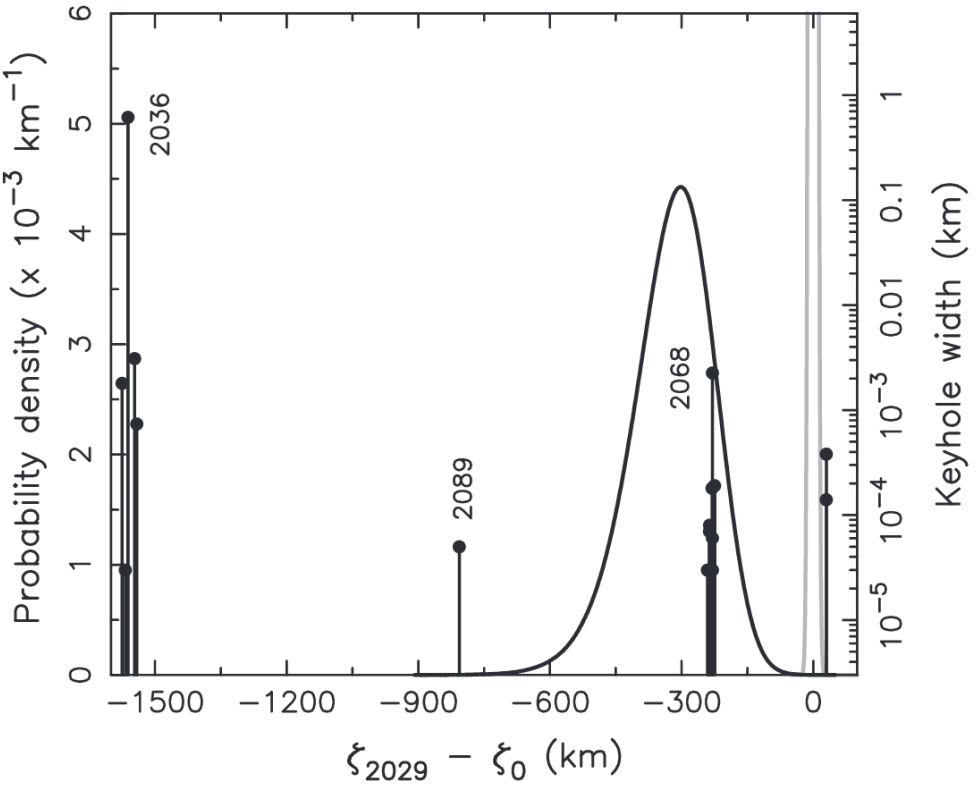

Figure 2.17: The gray curve denotes the probability density function of the variable ζ_{2029} obtained from the purely gravitational solution of the asteroid's orbital evolution. The maximum of this distribution is equal to 0.07 km^{-1} and it lies outside the plotted scale. The nominal value of ζ_0 is $\zeta_0 = 47667$ km. The black curve shows the same, only this time, the Yarkovsky effect was considered. The vertical lines indicate the positions and the widths of the keyholes. By multiplying the width of the keyhole by the probability density, we obtain the corresponding impact probability (see Tab. 2.2). It is apparent that the Yarkovsky effect causes a shift of the nominal value of the coordinate ζ_{2029} by ≈ 300 km. Source: Vokrouhlický et al. (2015b).

Positions of the keyholes as well as their impact probabilities are summarized in Fig. 2.17 and Tab. 2.2.

Currently, it seems that the close encounter in 2068 is potentially most dangerous (IP $\approx 6.7 \times 10^{-6}$). Note that the orbital evolution after 2029 cannot be found accurately, because we do not know how the rotational state of the asteroid will change during the close approach with the Earth.

In future, however, new corrections and improvements of the current results are to be expected. This is mostly thanks to fortunate conditions for further astrometric and radar measurements which will happen in 2020 and 2021 (Farnocchia et al., 2013a). Then we can also expect that the range of possible Yarkovsky drifts obtained by fitting the astrometric data will provide better results than the physical modeling of the Yarkovsky effect. On the other hand, the modeling is also likely to be improved, especially thanks to the close approach to Earth in March 2021. At that point, it will be possible to make detailed photometric observations and better constrain some thermophysical parameters (especially the pole orientation and the thermal inertia of the surface).

Date TBD	$\zeta_{2029} - \zeta_0$ [km]	Width [m]	PDF $\times 10^{-3}$ [km^{-1}]	IP $\times 10^{-6}$
2060-04-12.6	-241	0.03	3.3	0.1
2065-04-11.8	-237	0.08	3.2	0.3
2068-04-12.6	-230	2.25	3.0	6.7
2076-04-13.0	-224	0.19	2.8	0.5
2077-04-13.5	-230	0.06	3.0	0.2
2078-04-13.8	-236	0.07	3.2	0.2
2091-04-13.4	-236	0.07	3.2	0.2
2103-04-14.4	-230	0.18	3.0	0.5

Table 2.2: Parameters of the (99942) Apophis keyholes in 2029. For each impact epoch, the table lists the position of the respective keyhole, its width, the probability density function (PDF) for $\zeta_{2029} - \zeta_0$ and the impact probability (IP). Note that $\zeta_0 = 47667$ km.

2.4 Conclusion

This chapter dealt with the influence of the Yarkovsky effect and solar radiation pressure on the orbital evolution of near-Earth asteroid (99942) Apophis until 2029, when it will pass Earth approximately ≈ 38000 km away. We found that the change in the close approach distance due to the solar radiation pressure is in the order of hundreds of meters to kilometers for both the Hapke and Lambert scattering model, being roughly two orders smaller than the change induced by the Yarkovsky effect. Even though our results are negative in a way, they might be valuable for those who model the orbital evolution of selected bodies under the influence of non-gravitational perturbations. In these models, the solar radiation pressure can thus be neglected in the first approximation which would shorten the computational time.

As we did not have any information about the shape and rotational state of Apophis, we used a set of random Gaussian spheres and assumed random orientations of their spin axes in our simulation. Recently, however, the shape of Apophis has been determined, so it would be interesting to recalculate the whole problem even though we do not expect any significant differences compared to our results.

Let us note that the orbital evolution of Apophis considering the influence of the Yarkovsky effect was a subject of some monothematic studies which benefit from new information about its shape and rotational state. All of them confirmed that the dominant non-gravitational perturbation is the Yarkovsky effect. New models are, therefore, able to accurately revise and improve the impact probabilities of this near-Earth asteroid.

3. Young asteroid families and pairs

Families and pairs of asteroids are remnants of a fragmentation of larger parent bodies. In this chapter, we will focus primarily on very young families and pairs not exceeding ≈ 2 Myr in age. Asteroid families and pairs present a unique physical laboratory where one can test hypotheses about their origin, investigate their age and, in some cases, even reconstruct the break-up event. Younger systems are, in this regard, more suitable than older ones since the members of older families have been under longer lasting influence of gravitational and non-gravitational perturbations. We briefly discuss young families and provide a detailed account of asteroid pairs and their selected representatives. We will especially focus on a very young and compact pair (6070) Rheinland – (54827) 2001 NQ8. The next chapter is then dedicated to the youngest asteroid pair (87887) 2000 SS286 – (415992) 2002 AT49. We note that the author of this dissertation contributed by his calculations to determining the age of selected asteroid pairs in Vokrouhlický et al. (2011), Pravec et al. (2013), Polishook et al. (2014), Galád et al. (2014) and Pravec et al. (2016). He also modified the classical method for finding the age of asteroid pairs to be more suitable for weakly convergent cases (see Žižka and Vokrouhlický, 2011a, or Appendix A, Paper 2).

3.1 Young asteroid families

The research on asteroid families practically started already at the beginning of the last century with the works of Hirayama (1918, 1922) in which the first members of the Koronis, Eos and Themis families were identified. Over the years, their number rapidly grew and other new families were discovered (see Nesvorný et al., 2015). In the last decade the research into asteroid families has rapidly accelerated especially owing to sky surveys such as Sloan Digital Sky Survey (SDSS), Wide-field Infrared Survey Explorer (WISE) or AKARI All-Sky Survey which provided valuable data about the physical properties of the main belt asteroids[1] (Ivezić et al., 2001; Mainzer et al., 2011; Usui et al., 2013).

Studying the dynamics of asteroid families provides insight into extreme collisions and asteroid fragmentation in the Solar System. The fragments after these energetic events are nowadays observed as separate asteroids which form clusters in the orbital elements space, indicating that they probably share a common origin. Young families are, however, more suitable if we want to determine their age, because the gravitational and non-gravitational perturbations act on their members for a much shorter period of time, compared to the older families.

Our attention in this chapter is focused on very young asteroid families and pairs with age not exceeding ≈ 2 Myr. However, note that a slightly older, but still young Karin family was the first discovered in this class (Nesvorný et al., 2002). Its age is estimated to be $T_{\rm age} \approx 5.75$ Myr and it was probably formed in

[1]Especially broadband photometry has enabled mineralogical classification of tens of thousands of asteroids and provided information about their albedos and sizes. The WISE mission was succeeded in 2010 by the NEOWISE mission, focused primarily on NEAs.

an impact of a ≈ 5.8 km sized projectile to a ≈ 33 km sized parent body. The impact velocity was approximately $5-6$ km s^{-1} and after this collision about 100 family members larger than ≈ 2.5 km were created (Nesvorný et al., 2006b).

3.1.1 Family identification

The classical method for asteroid family identification consists of three steps: (i) calculation of proper (or osculating) elements for a chosen set of asteroids, (ii) identification of clusters or groups in the space of these elements and (iii) analysis of their statistical significance[2].

As already mentioned, asteroid families are created by fragmentation of parent bodies. We assume that for a vast majority of fragments, their relative velocities just after the break-up event are considerably smaller than orbital velocities. After the disintegration, we then expect that the family members will orbit together in a cluster. However, with time, they start drifting apart as a consequence of both gravitational and non-gravitational perturbations. For a short time though, the fragments are rather apparent as clusters in the space of osculating elements $(a, e, i, \Omega, \omega)$.

To describe older asteroid families, we use proper elements (a_p, e_p, i_p) which represent quasi-integrals of motion (see Knežević et al., 2002). They can be calculated from osculating elements by suppressing the periodical oscillations caused by gravitational perturbations. This can be done either analytically using the perturbation theory (see Milani and Knežević, 1990, 1994) or numerically by integration of asteroid orbits[3] (Knežević and Milani, 2000; Knežević et al., 2002). The identification of old families is then based on the Hierarchical Clustering Method (HCM) (Zappalà et al., 1990; Bendjoya and Zappalà, 2002), which introduces the following metric in the proper elements space

$$d^2 \equiv (na_p)^2 \left[k_a \left(\frac{\delta a_p}{a_p} \right)^2 + k_e (\delta e_p)^2 + k_i (\delta i_p)^2 \right], \tag{3.1}$$

where na_p is the heliocentric velocity of an asteroid on a circular orbit with semi-major axis a_p, $(\delta a_p, \delta e_p, \delta i_p)$ is the separation vector of neighboring bodies and $k_a = 5/4$ and $k_e = k_i = 2$ are the weighting factors (see Zappalà et al., 1990). Let us note that clustering algorithms can also benefit from information about the color and/or albedo. The homogeneity of asteroid families with regard to the color or albedo is summarized for example in Ivezić et al. (2001) or Parker et al. (2008). These references mostly utilize data from SDSS and WISE surveys. For example, thanks to the SDSS survey, the asteroids in the S-complex can be distinguished from the C/X-complex bodies (Nesvorný et al., 2005). Similarly, the data from the WISE/NEOWISE surveys allowed us to distinguish high-albedo asteroids from the low-albedo ones (Masiero et al., 2013).

[2]There might be interlopers into the families - asteroids that have similar values of the orbital elements. These asteroids can be ruled out for example by working in an extended space. In other words, we extend the space of orbital elements with physical parameters such as the color and/or albedo (see Parker et al., 2008; Masiero et al., 2013; Carruba et al., 2013).

[3]Proper elements of numbered and non-numbered multi-opposition asteroids are provided by `AstDyS` database which is available at `http://hamilton.dm.unipi.it/astdys/`.

These populations can then be treated separately by the HCM method. A more general approach, however, includes the color and/or albedo directly in the d metric, practically creating a modified HCM method in a four- or five-dimensional space (see Parker et al., 2008; Carruba et al., 2013). For instance, we can define the distance d' as follows

$$d'^2 \equiv d^2 + (na_p)^2[k_1(\delta C_1)^2 + k_2(\delta C_2)^2], \tag{3.2}$$

where the distance d is given by the expression (3.1) and the parameters C_1 and C_2 are diagnostic colors based on the SDSS observations (see Ivezić et al., 2001; Nesvorný et al., 2005). The coefficients k_1 and k_2 are again weighting factors and should be chosen reasonably with regard to the k_a, k_e, k_i coefficients (Nesvorný et al., 2006a). Let us note that the albedo $p_{\rm V}$, which can be obtained, for instance, from WISE measurements, can also act as an additional parameter

$$d''^2 \equiv d'^2 + (na_p)^2 k_p(\delta p_{\rm V})^2. \tag{3.3}$$

It is obvious that with each added dimension, increasingly strict requirements are imposed on the family members.

However, in the case of very young asteroid families, we may assume that the trajectories of individual members have not undergone such dramatic changes due to gravitational and non-gravitational perturbations. Typically, gravitational perturbations from planets cause dispersion of secular angles ϖ and Ω on the time scale of $\approx\ 1-2$ Myr (see Nesvorný et al., 2015; Nesvorný and Vokrouhlický, 2006). The clustering methods of identification can then directly use the osculating elements. These do change in time as well but we may expect that very young families with $T_{\rm age} < 2$ Myr will appear as clusters even in the 5-dimensional space of osculating elements. Let us note that we do not expect any clustering in the mean anomaly M because the Keplerian shear spreads individual fragments with disintegration velocities $\delta v = 1 - 100$ m s^{-1} around the Sun on the time scale of $\approx\ 300\ -\ 30000$ years (see Nesvorný et al., 2015).

Nesvorný and Vokrouhlický (2006) introduced the following metric in osculating elements

$$\left(\frac{d}{na}\right)^2 = k_a\left(\frac{\delta a}{a}\right)^2 + k_e(\delta e)^2 + k_i(\delta \sin i)^2 + k_\Omega(\delta\Omega)^2 + k_\varpi(\delta\varpi)^2, \tag{3.4}$$

where n is again the mean motion and $(\delta a, \delta e, \delta \sin i, \delta\varpi, \delta\Omega)$ vector separating two neighboring bodies. From linear perturbation theory (see Brouwer and Clemence, 1961), it follows that the precession speeds of secular angles Ω and ϖ should be about the same. We therefore assume that $k_\Omega \simeq k_\varpi$. In addition, Nesvorný and Vokrouhlický (2006) empirically found that the best results in identifying young clusters are achieved by choosing $k_\Omega = k_\varpi = 10^{-6}$. The first application of the metric function d in 5D space $(a, e, i, \Omega, \omega)$ was presented by Nesvorný et al. (2006c), who discovered the Datura family. In the same year, Nesvorný and Vokrouhlický (2006) recognised other three new clusters (Emilkowalski, 1992 YC2 and Lucascavin) exhibiting $d\ \in\ [20,\ 40]$ m s^{-1} and to them they did not find any additional members with $d\ \in\ [40, 200]$ m s^{-1}. Let us note that other forms of metric functions can be found in Rożek et al. (2011).

After identifying clusters in orbital elements space using the HCM method, it is necessary to decide, whether they really represent real families or whether

they are just a consequence of random fluctuations in the asteroid distribution in the orbital elements space.

The problem of statistical significance of asteroid clusters was first addressed by Nesvorný and Vokrouhlický (2006). They created 320,000 synthetic asteroid belts and within each of them they randomly spread 316599 bodies[4]. Then they applied the HCM method onto each synthetic asteroid belt. In any of the synthetic belts, they did not find clusters containing at least three members with $d < 50$ m s^{-1}. From the above, it is thus evident that the clusters should not be a result of random fluctuations but that they probably share a common origin.

An estimation of the formation probability of a random cluster with at least three members is rather straightforward. We divide the synthetic asteroid belt into M cells of the same size. Let each cell occupy in the 5D space $(a, e, i, \varpi, \Omega)$ a volume comparable to the volume of the studied cluster. Further, let N be the number of asteroids in the synthetic belt. The probability of finding at least 3 asteroids in one cell is then given by[5]

$$p_3 = \binom{N}{3} \frac{1}{M^2}. \tag{3.5}$$

Nesvorný and Vokrouhlický (2006) chose, when analysing the Emilkowalski, 1992 YC2 and Lucascavin clusters the conservative value of $M \approx 10^{12}$. For $N \approx 3 \times 10^5$, one obtains $p_3 \approx 10^{-8}$ according to (3.5). This is, in fact, the reason why the authors did not find a single cluster with at least three members in the 320,000 runs of the algorithm.

3.1.2 Finding the age of very young families

After we identify a young family in the 5D space, the question of its age immediately arises. To find the real age of young asteroid families, we can use a direct numerical integration of individual members' orbits into the past. Let us note that during the backward propagation, it is not sufficient to just rely on nominal orbits. Apart from the orbital uncertainties and deterministic chaos, the dynamical evolution of family members is also influenced by gravitational and non-gravitational perturbations. Thus, all these effects have to be taken into account during the simulation.

Nesvorný and Vokrouhlický (2006), therefore, took the following approach. For each family member, they generated, within the 1σ interval of its orbital uncertainty, 20 geometrical clones and to each of them attributed 41 admissible values of the Yarkovsky drift $\mathrm{d}a/\mathrm{d}t$ (yarko clones). The drifts da/dt uniformly covered the interval $[-|\mathrm{d}a/\mathrm{d}t|_{\max}, |\mathrm{d}a/\mathrm{d}t|_{\max}]$, where $|\mathrm{d}a/\mathrm{d}t|_{\max}$ and $-|\mathrm{d}a/\mathrm{d}t|_{\max}$ are the limit values corresponding to the obliquities $\gamma = 0°$ and $\gamma = 180°$ (see Section 1.1.3 and the equation (1.90)). Overall, each fragment is thus represented by 820 test particles. It has to be noted that the maximum drift $|\mathrm{d}a/\mathrm{d}t|_{\max}$ is determined individually for each fragment, considering its estimated thermophysical properties. In the zeroth approximation, $|\mathrm{d}a/\mathrm{d}t|_{\max}$ can be computed from the linear theory of the Yarkovsky effect.

[4]This number corresponds to the number of asteroids listed in the AstOrb catalogue on March 1, 2006.

[5]We assume $M >> N$.

Note that due to the Yarkovsky-induced semi-major axis drift, all clones subsequently spread around the Sun and after a sufficiently long time, their mean anomalies uniformly cover the interval $[0°, 360°]$. This effect is known as the Keplerian shear. Let us briefly describe its role.

An infinitesimally small change of the mean anomaly $\mathrm{d}M$ caused by an infinitesimally small change of the mean motion $\mathrm{d}n$ is given by $\mathrm{d}M = t\,\mathrm{d}n$. If it holds that $\mathrm{d}n = \frac{\partial n}{\partial a}\,\mathrm{d}a$, we obtain

$$\mathrm{d}M = \left(\frac{\partial n}{\partial a}\right)\,\left(\frac{\mathrm{d}a}{\mathrm{d}t}\right)\,t\,\mathrm{d}t. \tag{3.6}$$

From the third Kepler law, it follows that $\frac{\partial n}{\partial a} = -\frac{3}{2}\frac{n}{a}$. After substituting this equation into (3.6), we see that the mean anomaly difference between two clones is given by[6]

$$|\Delta M| = \frac{3}{4}\,\left[\frac{1}{a}\frac{\mathrm{d}a}{\mathrm{d}t}\right]\,nt^2. \tag{3.7}$$

The maximum Yarkovsky drift for approximately kilometer-sized asteroids has the order of magnitude $\mathrm{d}a/\mathrm{d}t \sim 2 \times 10^{-4}$ au Myr^{-1} (see Morbidelli and Vokrouhlický, 2003). Using equation (3.7), we can see that the complete shear of clones along an orbit in the main belt takes roughly $\sim 200 - 300$ kyr. On the other hand, the dispersion of secular angles Ω and ϖ occurs at longer time scales (Nesvorný and Vokrouhlický, 2006).

Thus, during the backward propagation of the clones, Nesvorný and Vokrouhlický (2006) focused mainly on the secular angles. They used a freeware symplectic integrator `SWIFT-MVS` (Levison and Duncan, 1994) into which they implemented the Yarkovsky effect-caused perturbations. For each member of the Emilkowalski, 1992 YC2 and Lucascavin cluster, they generated a set of geometrical and Yarkovsky clones and propagated these clones from MJD 2,453,700.5 for 2 Myr into the past. They selected a specific cluster and in each time step of the backward propagation calculated the function $\Delta V(t)$, which is defined as

$$\Delta V(t) = na\sqrt{k_1(\sin i\Delta\Omega)^2 + k_2(e\Delta\varpi)^2}, \tag{3.8}$$

where

$$(\Delta\Omega)^2 = \sum_{\substack{ijkl \\ i\neq j,k>l}} (\delta\Omega_{ijkl})^2/N_{\mathrm{pairs}}, \qquad (\Delta\varpi)^2 = \sum_{\substack{ijkl \\ i\neq j,k>l}} (\delta\varpi_{ijkl})^2/N_{\mathrm{pairs}}. \tag{3.9}$$

Here, for instance, $\delta\Omega_{ijkl}$ is the difference in the Ω angle between the i-th clone of the k-th fragment and the j-th clone of the l-th fragment. We sum over all clone-clone combinations ($i \neq j$) and take into account all pairs of fragments[7] N_{pairs}. The parameters k_1, k_2 are again weighting coefficients. Nesvorný and Vokrouhlický (2006) used $k_1 = 1$ and $k_2 = 1/2$ and showed that if they are comparable, their specific values do not influence the age distribution of the family. If the convergence criterion $\Delta V(t) < V_{\max} \wedge \Delta M < M_{\max}$ is met ($V_{\max}$, $M_{\max}$ are pre-estimated individually for each cluster), then the time of convergence t is recorded. From the distribution of t, we can determine the age T_{age} of the family.

[6] We assumed $da/dt = const.$ and $n = const.$

[7] The results, however, do not change if we use only pairs with the largest fragment.

The threshold of the ejection speed $V_{\max}$ can be estimated from the distribution of proper elements a_p, e_p and i_p within the studied cluster (see Nesvorný and Vokrouhlický, 2006, for further details). Usually, $V_{\max}$ has the order of magnitude $\approx$ m s^{-1}. Note that an artificial increase of $V_{\max}$ gives a less conservative distribution of possible ages, whereas its decrease leads to rather restrictive results. Regarding the $M_{\max}$ value, Nesvorný and Vokrouhlický (2006) typically use $M_{\max} = 1^\circ - 10^\circ$. Lower values of $M_{\max}$ would probably face the problem of insufficient number of clones.

However, some young families were also studied directly in Cartesian space. For instance, when solving the age of the Datura family, Vokrouhlický et al. (2017a) calculated in each integration step the relative distances and velocities between clones of individual fragments and clones of the largest family member. These were then compared with the characteristic Hill radius $R_{\rm Hill}$ and the escape velocity $V_{\rm esc}$ of the parent body. They found that at least in the case of Datura family, the previous method practically gives identical distribution of possible ages as the similar method in Cartesian space.

Let us note that the characteristic radius of the Hill sphere can be obtained from $R_{\rm Hill} \simeq aD_1\frac{1}{2}\left(\frac{4\pi}{9}\frac{G\rho_1}{\mu}\right)^{1/3}$ where a is the semi-major axis, D_1 is the estimated diameter of the parent body, G is the gravitational constant, ρ_1 is the density of the parent asteroid and μ is the gravitational parameter of the Sun. The escape velocity is given by the equation $V_{\rm esc} \simeq D_1\frac{1}{2}\left(\frac{8\pi}{3}G\rho_1\right)^{1/2}$ (see Pravec et al., 2010).

3.1.3 Selected examples of young families

The first-discovered families with ages in the range of 1-10 Myr were (i) the Iannini cluster (1 - 5 Myr), (ii) the Karin cluster (5.75 $\pm$ 0.05 Myr) and (iii) the Veritas family (8.2 $\pm$ 0.1 Myr) (see Nesvorný et al., 2002, 2003; Nesvorný and Bottke, 2004). During the past decade, however, 14 new asteroid families younger than $\approx$ 3 Myr have been found. Three of them were recently identified by Pravec et al. (2018). The rest was revised and updated by Vokrouhlický et al. (2016), Vokrouhlický et al. (2017a) and Pravec et al. (2018).

The first-discovered family with an age less than 1 Myr was the Datura family (Nesvorný et al., 2006c). It was then followed by the discovery of small clusters (14627) Emilkowalski, (16598) Brugmansia = 1992 YC and (21509) Lucascavin (Nesvorný and Vokrouhlický, 2006). Five clusters (6825) Irvine, (10321) Rampo, (18777) Hobson, (39991) Iochroma and (81337) 2000 GP36[8] were discovered by Pravec and Vokrouhlický (2009). The most recent cases also include the clusters (20674) 1999 VT1 (Novaković et al., 2014), (2384) Schulhof (Vokrouhlický and Nesvorný, 2011) and a triplet of clusters (11842) Kap'bos, (22280) Mandragora and (66583) Nicandra (Pravec et al., 2018).

From what we know today about young asteroid families, it is apparent that each of them is unique, in a way. Many have been, therefore, a subject of multi-topic publications. Since a complete account of all young families including a detailed physical description would exceed the extent of this work, we only briefly

[8]It was uncertain whether the (18777) Hobson asteroid belonged to the Hobson cluster. This was confirmed by Rosaev and Plávalová (2017). The cluster (81337) 2000 GP36 turned out to be a part of a larger cluster (2384) Schulhof (Vokrouhlický and Nesvorný, 2011).

discuss the three youngest representatives - (16598) Brugmansia, (22280) Mandragora and (39991) Iochroma. Note that in the following text, the distance d in the space of osculating or proper elements will be related to the largest body.

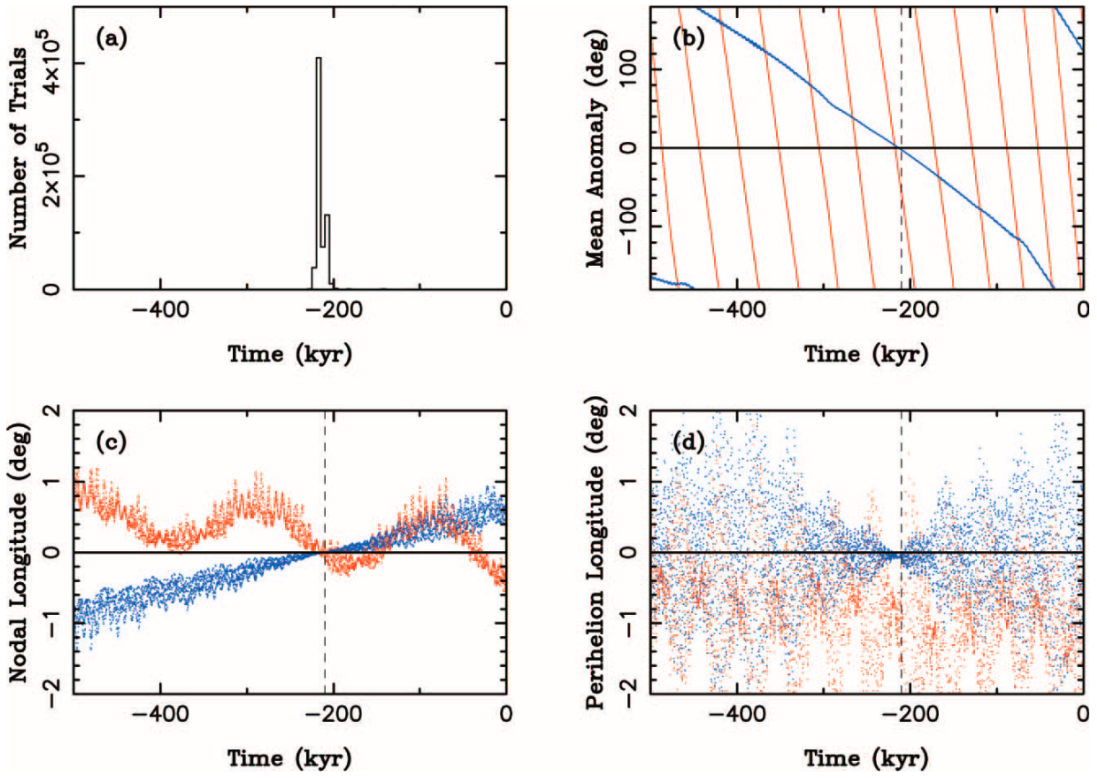

Figure 3.1: Convergent solutions of the Emilkowalski cluster which consists of asteroids (14627) Emilkowalski, (126761) 2002 DW10 and (224559) 2005 WU178. Part (a) shows the resulting distribution of possible ages, the other parts show the best convergent solutions of the asteroids (126761) 2002 DW10 (red) and (224559) 2005 WU178 (blue). Parts (b), (c) and (d) demonstrate the time evolution (into the past) of the mean anomaly ΔM, the longitude of the ascending node $\Delta\Omega$ and the longitude of the pericenter $\Delta\varpi$ relative to the asteroid (14627) Emilkowalski. Taken from Nesvorný and Vokrouhlický (2006).

(16598) Brugmansia cluster

The Brugmansia cluster was discovered in 2006 and originally, it was estimated to be 50-250 kyr old (Nesvorný and Vokrouhlický, 2006). It consists of asteroids (165980) Brugmansia, (190603) 2000 UV80 and (218697) 2005 TT99. Pravec et al. (2018) confirmed[9] that there is no other multi-opposition asteroid in the vicinity of this cluster with $d < 87$ m s^{-1}. Backward propagation of its members showed that the convergent solutions for the pairs (165980) Brugmansia - (190603) 2000 UV80 and (165980) Brugmansia - (218697) 2005 TT99 overlap in the time interval $120 - 230$ ky. According to Pravec et al. (2018), the separation of the primary from the secondaries thus probably occurred 170^{+60}_{-50} thousand years ago (see Fig. 3.2). Let us note that at a relatively large distance of $d = 87$ m s^{-1}, there

[9]Choosing $k_a = 5/4, k_e = k_i = 2$ and $k_\varpi = k_\Omega = 10^{-4}$ in the metric (3.4).

is another asteroid - (84329) 2002 TU51. This body, however, most likely belongs to the background population because its clones do not show any convergence with the clones of (165980) Brugmansia.

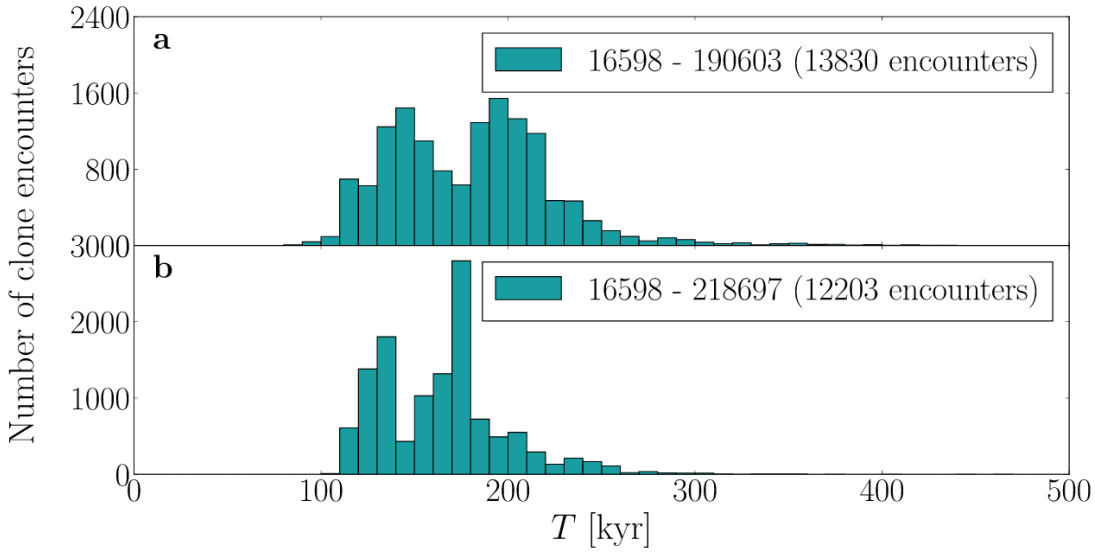

Figure 3.2: Brugmansia cluster. The distribution of convergent solutions between secondaries (190603) 2000 UV80 and (218697) 2005 TT99 and the primary (16598) Brugmansia. In this cluster $R_{\mathrm{Hill}} \approx 1063$ km and $V_{\mathrm{esc}} \approx 2.6$ m s^{-1}. Convergence criteria were set to be less strict - specifically $r_{\mathrm{rel}} \leq 10 R_{\mathrm{Hill}} \wedge v_{\mathrm{rel}} \leq 2 V_{\mathrm{esc}}$ where r_{rel} and v_{rel} are the distance and relative velocity between the clones of a secondary and clones of the primary. Taken from Pravec et al. (2018).

(22280) Mandragora cluster

The Mandragora cluster was discovered by Pravec et al. (2018) during their search for asteroid pairs. This cluster currently contains 19 asteroids. Let us describe how individual members were discovered. The closest pair of the cluster consists of asteroids (324154) 2005 YN176 and (459310) 2012 GZ32 which are separated in the 5D space $(a, e, i, \varpi, \Omega)$ by the distance $d \approx 7.1$ m s^{-1}. Pravec et al. (2018) complemented this pair with two other bodies (including the primary (22280) Mandragora). The newly created system of three secondaries then appeared to be a good candidate for a young family since the distances between all of them did not exceed 35 m s^{-1}. This ensemble was further extended by 6 more asteroids (we do not list them here explicitly) with[10] $d \in [82, 161]$ m s^{-1}.

Consequently, Pravec et al. (2018) used the HCM method to inspect also the wider surrounding of the primary (22280) Mandragora. They found 7 additional bodies with distances of 45-65 m s^{-1} in the proper elements space, which corresponded to 322 - 2094 m s^{-1} in the osculating elements space. This difference is, possibly, caused by the fact that the cluster is close to the J9/4 resonance. Later, two other candidates were discovered at the distances 13 and 31 m s^{-1} in the proper elements space, extending the whole ensemble to the current 19 members.

[10]Note that their distance relative to the original secondaries did not exceed 100 m s^{-1}.

The affiliation of the whole ensemble to a single family was then confirmed by backward numerical propagation of geometrical and Yarkovsky clones. Individual convergent solutions between the secondaries and the primary overlap in the interval 100 - 1000 kyr in the past and the age of the family is estimated to be 250^{+290}_{-90} kyr. The Hill radius and the escape velocity of the parent body are in this case $R_{\mathrm{Hill}} \approx 2499$ km and $V_{\mathrm{esc}} \approx 5.2$ m s^{-1}. Pravec et al. (2018) again used less conservative criteria of convergence $r_{\mathrm{rel}} \leq 20 R_{\mathrm{Hill}} \wedge v_{\mathrm{rel}} \leq 4 V_{\mathrm{esc}}$.

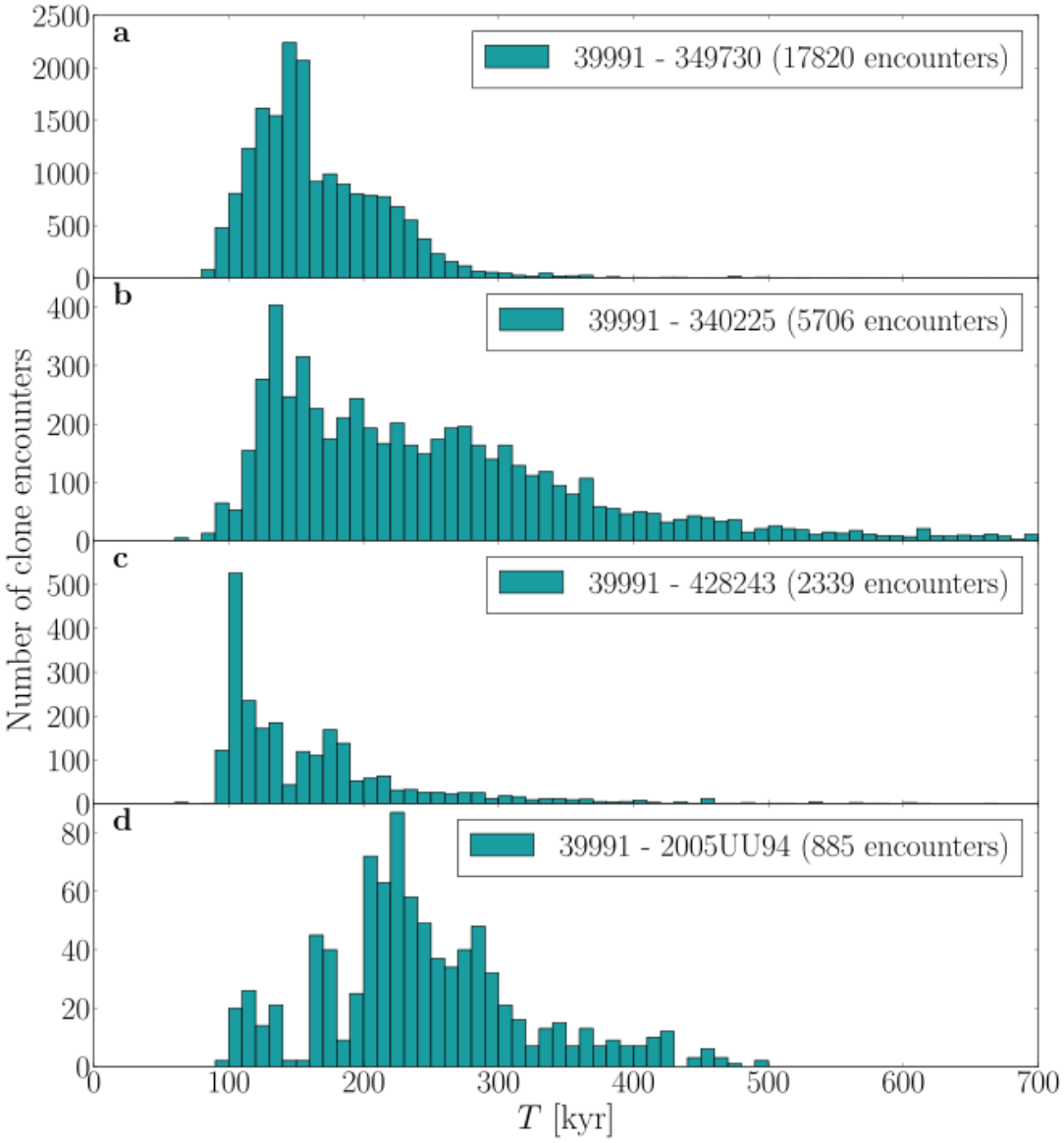

Figure 3.3: Iochroma cluster. An illustration of the distribution of convergent solutions between the secondaries and the primary (39991) Iochroma. In this cluster $R_{\mathrm{Hill}} = 879$ km and $V_{\mathrm{esc}} = 2.3$ m s^{-1}. The convergence criteria were set so that $r_{\mathrm{rel}} \leq 10 R_{\mathrm{Hill}} \wedge v_{\mathrm{rel}} \leq 2 V_{\mathrm{esc}}$ where r_{rel} and v_{rel} are the distance and relative velocity between the clones of a secondary and clones of the primary. Taken from Pravec et al. (2018).

(39991) Iochroma cluster

This cluster consists of 5 asteroids - the primary (39991) Iochroma and 4 secondaries. Its discovery was first published in 2009 by Pravec and Vokrouhlický (2009). Note that in this case, they did not find any other multi-opposition asteroids closer than 100 m s^{-1}. The distribution of convergent solutions between the secondaries and the primary overlap in the interval 90-390 kyr and the age is estimated to be 190^{+200}_{-100} kyr.

3.1.4 Formation of young families

In today's view, young asteroid families are created by either (i) rotational fission of the parent body due to the YORP effect, followed by subsequent rotational fission of the new secondary/secondaries (fission origin) or (ii) as a consequence of a projectile hitting the parent object (impact origin).

Let us consider a rubble-pile asteroid which disrupted into N fragments. It can be shown (see Scheeres, 2016a) that the total energy of such a system reads

$$E = \sum_{j=1}^{N} \frac{1}{2} \boldsymbol{\omega}_c \cdot \mathbf{I}_j \cdot \boldsymbol{\omega}_c + \frac{1}{2M} \sum_{i=1}^{N-1} \sum_{j=i+1}^{N} M_i M_j \boldsymbol{v}_{ij} \cdot \boldsymbol{v}_{ij} + \sum_{i,j=1}^{N} U_{ij}, \tag{3.10}$$

where $\boldsymbol{\omega}_c$ is the critical angular velocity at which the fragments start to escape the parent asteroid, M is the total mass of the system, $\mathbf{I}_j$, M_j are the inertia tensor and the mass of the j-th fragment and $\boldsymbol{v}_{ij}$, U_{ij} are the relative velocity and potential energy between the i-th and j-th component. It holds that

$$U_{ij} = -\frac{G}{2} \int_{\beta_i} \int_{\beta_j} \frac{dm_i dm_j}{|\boldsymbol{\rho}_i - \boldsymbol{\rho}_j|}, \tag{3.11}$$

where β_i, β_j are the integration regions of the i-th and j-th component. We define the free energy of the system as the total energy minus the self-potentials U_{ii}. If the free energy is positive, all secondaries can escape the parent body (Scheeres, 2002, 2016b).

According to the hypothesis (i), family members are produced by rotational fission of the parent asteroid (e.g. due to the YORP effect), followed by subsequent fragmentation of the secondary/secondaries. This mechanism was proposed by Jacobson and Scheeres (2011a). At first, disruption of the parent body creates a proto-binary system and thanks to spin-orbit coupling, the free energy is temporarily stored in the rotational energy of the components and in the kinetic energy of their relative motion. If too much energy is stored in the relative motion, the distance of the components keeps increasing and the system falls apart. If too much energy is stored in the rotational motion of the secondary, it can be further fragmented. The positive free energy leads to a possible escape of one or more secondaries from the system.

The hypothesis (ii) which considers the impact origin of young families is presented in Vokrouhlický et al. (2017a). According to this hypothesis, the origin of very numerous populations of secondaries is rather a consequence of cratering of the parent body than its catastrophic disruption. Vokrouhlický et al. (2017a) estimated that there are up to $\simeq 300$ fragments of the Datura family with the diameter > 200 m. Such a numerous population can hardly be created by gradual rotational fission of the secondaries.

3.2 Young asteroid pairs

In this section, we briefly discuss the general theory of asteroid pairs, especially the methods of their identification and age determination. We also present the best studied pair (6070) Rheinland – (54827) 2001 NQ8. The author of this thesis contributed to the age solution of this pair in the work of Vokrouhlický et al. (2011) and also modified the classical method of age determination (Vokrouhlický et al., 2008) to be more suitable for poorly convergent cases (see Žižka and Vokrouhlický, 2011a, or Appendix A, Paper 2).

Asteroid pairs did probably form a single parent body in the past. This body disrupted into two (and potentially more) pieces which are nowadays observed as separate asteroids on similar heliocentric orbits.

The population of asteroid pairs was discovered by Vokrouhlický et al. (2008) by comparing cumulative distributions $N(< d)$ of real and randomly generated asteroids[11] in the main belt. For the analysis, Vokrouhlický et al. (2008) used $\approx$ 370,000 available trajectories with semi-major axes in the range $[1.7, 3.6]$ au and arc lengths longer than 10 days. Note that for a random distribution of orbits in the 5D space of osculating elements, we expect the theoretical dependence $N(< d) \sim d^5$ (see Fig. 3.4).

3.2.1 Identification and statistical analysis of young pairs

Identification of young asteroid pairs is, in many aspects, similar to the identification of young families (see Section 3.1.1). Vokrouhlický et al. (2008) identified pairs in 5D space $(a, e, i, \varpi, \Omega)$ using the expression (3.4) with the weighting coefficients $k_a = 5/4$, $k_e = k_i = 2$ and $k_\Omega = k_\varpi = 10^{-5}$. At this point, let us note that the choice of weighting factors k_Ω and k_ϖ plays a key role in the pre-selection of young pairs, because higher values of the k_Ω and k_ϖ coefficients increase the sensitivity of the metric d to the changes of secular angles $(\delta\Omega)^2$ and $(\delta\varpi)^2$ which are smaller for young pairs than for older ones.

Probability of close orbits occurrence

Even though the orbits of the primary and secondary are very close, it is necessary to express the probability that one is not dealing with a random fluctuation in the space of osculating elements. This problem was addressed by Vokrouhlický et al. (2008) and Pravec and Vokrouhlický (2009).

Let us define the local density of orbits $\eta = \eta(a, e, i, \Omega, \varpi)$ in the 5D space of osculating elements by the equation $\nu = \eta V$, where ν is the number of orbits in the box[12] with volume $V = d^5$. The probability $p_n(d)$ of finding n trajectories in a 5D box with the volume d^5 follows the Poisson distribution

$$p_n(d) = \frac{\nu^n}{n!} e^{-\nu}, \tag{3.12}$$

where we set $n = 2$ for asteroid pairs.

[11] $N(< d)$ is the number of pairs with the distance in 5D space smaller than d.

[12] The side lengths of the 5D cube are chosen so that $\Delta a = d/(n\sqrt{k_a})$, $\Delta e = d/(na\sqrt{k_e})$, ... for a given distance d. Then $V = d^5 = \sqrt{k_a k_e k_i k_\Omega k_\varpi}(na)^5 \frac{\Delta a}{a} \Delta e \Delta \sin i \Delta\Omega\Delta\varpi$.

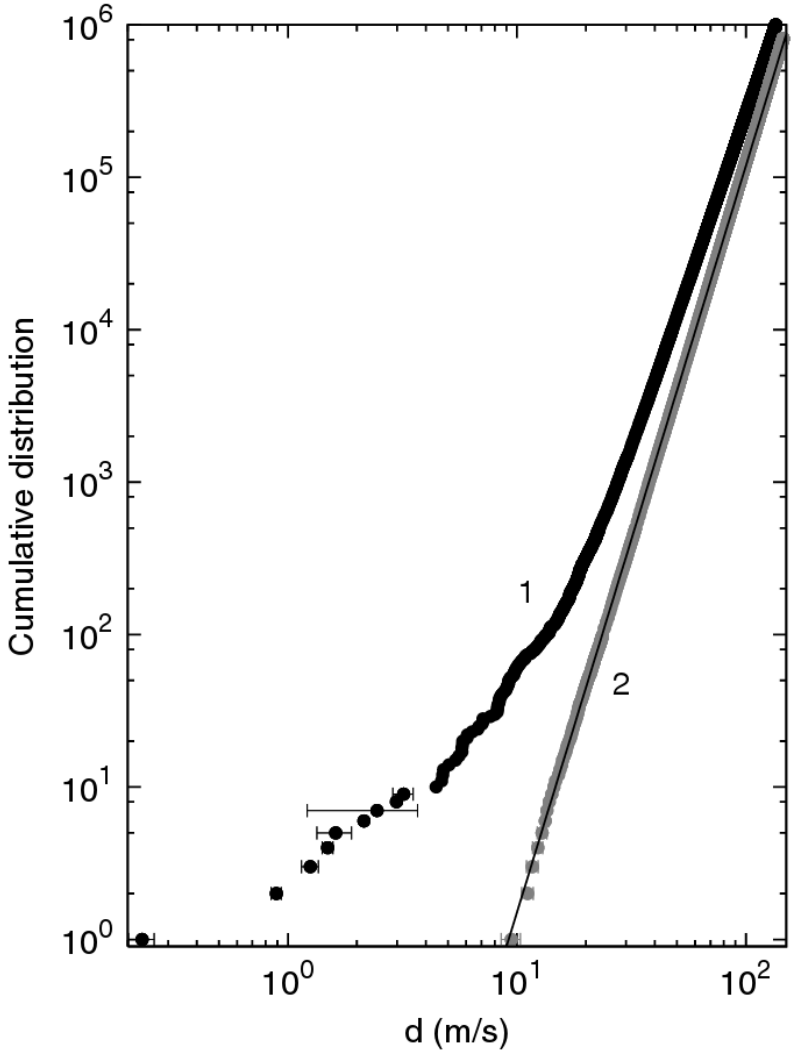

Figure 3.4: Cumulative distribution $N(< d)$ for an ensemble of real asteroids (black symbols) and randomly generated orbits in the main belt (gray symbols). The error intervals show the uncertainty of d derived from orbital uncertainties of the primaries and secondaries. The fitted power-law function holds $N(< d) \sim d^{4.91}$. The observed excess of the real cumulative distribution ($d \leq 10$ m s^{-1}) cannot be a consequence of randomly generated orbits. It is thus probable, that the pairs from this part of distribution have the same origin. Taken from Vokrouhlický et al. (2008).

The probability of occurrence of n trajectories in *any* volume V is then expressed by a 5-dimensional integral

$$P_n(d) = \sum_M p_n(d) = \frac{V^{n-1}}{n!} \int \eta^n e^{-\nu}\, dV. \tag{3.13}$$

Since we assume a small ν, it approximately holds that $e^{-\nu} \approx 1$ and the equation above takes the form

$$P_n(d) \approx \frac{1}{n!} \frac{\langle \eta^n \rangle\, V_{\rm tot}^n}{M^{n-1}}, \tag{3.14}$$

where $\langle \eta^n \rangle$ is η^n averaged over the main belt, $V_{\rm tot}$ is the volume of the main belt and M is the number of cells for which it holds that $M = V_{\rm tot}/V$.

If we assumed a constant density η, the equation (3.14) would take the form

$$P_n(d) \approx \frac{1}{n!}\frac{N^n}{M^{n-1}}, \tag{3.15}$$

with N being the total number of orbits in the main belt. Applying the expression (3.15) to asteroid pairs ($n = 2$) immediately yields

$$P_2(d) \approx \frac{1}{2}\frac{N^2}{M}. \tag{3.16}$$

Vokrouhlický et al. (2008) made a specific estimation of $P_2(5)$ for the distance of 5 m s^{-1}, assuming a constant density η. Originally, they covered the main belt ($N = 370000$) with $M \approx 10^{13}$ cells and using the expression (3.16) found that $P_2(5) \approx 0.002$.

Vokrouhlický et al. (2008), however, also modeled a more realistic situation and attempted to express the probability $P_2(d)$ for a non-constant orbit density η. Considering the uniform distribution of secular angles within large families, they only assumed the density η in the form $\eta = \eta(a, e, i)$. The dependency of $\eta(a, e, i)$ was found numerically by sampling the main belt region in the intervals $\Delta a = d_{\mathrm{smooth}}/n\sqrt{k_a}$ for a given smoothing distance d_{smooth}. Then they calculated the occurrence probability of close orbits for different Δa values. For $\Delta a = 0.1$ au and $\Delta a = 0.01$ au they obtained $P_2(5) \approx 0.01$ and $P_2(5) \approx 0.03$, respectively. It is apparent that $P_2(5)$ slightly increases as the step Δa decreases. This means, that even if $P_2(5)$ is still relatively small, it reaches higher values in close and compact systems, such as young asteroid families. To conclude, the probability that a close pair with $d = 5$ m s^{-1} is merely a result of a random orbit fluctuation is in the order of a few percent or less.

Local density of orbits around a pair

An extended method which considers also the local density of orbits around a pair was presented by Pravec and Vokrouhlický (2009). Pravec and Vokrouhlický (2009) showed that the expected number of pairs $P_2(V)$ in a population of N asteroids is given by

$$P_2(V) = P_2(d) = \frac{N}{2}\left(\frac{d}{R_0}\right)^5 e^{-\left(\frac{d}{R_0}\right)^5}, \tag{3.17}$$

where

$$R_0 = \left(\frac{15}{8\pi^2\eta}\right)^{1/5}, \tag{3.18}$$

while η is the local density of orbits around the pair. Pravec and Vokrouhlický (2009) investigated the occurrence of asteroid pairs separately in 6 specific zones (Hungaria, Inner main belt, Central main belt, Outer main belt, Cybele, Hilda). For a candidate pair[13] in a specific population, they calculated d/R_0. Consequently, they determined the number of expected (P_2) and found (N_p) pairs. If $P_2/N_p << 1$, then one can assume that the candidate is a real pair. Pravec and Vokrouhlický (2009) used this methodology to identify tens of statistically significant cases which do not belong to any known asteroid family.

[13]They took the threshold distance value of $d = 36$ m s^{-1}.

3.2.2 Finding the age of young pairs

The standard approach for finding the age of asteroid pairs is based on the backward propagation of clone clouds representing orbital and thermophysical uncertainties of the primary and secondary, focusing on close encounters between particular clones (Vokrouhlický et al., 2008).

The clones must, above all, (i) represent the orbital uncertainty of each member resulting from astrometric measurements (geometrical clones) and (ii) take into account the uncertainty of the Yarkovsky drift da/dt (Yarkovsky clones) resulting from incomplete or limited information about the member's thermophysical properties and size (see Chapter 1).

We require that the geometrical clones represent, in the space of osculating elements $(a, e, i, \Omega, \omega, M)$, the orbital uncertainty ellipsoids centered on the nominal orbits of the primary and secondary. Generating of the geometrical clones follows the equation for multi-dimensional normal distribution. Let $\boldsymbol{e}^*$ be, for a certain epoch T_0, the nominal (best-fit) trajectory derived from astrometric observations. Furthermore, let the covariance matrix $\boldsymbol{\Sigma}$ locally describe the normal distribution of plausible orbital realizations $\boldsymbol{e}$. The infinitesimal probability of finding a trajectory in the volume $\mathrm{d}^6\boldsymbol{e}$ around $\boldsymbol{e}$ is then $\mathrm{d}N(\boldsymbol{e}) = p(\boldsymbol{e})\mathrm{d}^6\boldsymbol{e}$, where the probability density $p(\mathbf{e})$ is given by the expression (e.g. Gentle, 2006; Milani and Gronchi, 2010)

$$p(\boldsymbol{e}) = \frac{1}{(2\pi)^3\boldsymbol{\Sigma}^{\frac{1}{2}}}\exp\left[-\frac{1}{2}(\boldsymbol{e}-\boldsymbol{e}^*)^{\mathrm{T}}\boldsymbol{\Sigma}^{-1}(\boldsymbol{e}-\boldsymbol{e}^*)\right]. \tag{3.19}$$

Thus, we have to use as many various orbital realizations as possible, because each of them can represent the real orbital solution. Generating of the geometrical clones can be done using the expression (see Gentle, 2006)

$$\boldsymbol{e} = \mathbf{T}^{\mathrm{T}}\mathbf{z} + \boldsymbol{e}^*, \tag{3.20}$$

where $\mathbf{z}$ is a 6-dimensional vector whose components are random deviates of the standard normal distribution and $\mathbf{T}$ is a [6 x 6] matrix. Matrix $\mathbf{T}$ obeys $\mathbf{T}^T\mathbf{T} = \boldsymbol{\Sigma}$ and it can be determined by Cholesky decomposition of matrix $\boldsymbol{\Sigma}$. While creation of geometrical clones is, in a way, straightforward, the generating of Yarkovsky clones requires a more specific approach, because each asteroid has unique thermophysical parameters.

The uncertainties of thermophysical parameters of the primary and secondary allow different values of their Yarkovsky drifts. We, therefore, must assign to each geometrical clone a set (let say N_{y}) of plausible values da/dt (yarko clones). Let, for instance, $|da/dt|_{\max}$ be the maximum drift of the primary, derived from limit values of its thermophysical parameters[14] (see Eq. 1.90). Once we know $|da/dt|_{\max}$, we can calculate the Yarkovsky drift da/dt as

$$\frac{da}{dt} = \left|\frac{da}{dt}\right|_{\max}\cos\gamma, \tag{3.21}$$

where γ is the obliquity. From the last equation, it is evident that da/dt depends also on the pole orientation of the body. The obliquity γ can be, in some cases,

[14] Or we can use precalculated values for different types of asteroids (see Morbidelli and Vokrouhlický, 2003).

determined or at least constrained from photometric observations. If that is not the case, it is necessary to sample $\cos\gamma$ uniformly in the range $[-1, 1]$, calculating da/dt for each yarko clone. In other words, we must assume, with the same probability, prograde and retrograde motion. To conclude, we propagate, in total, $2 \times N_{\rm y} N_{\rm g}$ clones representing the orbital and thermophysical uncertainties of the pair members back in time.

Let N_1 and N_2 denote the total numbers of clones of the primary and secondary, respectively. In each integration step, we control for all clone combinations $N_{\rm comb} = N_1 N_2$ the convergence criterion $r_{\rm rel} < R_{\rm Hill} \wedge v_{\rm rel} < V_{\rm esc}$. Note that $R_{\rm Hill}$ and $V_{\rm esc}$ are the Hill radius and the escape velocity of the parent body and $r_{\rm rel}$ and $v_{\rm rel}$ are the distance and relative velocity between two particular clones. If $N(t)$ is the number of convergent solutions recorded in time $[t, t + dt]$, then it provides basic insight into the distribution of possible ages of the asteroid pair.

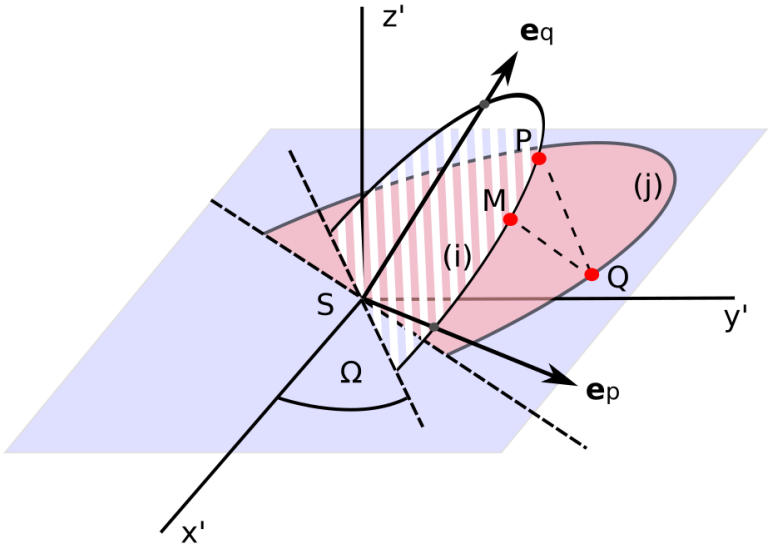

Figure 3.5: Geometrical insight into the improved convergence method. The ellipses (i) and (j) represent the osculating trajectories of the i-th clone of the primary and j-th clone of the secondary. The clones' positions at a given time t are denoted by P and Q. We start, for example with the clone Q and seek the hypothetical clone M on the osculating orbit of the clone P which has the minimum distance to Q. If the clones M and Q satisfy the convergence criteria and the hypothetical clone M is inside the real clone cloud of the primary, we record the time of convergence. Then we take the clone P as reference and repeat the whole process. Source: Žižka and Vokrouhlický (2011a).

Note that with time the clone clouds spread around the Sun as a consequence of gravitational and non-gravitational perturbations. Thus, after some time, we will face the problem of an insufficient number of clones. In an ideal situation we would require an infinite (or huge) number of clones, which is impossible to achieve because of the CPU limitations[15]. The lack of clones then, in some cases, prevents us from finding the age distribution for weakly convergent (suspect) pairs. Moreover, the classical clone-clone method might also favour younger convergent solutions over older ones. This effect is discussed in Žižka et al. (2016).

[15] We typically use thousands of clones.

Žižka and Vokrouhlický (2011a) partly bypassed the lack of clones by introducing hypothetical clones continuously distributed along all osculating orbits of real clones. In each integration step they controlled all clone-clone combinations of real clones, and for each couple (i) calculated the distance between the first clone and the nearest point (hypothetical clone) on the osculating ellipse of the second clone (and vice versa), (ii) checked, whether the found hypothetical clones are inside the real clone clouds and if so, (iii) recorded the time of convergence t if the real and hypothetical clones met the convergence criteria.

Using this method, Žižka and Vokrouhlický (2011a) discovered 7 asteroid pairs (we do not list them here explicitly, see the Appendix A, Paper 2 for further details), which indicated a solid convergence within the past 500 ky. These pairs are interesting, because their components exhibit very similar mean absolute magnitudes ($\Delta H < 1$ mag), indicating they are similar in size. However, this result might be in contradiction with the theory of pair formation (see Pravec et al., 2010), which implies that the ratio $q = M_2/M_1$, where M_1 is the mass of the primary and M_2 the mass of the secondary, should be less than $\simeq 0.2$. This discrepancy can be, however, caused by poorly determined absolute magnitudes of the primaries and secondaries. Thus, the set of pairs presented by Žižka and Vokrouhlický (2011a) would be a good target for further observations.

3.2.3 The pair (6070) Rheinland – (54827) 2001 NQ8

In this section, we focus our attention to one of the youngest and also most extensively studied pair with the components (6070) Rheinland and (54827) 2001 NQ8. This pair was first noticed by Vokrouhlický et al. (2008) as a close system with $d = 5.8$ m s^{-1}. Since then, it has been subject to a number of studies and presently, we have a rather detailed account of its age and physical characteristics of both members. Vokrouhlický and Nesvorný (2009) were the first to focus on this pair exclusively. They estimated its age as 17.22 ± 0.28 kyr and found the mean relative velocity between convergent clones to be ≈ 17 cm s^{-1} with the component perpendicular to the primary's orbital plane being as low as 21 mm s^{-1}. From the geometry of the best convergent solutions, they also modeled, taking into account mutual gravitational interaction, the orbital evolution of both fragments in early stages after the disruption. Consequently, Vokrouhlický and Nesvorný (2009) proposed a scenario, in which the secondary (54827) 2001 NQ8 could originally reside on the primary (6070) Rheinland or was its very close satellite. They also noticed that the convergent clones of the primary slightly prefer retrograde rotation.

Vokrouhlický et al. (2011) confirmed[16] the retrograde rotation of the primary with the ecliptic longitude of the rotational pole being less than $\simeq -50°$. Furthermore, we obtained (see Vokrouhlický et al., 2011), under the assumption of retrograde rotation of the primary, a more statistically significant set of convergent solutions for the retrograde-rotating secondary (54827) 2001 NQ8 (see Fig. 3.6). We used an open source integrator `SWIFT_RMVS` (Levison and Duncan, 1994) and propagated 20 geometrical and 30 Yarkovsky clones for each asteroid (altogether 1200 clones of the pair) into the past. The convergence criteria were controlled online every 0.25 yr during the simulation.

[16]Note that the retrograde rotation was further confirmed by Polishook (2014).

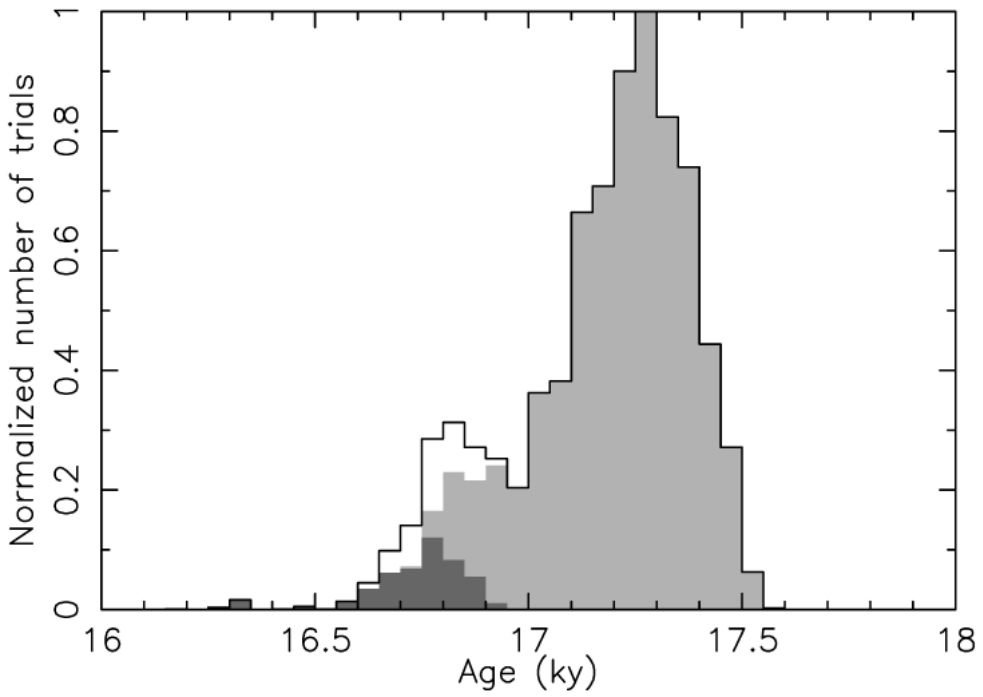

Figure 3.6: Distribution of possible ages of the pair (6070) Rheinland – (54827) 2001 NQ8. Each bin (50 yr) shows the number of convergent solutions with respect to the most occupied bin. Owing to the new pole solution of the primary (6070) Rheinland (see the text), we generated only clones corresponding to its retrograde rotation. Note, that these clones had $da/dt > 0$ in our model, because before we started the backward propagation, we just reversed the velocity vectors of all massive bodies (and clones) and let positive integration step dt. The clones of the secondary (54827) 2001 NQ8 were generated so that they represented: (i) both prograde and retrograde rotation (open histogram), (ii) prograde rotation (dark gray histogram) and (iii) retrograde rotation (light gray histogram). Thus, we can clearly see that the retrograde rotation of both pair members is the most probable realization of the pair. Source: Vokrouhlický et al. (2011).

Vokrouhlický et al. (2011) estimated the sizes of the primary and secondary as $D_1 \approx 3.9$ km and $D_2 \approx D_1/2$, respectively. As we did not know the surface thermal inertia for any component, we used the results of Bottke et al. (2006) and conservatively considered $da/dt \in [-5.3 \times 10^{-5}, 0]$ au Myr^{-1} for (6070) Rheinland and $da/dt \in [-10^{-4}, 10^{-4}]$ au Myr^{-1} for (54827) 2001 NQ8. The convergent criteria were chosen more strictly as follows: $r_{\rm rel} < 0.75 R_{\rm Hill} \wedge v_{\rm rel} < V_{\rm esc}$, where $R_{\rm Hill} \approx 1000$ km and $V_{\rm esc} \approx 2$ m s^{-1} are the Hill radius and escape velocity of Rheinland. To conclude, we found that the most probable age corresponding to retrograde rotation of both components is $T_{\rm age} = 17.2 \pm 0.2$ kyr.

The results of Vokrouhlický et al. (2011) and Polishook (2014) suggest that (6070) Rheinland has a nearly-convex shape with a sharp, planar-like edge which could originate from the rotational fission of the parent asteroid. Moreover, spectroscopic measurements performed by Polishook et al. (2014) revealed that the spectra of both the components fall into the S-group category. This finding is consistent with the asteroids belonging to either Nysa family (Nesvorný et al., 2015) or the Hertha family (Milani et al., 2014). Nonetheless, even though the

spectra are close, they are not identical. Polishook et al. (2014) also studied the influence of space weathering, finding that the secondary (54827) 2001 NQ8 is less affected. They explain this result by more dust particles settling on the primary than the secondary in the early stages after disruption. Let us note, that for precise age determination of asteroid pairs, including (6070) Rheinland – (54827) 2001 NQ8, it is also necessary to consider gravitational perturbations from large main belt perturbers (see Galád, 2012).

Currently the most detailed study focusing on the pair (6070) Rheinland – (54827) 2001 NQ8 is that by Vokrouhlický et al. (2017b). Vokrouhlický et al. (2017b) considered new findings about the rotational states of both the asteroids and numerically propagated their clones 250 kyr into the past. Using the light-curve inversion method (see Kaasalainen and Torppa, 2001; Kaasalainen et al., 2001), they derived[17] their probable shapes and found the sidereal rotation periods $P_1 = (4.2737137 \pm 0.0000005)$ hr and $P_2 = (5.877186 \pm 0.000002)$ hr of the primary and secondary. New photometric measurements also provided information about the characteristic diameters $D_1 = 4.4 \pm 0.6$ km and $D_2 = 2.2 \pm 0.3$ km, which gives $D_2/D_1 = 0.494 \pm 0.014$. Assuming that no other fragments were created during the disruption, we estimate that the parent object had the diameter of 4.6 ± 0.6 km. The expected bulk density $\rho = 2.3 \pm 0.3$ g cm^{-3} (Carry, 2012) then gives the Hill radius $R_{\rm Hill} = 940 \pm 140$ km and the escape velocity $V_{\rm esc} = 2.6 \pm 0.4$ m s^{-1} of the parent asteroid.

From the available observations, Vokrouhlický et al. (2017b) found the pole orientation of the primary to be $(\lambda, \beta) = (124°, -87°)$ and confirmed earlier hints of retrograde rotation. The uncertainty in the longitude, with confidence level 3σ, was determined as $\delta\beta_{3\sigma} \approx 10°$. The uncertainty in the latitude $\delta\lambda_{3\sigma}$ was not expressed because the spin axis is practically pointing to the south pole of the ecliptic. The uncertainty region of the Rheinland's pole orientation is shown in Fig. 3.7. In the case of the secondary, it turned out that two options $(\lambda, \beta) = (72°, -49°)$ and $(\lambda, \beta) = (242°, -46°)$ are possible. None of them corresponds to the prograde rotation of the secondary. The corresponding uncertainties are $\delta\lambda_{3\sigma} \approx 10°$ and $\delta\beta_{3\sigma} \approx 15°$ (see Fig. 3.8).

Let us note that, so far, the Yarkovsky effect was modeled by estimating the maximum drift $|da/dt|_{\rm max}$, from which Yarkovsky clones were generated, considering the acceptable intervals of obliquities (see Eq. (3.21)). If we know the pole orientation and thermophysical properties of the pair members, we can either (i) apply equation (3.21) and constrain the Yarkovsky drifts or (ii) directly model the Yarkovsky and YORP effects for both the asteroids, e.g. by using the linear theory of the Yarkovsky effect (Vokrouhlický, 1998a, 1999).

The pair (6070) Rheinland – (54827) 2001 NQ8 is the first pair, for which the latter approach has been applied. Vokrouhlický et al. (2017b) focused only on the diurnal variant of the Yarkovsky effect and expected the thermal inertia of both components in order of hundreds SI (see Delbo' et al., 2007b). Formally, they also included the perturbations caused by direct radiation pressure, even though these only have short-period effects with small amplitudes and are negligible compared to the Yarkovsky effect (Žižka and Vokrouhlický, 2011b).

[17] Assuming of convex shape of both components and rotation around the shortest axis of the inertia tensor.

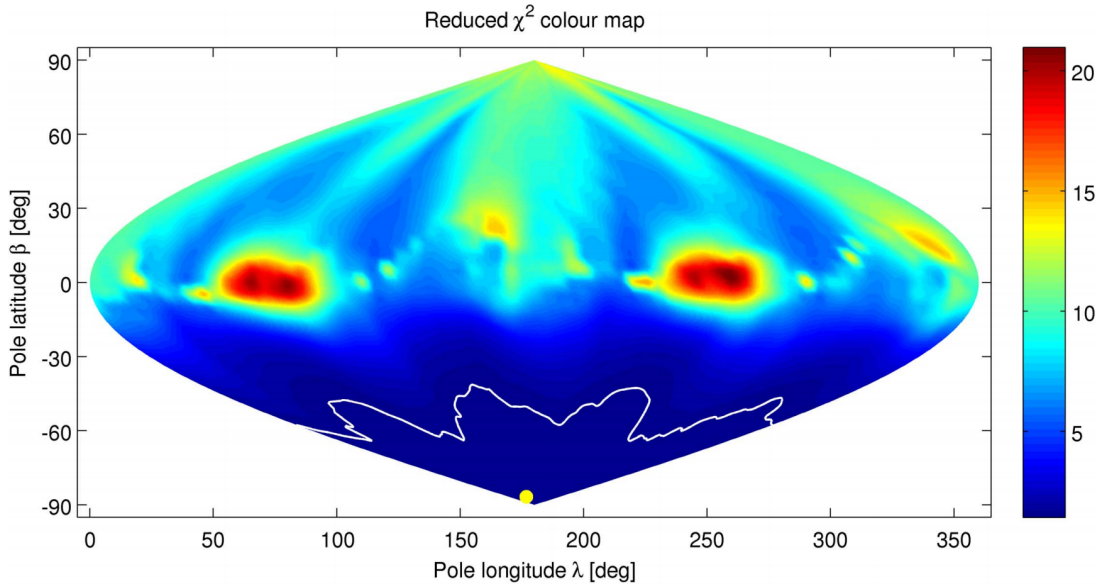

Figure 3.7: A map of the statistical quality of the light curve fit for any convex shape of Rheinland according to Vokrouhlický et al. (2017b). Blue regions show the acceptable solutions of the pole orientation. The yellow circle corresponds to the best-fit solution surrounded by 3σ confidence interval (white line).

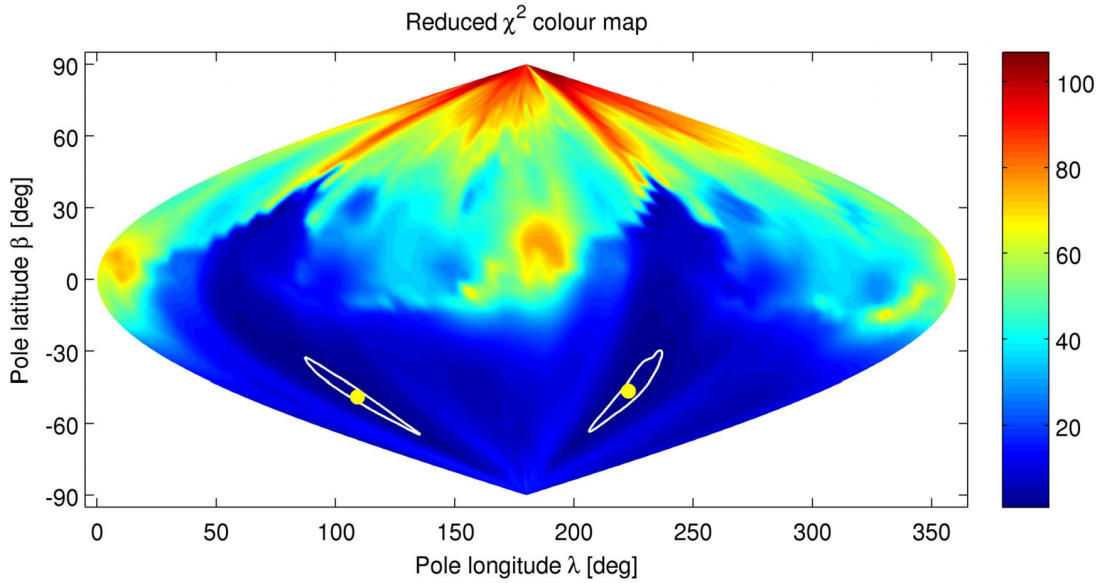

Figure 3.8: Same as Fig. 3.7 but relating to the secondary (54827) 2001 NQ8. Taken from Vokrouhlický et al. (2017b).

Each geometrical clone in their model, contains the set of all acceptable values of thermophysical parameters (e.g. thermal inertia Γ, obliquity γ, density ρ, ...) which effectively replace the previous simple model (see (3.21)). Let us note that so far, we have assumed a constant orientation of the spin axis $\mathbf{s}$ which is a crude approximation considering the influence of the YORP effect. Even if the YORP effect vanishes for a spherical body, one has to consider the time evolution of the vector $\mathbf{s}$ for convex bodies[18].

[18]The evolution of the spin axis is also influenced by the Sun and planets.

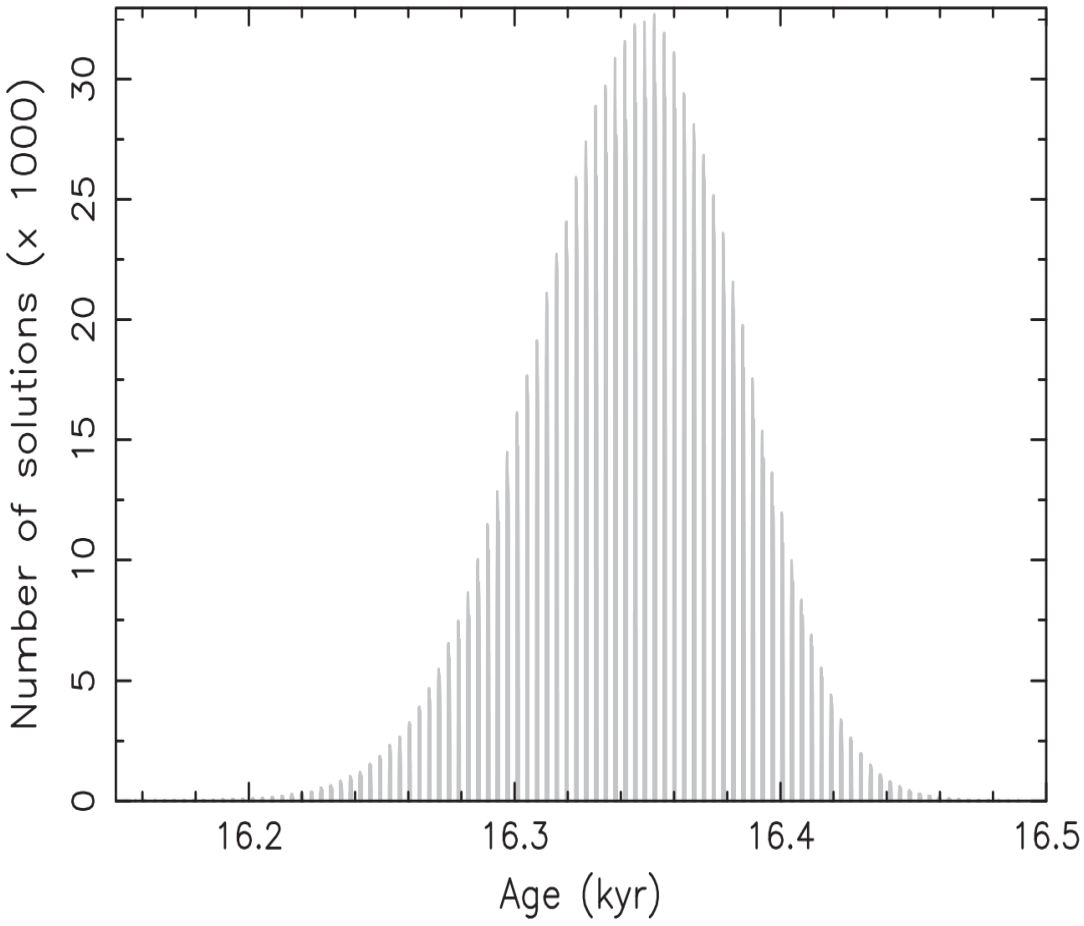

Figure 3.9: Distribution of possible ages of the pair (6070) Rheinland – (54827) 2001 NQ8. The vertical axis is the number of convergent solutions in each bin. The time step was set to $dt = 0.25$ day. In total, 5000 clones of the primary and 5000 clones of the secondary were used. The convergence criteria were controlled every ≈ 3.65 days. The white spaces result from the fact that the convergence of a selected clone pair repeats approximately once per orbit around the Sun. Taken from Vokrouhlický et al. (2017b).

For this reason, Vokrouhlický et al. (2017b) also calculated the dynamical evolution of the spin axis for each realization. Finally, in each integration step, they found the corresponding perturbing accelerations and checked the convergence criteria between the clones of the primary and secondary.

From the time distribution of convergent solutions, the age of the pair (6070) Rheinland – (54827) 2001 NQ8 was found to be $T_{\rm age} = 16.34 \pm 0.04$ kyr (see figures 3.9 and 3.11). In conclusion, let us note that the convergent clones can approach each other within one synodic period also at much later integration times. These close encounters can, in principle, lead to an ambiguous pair age. This problem was addressed by Žižka et al. (2016) for the case of asteroids (87887) 2000 SS286 and (415992) 2002 AT49 (see Chapter 4 for further details). Vokrouhlický et al. (2017b), however, did not find any other solutions up to 250 kyr into the past for the (6070) Rheinland – (54827) 2001 NQ8 pair.

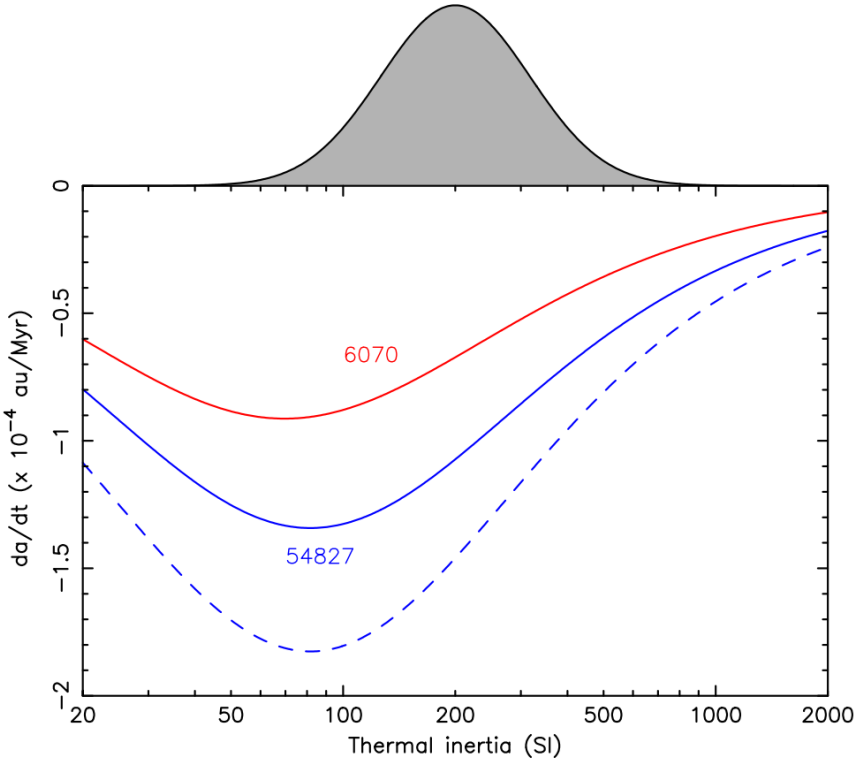

Figure 3.10: Distribution of secular drifts $\left\langle \frac{da}{dt} \right\rangle$ for nominal obliquities of (6070) Rheinland and (54827) 2001 NQ8 (see the text). The blue dashed line shows $\left\langle \frac{da}{dt} \right\rangle$ for the secondary with obliquity 180°. The gray Gaussian distribution in the upper part of the figure corresponds to expected values of the thermal inertia Γ. Taken from Vokrouhlický et al. (2017b).

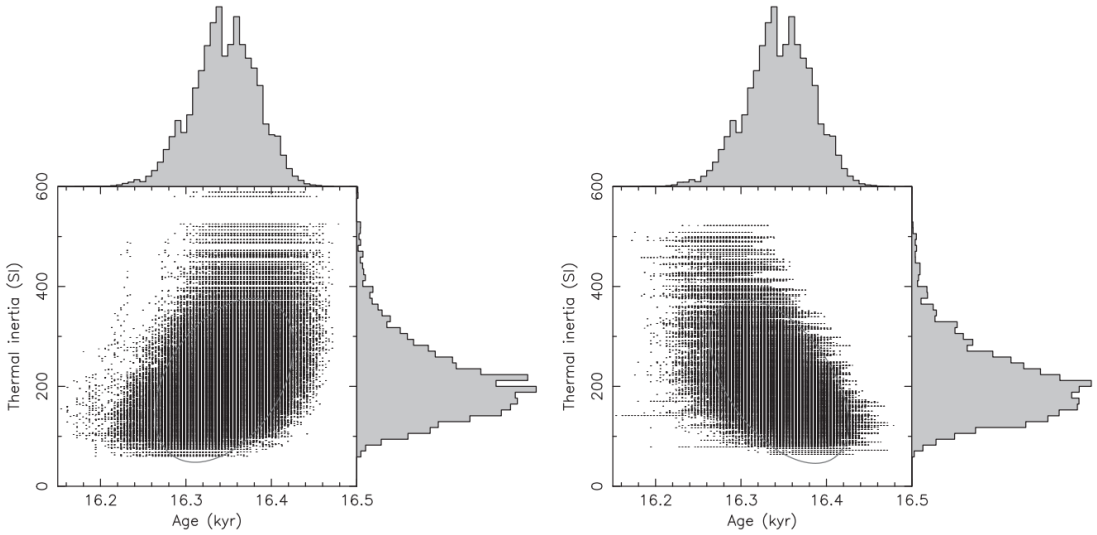

Figure 3.11: Thermal inertia distribution for convergent clones of the primary (left) and the secondary (right) as a function of the pair's age. Upper histograms demonstrate the distribution of possible ages. It is evident that further constraining of thermal inertia of both components would make the age estimation more accurate. Taken from Vokrouhlický et al. (2017b).

3.2.4 Formation of young pairs

Backward integrations show, that the encounter velocities between the primaries and secondaries are very small - in the order of meters per second or less. This fact suggests that the break-up event itself can be seen as a relatively gentle process. Let us consider only pairs which do not belong to any of the young asteroid families (see Section 3.1.4). As mentioned in the previous paragraph, asteroid pairs mostly consist of kilometer-sized bodies and from a certain perspective, these systems are comparable in size to binary asteroids. This observation fact could suggest that there is a similar mechanism of origin for binary asteroids and for asteroid pairs. Research in the field of binary asteroids implies that these systems are either formed (i) by the rotational fission of a parent body as a consequence of the YORP effect (e.g. Scheeres, 2007a; Pravec and Harris, 2007; Walsh et al., 2008), (ii) by tidal tearing of a parent asteroid (whose fragments can then merge to a new body) during a close approach with a planet or (iii) by a collision between large asteroids with smaller fragments being captured by larger ones (Durda et al., 2004).

Rotational fission caused by the YORP effect is, nowadays, the most promising and observation-supported mechanism (e.g. Vokrouhlický and Nesvorný, 2008; Pravec et al., 2010). Pairs of asteroids are thus probably a direct consequence of dynamic instabilities of binary or proto-binary systems (see Fig. 3.12), whose dynamical evolution strongly depends on the free energy (see Section 3.1.4). Let $q = M_2/M_1$, where M_1 is the mass of the primary and M_2 is the mass of the secondary. It can be shown (Pravec et al., 2010) that if q is smaller than ≈ 0.2, the free energy of the system is positive and the components of the binary drift apart[19].

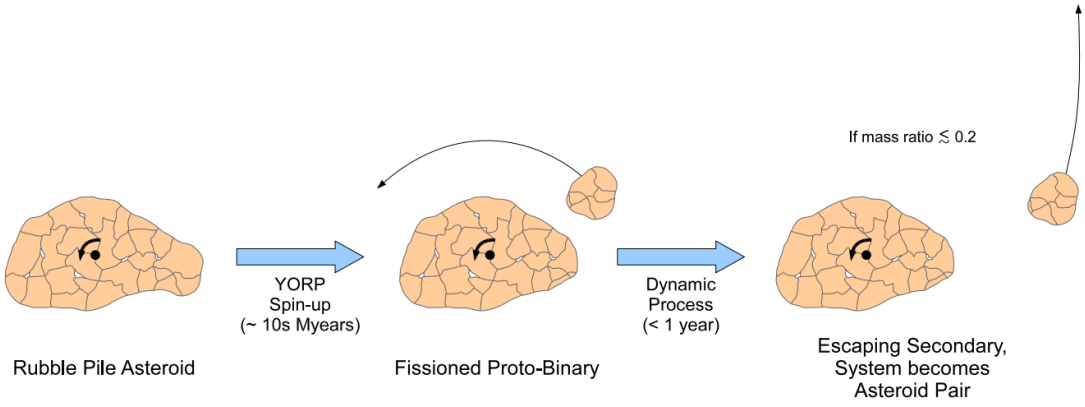

Figure 3.12: Schematic illustration of the origin of an asteroid pair. Initially, a rubble-pile asteroid's rotation is being accelerated by the YORP effect. Upon reaching the critical rotational speed, the secondary separates, creating an asteroid pair. Taken from Pravec et al. (2010).

On the other hand, for the ratio higher than ≈ 0.2, the free energy is negative and the components remain together. With the mass ratio approaching 0.2, the rotational energy of the primary is transformed to the kinetic energy of relative motion. This idea explains, above all, that (i) primaries of pairs with very small

[19]For elongated bodies, this limit can be somewhat higher.

mass ratios rotate close to critical angular frequency, (ii) beyond the limit value of 0.2, the period of rotation of the primary increases and (iii) for systems with mass ratio larger than ≈ 0.2, the proto-binary does not disintegrate and no pair is formed (the two components can also recollapse into a single asteroid).

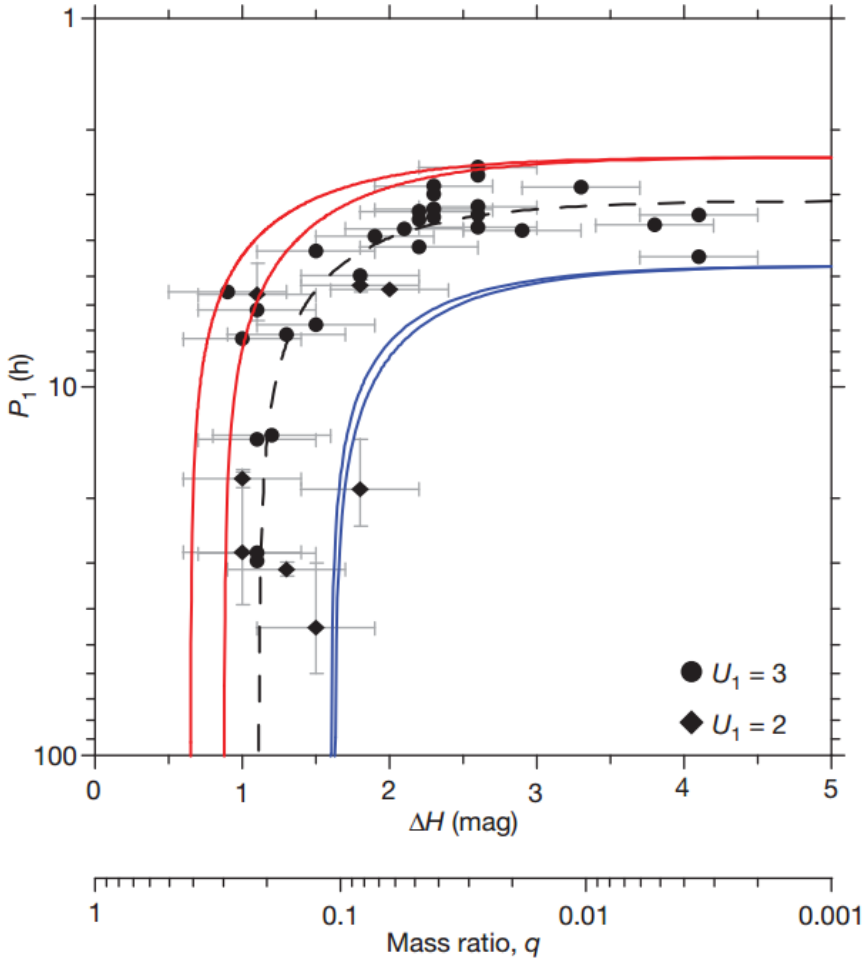

Figure 3.13: The dependence between rotational period of the primary P_1 and the mass ratio q for 35 pairs. Red and blue curves correspond to the upper and lower bounds of the dependence $P_1(q)$ according to the analytical theory presented in Pravec et al. (2010).

3.3 Conclusion

Young asteroid families and pairs have become an attractive topic during the past years, because they preserve the initial conditions of the break-up event better than older populations in our Solar System. According to the contemporary view, young asteroid families were probably formed either by rotational fission of the parent asteroid due to the YORP effect followed by subsequent fissions of new secondaries or by its collision with another asteroid. Moreover, the YORP effect was probably at the origin of young asteroid pairs and currently is the most promising and most observation-supported mechanism of their formation. In short, it gradually speeds up the rotation of the parent asteroid until it breaks

up in two (or more) fragments which, with time, drift apart as a consequence of both gravitational and non-gravitational perturbations. These fragments are nowadays observed as separate asteroids.

Therefore, if we want to study the orbital history of asteroid families and pairs, it is necessary to perform backward numerical integration of their members until they meet in a certain time and space. Nevertheless, due to their orbital and thermophysical uncertainties, we cannot rely only on nominal orbits. Each asteroid is, therefore, replaced by many clones, representing all plausible orbital and thermophysical realizations. During the backward integration, in each integration step we seek close encounters between particular clones and record the time of convergence. From the time distribution of the convergent solutions we can estimate the age of the pair/family. However, due to the Keplerian shear, the mean distance between individual clones increases with time. As a result, for some weakly convergent pairs we may face the problem of an insufficient number of clones. To partly bypass this problem, we modified the classic approach and introduced hypothetical clones continually distributed along the osculating ellipse of each clone.

During our research, we discovered 7 young pairs with similar-sized components, which is in contradiction with the current theory of pair formation. There are two main explanations for this: (i) the sizes of the primaries and/or secondaries of our set were determined inaccurately, or (ii) it is necessary to revise the existing theory.

Another subject of this chapter was the well-known pair (6070) Rheinland – (54827) 2001 NQ8. In addition to determining its age, we also investigated rotational states of the primary and secondary. By using statistical methods, we found that the secondary (54827) 2001 NQ8 should exhibit retrograde rotation. Further studies, however, determined the shape of both the asteroids and conducted even better simulations including precise modeling of the Yarkovsky effect, resulting in a more accurate estimation of its age.

4. Extremely young asteroid pair (87887) 2000 SS286 and (415992) 2002 AT49

The aim of this chapter is to present a detailed study of the asteroid pair (87887) 2000 SS286 and (415992) 2002 AT49, with an emphasis on describing our new method which we developed to solve the problem of its ambiguous age. Note that this chapter is based on the work of Žižka et al. (2016) that can be found in the Appendix A (Paper 3). We highly recommend to first read the Chapter 3 about the theory of young asteroid families and pairs.

4.1 Introduction

Since the discovery of asteroid pairs (see Vokrouhlický and Nesvorný, 2008) there has been a great interest in very young representatives because they might well preserve the initial conditions at the time of their formation. In contrast to young pairs, old pairs are less appropriate for studying and understanding the break-up event. The reason is that with time, many dynamical and physical processes influence the orbital evolution, rotational states and spectral properties of their members. Indeed, even a rough approximation based on neglecting both the gravitational and non-gravitational perturbations such as the Yarkovsky and YORP effects, would still lead to a fairly good age estimation of extremely young pairs with $T_{\rm age} \leq 10$ kyr.

Nevertheless, by taking into account all the perturbations, we are able to better constrain the pair's age and also uncover what happened immediately after the break-up event. For instance, the best-studied pair (6070) Rheinland and (54827) 2001 NQ8 allowed us to propagate the orbits of its members back in time to a near-contact system (Vokrouhlický et al., 2017b).

Due to the Keplerian shear and differential Yarkovsky effect, components of asteroid pairs that are several tens of thousands years old, have unrelated values of mean longitudes λ_1 and λ_2. On the contrary, in the case of extremely young pairs, mean longitudes of their members are much more similar. From the third Kepler law we get $|\Delta\lambda|/360^\circ \simeq 1.5(|\Delta a|/a)(T/P)$, where P is the orbital period, T is the time elapsed and Δa is the corresponding semi-major axis difference between the primary and secondary. To be more specific, for extremely young pairs ($T_{\rm age} < 10$ kyr) which typically have $|\Delta a| \simeq 10^{-5}$ au and are located in the inner main belt, we obtain from the previous formula $|\Delta\lambda| \simeq 10^\circ - 20^\circ$. However, the similarity of λ values is necessary but not sufficient condition for a pair to be extremely young. For example, Vokrouhlický and Nesvorný (2008) studied a very tight pair of asteroids (1270) Datura and (215619) 2003 SQ168 with $|\Delta\lambda| \approx 1.6^\circ$ and $|\Delta a| \approx 3 \times 10^{-5}$ au in osculating elements space and found that this close configuration repeats in time with the period of about 100 kyr. Consequently, we need a mathematical tool, which would be able to decide whether a given pair is young, or older than the duration of one synodic cycle of its components. Thus, an important task is to correctly determine when precisely a particular pair formed.

This problem is not as easy as it might look. For example, previous studies showed that the uncertainties in thermophysical parameters of pair members lead to different thermal accelerations, which result in a wide distribution of possible ages.

However, there is yet another motivation for seeking very young pairs. Even though the YORP effect is presently the most promising process of asteroid pair formation, it still remains as a theoretical possibility and needs closer inspection and further justification. For instance, the evidence that YORP effect is genuinely responsible for the break-up event, can be based on the statistics of pair formation in time, which might be compared with the prediction of the YORP theory. Ideally, we would then choose a size category of asteroid pairs and get a complete sample of those pairs that formed in the main belt, for instance, within the past 100 kyr. Unfortunately, we still face observation-incompleteness effects that prevent us from obtaining this data set. On the other hand, an easier but still interesting task is to find the age of the youngest pairs in each size category.

4.2 Candidate search

So far, only a few candidates for real pairs younger than 20 kyr have been discovered. One of the best studied cases with a well constrained age is the pair (6070) Rheinland – (54827) 2001 NQ8, whose age of 16.34 ± 0.04 kyr was determined by Vokrouhlický et al. (2017b)[1]. Other suspect cases which might be very young were first presented in Pravec et al. (2010) and Galád et al. (2014).

We used the updated catalog of the Minor Planet Center (April 15, 2016) and searched for very close orbits among the multi-opposition asteroids. For this purpose, we adopted the method described in Vokrouhlický and Nesvorný (2008) and in equation (3.4) we set $k_a = 5/4$, $k_e = k_i = 2$ and $k_\Omega = k_\varpi = 10^{-5}$. In total, 23 potential candidates had $d \leq 15$ m s^{-1} and $|\Delta\lambda| \leq 15°$. After discarding the cases belonging to known, compact and very young asteroid families, such as the asteroids (1270) Datura and (215619) 2003 SQ168, 16 candidates remained in our set and were examined in more detail. Some of them, however, have already been studied (e.g., Pravec et al., 2010) and their age was found to be beyond our limit of 10 kyr. This was the case of

–(21436) Chaoyichi and (334916) 2003 YK39,
–(23998) 1999 RP29 and (205383) 2001 BV47,
–(56232) 1999 JM31 and (115978) 2003 WQ56,
–(63440) 2001 MD and (331933) 2004 TV14 and
–(76111) 2000 DK106 and (354652) 2005 JY103.

Next, we integrated nominal orbits of the 11 remaining pairs and revealed that some of them did not converge within the past 10 kyr. Particularly, this was the case of

–(70208) 1999 RX33 and 2013 GZ99,
–(74096) 1998 QD15 and (224857) 2006 YE45,

[1]For further information related to this pair see Section 3.2.3.

–(188577) 2005 GM1 and (420756) 2013 EW4,
–(267333) 2001 UZ193 and 2007 DY95 and
–(320025) 2007 DT76 and 2007 DP16.

Thus, we were left with the following six last cases

–(229401) 2005 SU152 and 2005 UY97 ($|\Delta\lambda| \approx 1.1°$),
–(17198) Gorjup and (229056) 2004 FC126 ($|\Delta\lambda| \approx 1.1°$),
–(355258) 2007 LY4 and (404118) 2013 AF40 ($|\Delta\lambda| \approx 4.7°$),
–(87887) 2000 SS286 and (415992) 2002 AT49 ($|\Delta\lambda| \approx 5.3°$),
–(356713) 2011 UK160 and 2014 QX220 ($|\Delta\lambda| \approx 9.8°$),
–(99052) 2001 ET15 and (291788) 2006 KM53 ($|\Delta\lambda| \approx 10.5°$).

Even though some of these pairs do converge within 10 kyr in the past, they also have many convergent solutions far beyond 10 kyr. This behaviour is similar to the studied case (87887) 2000 SS286 – (415992) 2002 AT49, but the most important difference is that some of the members except (87887) 2000 SS286 and (415992) 2002 AT49 still have rather poorly constrained orbits. Moreover, the small sizes of 2005 UY97, (355258) 2007 LY4, (404118) 2013 AF40, (356713) 2011 UK160 and 2014 QX220 imply that Yarkovsky forces might be potentially strong and therefore the clone variants of these asteroids can converge in a widely spread period in the past. Discarding of (17198) Gorjup – (229056) 2004 FC126 and (99052) 2001 ET15 – (291788) 2006 KM53 was motivated by another reason. We performed a detailed backward integration of clones of asteroids (17198) Gorjup and (229056) 2004 FC126. It turned out that the clone clouds of the primary and secondary closely approached about 230 yr ago. However, during the backward propagation, we did not record any pair of clones with mutual distance and relative velocity less than $\approx$ 50,000 km and $\approx$ 3.0 m s^{-1}, respectively. These values do not meet our convergence criteria where the encounter distance should not exceed the Hill radius ($\approx$ 750 km) and the relative velocity must be lower than the escape velocity ($\approx$ 1.5 m s^{-1}) of the parent body. A similar situation occurred for the pair (99052) 2001 ET15 and (291788) 2006 KM53. Clone variants of this pair had a chance to encounter 5 kyr ago, but the minimal recorded distance was $\approx 10,000$ km with a relative velocity of $\approx$ 1.5 m s^{-1}. While the relative velocity is comparable with the escape velocity of the parent object, the minimal distance is approximately 15 times larger than the characteristic radius of the Hill sphere.

Finally, the most promising case for our study was the pair (87887) 2000 SS286 and (415992) 2002 AT49. A preliminary backward integration indicated that this pair could have been only 7 kyr old. However, some convergent solutions were also found beyond 50 kyr, which made the problem of age determination more complex. The question then arises: is the pair younger than 10 kyr or older than 50 kyr? To tackle this problem, we had to get as much information as possible about the primary and secondary. Then we developed a new statistical method suitable for asteroid pairs with ambiguous age. The case of (87887) 2000 SS286 – (415992) 2002 AT49 clearly shows that each asteroid pair is unique, in a way. Unfortunately, a general method of age determination appropriate for all pairs has not been developed yet.

4.3 Asteroids (87887) 2000 SS286 and (415992) 2002 AT49

The semi-major axis of our pair is ≈ 2.755 au, which corresponds to the central part of the main belt near the 5/2 mean motion resonance with Jupiter. As can be seen in Tab. 4.1, both components have similar mean longitudes ($\Delta\lambda \approx 5.3°$). There is also an exceptionally small[2] difference between their semi-major axes ($\Delta a \approx 1.5 \times 10^{-4}$ au).

Asteroid	a [au]	h	k	p	q	λ [deg]	H [mag]
87887 2000 SS286	2.75480910	0.11083546	-0.02636157	-0.06375451	0.03574610	132.305893	15.44
415992 2002 AT49	2.75496372	0.11110586	-0.02644782	-0.06375849	0.03575475	137.633071	16.69
			Uncertainty				
	δa	δh	δk	δp	δq	$\delta\lambda$	
87887 2000 SS286	1.9e-8	6.2e-8	8.0e-8	6.1e-8	6.5e-8	6.4e-6	0.05
415992 2002 AT49	2.4e-8	8.2e-8	2.1e-7	8.5e-8	1.0e-7	1.3e-5	0.04

Table 4.1: Nonsingular elements and absolute magnitudes of the primary (87887) 2000 SS286 and the secondary (415992) 2002 AT49 taken from the `AstDyS` database for the epoch MJD 57,400. Note that a is the semi-major axis, $(h,k) = e(\sin\varpi, \cos\varpi)$ and $(p,q) = \tan(i/2)(\sin\Omega, \cos\Omega)$, where i is the inclination, e is the eccentricity, ϖ is the longitude of pericenter and Ω is the longitude of node. The mean longitude is given by $\lambda = \varpi + M$, while M is the mean anomaly.

A closer look at the location of the pair suggests that it belongs to the Gefion family (see Nesvorný et al., 2015). It can be also associated to the asteroid (94) Minerva - the largest family member (see Milani et al., 2014). In our work, we adopted the mean albedo for S-type asteroids $p_V = 0.20 \pm 0.05$, which is less than the probably overestimated value $p_V = 0.27 \pm 0.06$ based on WISE spacecraft observations (see Pravec et al., 2012).

It is interesting to calculate the distance $d_{\rm prop}$ between both asteroids in the proper elements space. Note that one would expect $d_{\rm prop}$ to be very small, for example on the order of m s^{-1}. Surprisingly, by using the synthetic proper elements taken from the `AstDyS`[3] database and the standard metric (3.1) (e.g., Zappalà et al., 1990), we obtained $d_{\rm prop} \approx 32$ m s^{-1}. This unexpected result was probably caused by (i) the occurrence of the three body (3, -1, -1) mean motion resonance (e.g., Nesvorný and Morbidelli, 1998), (ii) large value of the nominal $\delta e_p \approx 1.25 \times 10^{-3}$ and (iii) large 1σ uncertainties of proper eccentricities of the primary and secondary ($\approx 1.7 \times 10^{-3}$ for both components). In addition, the synthetic proper elements are usually obtained from long-term numerical integrations for at least 2 Myr time period (e.g., Knežević and Milani, 2000; Knežević et al., 2002), which is much longer than the suggested age of the pair.

[2]For asteroids located in the same region, the typical amplitude of short-period oscillations of the semi-major axis is 40 times larger than the current difference Δa. This fact indicates that the pair should be extremely young.

[3]`http://hamilton.dm.unipi.it/astdys/`

For determination of the members' physical properties, precise photometric observations are of great importance. In our case, all observations were carried out using the 1.54 m Danish telescope at La Silla, Chile in 2014 and 2016. We processed our photometric data using the standard Fourier series method (e.g., Harris et al., 1989; Pravec et al., 1996, 2000)

(87887) 2000 SS286

The rotation period of the primary was found to be $P = 5.7773 \pm 0.0004$ h. Note that this value is a weighted average of the determined periods from apparitions in 2014 and 2016. The light curves are shown in Fig. 4.1 and Fig. 4.2.

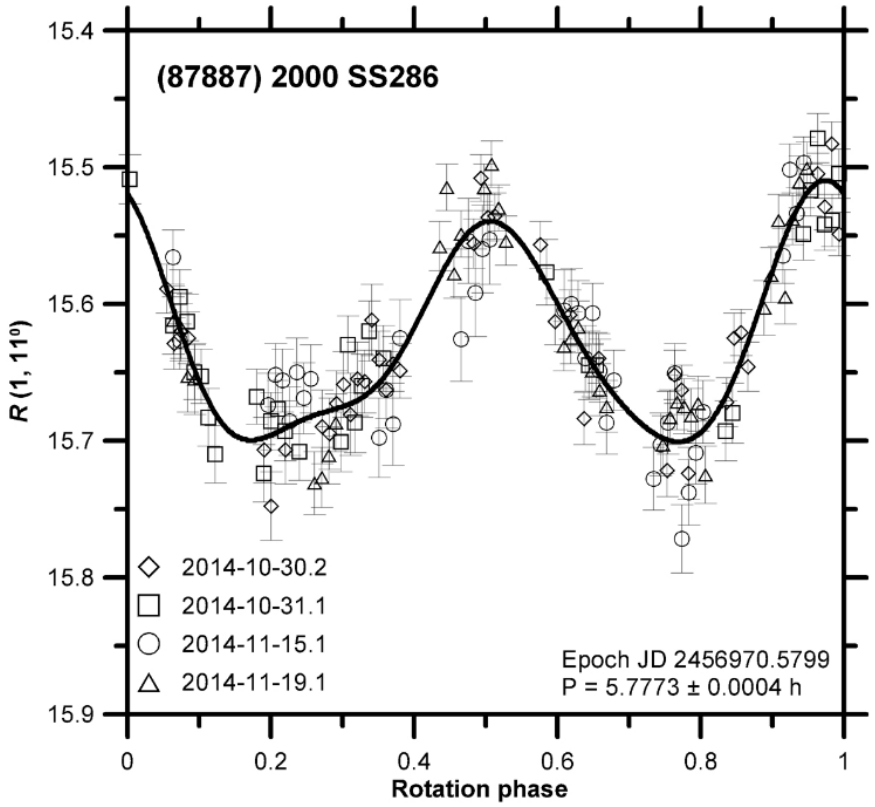

Figure 4.1: Composite light curve of the primary (87887) 2000 SS286 based on observations in 2014. Taken from: Žižka et al. (2016).

The mean amplitude 0.22 mag of the light-curve, the color index $V - R = 0.45 \pm 0.02$ and the slope parameter $G = 0.21 \pm 0.05$ suggest that the primary has probably a moderately elongated shape and belongs to S-type asteroids. Using the mean absolute magnitude of the primary in the Cousins R band ($H_R = 14.99 \pm 0.04$), the corresponding mean absolute magnitude in Johnson's V band ($H = 15.44 \pm 0.05$) and the mean geometric albedo $p_V = 0.20 \pm 0.05$, we were able to calculate the diameter $D_1 = 2.43 \pm 0.32$ km. Our photometric data also do not indicate any significant signs of tumbling and even if the primary was a tumbler, the angle between the spin axis and the angular velocity vector should be very small. Let us remind that the characteristic timescale τ for damping of the tumbling state can be described by the formula (1.106) presented

in the work of Harris (1994). In our case[4] $\tau \approx 600$ kyr which is roughly one hundred times longer than the young variant of the pair's age and approximately more than one order of magnitude higher than the older variant. This implies that the primary and secondary probably separated very gently, leaving (87887) 2000 SS286 to rotate around the principal axis of the inertia tensor.

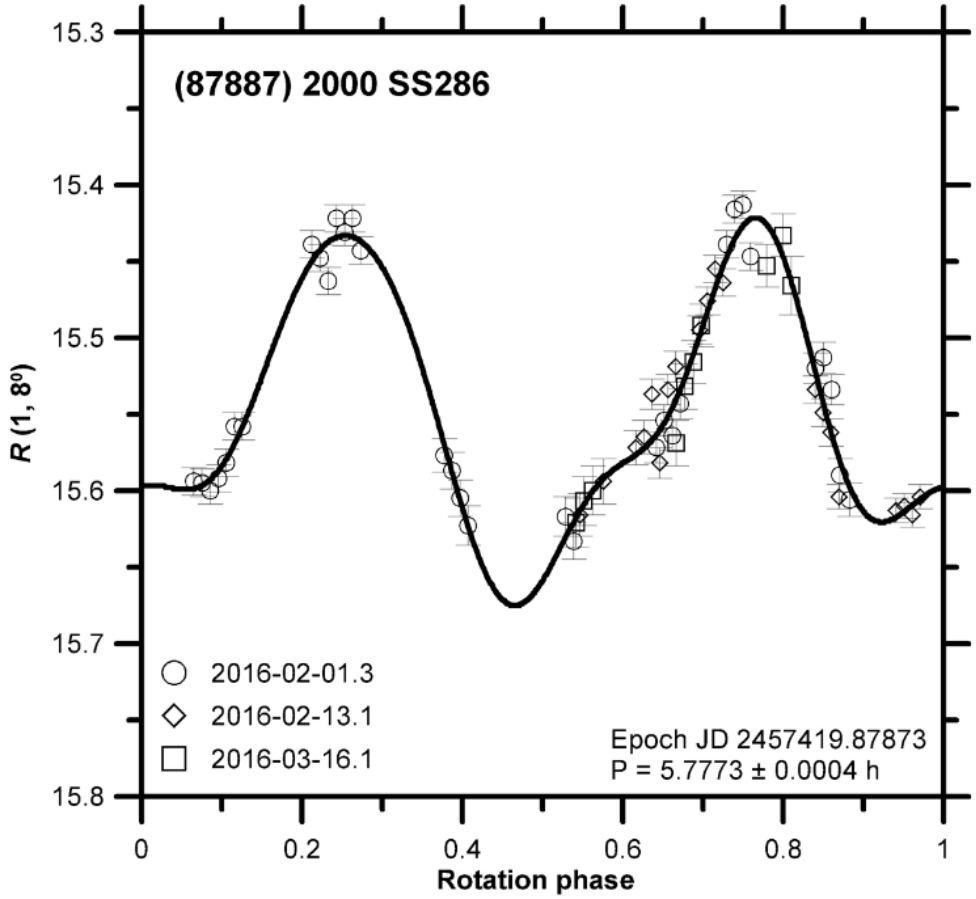

Figure 4.2: Composite light curve of the primary (87887) 2000 SS286 based on observations in 2016. Taken from: Žižka et al. (2016).

(415992) 2002 AT49

The photometric observations of the secondary were not as conclusive as those of the primary. This was mainly caused by the low light-curve amplitude (0.12 mag) and the relatively low apparent brightness of (415992) 2002 AT49. The formal best-fit solution based on observations from 2016 led to the rotational period $P = 2.6366 \pm 0.0003$ h. However, this solution was not unique. Due to the broad χ^2 minimum of the Furier fit, other values were also possible. Taking into account all the statistically admissible χ^2 realizations, we obtained a fairly wide range of possible rotational periods from ≈ 2.5 h to ≈ 6.0 h. Assuming that the secondary has the same values of G, $V - R$ and p_V as the primary, we obtain $H_R = 16.24 \pm 0.03$, $H = 16.69 \pm 0.04$ and $D_2 = 1.36 \pm 0.18$ km.

[4]We used $K = 38$ in the formula (1.106).

From the sizes D_1 and D_2 we estimated the size of the parent asteroid to be $D_{\rm par} = 2.56 \pm 0.34$ km. The typical bulk density for S-type asteroids is between 2.0 g cm^{-3} and 2.7 g cm^{-3} (e.g., Carry, 2012), which gives the characteristic Hill radius $R_{\rm Hill} = 600^{+35}_{-50}$ km and the escape velocity $V_{\rm esc} = 1.5 \pm 0.1$ m s^{-1} of the parent body. However, for simplicity, we adopted $V_{\rm esc} = 1.5$ m s^{-1} and $R_{\rm Hill} = 600$ km.

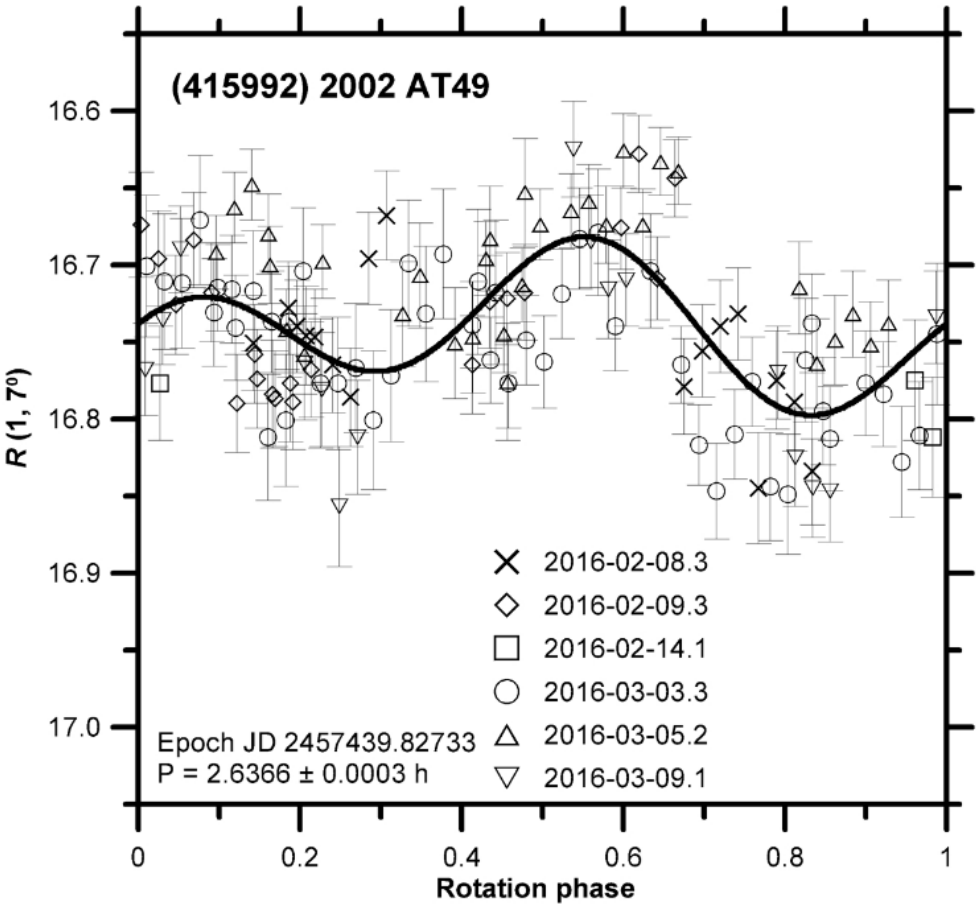

Figure 4.3: Composite light curve of the secondary (415992) 2002 AT49 based on observations in 2016. Taken from Žižka et al. (2016).

4.4 Determination of the right age

The traditional methods of finding the distribution of possible ages of asteroid pairs are based on the work of Vokrouhlický and Nesvorný (2008). The main idea implies a backward propagation of clone variants of the primary and secondary together with focusing on their close encounters. Let us note that the problem of the age determination of asteroid pairs is discussed in Section 3.2.2 in more detail. However, we slightly modified the standard approach of Vokrouhlický and Nesvorný (2008) to decide whether our pair is younger than 10 kyr or older than 50 kyr.

4.4.1 Nominal orbits

First we numerically integrated nominal orbits of (87887) 2000 SS286 and (415992) 2002 AT49 without considering the thermal accelerations. At every time step $dt = 3$ days we computed the distance and relative velocity between the components (Fig. 4.4). The first deep encounter occured ≈ 7.42 kyr ago when their mutual distance and relative velocity were ≈ 3900 km and ≈ 0.14 m s^{-1}, respectively. This might indicate that we have found the first pair younger than the psychological limit of 10 thousand years. However, when the propagation is continued back in time, other minima appear. The length of the first synodic cycle is ≈ 250 kyr, so ≈ 257 ky ago the asteroids could have experienced another close encounter with the mutual distance of $\approx 11,000$ km and the relative velocity of $\approx$ 1.52 m s^{-1}. Note that this situation repeats with time[5].

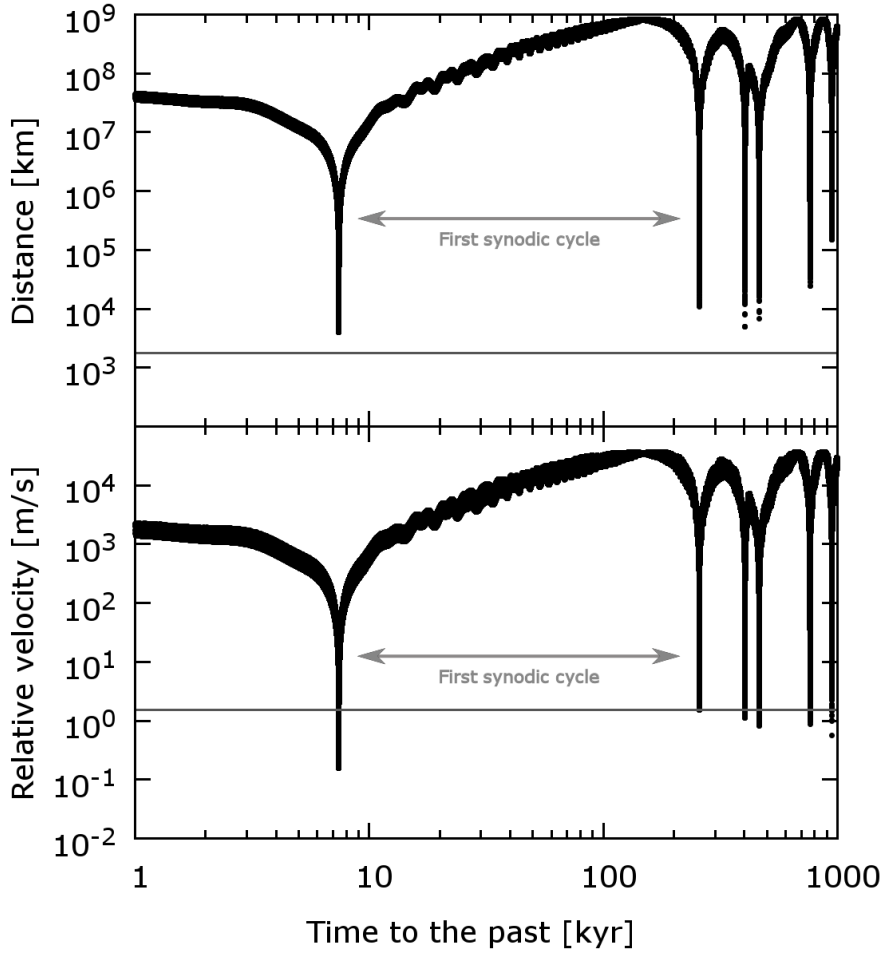

Figure 4.4: Backward propagation of nominal orbits of the asteroids (87887) 2000 SS286 and (415992) 2002 AT49 (both without thermal accelerations). The top panel depicts their mutual distance, the bottom panel shows their relative velocity. We can clearly distinguish deep minima - first occuring ≈ 7.42 kyr ago, followed by the second ≈ 257 kyr ago. They are separated by one synodic cycle of the primary and secondary. The grey horizontal lines mark the distance of $3R_{\rm Hill}$ and the escape velocity $V_{\rm esc}$. Taken from: Žižka et al. (2016).

[5]Note that the synodic period varies due to orbital perturbations.

In addition, similar behaviour is observed also for other clone variants representing the orbital and thermophysical uncertainties of the primary and secondary.

4.4.2 Backward propagation

We followed the method described in Section 3.2.2 and generated 1000 geometric clones for each asteroid. Assuming all possible spin axes orientations[6] of both components, we assigned to each clone a random value of da/dt uniformly chosen from the interval $[-|da/dt|_{\max}, |da/dt|_{\max}]$, where $|da/dt|_{\max}$ is the maximal Yarkovsky drift for the corresponding asteroid. Let us remind that the Yarkovsky drift da/dt of an asteroid can be calculated as follows (3.21)

$$\frac{da}{dt} = \left|\frac{da}{dt}\right|_{\max} \cos\gamma, \tag{4.1}$$

where γ is the obliquity. At the same heliocentric distance as (87887) 2000 SS286 and (415992) 2002 AT49 we expect the maximum semi-major axis drift for a kilometer-sized asteroid to be $|da/dt|_{\max} = 2 \times 10^{-4}$ au Myr^{-1} (e.g., Bottke et al., 2006). Thus, to obtain uniform distribution of da/dt we choose random values of $\cos\gamma$ which has uniform probability density distribution within the interval [-1,1]. Note that the sign of da/dt depends on the orientation of the spin axis so that da/dt is positive for prograde and negative for retrograde motion[7]. In our model, both the prograde and retrograde realizations are equally probable.

In other words, we propagated 1000 orbital realizations (geometric clones) of each pair member. Their initial state vectors were constructed according to the equation (3.20) and each clone had a random value of da/dt. The initial positions and velocity vectors of the planets at $T_0 = 57,400.0$ MJD epoch were taken from the JPL ephemerides file. We also considered the gravitational perturbations from three massive objects in the main belt - Ceres, Pallas and Vesta. Their initial orbits were taken from the `AstDyS` database. Then we simulated the orbital evolution of the clone clouds back in time by using the well-tested symplectic integrator `Swift_rmvs3`[8], which we extended by our subroutines modeling the thermal accelerations. We also included analysis subroutines necessary for backward propagation of asteroid pairs, such as the calculation of the mutual distance and relative velocity for a specific couple of clones. Note that our choice of the time step (dt = 3 days) should be sufficient for recording all close encounters. For instance, two clones with relative velocity of $\approx$ 1 m s^{-1} will move away by $\approx$ 260 km in 3 days, which is smaller than the estimated Hill radius of the parent body.

We also studied the spreading time of the primary's clone cloud around the Sun. The result of our test is depicted in the Fig. 4.5. Figure 4.5 clearly shows that during the backward integration, the clones of the primary will completely spread around the Sun in $\approx$ 240 kyr. Note that this period should be undoubtedly shorter for the secondary, because its orbit is less constrained and also affected by stronger thermal perturbations than the primary. It is then important to bear

[6] We do not know the obliquites of the primary and secondary.

[7] With time to the future, where dt is positive.

[8] `http://www.boulder.swri.edu/~hal/swift.html`

in mind that the mean distance between clones increases with time so the chance that a couple of clones will meet our convergent criteria decreases. Thus the traditional method of age determination described in Vokrouhlický and Nesvorný (2008) might prefer young solutions to the older ones.

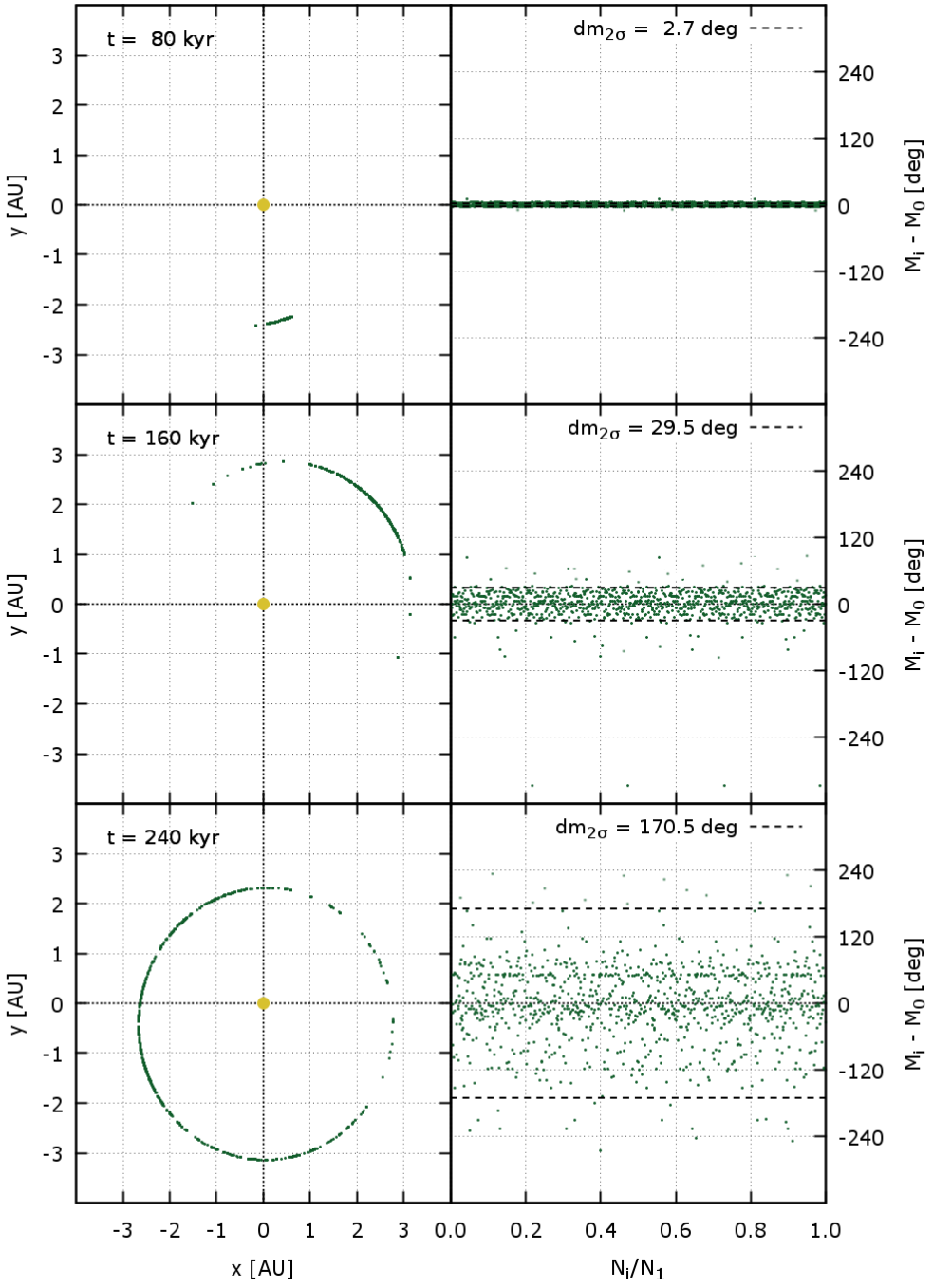

Figure 4.5: Keplerian shear of the clone cloud of the primary (87887) 2000 SS286. In the backward propagation we used $N_1 = 1000$ clones each with a random value da/dt of the Yarkovsky drift (see the text). The three plots correspond to the discrete times 80, 160 and 240 kyr in the past. It is evident, that the clones with mean anomalies M_i are nearly distributed along the whole orbit after 240 kyr. The M_0 and $dm_{2\sigma}$ are the mean value and the 2σ confidence level of the distribution.

To illustrate this point, imagine an asteroid pair which originated hundreds of thousands years ago and whose members experienced a close and slow encounter a few thousands years ago. Due to the Keplerian shear, we would obtain more convergent solutions around the time of the close encounter than around the real age of the pair[9].

However, there is another effect which could influence the distribution of possible ages of an asteroid pair. Let $\delta v(t_1)$, $\delta v(t_2)$ and $\delta r(t_1)$, $\delta r(t_2)$ denote relative velocities and mutual distances of two clones at times t_1 and t_2 in the past. For example, if

$$\delta v(t_1) << \delta v(t_2) < V_{\rm esc} \wedge \delta r(t_1) < R_{\rm Hill} \wedge \delta r(t_2) < R_{\rm Hill} \wedge t_1 < t_2, \qquad (4.2)$$

then both clones remain *longer* together after the time t_1 than t_2. Thus, the classical method of Vokrouhlický and Nesvorný (2008), which controls the convergent criteria in every integration step, might in these specific cases wrongly favour the younger age t_1.

We adopted a different approach and focused our attention only on deep encounters. If the encounter distance of two particular clones was less than a predefined threshold (usually 1-3$R_{\rm Hill}$) and their encounter velocity did not exceed the escape velocity $V_{\rm esc}$ of the parent asteroid, then we recorded their state vectors and the time of convergence. We believe that this modification better reflects the break-up event. After that we investigated the convergent solutions in each time period separately.

Fig. 4.4 shows that during the backward propagation of nominal clones, the first deep encounter occured at $\approx$ 7.42 kyr and after one synodic cycle the clones experienced another close approach at $\approx$ 257 kyr. The same pattern repeats when the clone clouds of the primary and secondary are propagated back in time. We found that for *all* clone combinations, the first deep minima at $\approx$ 7.4 kyr remained roughly the same, while the second took part any time between $\approx$ 50 kyr and $\approx$ 500 kyr (see Fig. 4.6).

Let us first focus on deep encounters in the time interval 7.1 – 7.9 kyr. The encounter velocities of *all* possible clone combinations were less than 0.18 m s^{-1} and some of them even reached extraordinarily small values on the order of mm s^{-1}. The encounter distances varied between $\approx$ 900 km and $\approx$ 4800 km – slightly higher than the characteristic Hill radius of the parent object. Even though they exceed the threshold $R_{\rm Hill}$, we should allow some tolerance (3$R_{\rm Hill}$ in our case), because our propagation model (i) approximates the Yarkovsky acceleration only by the transverse component and (ii) neglects the mutual gravitational interaction between particular clones. We found, that about half of the clone combinations satisfied our liberal limit of 3$R_{\rm Hill}$.

The situation beyond 50 kyr is different. Some of the second deep encounters occured as early as $\approx$ 50 kyr ago. These minima are probably a consequence of clones having extreme Yarkovsky accelerations. Fig. 4.6 clearly shows that there are also many distant solutions ($\geq$ 20000 km) with relative velocities of tens or even hundreds of meters per second. These cases are considered as false. On the other hand, many clones encountered each other at minimal distances smaller than our limit of 3$R_{\rm Hill}$ with relative velocities below $V_{\rm esc}$.

[9]This could be the case of our pair.

Thus, our pair is either very young ($\approx$ 7 kyr) or older than 50 kyr and without further analysis we are not able to decide which solution is the correct one.

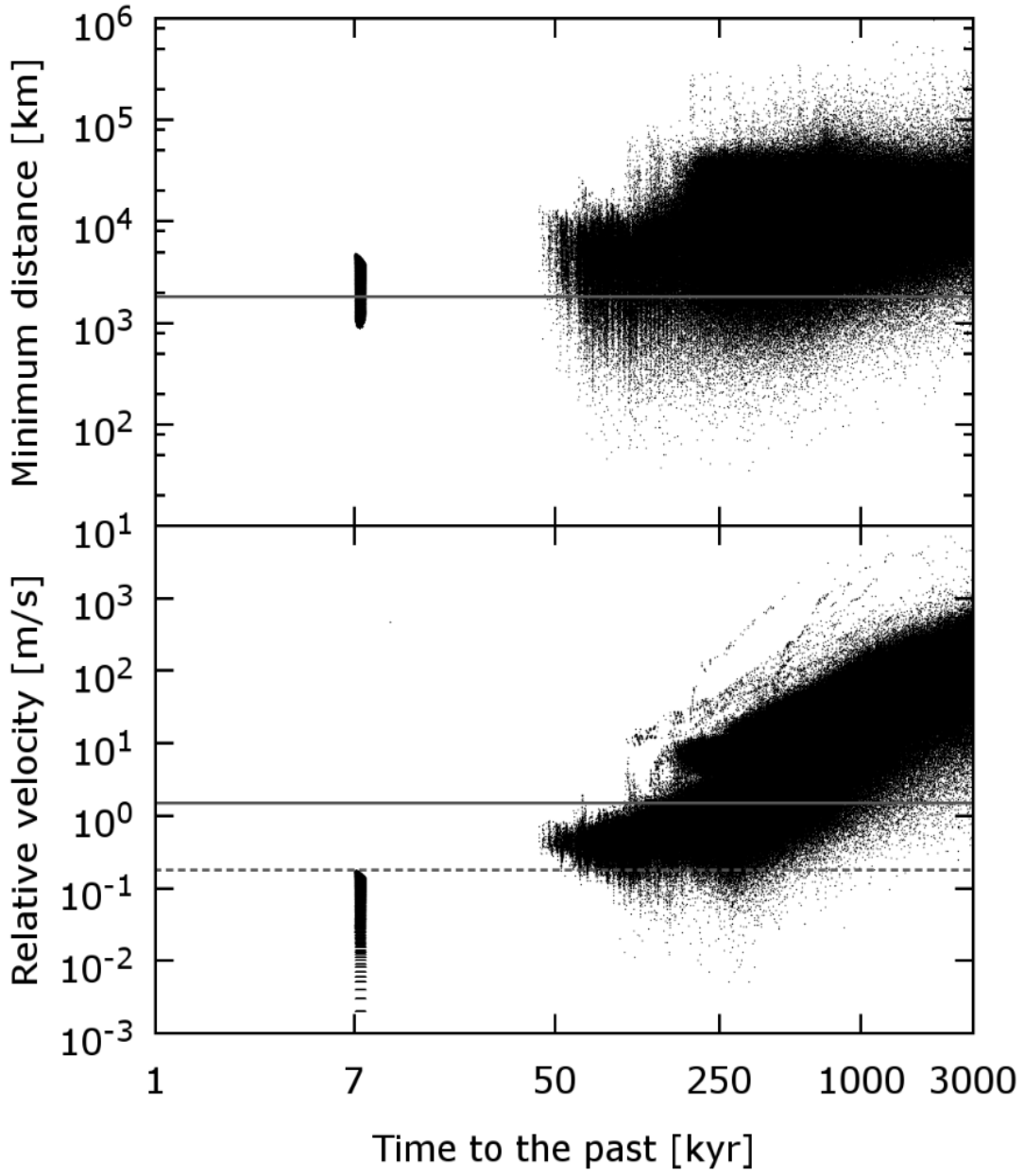

Figure 4.6: *Top:* Encounter distances between clones of the primary and secondary. In total, we investigated all 10^6 clone combinations, while each asteroid was represented by 1000 clones. First deep encounters are well localized at some 7.4 kyr ago, whereas the second deep encounters are spread in time starting from $\approx$ 50 kyr. *Bottom:* Corresponding encounter velocities of the clone pairs from the top panel. During the first close approach, all the pairs had relative velocities smaller than $V_{\rm cut} \approx 0.18$ m s^{-1}. The gray solid lines mark the distance of $3R_{\rm Hill}$ and the escape velocity $V_{\rm esc}$. The dashed line corresponds to the maximal encounter velocity $V_{\rm cut}$. Source: Žižka et al. (2016).

4.4.3 Synthetic pairs

To deal with the true-age problem, we performed a numerical simulation of 240,000 synthetic pairs. In our experiment, each secondary ejected from the primary at $T_0 = 57400.0$ MJD epoch in a random direction with a random separation velocity from the interval $(0, V_{\max})$. We set $V_{\max} = V_{\rm esc}$, where $V_{\rm esc} \approx 1.5$ m s^{-1} is the escape velocity of the parent body. All primaries and secondaries had random Yarkovsky drifts da/dt taken from respective intervals $[-|da/dt|_{\max}, |da/dt|_{\max}]$ (see Section 4.4.2). Then we propagated all synthetic pairs to the future for 3 Myr and focused on *deepest* encounters between the primaries and secondaries, recording their encounter velocities $v_{\rm enc}$. Let us note that in our experiment, mutual gravitational interaction between the components of each synthetic pair was neglected.

Let us introduce the probability $\mathrm{d}P$ that two components which separated with relative velocity $(v_{\rm ej}, v_{\rm ej}+\mathrm{d}v_{\rm ej})$ will encounter with relative velocity $(v_{\rm enc}, v_{\rm enc}+\mathrm{d}v_{\rm enc})$ in time $(t, t+\mathrm{d}t)$ after their separation. Then we can define the asociated probability density function $\rho(v_{\rm ej}; v_{\rm enc}, t)$ by the following formula

$$\mathrm{d}P = \rho(v_{\rm ej}; v_{\rm enc}, t)\, \mathrm{d}v_{\rm ej}\, \mathrm{d}v_{\rm enc}\, \mathrm{d}t, \tag{4.3}$$

where $\rho(v_{\rm ej}; v_{\rm enc}, t)$ must satisfy the normalization condition

$$\int_0^{V_{\max}} \int_0^{\infty} \int_0^{\infty} \rho(v_{\rm ej}; v_{\rm enc}, t)\, \mathrm{d}v_{\rm ej}\, \mathrm{d}v_{\rm enc}\, \mathrm{d}t = 1. \tag{4.4}$$

Note that in practice it is, however, necessary to replace the integral bounds by some sufficiently high values. In real situation it is also impossible to work with infinitesimal quantities and therefore we used their finite realizations, such as

$$dP \to \Delta P_{ijk} \simeq \frac{N_{ijk}(\Delta v_{\rm ej}; \Delta v_{\rm enc}, \Delta t)}{N}, \tag{4.5}$$

where N is the number of all synthetic pairs and $N_{ijk}(\Delta v_{\rm ej}; \Delta v_{\rm enc}, \Delta t)$ is the number of recorded pairs whose components separated with relative velocity $(v_{\rm ej\ i}, v_{\rm ej\ i} + \Delta v_{\rm ej})$ and later, in time $(t_k, t_k + \Delta t)$ after their separation, experienced their *closest* approach with relative velocity $(v_{\rm enc\ j}, v_{\rm enc\ j} + \Delta v_{\rm enc})$. In our model, we sought for the *closest* approach in time interval [0, 3] Myr and used $\Delta v_{\rm ej} = \Delta v_{\rm enc} = 0.04$ m s^{-1} and $\Delta t = 10$ kyr. The indexes i, j, k are positive integers and sample the space of parameters $(v_{\rm ej}, v_{\rm enc}, t)$ with steps $\Delta v_{\rm ej}, \Delta v_{\rm enc}, \Delta t$. The raw data of our simulation are presented in Fig. 4.7. We see two clear trends. First, $v_{\rm enc}$ increases with time due to the cumulative effect of gravitational and thermal perturbations. Second, $v_{\rm enc}$ is in the vast majority of cases higher than $v_{\rm ej}$.

Using the raw data of our numerical experiment, we calculated ΔP_{ijk} for all possible indexes i, j, k. Next, we investigated the probability P that two components which separated with a relative velocity $v_{\rm ej} \in [0, V_{\max}]$ will experience their closest approach within 3 Myr with encounter velocity $v_{\rm enc} \in [0, V_{\rm cut}]$. We set $V_{\max} = V_{\rm esc}$ and $V_{\rm cut} = 0.18$ m s^{-1}, because during the backward propagation of (87887) 2000 SS286 and (415992) 2002 AT49, none of the pair clones exceeded this value ≈ 7.4 kyr ago (see Fig. 4.6).

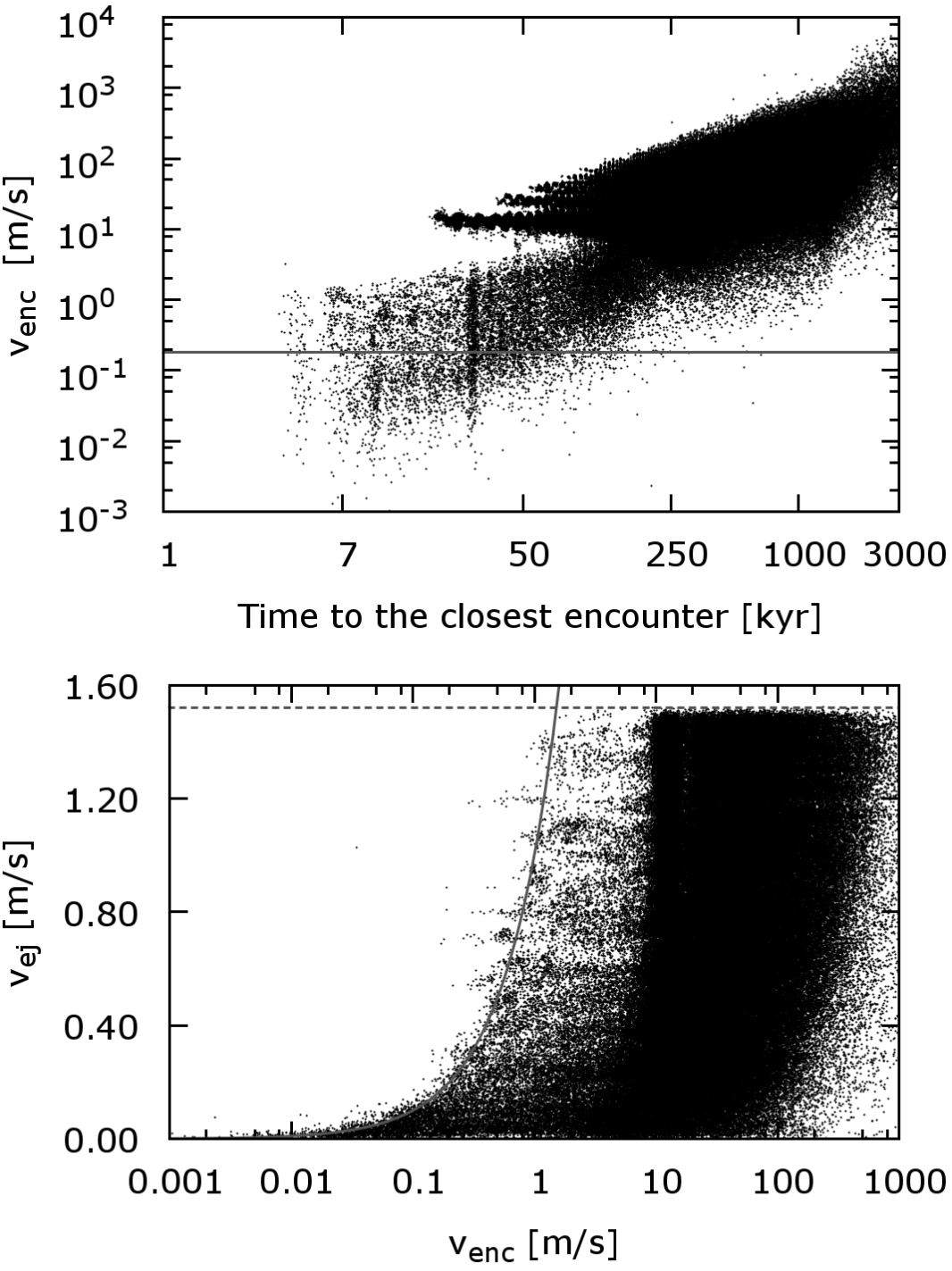

Figure 4.7: Raw data of our numerical experiment with 240,000 synthetic pairs. All pairs formed at $T_0 = 57,400$ MJD epoch and their components separated by a low relative velocity $v_{ej} < V_{esc}$. We propagated each synthetic pair to the future for 3 Myr. After finding the *closest* encounter between its components, we recorded their relative velocity v_{enc} and the time t. *Top:* The dependence of v_{enc} vs. t. The grey line corresponds to the velocity V_{cut} (see the text). *Bottom:* v_{ej} vs. v_{enc}. The dashed line marks the escape velocity V_{esc} and the solid curve represents the border $v_{ej} = v_{enc}$. Taken from Žižka et al. (2016).

The probability P is, in our case, formally given by[10]

$$P = \int_0^{V_{\max}} \int_0^{V_{\text{cut}}} \int_0^{T_{\max}} \rho(v_{\text{ej}}; v_{\text{enc}}, t)\, \mathrm{d}v_{\text{ej}}\, \mathrm{d}v_{\text{enc}}\, \mathrm{d}t, \tag{4.6}$$

where $T_{\max} = 3$ Myr. We evaluated two variants[11] of P:

$$V_{\max} = V_{\text{esc}} \implies P \approx 0.02 = 2\%, \qquad V_{\max} = V_{\text{cut}} \implies P \approx 0.13 = 13\%.$$

For interest, we determined the maximum separation velocity $V_{\max}$ for which the probability P increases to 50%. We obtained $V_{\max} \approx 0.02$ m s^{-1} which is an order of magnitude smaller than expected for pairs in this size category (see Jacobson and Scheeres, 2011a).

From our numerical experiment it is then obvious that if the real primary and secondary separated beyond 50 kyr with relative velocity $v_{\text{ej}} < V_{\text{esc}}$, then the probability that they approached each other ≈ 7.4 kyr ago with encounter velocity $v_{\text{enc}} < V_{\text{cut}}$, is only 2%. However, if we adopt a more strict condition $v_{\text{ej}} < V_{\text{cut}}$, we get $P \approx 13\%$. In other words, the scenario where our pair is older than 50 kyr and both asteroids just experienced close approach ≈ 7.4 kyr ago is rather unlikely. Moreover, in the limits of integration, we did not consider the gap $\Delta T \approx 40 - 50$ kyr which separates the young and old solutions (see Fig. 4.6). So, after substituting the time domain $[0, T_{\max}]$ in (4.6) by $[\Delta T, T_{\max}]$, we get

$$V_{\max} = V_{\text{esc}} \implies P \approx 0.01 = 1\%, \qquad V_{\max} = V_{\text{cut}} \implies P \approx 0.08 = 8\%.$$

4.4.4 The age distribution

Let us investigate encounter conditions at ≈ 7.4 kyr ago. We conducted basically a similar analysis as we did in the case of the pair (6070) Rheinland – (54827) 2001 NQ8 (see Fig. 3.6) and examined the influence of clones' obliquities on the age distribution between 7 - 8 kyr. Let us note that we compared three different subsets of convergent solutions constrained by maximum encounter distances $2R_{\text{Hill}}$, $3R_{\text{Hill}}$ and $8R_{\text{Hill}}$, not finding any difference in final age distributions. Our results are summarized in Tab. 4.2.

$[\cos\gamma_1, \cos\gamma_2]$	T_{age}[kyr]	δT_{age}[kyr]	$P = N_{\text{conv}}/N_{\text{tot}}$
$\cos\gamma_1 > 0,\ \cos\gamma_2 > 0$	7.37	0.09	0.25
$\cos\gamma_1 < 0,\ \cos\gamma_2 > 0$	7.26	0.08	0.25
$\cos\gamma_1 > 0,\ \cos\gamma_2 < 0$	7.62	0.10	0.25
$\cos\gamma_1 < 0,\ \cos\gamma_2 < 0$	7.49	0.10	0.25

Table 4.2: Possible ages of the pair vs. rotational senses of the primary and secondary (see Fig. 4.8) (e.g. $\cos\gamma_1 < 0$ corresponds to the retrograde rotation of the primary). For each rotational state of the real pair, we selected respective convergent clone pairs with encounter distances smaller than $8R_{\text{Hill}} \approx 4800$ km and determined the age $T_{\text{age}} \pm \delta T_{\text{age}}$. P is the fraction of solutions for each variant. Source: Žižka et al. (2016).

[10] We replaced the integral by the sum $P \approx \sum_{i,j,k} P_{ijk}$.

[11] For both cases we recalculated the normalization (4.4) of the density $\rho(v_{\text{ej}}; v_{\text{enc}}, t)$.

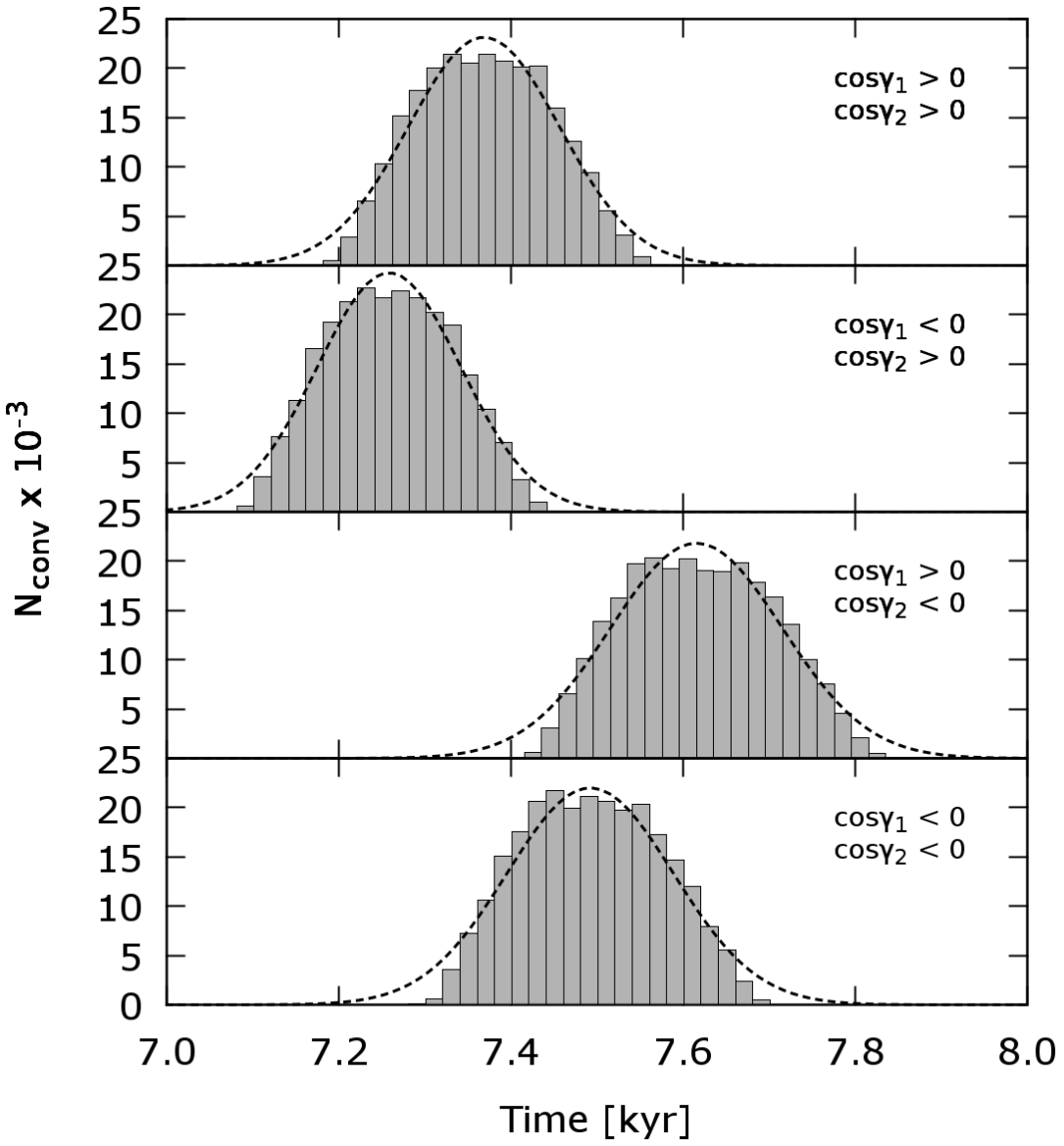

Figure 4.8: Statistical distribution of convergent solutions of the pair (87887) 2000 SS286 – (415992) 2002 AT49 between 7 and 8 kyr in the past. We used all (10^6) clone pairs with the close-approach distances smaller than $\approx 8R_{\mathrm{Hill}}$. The abscissa is the time to the past in kyr, the ordinate gives the number of convergent solutions grouped in 20 yr bins. Each part of the graph shows one of the four possible variants of rotational senses of the primary and secondary. For example, the distribution where $\cos\gamma_1 > 0$ and $\cos\gamma_2 < 0$ corresponds to those convergent clone pairs which represent prograde rotation of the primary and retrograde rotation of the secondary. Source: Žižka et al. (2016).

4.5 Conclusion

With regard to asteroids (87887) 2000 SS286 and (415992) 2002 AT49, it is clear that the determination of the age of asteroid pairs is by no means a simple matter. First of all, it is necessary to take into account both the orbital and thermophysical uncertainties of the individual asteroids and carefully interpret

the resulting distribution of convergent solutions. The asteroid pair (87887) 2000 SS286 – (415992) 2002 AT49 is an obvious example of how a simple statistical processing of the convergent solutions may not reflect the real age of the system. There were two possible solutions of its age – $T_{\rm age} \approx 7.4$ kyr and $T_{\rm age} > 50$ kyr. We found that if the pair had formed later, the components would have to meet at a very low relative velocity (< 0.18 m s^{-1}) ≈ 7.4 kyr ago. This is very unlikely considering the effects of the gravitational and non-gravitational perturbations. The results of our numerical experiments with synthetic pairs suggest that the probability of such a scenario is in the order of a few percent. Thus, asteroids (87887) 2000 SS286 and (415992) 2002 AT49 are very likely the youngest discovered asteroid pair.

This pair also presents many peculiarities. Especially the encounter velocity of both asteroids (in the order of cm s^{-1}) and the absence of convergent solutions under $1R_{\rm Hill}$, even with a larger number of clones, are worth noting. Why do we not observe convergent solutions at distances smaller than $1R_{\rm Hill}$ for such a young pair with exceptionally low encounter velocities of its clones?

A possible cause could be a certain tolerance of our numerical model - especially in the modeling of the Yarkovsky effect with only the transversal component of the Yarkovsky acceleration. On the other hand, we used the same model for other pairs - for example, the pair (6070) Rheinland – (54827) 2001 NQ8, where we did not observe this phenomenon.

Another possible cause could be inaccurately determined nominal orbits of the pair members, or covariance matrices that describe their plausible orbital realizations. Without further observations, this statement cannot be confirmed or refuted.

Last but not least, we suggest that the cause of the absence of convergent solutions under $1R_{\rm Hill}$ might be the presence of another body that influenced the post-disintegration evolution of the primary and secondary. Note that we neglected the mutual gravitational interaction between clones in our simulation due to the very time-consuming calculation. However, it was also neglected in all the other studied pairs, including the pair (6070) Rheinland – (54827) 2001 NQ8.

Another interesting issue is the extent to which the existence of such a young pair corresponds to the collision lifetimes of the main belt asteroids. Bottke et al. (2005) statistically calculated the collision lifetimes $T_{\rm coll}(D)$ of the main belt asteroids, depending on their diameter D. If we choose the diameter of the parent body as $D = 2.5$ km, we get $T_{\rm coll} = 15$ kyr, which is twice as long as the estimated age of our pair. However, if we compare the current number of asteroids which are $2 - 2.5$ km in size with the estimated number according to Bottke et al. (2005), it appears that Bottke et al. (2005) overestimated this number by factor 2. The time scale $T_{\rm coll}$ is then ≈ 30 kyr, which is noticeably longer period than the age of the pair (87887) 2000 SS286 – (415992) 2002 AT49. The pair (87887) 2000 SS286 and (415992) 2002 AT49 then seems unlikely to be of a collision origin. For this reason, we believe that this pair formed by rotational fission of the parent asteroid, a process powered by the YORP effect.

Conclusion

The dissertation presents our results obtained through the modeling of the Yarkovsky/YORP effect and solar radiation pressure on selected asteroids in the Solar System. These non-gravitational perturbations, to a varying extent, change the orbital evolution and rotational states of asteroids, particularly meter-sized to kilometer-sized ones. Whether we look into the future or we are interested in past events, the further we go in time, the more they cumulate and influence the secular orbital evolution of asteroids. In order to gain a deeper understanding of the dynamic evolution of both separate asteroids and asteroid families and pairs, these perturbations need to be taken into account in numerical simulations. Let us briefly conclude the main results of our research and some motivation for future work.

The first chapter contains the theoretical background to the Yarkovsky and YORP effects - the key concepts of the dissertation. We provided examples of their use in the Solar System and also mentioned some asteroids for which these non-gravitational perturbations were first detected and confronted with theory.

Chapter 2 presents our research on the orbital evolution of near-Earth asteroid (99942) Apophis until the year 2029. We investigated the influence of solar radiation pressure on its close-approach distance to Earth in 2029 compared to the Yarkovsky effect. Our motivation for this study were differing views on the given issue published in the literature. We developed numerical models for two types of scattering (Lambert's and Hapke's) and showed that orbital perturbations of Apophis caused by solar radiation pressure are roughly two orders lower than those caused by the Yarkovsky effect. Thus they can be neglected in the first approximation, leading to a significant shortening of the computational time. Let us note that we modeled the shape of Apophis by using random Gaussian spheres. Recently, however, its shape has been determined, so it would be interesting to provide another calculation in the light of these new observations.

In chapter 3, we focused on asteroid families and pairs. We modified the existing algorithm for determining the age of asteroid pairs to be suitable for weakly convergent (or suspect) cases. Using our modification we discovered and estimated the age of seven young pairs with similarly-sized components. Note that they should not exist according to the theory of pair formation. This means either that the sizes of the primaries and/or secondaries of our set were determined inaccurately, or it is necessary to revise the existing theory. Our set could therefore be a worthy target for astronomical observations. The second part of the chapter deals with the well-known pair (6070) Rheinland – (54827) 2001 NQ8. In addition to determining its age, we also investigated rotational states of both asteroids. By using statistical methods, we discovered that the secondary (54827) 2001 NQ8 should exhibit retrograde rotation. This result was later confirmed by photometric observations.

Chapter 4 is monothematic and discusses the asteroid pair (87887) 2000 SS286 — (415992) 2002 AT49. We integrated the orbits of the primary and secondary back in time and revealed that there are two possible solutions of its age - the pair is either older than 50 kyr or younger than 10 kyr. By classic methods, unfortunately, it was not possible to decide which solution was the correct one. Subsequently, we developed and applied a statistical numerical method by which we found that (87887) 2000 SS286 – (415992) 2002 AT49 is very likely the youngest known pair and estimated its age to be ≈ 7.4 kyr. However, we were not able to explain why the clones of the primary and secondary did not meet below $\approx 1R_{\mathrm{Hill}}$ in our simulation. This effect may have been caused either by (i) inaccurately determined nominal orbits of the primary and/or secondary, (ii) the presence of another yet unknown body, or (iii) a certain tolerance of our numerical model of the Yarkovsky effect.

Our attention will also turn to parallel computing, because it might be suitable for many problems related to young asteroid families and pairs. We are currently developing an N-particle symplectic integrator in CUDA C for NVIDIA graphics cards. However, our software is not yet finished and currently is in the testing phase.

Bibliography

Abe, S., Mukai, T., Hirata, N., Barnouin-Jha, O. S., Cheng, A. F., Demura, H., Gaskell, R. W., Hashimoto, T., Hiraoka, K., Honda, T., Kubota, T., Matsuoka, M., Mizuno, T., Nakamura, R., Scheeres, D. J., and Yoshikawa, M. (2006). Mass and local topography measurements of Itokawa by Hayabusa. *Science*, 312:1344–1349.

Adams, J. C. (1853). On the secular variation of the Moon's mean motion. *Monthly Notices of the Royal Astronomical Society*, 14:59–62.

Agol, E., Steffen, J., Sari, R., and Clarkson, W. (2005). On detecting terrestrial planets with timing of giant planet transits. *Monthly Notices of the Royal Astronomical Society*, 359:567–579.

Bancelin, D., Colas, F., Thuillot, W., Hestroffer, D., and Assafin, M. (2012). Asteroid (99942) Apophis: new predictions of Earth encounters for this potentially hazardous asteroid. *Astronomy and Astrophysics*, 544:A15.

Beekman, G. (2006). I. O. Yarkovsky and the discovery of 'his' effect. *Journal for the History of Astronomy*, 37:71–86.

Behrend, R., Damerdji, Y., Reddy, V. V., Gary, B. L., and Correia, H. (2005). (99942) 2004 MN4 combined light-curve. Available on-line at http://obswww.unige.ch/%7Ebehrend/r099942a.png.

Bendjoya, P. and Zappalà, V. (2002). Asteroid family identification. In Bottke, Jr., W. F., Cellino, A., Paolicchi, P., and Binzel, R. P., editors, *Asteroids III*, pages 613–618. Univ. of Arizona Press, Tucson.

Bertotti, B., Farinella, P., and Vokrouhlický, D. (2003). *Physics of the Solar System: Dynamics and Evolution, Space Physics, and Spacetime Structure*. 1. Kluwer Academic Publishers, Dordrecht.

Binzel, R. P. (2003). Planetary science: Spin control for asteroids. *Nature*, 425:131–132.

Boquet, F. (1889). Developpement de la fonction perturbatrice : calcul des termes du huitie ME ordre. *Annales de l'Observatoire de Paris, Memoires*, 19:B1–B75.

Bottke, W. F., Durda, D. D., Nesvorný, D., Jedicke, R., Morbidelli, A., Vokrouhlický, D., and Levison, H. F. (2005). Linking the collisional history of the main asteroid belt to its dynamical excitation and depletion. *Icarus*, 179:63–94.

Bottke, W. F., Jedicke, R., Morbidelli, A., Petit, J.-M., and Gladman, B. (2000a). Understanding the distribution of near-Earth asteroids. *Science*, 288:2190–2194.

Bottke, W. F., Vokrouhlický, D., Brož, M., Nesvorný, D., and Morbidelli, A. (2001). Dynamical spreading of asteroid families by the Yarkovsky effect. *Science*, 294:1693–1696.

Bottke, W. F., Vokrouhlický, D., and Nesvorný, D. (2007). An asteroid breakup 160 Myr ago as the probable source of the K/T impactor. *Nature*, 449:48–53.

Bottke, Jr., W. F., Rubincam, D. P., and Burns, J. A. (2000b). Dynamical evolution of main belt meteoroids: Numerical simulations incorporating planetary perturbations and Yarkovsky thermal forces. *Icarus*, 145:301–331.

Bottke, Jr., W. F., Vokrouhlický, D., Rubincam, D. P., and Nesvorný, D. (2006). The Yarkovsky and YORP effects: Implications for asteroid dynamics. *Annual Review of Earth and Planetary Sciences*, 34:157–191.

Brandt, J. C. (2010). St. Helena, Edmond Halley, the discovery of stellar proper motion, and the mystery of Aldebaran. *Journal of Astronomical History and Heritage*, 13(2):149–158.

Breiter, S. and Michalska, H. (2008). YORP torque as the function of shape harmonics. *Monthly Notices of the Royal Astronomical Society*, 388:927–944.

Breiter, S., Rożek, A., and Vokrouhlický, D. (2012). Stress field and spin axis relaxation for inelastic triaxial ellipsoids. *Monthly Notices of the Royal Astronomical Society*, 427:755–769.

Breiter, S. and Vokrouhlický, D. (2011). Yarkovsky-O'Keefe-Radzievskii-Paddack effect with anisotropic radiation. *Monthly Notices of the Royal Astronomical Society*, 410:2807–2816.

Breiter, S., Vokrouhlický, D., and Nesvorný, D. (2010). Analytical YORP torques model with an improved temperature distribution function. *Monthly Notices of the Royal Astronomical Society*, 401:1933–1949.

Brewster, M. Q. (1992). *Thermal Radiative Transfer and Properties*. A Wiley-Interscience publication. John Wiley & Sons, New York.

Brinker, R. C. and Minnick, R. (1987). *The Surveying Handbook*. 1. Springer Science + Business Media, New York.

Brouwer, D. and Clemence, G. M. (1961). *Methods of Celestial Mechanics*. First Edition. Academic Press Inc., New York.

Brož, M. (2006). *Yarkovsky Effect and the Dynamics of the Solar System*. PhD thesis, Charles University in Prague.

Brož, M. and Morbidelli, A. (2013). The Eos family halo. *Icarus*, 223:844–849.

Brož, M. and Vokrouhlický, D. (2008). Asteroid families in the first-order resonances with Jupiter. *Monthly Notices of the Royal Astronomical Society*, 390:715–732.

Brož, M., Vokrouhlický, D., Roig, F., Nesvorný, D., Bottke, W. F., and Morbidelli, A. (2005). Yarkovsky origin of the unstable asteroids in the 2/1 mean motion resonance with Jupiter. *Monthly Notices of the Royal Astronomical Society*, 359:1437–1455.

Brown, E. W. (1896). *An Introductory Treatise on the Lunar Theory.* The University Press, Cambridge.

Buratti, B. and Veverka, J. (1983). Voyager photometry of Europa. *Icarus*, 55:93–110.

Burns, J. A., Lamy, P. L., and Soter, S. (1979). Radiation forces on small particles in the solar system. *Icarus*, 40:1–48.

Čapek, D. (2007). *Thermal Effects in Physics and Dynamics of Small Bodies of the Solar System.* PhD thesis, Charles University in Prague.

Čapek, D. and Vokrouhlický, D. (2004). The YORP effect with finite thermal conductivity. *Icarus*, 172:526–536.

Čapek, D. and Vokrouhlický, D. (2005). Accurate model for the Yarkovsky effect. In Knežević, Z. and Milani, A., editors, *IAU Colloq. 197: Dynamics of Populations of Planetary Systems*, pages 171–178.

Carruba, V. (2009). The (not so) peculiar case of the Padua family. *Monthly Notices of the Royal Astronomical Society*, 395:358–377.

Carruba, V., Domingos, R. C., Nesvorný, D., Roig, F., Huaman, M. E., and Souami, D. (2013). A multidomain approach to asteroid families' identification. *Monthly Notices of the Royal Astronomical Society*, 433:2075–2096.

Carruba, V. and Morbidelli, A. (2011). On the first ν_6 anti-aligned librating asteroid family of Tina. *Monthly Notices of the Royal Astronomical Society*, 412:2040–2051.

Carry, B. (2012). Density of asteroids. *Planetary and Space Science*, 73:98–118.

Chapront-Touze, M. and Chapront, J. (1983). The lunar ephemeris ELP 2000. *Astronomy and Astrophysics*, 124(1):50–62.

Chesley, S. R. (2006). Potential impact detection for near-Earth asteroids: the case of 99942 Apophis (2004 MN4). In Lazzaro, D., Ferraz-Mello, S., and Fernández, J., editors, *Asteroids, Comets, Meteors*, volume 229 of *IAU Symposium*, pages 215–228, Cambridge. Cambridge University Press.

Chesley, S. R., Farnocchia, D., Nolan, M. C., Vokrouhlický, D., Chodas, P. W., Milani, A., Spoto, F., Rozitis, B., Benner, L. A. M., Bottke, W. F., Busch, M. W., Emery, J. P., Howell, E. S., Lauretta, D. S., Margot, J.-L., and Taylor, P. A. (2014). Orbit and bulk density of the OSIRIS-REx target asteroid (101955) Bennu. *Icarus*, 235:5–22.

Chesley, S. R., Farnocchia, D., Pravec, P., and Vokrouhlický, D. (2016). Direct detections of the Yarkovsky effect: Status and outlook. In Chesley, S. R., Morbidelli, A., Jedicke, R., and Farnocchia, D., editors, *Asteroids: New Observations, New Models*, volume 318 of *IAU Symposium*, pages 250–258.

Chesley, S. R., Milani, A., Tholen, D., Bernardi, F., Chodas, P., and Micheli, M. (2009). An updated assessment of the impact threat from (99942) Apophis. In *AAS/Division for Planetary Sciences Meeting Abstracts #41*, volume 41 of *AAS/Division for Planetary Sciences Meeting Abstracts*, page 43.06.

Chesley, S. R., Ostro, S. J., Vokrouhlický, D., Čapek, D., Giorgini, J. D., Nolan, M. C., Margot, J.-L., Hine, A. A., Benner, L. A. M., and Chamberlin, A. B. (2003). Direct detection of the Yarkovsky effect by radar ranging to asteroid 6489 Golevka. *Science*, 302:1739–1742.

Chesley, S. R., Vokrouhlický, D., Ostro, S. J., Benner, L. A. M., Margot, J.-L., Matson, R. L., Nolan, M. C., and Shepard, M. K. (2008). Direct estimation of Yarkovsky accelerations on near-Earth asteroids. In *Asteroids, Comets, Meteors 2008*, volume 1405 of *LPI Contributions*, page 8330.

Chodas, P. W. (1999). Orbit uncertainties, keyholes, and collision probabilities. In *Bulletin of the American Astronomical Society*, volume 31 of *Bulletin of the Astronomical Society*, page 1117.

Chrenko, O., Brož, M., Nesvorný, D., Tsiganis, K., and Skoulidou, D. K. (2015). The origin of long-lived asteroids in the 2:1 mean-motion resonance with Jupiter. *Monthly Notices of the Royal Astronomical Society*, 451:2399–2416.

Cohen, C. J. and Hubbard, E. C. (1965). Libration of the close approaches of Pluto to Neptune. *Astronomical Journal*, 70:10–13.

Ćuk, M. and Burns, J. A. (2005). Effects of thermal radiation on the dynamics of binary NEAs. *Icarus*, 176:418–431.

Danby, J. M. A. (1992). *Fundamentals of celestial mechanics*. Willman-Bell, Richmond, VA, second edition.

D'Angelo, G. and Bodenheimer, P. (2016). In situ and ex situ formation models of Kepler 11 planets. *The Astrophysical Journal*, 828:33.

D'Angelo, G. and Lubow, S. H. (2008). Evolution of migrating planets undergoing gas accretion. *The Astrophysical Journal*, 685:560–583.

Delbo', M., Cellino, A., and Tedesco, E. F. (2007a). Albedo and size determination of potentially hazardous asteroids: (99942) Apophis. *Icarus*, 188:266–269.

Delbo', M., Dell'Oro, A., Harris, A. W., Mottola, S., and Mueller, M. (2007b). Thermal inertia of near-Earth asteroids and implications for the magnitude of the Yarkovsky effect. *Icarus*, 190:236–249.

Delbo', M., Nesvorný, D., Licandro, J., and Ali-Lagoa, V. (2012). New analysis of the Baptistina asteroid family: Implications for its link with the K/T impactor. In *AAS/Division for Planetary Sciences Meeting Abstracts*, volume 44 of *AAS/Division for Planetary Sciences Meeting Abstracts*, page 202.01.

Deprit, A., Henrard, J., and Rom, A. (1971). Analytical lunar ephemeris: Delaunay's theory. *Astronomical Journal*, 76:269–272.

Dobrovolskis, A. R. (1996). Inertia of any polyhedron. *Icarus*, 124:698–704.

Doody, D. (2009). *Deep Space Craft: An Overview of Interplanetary Flight*. Springer, Berlin.

Duncan, M., Quinn, T., and Tremaine, S. (1987). The formation and extent of the solar system comet cloud. *Astronomical Journal*, 94:1330–1338.

Durda, D. D., Bottke, W. F., Enke, B. L., Merline, W. J., Asphaug, E., Richardson, D. C., and Leinhardt, Z. M. (2004). The formation of asteroid satellites in large impacts: results from numerical simulations. *Icarus*, 170:243–257.

Ďurech, J., Vokrouhlický, D., Baransky, A. R., Breiter, S., Burkhonov, O. A., Cooney, W., Fuller, V., Gaftonyuk, N. M., Gross, J., Inasaridze, R. Y., Kaasalainen, M., Krugly, Y. N., Kvaratshelia, O. I., Litvinenko, E. A., Macomber, B., Marchis, F., Molotov, I. E., Oey, J., Polishook, D., Pollock, J., Pravec, P., Sárneczky, K., Shevchenko, V. G., Slyusarev, I., Stephens, R., Szabó, G., Terrell, D., Vachier, F., Vanderplate, Z., Viikinkoski, M., and Warner, B. D. (2012). Analysis of the rotation period of asteroids (1865) Cerberus, (2100) Ra-Shalom, and (3103) Eger - search for the YORP effect. *Astronomy and Astrophysics*, 547:A10.

Ďurech, J., Vokrouhlický, D., Kaasalainen, M., Higgins, D., Krugly, Y. N., Gaftonyuk, N. M., Shevchenko, V. G., Chiorny, V. G., Hamanowa, H., Hamanowa, H., Reddy, V., and Dyvig, R. R. (2008a). Detection of the YORP effect in asteroid (1620) Geographos. *Astronomy and Astrophysics*, 489:L25–L28.

Ďurech, J., Vokrouhlický, D., Kaasalainen, M., Weissman, P., Lowry, S. C., Beshore, E., Higgins, D., Krugly, Y. N., Shevchenko, V. G., Gaftonyuk, N. M., Choi, Y.-J., Kowalski, R. A., Larson, S., Warner, B. D., Marshalkina, A. L., Ibrahimov, M. A., Molotov, I. E., Michałowski, T., and Kitazato, K. (2008b). New photometric observations of asteroids (1862) Apollo and (25143) Itokawa - an analysis of YORP effect. *Astronomy and Astrophysics*, 488:345–350.

Eckert, W. J. and Smith, H. F. (1966a). The equations of variation in a numerical lunar theory. *Symposium - International Astronomical Union. 1966.*, 25:242–260.

Eckert, W. J. and Smith, H. F. (1966b). The solution of the main problem of the lunar theory by the method of Airy. *Astron. Pap., U.S. Naval Obs.*, 19:187–407.

Edgeworth, K. E. (1943). The evolution of our planetary system. *Journal of the British Astronomical Association*, 53:181–188.

Farinella, P., Vokrouhlický, D., and Hartmann, W. K. (1998). Meteorite delivery via Yarkovsky orbital drift. *Icarus*, 132:378–387.

Farnocchia, D., Chesley, S. R., Chodas, P. W., Micheli, M., Tholen, D. J., Milani, A., Elliott, G. T., and Bernardi, F. (2013a). Yarkovsky-driven impact risk analysis for asteroid (99942) Apophis. *Icarus*, 224:192–200.

Farnocchia, D., Chesley, S. R., Vokrouhlický, D., Milani, A., Spoto, F., and Bottke, W. F. (2013b). Near Earth asteroids with measurable Yarkovsky effect. *Icarus*, 224:1–13.

Galád, A. (2012). Effect of main belt perturbers on asteroid-pair age estimation. *Astronomy & Astrophysics*, 548:A25.

Galád, A., Vokrouhlický, D., and Žižka, J. (2014). Prospective very young asteroid pairs. In Muinonen, K., Penttilä, A., Granvik, M., Virkki, A., Fedorets, G., Wilkman, O., and Kohout, T., editors, *Asteroids, Comets, Meteors 2014*.

Gentle, J. (2006). *Random Number Generation and Monte Carlo Methods*. Statistics and Computing. Springer.

Gilmore, A. C., Kilmartin, P. M., Young, J., McGaha, J. E., Garradd, G. J., Beshore, E. C., Casey, C. M., Christensen, E. J., Hill, R. E., Larson, S. M., McNaught, R. H., and Smalley, K. E. (2004). 2004 MN4. *Minor Planet Electronic Circulars*, 2004-Y25.

Giorgini, J. D., Benner, L. A. M., Ostro, S. J., Nolan, M. C., and Busch, M. W. (2008). Predicting the Earth encounters of (99942) Apophis. *Icarus*, 193:1–19.

Gleason, A. E., Larsen, J. A., Descour, A. S., and Williams, G. V. (2004). 2004 MN4. *Minor Planet Electronic Circulars*, 2004-Y70.

Golubov, O., Kravets, Y., Krugly, Y. N., and Scheeres, D. J. (2016). Physical models for the normal YORP and diurnal Yarkovsky effects. *Monthly Notices of the Royal Astronomical Society*, 458:3977–3989.

Golubov, O. and Krugly, Y. N. (2012). Tangential component of the YORP effect. *The Astrophysical Journal Letters*, 752:L11.

Golubov, O., Scheeres, D. J., and Krugly, Y. N. (2014). A three-dimensional model of tangential YORP. *The Astrophysical Journal*, 794:22.

Gomes, R., Levison, H. F., Tsiganis, K., and Morbidelli, A. (2005). Origin of the cataclysmic Late Heavy Bombardment period of the terrestrial planets. *Nature*, 435:466–469.

Greenberg, R., Bottke, W. F., Nolan, M., Geissler, P., Petit, J.-M., Durda, D. D., Asphaug, E., and Head, J. (1996). Collisional and dynamical history of Ida. *Icarus*, 120:106–118.

Gutzwiller, M. C. (1998). Moon-Earth-Sun: The oldest three-body problem. *Reviews of Modern Physics*, 70(2):589–639.

Hanuš, J., Ďurech, J., Brož, M., Marciniak, A., Warner, B. D., Pilcher, F., Stephens, R., Behrend, R., Carry, B., Čapek, D., Antonini, P., Audejean, M., Augustesen, K., Barbotin, E., Baudouin, P., Bayol, A., Bernasconi, L., Borczyk, W., Bosch, J.-G., Brochard, E., Brunetto, L., Casulli, S., Cazenave, A., Charbonnel, S., Christophe, B., Colas, F., Coloma, J., Conjat, M., Cooney, W., Correira, H., Cotrez, V., Coupier, A., Crippa, R., Cristofanelli, M., Dalmas, C., Danavaro, C., Demeautis, C., Droege, T., Durkee, R., Esseiva, N.,

Esteban, M., Fagas, M., Farroni, G., Fauvaud, M., Fauvaud, S., Del Freo, F., Garcia, L., Geier, S., Godon, C., Grangeon, K., Hamanowa, H., Hamanowa, H., Heck, N., Hellmich, S., Higgins, D., Hirsch, R., Husarik, M., Itkonen, T., Jade, O., Kamiński, K., Kankiewicz, P., Klotz, A., Koff, R. A., Kryszczyńska, A., Kwiatkowski, T., Laffont, A., Leroy, A., Lecacheux, J., Leonie, Y., Leyrat, C., Manzini, F., Martin, A., Masi, G., Matter, D., Michałowski, J., Michałowski, M. J., Michałowski, T., Michelet, J., Michelsen, R., Morelle, E., Mottola, S., Naves, R., Nomen, J., Oey, J., Ogłoza, W., Oksanen, A., Oszkiewicz, D., Pääkkönen, P., Paiella, M., Pallares, H., Paulo, J., Pavic, M., Payet, B., Polińska, M., Polishook, D., Poncy, R., Revaz, Y., Rinner, C., Rocca, M., Roche, A., Romeuf, D., Roy, R., Saguin, H., Salom, P. A., Sanchez, S., Santacana, G., Santana-Ros, T., Sareyan, J.-P., Sobkowiak, K., Sposetti, S., Starkey, D., Stoss, R., Strajnic, J., Teng, J.-P., Trégon, B., Vagnozzi, A., Velichko, F. P., Waelchli, N., Wagrez, K., and Wücher, H. (2013). Asteroids' physical models from combined dense and sparse photometry and scaling of the YORP effect by the observed obliquity distribution. *Astronomy and Astrophysics*, 551:A67.

Hapke, B. (1981). Bidirectional reflectance spectroscopy. I - Theory. *Journal of Geophysical Research*, 86:3039–3054.

Hapke, B. (1984). Bidirectional reflectance spectroscopy. III - Correction for macroscopic roughness. *Icarus*, 59:41–59.

Hapke, B. (1986). Bidirectional reflectance spectroscopy. IV - The extinction coefficient and the opposition effect. *Icarus*, 67:264–280.

Hapke, B. (2002). Bidirectional reflectance spectroscopy. 5. The coherent backscatter opposition effect and anisotropic scattering. *Icarus*, 157:523–534.

Hapke, B. (2008). Bidirectional reflectance spectroscopy. 6. Effects of porosity. *Icarus*, 195:918–926.

Hapke, B. (2012). Bidirectional reflectance spectroscopy 7. The single particle phase function hockey stick relation. *Icarus*, 221:1079–1083.

Hapke, B. (2012). *Theory of Reflectance and Emittance Spectroscopy*. Cambridge University Press, New York, second edition.

Harris, A. W. (1994). Tumbling asteroids. *Icarus*, 107:209.

Harris, A. W., Young, J. W., Bowell, E., Martin, L. J., Millis, R. L., Poutanen, M., Scaltriti, F., Zappala, V., Schober, H. J., Debehogne, H., and Zeigler, K. W. (1989). Photoelectric observations of asteroids 3, 24, 60, 261, and 863. *Icarus*, 77:171–186.

Heath, T. (1913). *Aristarchus of Samos the ancient Copernicus*. Clarendon press, Oxford.

Helfenstein, P. and Shepard, M. K. (2011). Testing the Hapke photometric model: Improved inversion and the porosity correction. *Icarus*, 215:83–100.

Helfenstein, P. and Veverka, J. (1989). Physical characterization of asteroid surfaces from photometric analysis. In Binzel, R. P., Gehrels, T., and Matthews, M. S., editors, *Asteroids II*, pages 557–593, Tucson. Arizona University Press.

Hirayama, K. (1918). Groups of asteroids probably of common origin. *Astronomical Journal*, 31:185–188.

Hirayama, K. (1922). Families of asteroids. *Japanese Journal of Astronomy and Geophysics*, 1:55.

Holman, M. J. and Murray, N. W. (2005). The use of transit timing to detect terrestrial-mass extrasolar planets. *Science*, 307:1288–1291.

Huygens, C. (1690). *Traitée de la Lumière*. Pieter van der Aa, Leiden.

Ivezić, Ž., Tabachnik, S., Rafikov, R., Lupton, R. H., Quinn, T., Hammergren, M., Eyer, L., Chu, J., Armstrong, J. C., Fan, X., Finlator, K., Geballe, T. R., Gunn, J. E., Hennessy, G. S., Knapp, G. R., Leggett, S. K., Munn, J. A., Pier, J. R., Rockosi, C. M., Schneider, D. P., Strauss, M. A., Yanny, B., Brinkmann, J., Csabai, I., Hindsley, R. B., Kent, S., Lamb, D. Q., Margon, B., McKay, T. A., Smith, J. A., Waddel, P., York, D. G., and SDSS Collaboration (2001). Solar system objects observed in the Sloan Digital Sky Survey commissioning data. *The Astronomical Journal*, 122:2749–2784.

Jacobson, S. A. and Scheeres, D. J. (2011a). Dynamics of rotationally fissioned asteroids: Source of observed small asteroid systems. *Icarus*, 214:161–178.

Jacobson, S. A. and Scheeres, D. J. (2011b). Long-term stable equilibria for synchronous binary asteroids. *The Astrophysical Journal Letters*, 736:L19.

Jedicke, R. and Metcalfe, T. S. (1998). The orbital and absolute magnitude distributions of main belt asteroids. *Icarus*, 131:245–260.

Jewitt, D. and Luu, J. (1993). Discovery of the candidate Kuiper belt object 1992 QB1. *Nature*, 362:730–732.

Kaasalainen, M. (2001). Interpretation of lightcurves of precessing asteroids. *Astronomy and Astrophysics*, 376:302–309.

Kaasalainen, M. and Torppa, J. (2001). Optimization methods for asteroid lightcurve inversion. I. Shape determination. *Icarus*, 153:24–36.

Kaasalainen, M., Torppa, J., and Muinonen, K. (2001). Optimization methods for asteroid lightcurve inversion. II. The complete inverse problem. *Icarus*, 153:37–51.

Kaasalainen, M., Ďurech, J., Warner, B. D., Krugly, Y. N., and Gaftonyuk, N. M. (2007). Acceleration of the rotation of asteroid 1862 Apollo by radiation torques. *Nature*, 446:420–422.

Kepler, J. (1609). *Astronomia nova*. Heidelberg.

Kinoshita, H. and Nakai, H. (1984). Motions of the perihelions of Neptune and Pluto. *Celestial Mechanics*, 34:203–217.

Kirkwood, D. (1867). *Meteoric Astronomy: a treatise on shooting-stars, fire-balls, and aerolites*. Lippincott & Co., Philadelphia.

Knežević, Z., Lemaître, A., and Milani, A. (2002). The determination of asteroid proper elements. In Bottke, Jr., W. F., Cellino, A., Paolicchi, P., and Binzel, R. P., editors, *Asteroids III*, pages 603–612. Univ. of Arizona Press, Tucson.

Knežević, Z. and Milani, A. (2000). Synthetic proper elements for outer main belt asteroids. *Celestial Mechanics and Dynamical Astronomy*, 78:17–46.

Kowal, C. T., Liller, W., and Marsden, B. G. (1979). The discovery and orbit of /2060/ Chiron. In Duncombe, R. L., editor, *Dynamics of the Solar System*, volume 81 of *IAU Symposium*, pages 245–250.

Kruse, R. (2006-2011). Historic spacecraft, url: `http://www.historicspacecraft.com`.

Kuiper, G. P. (1951). On the origin of the Solar System. *Proceedings of the National Academy of Sciences*, 37(1):1–14.

La Spina, A., Paolicchi, P., Kryszczyńska, A., and Pravec, P. (2004). Retrograde spins of near-Earth asteroids from the Yarkovsky effect. *Nature*, 428:400–401.

Lagerros, J. S. V. (1996a). Thermal physics of asteroids. I. Effects of shape, heat conduction and beaming. *Astronomy and Astrophysics*, 310.

Lagerros, J. S. V. (1996b). Thermal physics of asteroids. II. Polarization of the thermal microwave emission from asteroids. *Astronomy and Astrophysics*, 315:625–632.

Lagerros, J. S. V. (1997). Thermal physics of asteroids. III. Irregular shapes and albedo variegations. *Astronomy and Astrophysics*, 325:1226–1236.

Lagerros, J. S. V. (1998). Thermal physics of asteroids. IV. Thermal infrared beaming. *Astronomy and Astrophysics*, 332:1123–1132.

Lambert, J. H. (1759). *La perspective affranchie de l'embaras du Plan géometral*. Chez Heidegguer et Comp, Zurich.

Laskar, J. (1988). Secular evolution of the solar system over 10 million years. *Astronomy and Astrophysics*, 198:341–362.

Laskar, J. (1994). Large scale chaos in the solar system. *Astronomy and Astrophysics*, 287:L9–12.

Laskar, J. and Gastineau, M. (2009). Existence of collisional trajectories of Mercury, Mars and Venus with the Earth. *Nature*, 459:817–819.

Le Verrier, U.-J. (1855). Développement de la fonction qui sert de base au calcul des perturbations des mouvements des planètes. *Annales de l'Observatoire de Paris*, 1:258–342.

Levison, H. F. and Duncan, M. J. (1994). The long-term dynamical behavior of short-period comets. *Icarus*, 108:18–36.

Levison, H. F. and Morbidelli, A. (2003). The formation of the Kuiper belt by the outward transport of bodies during Neptune's migration. *Nature*, 426:419–421.

Li, J.-Y., Helfenstein, P., Buratti, B., Takir, D., and Clark, B. E. (2015). Asteroid Photometry. In Michel, P., DeMeo, F. E., and Bottke, W. F., editors, *Asteroids IV*, Space Science Series, pages 129–150. University of Arizona Press, Tucson.

Licandro, J., Müller, T., Alvarez, C., Alí-Lagoa, V., and Delbo', M. (2016). GTC/CanariCam observations of (99942) Apophis. *Astronomy and Astrophysics*, 585:A10.

Lowry, S. C., Fitzsimmons, A., Pravec, P., Vokrouhlický, D., Boehnhardt, H., Taylor, P. A., Margot, J.-L., Galád, A., Irwin, M., Irwin, J., and Kusnirák, P. (2007). Direct detection of the asteroidal YORP effect. *Science*, 316:272.

Lowry, S. C., Weissman, P. R., Duddy, S. R., Rozitis, B., Fitzsimmons, A., Green, S. F., Hicks, M. D., Snodgrass, C., Wolters, S. D., Chesley, S. R., Pittichová, J., and van Oers, P. (2014). The internal structure of asteroid (25143) Itokawa as revealed by detection of YORP spin-up. *Astronomy and Astrophysics*, 562:A48.

Lumme, K. and Bowell, E. (1981). Radiative transfer in the surfaces of atmosphereless bodies. I - Theory. II - Interpretation of phase curves. *Astronomical Journal*, 86:1694–1721.

Mainzer, A., Grav, T., Masiero, J., Hand, E., Bauer, J., Tholen, D., McMillan, R. S., Spahr, T., Cutri, R. M., Wright, E., Watkins, J., Mo, W., and Maleszewski, C. (2011). NEOWISE Studies of spectrophotometrically classified asteroids: Preliminary results. *The Astrophysical Journal*, 741:90–115.

Malhotra, R. (1993). The origin of Pluto's peculiar orbit. *Nature*, 365:819–821.

Malhotra, R. (1995). The origin of Pluto's orbits: implications for the solar system beyond Neptune. *Astronomical Journal*, 110:420–429.

Marsden, B. G., Sekanina, Z., and Yeomans, D. K. (1973). Comets and nongravitational forces. V. *Astronomical Journal*, 78:211.

Marzari, F., Farinella, P., and Davis, D. R. (1999). Origin, aging, and death of asteroid families. *Icarus*, 142:63–77.

Masiero, J. R., Mainzer, A. K., Bauer, J. M., Grav, T., Nugent, C. R., and Stevenson, R. (2013). Asteroid family identification using the hierarchical clustering method and WISE/NEOWISE physical properties. *The Astrophysical Journal*, 770:7–29.

Masiero, J. R., Mainzer, A. K., Grav, T., Bauer, J. M., and Jedicke, R. (2012). Revising the age for the Baptistina asteroid family using WISE/NEOWISE data. *The Astrophysical Journal*, 759:14.

Mayor, M. and Queloz, D. (1995). A Jupiter-mass companion to a solar-type star. *Nature*, 378:355–359.

McMahon, J. and Scheeres, D. (2010). Secular orbit variation due to solar radiation effects: a detailed model for BYORP. *Celestial Mechanics and Dynamical Astronomy*, 106:261–300.

Mihalas, D. (1978). *Stellar atmospheres*. W.H. Freeman, San Francisco.

Milani, A., Cellino, A., Knežević, Z., Novaković, B., Spoto, F., and Paolicchi, P. (2014). Asteroid families classification: Exploiting very large datasets. *Icarus*, 239:46–73.

Milani, A. and Gronchi, G. (2010). *Theory of Orbit Determination*. Cambridge University Press, Cambridge.

Milani, A. and Knežević, Z. (1990). Secular perturbation theory and computation of asteroid proper elements. *Celestial Mechanics and Dynamical Astronomy*, 49:347–411.

Milani, A. and Knežević, Z. (1994). Asteroid proper elements and the dynamical structure of the asteroid main belt. *Icarus*, 107:219–254.

Milani, A., Sansaturio, M. E., Tommei, G., Arratia, O., and Chesley, S. R. (2005). Multiple solutions for asteroid orbits: Computational procedure and applications. *Astronomy and Astrophysics*, 431:729–746.

Minnaert, M. (1941). The reciprocity principle in lunar photometry. *Astrophysical Journal*, 93:403–410.

Morbidelli, A., Levison, H. F., Tsiganis, K., and Gomes, R. (2005). Chaotic capture of Jupiter's Trojan asteroids in the early Solar System. *Nature*, 435:462–465.

Morbidelli, A. and Vokrouhlický, D. (2003). The Yarkovsky-driven origin of near-Earth asteroids. *Icarus*, 163:120–134.

Moulton, F. R. (2012). *An Introduction to Celestial Mechanics*. Dover Books on Astronomy. Dover Publications, Inc., New York.

Muinonen, K. (1998). Introducing the Gaussian shape hypothesis for asteroids and comets. *Astronomy and Astrophysics*, 332:1087–1098.

Muinonen, K. and Lagerros, J. S. V. (1998). Inversion of shape statistics for small solar system bodies. *Astronomy and Astrophysics*, 333:753–761.

Müller, T. G., Kiss, C., Scheirich, P., Pravec, P., O'Rourke, L., Vilenius, E., and Altieri, B. (2014). Thermal infrared observations of asteroid (99942) Apophis with Herschel. *Astronomy and Astrophysics*, 566:A22.

Murdin, P. (2009). *Full meridian of glory*. 1. Copernicus Books/Springer, New York.

Murray, C. D. and Dermott, S. F. (1999). *Solar System Dynamics*. 1. Cambridge University Press, Cambridge.

Neiman, V. B., Romanov, E. M., and Chernov, V. M. (1965). Ivan Osipovich Yarkovsky [in Russian]. *Zeml'ya Vselennaya (Earth and Universe)*, 4:63–64.

Nesvorný, D. (2015). Evidence for slow migration of Neptune from the inclination distribution of Kuiper belt objects. *The Astronomical Journal*, 150:73.

Nesvorný, D. and Bottke, W. F. (2004). Detection of the Yarkovsky effect for main-belt asteroids. *Icarus*, 170:324–342.

Nesvorný, D., Bottke, W. F., Levison, H. F., and Dones, L. (2003). Recent origin of the solar system dust bands. *The Astrophysical Journal*, 591:486–497.

Nesvorný, D., Bottke, W. F., Vokrouhlický, D., Morbidelli, A., and Jedicke, R. (2006a). Asteroid families. In Daniela, L., Sylvio Ferraz, M., and Angel, F. J., editors, *Asteroids, Comets, Meteors*, volume 229 of *IAU Symposium*, pages 289–299.

Nesvorný, D., Bottke, Jr., W. F., Dones, L., and Levison, H. F. (2002). The recent breakup of an asteroid in the main-belt region. *Nature*, 417:720–771.

Nesvorný, D., Brož, M., and Carruba, V. (2015). Identification and dynamical properties of asteroid families. In Michel, P., DeMeo, F. E., and Bottke, W. F., editors, *Asteroids IV*, Space Science Series, pages 297–321. University of Arizona Press, Tucson.

Nesvorný, D., Enke, B. L., Bottke, W. F., Durda, D. D., Asphaug, E., and Richardson, D. C. (2006b). Karin cluster formation by asteroid impact. *Icarus*, 183:296–311.

Nesvorný, D., Jedicke, R., Whiteley, R. J., and Ivezić, Ž. (2005). Evidence for asteroid space weathering from the Sloan Digital Sky Survey. *Icarus*, 173:132–152.

Nesvorný, D. and Morbidelli, A. (1998). Three-body mean motion resonances and the chaotic structure of the asteroid belt. *The Astronomical Journal*, 116:3029–3037.

Nesvorný, D. and Morbidelli, A. (2008). Mass and orbit determination from transit timing variations of exoplanets. *The Astrophysical Journal*, 688:636–646.

Nesvorný, D. and Vokrouhlický, D. (2006). New candidates for recent asteroid breakups. *The Astronomical Journal*, 132:1950–1958.

Nesvorný, D. and Vokrouhlický, D. (2007). Analytic theory of the YORP effect for near-spherical objects. *The Astronomical Journal*, 134:1750.

Nesvorný, D. and Vokrouhlický, D. (2008). Analytic theory for the Yarkovsky-O effect on obliquity. *The Astronomical Journal*, 136:291–299.

Nesvorný, D., Vokrouhlický, D., and Bottke, W. F. (2006c). The breakup of a main-belt asteroid 450 thousand years ago. *Science*, 312:1490.

Newcomb, S. (1895). A development of the perturbative function in cosines of multiples of the mean anomalies and of angles of multiples of the mean anomalies and of angles between the perihelia and common node and in powers of the eccentricities and mutual inclination. *Astronomical Papers American Ephemeris*, 5:1–48.

Novaković, B., Hsieh, H. H., Cellino, A., Micheli, M., and Pedani, M. (2014). Discovery of a young asteroid cluster associated with P/2012 F5 (Gibbs). *Icarus*, 231:300–309.

Nugent, C. R., Margot, J. L., Chesley, S. R., and Vokrouhlický, D. (2012). Detection of semimajor axis drifts in 54 near-Earth asteroids: New measurements of the Yarkovsky effect. *The Astronomical Journal*, 144:60.

O'Keefe, J. A. (1976). *Tektites and Their Origin*. Developments in petrology, No. 4. Elsevier Scientific Publishing Company, Amsterdam.

Olmsted, J. W. (1942). *The scientific expedition of Jean Richer to Cayenne (1672-1673)*. History of Science Society.

Öpik, E. J. (1951). Collision probabilities with the planets and the distribution of interplanetary matter. *Proc. R. Irish Acad. Sect. A*, 54:165–199.

Öpik, E. J. (1976). *Interplanetary encounters: close-range gravitational interactions*. Elsevier Scientific Pub. Co., New York.

Paddack, S. J. (1969). Rotational bursting of small celestial bodies: Effects of radiation pressure. *Journal of Geophysical Research*, 74:4379–4381.

Paddack, S. J. (1973). *Rotational bursting of small particles.* PhD thesis, Catholic Univ. Washington, DC.

Paddack, S. J. and Rhee, J. W. (1975). Rotational bursting of interplanetary dust particles. *Geophysical Research Letters*, 2:365–367.

Parker, A., Ivezić, Ž., Jurić, M., Lupton, R., Sekora, M. D., and Kowalski, A. (2008). The size distributions of asteroid families in the SDSS Moving Object Catalog 4. *Icarus*, 198:138–155.

Parker, A. H., Kavelaars, J. J., Petit, J.-M., Jones, L., Gladman, B., and Parker, J. (2011). Characterization of seven ultra-wide trans-Neptunian binaries. *The Astrophysical Journal*, 743:1.

Peirce, B. (1849). Development of the perturbative function of planetary motion. *Astronomical Journal*, 1:1–8.

Peterson, C. (1976). A source mechanism for meteorites controlled by the Yarkovsky effect. *Icarus*, 29:91–111.

Picard, J. (1671). *Mesure de la terre*. Imprimerie royale, 1. Paris.

Poincaré, H. (1892). *Les Méthodes Nouvelles de la Mécanique Céleste I*. Gauthier-Villars, Paris.

Poincaré, H. (1899). *Les Méthodes Nouvelles de la Mécanique Céleste III.* Gauthier-Villars, Paris.

Polishook, D. (2014). Spin axes and shape models of asteroid pairs: Fingerprints of YORP and a path to the density of rubble piles. *Icarus*, 241:79–96.

Polishook, D., Moskovitz, N., Binzel, R. P., DeMeo, F. E., Vokrouhlický, D., Žižka, J., and Oszkiewicz, D. (2014). Observations of "fresh" and weathered surfaces on asteroid pairs and their implications on the rotational-fission mechanism. *Icarus*, 233:9–26.

Pravec, P., Fatka, P., Vokrouhlický, D., Scheeres, D. J., Kušnirák, P., Hornoch, K., Galád, A., Vraštil, J., Pray, D. P., Krugly, Y. N., Gaftonyuk, N. M., Inasaridze, R. Y., Ayvazian, V. R., Kvaratskhelia, O. I., Zhuzhunadze, V. T., Husárik, M., Cooney, W. R., Gross, J., Terrell, D., Világi, J., Kornoš, L., Gajdoš, Š., Burkhonov, O., Ehgamberdiev, S. A., Donchev, Z., Borisov, G., Bonev, T., Rumyantsev, V. V., and Molotov, I. E. (2018). Asteroid clusters similar to asteroid pairs. *Icarus*, 304:110–126.

Pravec, P. and Harris, A. W. (2007). Binary asteroid population. 1. Angular momentum content. *Icarus*, 190:250–259.

Pravec, P., Harris, A. W., Kušnirák, P., Galád, A., and Hornoch, K. (2012). Absolute magnitudes of asteroids and a revision of asteroid albedo estimates from WISE thermal observations. *Icarus*, 221:365–387.

Pravec, P., Harris, A. W., Scheirich, P., Kušnirák, P., Šarounová, L., Hergenrother, C. W., Mottola, S., Hicks, M. D., Masi, G., Krugly, Y. N., Shevchenko, V. G., Nolan, M. C., Howell, E. S., Kaasalainen, M., Galád, A., Brown, P., DeGraff, D. R., Lambert, J. V., Cooney, W. R., and Foglia, S. (2005). Tumbling asteroids. *Icarus*, 173:108–131.

Pravec, P., Harris, A. W., Vokrouhlický, D., Warner, B. D., Kušnirák, P., Hornoch, K., Pray, D. P., Higgins, D., Oey, J., Galád, A., Gajdoš, Š., Kornoš, L., Világi, J., Husárik, M., Krugly, Y. N., Shevchenko, V., Chiorny, V., Gaftonyuk, N., Cooney, W. R., Gross, J., Terrell, D., Stephens, R. D., Dyvig, R., Reddy, V., Ries, J. G., Colas, F., Lecacheux, J., Durkee, R., Masi, G., Koff, R. A., and Goncalves, R. (2008). Spin rate distribution of small asteroids. *Icarus*, 197:497–504.

Pravec, P., Hergenrother, C., Whiteley, R., Šarounová, L., Kušnirák, P., and Wolf, M. (2000). Fast rotating asteroids 1999 TY2, 1999 SF10, and 1998 WB2. *Icarus*, 147:477–486.

Pravec, P., Kušnirák, P., Hornoch, K., Galád, A., Krugly, Y. N., Chiorny, V., Inasaridze, R., Kvaratskhelia, O., Ayvazian, V., Parmonov, O., Pollock, J., Mottola, S., Oey, J., Pray, D., Žižka, J., Vraštil, J., Molotov, I., Reichart, D. E., Ivarsen, K. M., Haislip, J. B., and LaCluyze, A. (2013). (8306) Shoko. *IAU Circ.*, 9268.

Pravec, P., Scheirich, P., Kušnirák, P., Hornoch, K., Galád, A., Naidu, S. P., Pray, D. P., Világi, J., Gajdoš, Š., Kornoš, L., Krugly, Y. N., Cooney, W. R., Gross, J., Terrell, D., Gaftonyuk, N., Pollock, J., Husárik, M., Chiorny, V., Stephens, R. D., Durkee, R., Reddy, V., Dyvig, R., Vraštil, J., Žižka, J., Mottola, S., Hellmich, S., Oey, J., Benishek, V., Kryszczyńska, A., Higgins, D., Ries, J., Marchis, F., Baek, M., Macomber, B., Inasaridze, R., Kvaratskhelia, O., Ayvazian, V., Rumyantsev, V., Masi, G., Colas, F., Lecacheux, J., Montaigut, R., Leroy, A., Brown, P., Krzeminski, Z., Molotov, I., Reichart, D., Haislip, J., and LaCluyze, A. (2016). Binary asteroid population. 3. Secondary rotations and elongations. *Icarus*, 267:267–295.

Pravec, P., Scheirich, P., Ďurech, J., Pollock, J., Kušnirák, P., Hornoch, K., Galád, A., Vokrouhlický, D., Harris, A. W., Jehin, E., Manfroid, J., Opitom, C., Gillon, M., Colas, F., Oey, J., Vraštil, J., Reichart, D., Ivarsen, K., Haislip, J., and LaCluyze, A. (2014). The tumbling spin state of (99942) Apophis. *Icarus*, 233:48–60.

Pravec, P., Šarounová, L., and Wolf, M. (1996). Lightcurves of 7 near-Earth asteroids. *Icarus*, 124:471–482.

Pravec, P. and Vokrouhlický, D. (2009). Significance analysis of asteroid pairs. *Icarus*, 204:580–588.

Pravec, P., Vokrouhlický, D., Polishook, D., Scheeres, D. J., Harris, A. W., Galád, A., Vaduvescu, O., Pozo, F., Barr, A., Longa, P., Vachier, F., Colas, F., Pray, D. P., Pollock, J., Reichart, D., Ivarsen, K., Haislip, J., Lacluyze, A., Kušnirák, P., Henych, T., Marchis, F., Macomber, B., Jacobson, S. A., Krugly, Y. N., Sergeev, A. V., and Leroy, A. (2010). Formation of asteroid pairs by rotational fission. *Nature*, 466:1085–1088.

Rabinowitz, D., Helin, E., Lawrence, K., and Pravdo, S. (2000). A reduced estimate of the number of kilometre-sized near-Earth asteroids. *Nature*, 403:165–166.

Radzievskii, V. V. (1952). The influence of anisotropically emitted sunlight on orbital motion of asteroids and meteorites [in Russian]. *Astron. Zh.*, 29:162–170.

Rosaev, A. and Plávalová, E. (2017). On the young family of 18777 Hobson. *Icarus*, 282:326–332.

Roy, A. E., Walker, I. W., MacDonald, A. J., Williams, I. P., and Fox, K. (1988). Project LONGSTOP. *Vistas in Astronomy*, 32:95–116.

Rożek, A., Breiter, S., and Jopek, T. J. (2011). Orbital similarity functions - application to asteroid pairs. *Monthly Notices of the Royal Astronomical Society*, 412:987–994.

Rozitis, B., Duddy, S. R., Green, S. F., and Lowry, S. C. (2013). A thermophysical analysis of the (1862) Apollo Yarkovsky and YORP effects. *Astronomy and Astrophysics*, 555:A20.

Rozitis, B. and Green, S. F. (2012). The influence of rough surface thermal-infrared beaming on the Yarkovsky and YORP effects. *Monthly Notices of the Royal Astronomical Society*, 423:367–388.

Rozitis, B. and Green, S. F. (2013). The influence of global self-heating on the Yarkovsky and YORP effects. *Monthly Notices of the Royal Astronomical Society*, 433:603–621.

Rozitis, B. and Green, S. F. (2014). Physical characterisation of near-Earth asteroid (1620) Geographos. Reconciling radar and thermal-infrared observations. *Astronomy and Astrophysics*, 568:A43.

Rozitis, B., Maclennan, E., and Emery, J. P. (2014). Cohesive forces prevent the rotational breakup of rubble-pile asteroid (29075) 1950 DA. *Nature*, 512:174–176.

Rubincam, D. P. (1995). Asteroid orbit evolution due to thermal drag. *Journal of Geophysical Research*, 100:1585–1594.

Rubincam, D. P. (1998). Yarkovsky thermal drag on small asteroids and Mars-Earth delivery. *Journal of Geophysical Research*, 103:1725–1732.

Rubincam, D. P. (2000). Radiative spin-up and spin-down of small asteroids. *Icarus*, 148:2–11.

Rubincam, D. P. (2007). Orbital YORP and asteroid orbit evolution, with application to Apophis. *Icarus*, 192:460–468.

Scheeres, D. (2016a). Relative equilibria in the full N-body problem with applications to the equal mass problem. In Chyba, M. and Bonnard, B., editors, *Recent Advances in Celestial and Space Mechanics*. Springer.

Scheeres, D. J. (2002). Stability in the full two-body problem. *Celestial Mechanics and Dynamical Astronomy*, 83:155–169.

Scheeres, D. J. (2007a). Rotational fission of contact binary asteroids. *Icarus*, 189:370–385.

Scheeres, D. J. (2007b). The dynamical evolution of uniformly rotating asteroids subject to YORP. *Icarus*, 188:430–450.

Scheeres, D. J. (2016b). Hill stability of configurations in the full N-body problem. In Chesley, S. R., Morbidelli, A., Jedicke, R., and Farnocchia, D., editors, *Asteroids: New Observations, New Models*, volume 318 of *IAU Symposium*, pages 128–134.

Scheeres, D. J. and Mirrahimi, S. (2008). Rotational dynamics of a solar system body under solar radiation torques. *Celestial Mechanics and Dynamical Astronomy*, 101:69–103.

Seeliger, H. (1887). Zur theorie der Belechtung der grossen Planeten inbesondere Saturn. *Abh. Bayer. Akad. Wiss. Math. Naturw. Kl. II.*, 16:405–516.

Ševeček, P., Brož, M., Čapek, D., and Ďurech, J. (2015). The thermal emission from boulders on (25143) Itokawa and general implications for the YORP effect. *Monthly Notices of the Royal Astronomical Society*, 450:2104–2115.

Ševeček, P., Golubov, O., Scheeres, D. J., and Krugly, Y. N. (2016). Obliquity dependence of the tangential YORP. *Astronomy and Astrophysics*, 592:A115.

Shkuratov, Y. G., Kreslavsky, M. A., Ovcharenko, A. A., Stankevich, D. G., Zubko, E. S., Pieters, C., and Arnold, G. (1999). Opposition effect from Clementine data and mechanisms of backscatter. *Icarus*, 141:132–155.

Slivan, S. M. (2002). Spin vector alignment of Koronis family asteroids. *Nature*, 419:49–51.

Slivan, S. M., Binzel, R. P., Crespo da Silva, L. D., Kaasalainen, M., Lyndaker, M. M., and Krčo, M. (2003). Spin vectors in the Koronis family: comprehensive results from two independent analyses of 213 rotation lightcurves. *Icarus*, 162:285–307.

Smith, J. R. (1996). *Introduction to geodesy*. 1. Wiley, New York.

Spencer, J. R., Lebofsky, L. A., and Sykes, M. V. (1989). Systematic biases in radiometric diameter determinations. *Icarus*, 78:337–354.

Spitale, J. N. (2001). *Detailed study of the Yarkovsky effect on asteroids and solar system implications*. PhD thesis, The University of Arizona.

Statler, T. S. (2009). Extreme sensitivity of the YORP effect to small-scale topography. *Icarus*, 202:502–513.

Stuart, J. S. (2001). A near-Earth asteroid population estimate from the LINEAR survey. *Science*, 294:1691–1693.

Sussman, G. J. and Wisdom, J. (1988). Numerical evidence that the motion of Pluto is chaotic. *Science*, 241:433–437.

Taton, R., Wilson, C., and Hoskin, M. (2003). *Planetary astronomy from the Renaissance to the rise of astrophysics, Part A: Tycho Brahe to Newton*. General History of Astronomy. Cambridge University Press.

Taylor, P. A., Margot, J.-L., Vokrouhlický, D., Scheeres, D. J., Pravec, P., Lowry, S. C., Fitzsimmons, A., Nolan, M. C., Ostro, S. J., Benner, L. A. M., Giorgini, J. D., and Magri, C. (2007). Spin rate of asteroid (54509) 2000 PH5 increasing due to the YORP effect. *Science*, 316:274.

Trujillo, C. (2003). Discovering the edge of the solar system. *American Scientist*, 91:424–431.

Tsiganis, K., Gomes, R., Morbidelli, A., and Levison, H. F. (2005). Origin of the orbital architecture of the giant planets of the Solar System. *Nature*, 435:459–461.

Usui, F., Kasuga, T., Hasegawa, S., Ishiguro, M., Kuroda, D., Müller, T. G., Ootsubo, T., and Matsuhara, H. (2013). Albedo properties of main belt asteroids based on the all-sky survey of the infrared astronomical satellite AKARI. *The Astrophysical Journal*, 762:56–70.

Verbiscer, A. J. and Veverka, J. (1995). Interpretation of the IAU two-parameter magnitude system for asteroids in terms of Hapke photometric theory. *Icarus*, 115:369–373.

Vokrouhlický, D. (1998a). Diurnal Yarkovsky effect as a source of mobility of meter-sized asteroidal fragments. I. Linear theory. *Astronomy and Astrophysics*, 335:1093–1100.

Vokrouhlický, D. (1998b). Diurnal Yarkovsky effect as a source of mobility of meter-sized asteroidal fragments. II. Non-sphericity effects. *Astronomy and Astrophysics*, 338:353–363.

Vokrouhlický, D. (1999). A complete linear model for the Yarkovsky thermal force on spherical asteroid fragments. *Astronomy and Astrophysics*, 344:362–366.

Vokrouhlický, D., Bottke, W. F., Chesley, S. R., Scheeres, D. J., and Statler, T. S. (2015a). The Yarkovsky and YORP effects. In Michel, P., DeMeo, F. E., and Bottke, W. F., editors, *Asteroids IV*, pages 509–531.

Vokrouhlický, D., Brož, M., Bottke, W. F., Nesvorný, D., and Morbidelli, A. (2006a). The peculiar case of the Agnia asteroid family. *Icarus*, 183:349–361.

Vokrouhlický, D., Brož, M., Morbidelli, A., Bottke, W. F., Nesvorný, D., Lazzaro, D., and Rivkin, A. S. (2006b). Yarkovsky footprints in the Eos family. *Icarus*, 182:92–117.

Vokrouhlický, D. and Čapek, D. (2002). YORP-induced long-term evolution of the spin state of small asteroids and meteoroids: Rubincam's approximation. *Icarus*, 159:449–467.

Vokrouhlický, D., Chesley, S. R., and Matson, R. D. (2008). Orbital identification for asteroid 152563 (1992 BF) through the Yarkovsky effect. *The Astronomical Journal*, 135:2336–2340.

Vokrouhlický, D., Ďurech, J., Polishook, D., Krugly, Y. N., Gaftonyuk, N. N., Burkhonov, O. A., Ehgamberdiev, S. A., Karimov, R., Molotov, I. E., Pravec, P., Hornoch, K., Kušnirák, P., Oey, J., Galád, A., and Žižka, J. (2011). Spin vector and shape of (6070) Rheinland and their implications. *The Astronomical Journal*, 142:159.

Vokrouhlický, D., Ďurech, J., Pravec, P., Kušnirák, P., Hornoch, K., Vraštil, J., Krugly, Y. N., Inasaridze, R. Y., Ayvasian, V., Zhuzhunadze, V., Molotov, I. E., Pray, D., Husárik, M., Pollock, J. T., and Nesvorný, D. (2016). The Schulhof family: Solving the age puzzle. *The Astronomical Journal*, 151:56–68.

Vokrouhlický, D. and Farinella, P. (2000). Efficient delivery of meteorites to the Earth from a wide range of asteroid parent bodies. *Nature*, 407:606–608.

Vokrouhlický, D., Farnocchia, D., Čapek, D., Chesley, S. R., Pravec, P., Scheirich, P., and Müller, T. G. (2015b). The Yarkovsky effect for 99942 Apophis. *Icarus*, 252:277–283.

Vokrouhlický, D. and Milani, A. (2000). Direct solar radiation pressure on the orbits of small near-Earth asteroids: observable effects? *Astronomy and Astrophysics*, 362:746–755.

Vokrouhlický, D., Milani, A., and Chesley, S. R. (2000). Yarkovsky Effect on small near-Earth asteroids: Mathematical formulation and examples. *Icarus*, 148:118–138.

Vokrouhlický, D. and Nesvorný, D. (2008). Pairs of asteroids probably of a common origin. *The Astronomical Journal*, 136:280–290.

Vokrouhlický, D. and Nesvorný, D. (2009). The common roots of asteroids (6070) Rheinland and (54827) 2001 NQ8. *The Astronomical Journal*, 137:111–117.

Vokrouhlický, D. and Nesvorný, D. (2011). Half-brothers in the Schulhof family? *The Astronomical Journal*, 142:26–34.

Vokrouhlický, D., Nesvorný, D., and Bottke, W. F. (2003). The vector alignments of asteroid spins by thermal torques. *Nature*, 425:147–151.

Vokrouhlický, D., Nesvorný, D., Bottke, W. F., and Morbidelli, A. (2010). Collisionally born family about 87 Sylvia. *The Astronomical Journal*, 139:2148–2158.

Vokrouhlický, D., Pravec, P., Ďurech, J., Bolin, B., Jedicke, R., Kušnirák, P., Galád, A., Hornoch, K., Kryszczyńska, A., Colas, F., Moskovitz, N., Thirouin, A., and Nesvorný, D. (2017a). The young Datura asteroid family. Spins, shapes, and population estimate. *Astronomy & Astrophysics*, 598:A91.

Vokrouhlický, D., Pravec, P., Ďurech, J., Hornoch, K., Kušnirák, P., Galád, A., Vraštil, J., Kučáková, H., Pollock, J. T., Ortiz, J. L., Morales, N., Gaftonyuk, N. M., Pray, D. P., Krugly, Y. N., Inasaridze, R. Y., Ayvazian, V. R., Molotov, I. E., and Colazo, C. A. (2017b). Detailed analysis of the asteroid pair (6070) Rheinland and (54827) 2001 NQ8. *The Astronomical Journal*, 153:270.

Walsh, K. J., Richardson, D. C., and Michel, P. (2008). Rotational breakup as the origin of small binary asteroids. *Nature*, 454:188–191.

Wigner, E. (1959). *Group Theory: And Its Application to the Quantum Mechanics of Atomic Spectra*. Academic Press Inc., New York.

Wolszczan, A. and Frail, D. A. (1992). A planetary system around the millisecond pulsar PSR1257 + 12. *Nature*, 355:145–147.

Yu, L., Ji, J., and Ip, W.-H. (2017). Surface thermophysical properties investigation of the potentially hazardous asteroid (99942) Apophis. *ArXiv e-prints*.

Zappalà, V., Cellino, A., Farinella, P., and Knežević, Z. (1990). Asteroid families. I - Identification by hierarchical clustering and reliability assessment. *Astronomical Journal*, 100:2030–2046.

Žižka, J., Galád, A., Vokrouhlický, D., Pravec, P., Kušnirák, P., and Hornoch, K. (2016). Asteroids 87887 - 415992: the youngest known asteroid pair? *Astronomy & Astrophysics*, 595:A20.

Žižka, J. and Vokrouhlický, D. (2011a). Modified Method of Asteroid Pairs Convergence. In *WDS'11 Proceedings of Contributed Papers*, PART III, pages 19–24. Matfyzpress.

Žižka, J. and Vokrouhlický, D. (2011b). Solar radiation pressure on (99942) Apophis. *Icarus*, 211:511–518.

Appendix

A. Publications

Here we list all publications and reprints of *Paper 1*, *Paper 2* and *Paper 3*.

Paper 1: **Žižka, J.** and Vokrouhlický, D. (2011). Solar radiation pressure on (99942) Apophis. *Icarus*, 211:511–518.

Paper 2: **Žižka, J.** and Vokrouhlický, D. (2011). Modified Method of Asteroid Pairs Convergence. In *WDS'11 Proceedings of Contributed Papers*, PART III, pages 19–24. Matfyzpress.

Paper 3: **Žižka, J.**, Galád, A., Vokrouhlický, D., Pravec, P., Kušnirák, P., and Hornoch, K. (2016). Asteroids 87887 – 415992: the youngest known asteroid pair ? *Astronomy & Astrophysics*, 595:A20.

Galád A., Vokrouhlický D., and **Žižka, J.** (2014). Prospective very young asteroid pairs. In Muinonen, K., Penttilä, A., Granvik, M., Virkki, A., Fedorets, G., Wilkman, O., and Kohout, T., editors, *Asteroids, Comets, Meteors 2014*.

Polishook, D., Moskovitz, N., Binzel, R. P., DeMeo, F. E., Vokrouhlický, D., **Žižka, J.**, and Oszkiewicz, D. (2014). Observations of "fresh" and weathered surfaces on asteroid pairs and their implications on the rotational-fission mechanism. *Icarus*, 233:9–26.

Vokrouhlický, D., Ďurech, J., Polishook, D., Krugly, Y. N., Gaftonyuk, N. N., Burkhonov, O. A., Ehgamberdiev, S. A., Karimov, R., Molotov, I. E., Pravec, P., Hornoch, K., Kušnirák, P., Oey, J., Galád, A., and **Žižka, J.** (2011). Spin vector and shape of (6070) Rheinland and their implications. *The Astronomical Journal*, 142:159.

Pravec, P., Scheirich, P., Kušnirák, P., Hornoch, K., Galád, A., Naidu, S. P., Pray, D. P., Világi, J., Gajdoš, Š., Kornoš, L., Krugly, Y. N., Cooney, W. R., Gross, J., Terrell, D., Gaftonyuk, N., Pollock, J., Husárik, M., Chiorny, V., Stephens, R. D., Durkee, R., Reddy, V., Dyvig, R., Vraštil, J., **Žižka, J.**, Mottola, S., Hellmich, S., Oey, J., Benishek, V., Kryszczyńska, A., Higgins, D., Ries, J., Marchis, F., Baek, M., Macomber, B., Inasaridze, R., Kvaratskhelia, O., Ayvazian, V., Rumyantsev, V., Masi, G., Colas, F., Lecacheux, J., Montaigut, R., Leroy, A., Brown, P., Krzeminski, Z., Molotov, I., Reichart, D., Haislip, J., and LaCluyze, A. (2016). Binary asteroid population. 3. Secondary rotations and elongations. *Icarus*, 267:267–295.

Paper 1

Provided for non-commercial research and education use.
Not for reproduction, distribution or commercial use.

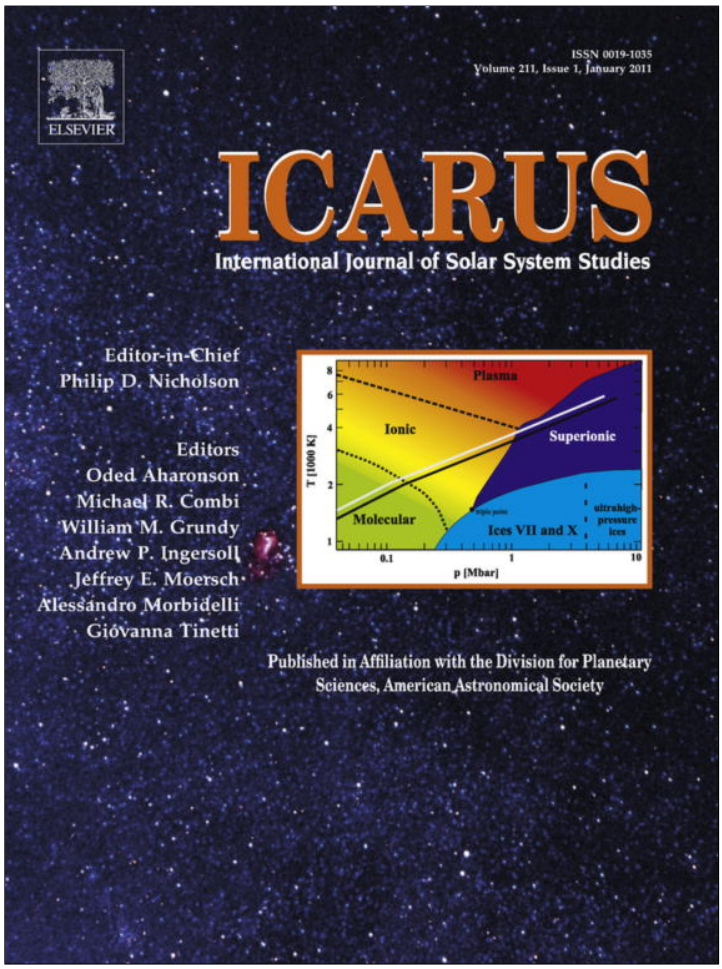

This article appeared in a journal published by Elsevier. The attached copy is furnished to the author for internal non-commercial research and education use, including for instruction at the authors institution and sharing with colleagues.

Other uses, including reproduction and distribution, or selling or licensing copies, or posting to personal, institutional or third party websites are prohibited.

In most cases authors are permitted to post their version of the article (e.g. in Word or Tex form) to their personal website or institutional repository. Authors requiring further information regarding Elsevier's archiving and manuscript policies are encouraged to visit:

http://www.elsevier.com/copyright

Author's personal copy

Icarus 211 (2011) 511–518

Contents lists available at ScienceDirect

Icarus

journal homepage: www.elsevier.com/locate/icarus

Solar radiation pressure on (99942) Apophis

J. Žižka [a,b], D. Vokrouhlický [a,*]

[a] Institute of Astronomy, Charles University, V Holešovičkách 2, 18000 Prague 8, Czech Republic
[b] Nicholas Copernicus Observatory and Planetarium, Kraví hora 2, 61600 Brno, Czech Republic

ARTICLE INFO

Article history:
Received 9 April 2010
Revised 12 August 2010
Accepted 18 August 2010
Available online 24 August 2010

Keywords:
Celestial mechanics
Asteroids, Dynamics

ABSTRACT

Near-Earth asteroid (99942) Apophis currently resides among the top positions on the list of objects with small, yet non-zero impact probability with the Earth. For that reason an unusual observational and theoretical effort has been dedicated to precisely characterize its future orbit. Here we discuss orbital perturbation of Apophis due to incident and reflected solar radiation pressure (SRP). We both revisit recent analytical estimate of the SRP effects for this body and also formulate a numerical approach allowing us to compute the SRP orbital perturbation under general assumptions. Contrary to some previous results, we show that SRP has a much smaller effect on the Apophis trajectory than does the thermal re-radiation force which produces the Yarkovsky effect. When the Yarkovsky effect becomes constrained enough in the future, our approach may be used to improve the orbit determination for this asteroid.

© 2010 Elsevier Inc. All rights reserved.

1. Introduction

Near-Earth asteroids present a threat by their possible impacts onto the Earth (e.g., Chesley et al., 2002; Chapman, 2004). Accurate orbital ephemeris and the impact likelihood analysis represent a starting point for further considerations such as mitigation actions. When the identified impact possibility is distant in future (i.e. tens of years and more), a very accurate orbital model, beyond the usual needs of the asteroid orbit computations, is required to analyze the problem. Vokrouhlický et al. (2000) and Vokrouhlický and Milani (2000) pointed out that several forces of non-gravitational origin may be needed for this task. The Yarkovsky effect due to the recoil of thermally re-radiated sunlight (e.g., Bottke et al., 2002, 2006) is the most important of them. Indeed, search efforts have detected this effect acting on several near-Earth asteroids (e.g., Chesley et al., 2003, 2008; Vokrouhlický et al., 2008) and detailed studies of orbital evolution for several potentially hazardous objects has identified the Yarkovsky effect as the most significant to obscure future position predictions (e.g., Giorgini et al., 2002, 2008; Chesley, 2006; Milani et al., 2009).

Asteroid (99942) Apophis, a former record-holder in the impact threat scale, has an unusually close approach to the Earth in April 13, 2029. At that date, it will pass some 38,000 km from the Earth center and subsequently will be perturbed by the Earth's gravity into a new heliocentric orbit, switching from the Aten to the Apollo category (Fig. 1). In fact, soon after its discovery in December 2004, Apophis was initially estimated to have an impact probability larger than any prior case (e.g., Chesley, 2006), but was quickly reduced in magnitude and pushed to the mid 2030s as additional measurements were reported (Chesley, 2006; Chesley et al., 2009; Giorgini et al., 2008). This is because a number of resonant return-orbits are within (or very close to) the orbital uncertainty region during the 2029 approach. Even if Apophis eventually does not impact the Earth, the high-accuracy orbit determination efforts developed for this complicated case will certainly be applicable to similar cases in the future.

A thorough analysis of the Apophis orbit, including its discovery circumstances and improvements of the orbital determination as a function of increasing observation dataset, has been published by Chesley (2006) and Giorgini et al. (2008). While both took into account the effects of the thermal forces (the Yarkovsky effect), perturbations due to the solar radiation pressure in optical waveband have been considered by the latter only. Using a very simple, but in fact satisfactory zero-order approximation in the numerical integration, Giorgini et al. (2008) concluded that the solar radiation pressure effect on Apophis is much less than the Yarkovsky effect. By contrast, Rubincam (2007) performed a specific analysis of the radiation pressure orbital effects for Apophis and concluded they can be as significant as those due to the thermal forces (the Yarkovsky effect). The contradictory conclusions from these two works[1] motivated us to take a closer look at the effects of the solar radiation pressure in the orbit of Apophis.

* Corresponding author.
E-mail addresses: jinziz@centrum.cz (J. Žižka), vokrouhl@cesnet.cz (D. Vokrouhlický).

[1] Note that Giorgini et al. (2008) were aware of a preprint version of Rubincam (2007) and noted the difference between their numerical results and those of Rubincam. They assumed the extreme shape adopted by Rubincam (2007) made the radiation pressure effect unrealistically large.

0019-1035/$ - see front matter © 2010 Elsevier Inc. All rights reserved.
doi:10.1016/j.icarus.2010.08.011

Author's personal copy

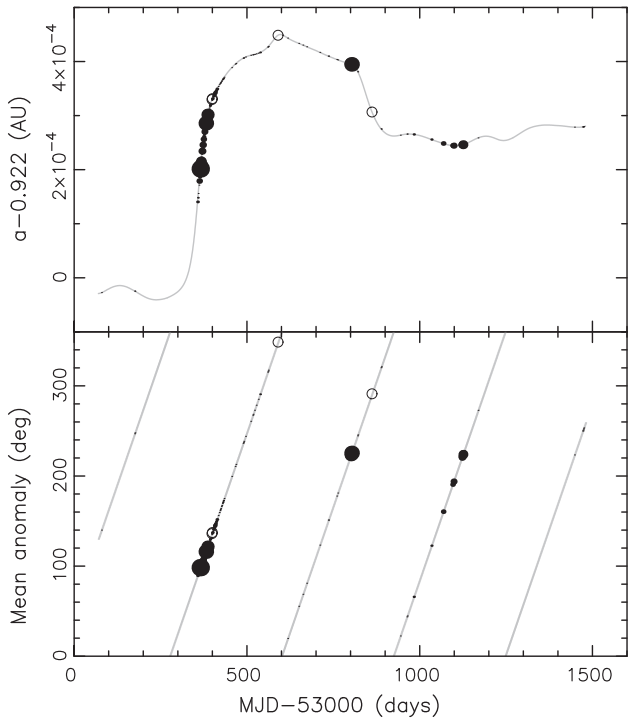

Fig. 1. Osculating semimajor axis (top) and mean anomaly (bottom) for the orbit of (99942) Apophis from 2004.0 till 2008.2 (grey curve). Symbols show where observations have been obtained so far and collected into 1-day bins; size of the symbol is scaled by number of observations acquired during that day. Full circles for optical astrometry, open circles for radar astrometry. Majority of observations (some 60%) was obtained during the 2004–2005 close approach. The significant increase of the heliocentric semimajor axis seen in December 2004 is due to the close approach to the Earth; a much more spectacular change will occur during the 400 times closer approach in April 2029, when the semimajor axis will increase to ~1.1 AU.

The theory of radiation force for an arbitrarily-shaped asteroid is given in Section 2 and its numerical implementation in Section 3. Results of our numerical simulations are summarized in Section 4. Section 2 also contains a minor correction of the analytical computations of Rubincam (2007).

2. Theory

Solar radiation impinging the surface of an asteroid is removed from the incident beam and reprocessed in two ways: (i) the first part, included in this paper, is directly scattered in the optical waveband (since the dominant part of sunlight is in optical) and (ii) the second part, not included in this paper, is absorbed and re-emitted in thermal waveband. The second part, namely the recoil acceleration due to thermal radiation, results in what is known as the Yarkovsky effect (e.g., Bottke et al., 2002, 2006).

The prime goal of our work is the accuracy of the solar radiation pressure computation. For that reason we do not restrict to (i) a simplest Lambertian reflection of the sunlight and (ii) a simplest possible geometric shapes of the asteroid (such as spherical or ellipsoidal), but instead we keep the formulation as general as possible. Such an approach is handled numerically rather than analytically, and requires that the fundamental level at which we describe the radiation pressure involves momentum budget for an infinitesimal surface facet upon which some fraction of the incident sunlight is absorbed, the rest scattered through reflection. The total effect is then obtained by numerical integration over all surface facets.

2.1. Incident sunlight

The dynamical effect of the incident sunlight arises simply by virtue of its removal from the solar radiation flux as a momentum transfer to the object. It is thus given by (e.g., Vokrouhlický and Milani, 2000)

$$\mathbf{f}_{\rm inc} = -\frac{FS_\perp}{mc}\mathbf{n}_0, \tag{1}$$

where F is the sunlight flux at the asteroid heliocentric distance, $S_\perp$ is the instantaneous cross-section of the asteroid with respect to the solar radiation, m is the asteroid mass, c the velocity of light and $\mathbf{n}_0$ is the instantaneous unit vector directed from the asteroid to the Sun. Note $\mathbf{f}_{\rm inc}$ is radially directed acceleration with two primary sources of temporal variability: (i) the flux F varies along an eccentric orbit as the heliocentric distance d changes ($F \propto d^{-2}$) and (ii) the cross-section $S_\perp$ changes due to asteroid rotation and its revolution about the Sun for an irregularly-shaped body. If only the first phenomenon existed, the dynamical effect of the impinging sunlight would be equivalent to redefining the orbital elements due to effectively smaller value of Sun's gravitational mass (e.g., Dermott et al., 2001). However, the cross-section $S_\perp$ variation slightly complicates the situation and adds short-period perturbations that needs to be modeled numerically. At each timestep of the integrator we thus need to evaluate

$$S_\perp = \int_{S_0} (d\mathbf{S}\cdot\mathbf{n}_0)\Sigma(\mathbf{R},\mathbf{n}_0), \tag{2}$$

where the integration is performed over the illuminated portion S_0 of the asteroid surface, $d\mathbf{S}$ is an outward-oriented surface element and Σ is the shadow function.[2] The latter is either 1, if the surface facet is illuminated, or 0, if the surface facet is shadowed by other parts of the asteroid; Σ is a function of $\mathbf{n}_0$, the transformation matrix $\mathbf{R}$ from the ecliptic inertial system to the body-frame system, and the overall shape model. An effective analysis of Σ is not a trivial task for highly irregular shapes. Since we have the asteroid shape models available as discrete polyhedrons (with typically thousands of facets), we replace the integration in (2) by summation over the surface facets. The mutual shadowing conditions are treated with a rather inefficient "N^2 method" described in Appendix B.2 of Čapek (2007) (available through http://sirrah.troja.mff.cuni.cz/~davok/). The procedure basically inspects each of the N surface elements and, given the instantaneous solar position, seeks whether it projects a shadow on another surface element. The algorithm was somewhat accelerated by proper sorting of the elements, such that they are listed according to their increasing distance from the asteroid's center-of-mass and thus the origin of the body-centered reference frame.

2.2. Sunlight scattered on the asteroid surface

We now turn to discuss the dynamical effects of the sunlight scattered by the asteroid surface. Assume an infinitesimal surface facet $d\mathbf{S} = \mathbf{N}dS$ with outward normal vector $\mathbf{N}$. Let $\mathbf{N}_0$ denote unit vector of the local direction to the Sun and choose an arbitrary unit vector $\mathbf{N}_{\rm ray}$ directed to the hemisphere above the given surface element. The specific radiation intensity I of the scattered sunlight along $\mathbf{N}_{\rm ray}$ is given by

$$I = I(\mathbf{N}_0,\mathbf{N}_{\rm ray}) = Fr(\mathbf{N}_0,\mathbf{N}_{\rm ray}), \tag{3}$$

[2] Here we formally define S_0 as a sample of surface facets for which $d\mathbf{S}\cdot\mathbf{n}_0 > 0$, a necessary condition for illumination. The complete analysis of the facet illumination requires $\Sigma = 1$ to make sure other parts of the surface do not produce a shadow at the location of $d\mathbf{S}$. We display these two conditions explicitly to describe the complexity of the illumination condition.

Author's personal copy

where F is the incident radiation flux and $r(\mathbf{N}_0,\mathbf{N}_{\rm ray})$ is the bidirectional reflectance function (e.g., Mihalas, 1978). Assuming that r is a macroscopic quantity, that characterizes reflectance of random sample of microscopic scatterers, we have a reduced dependence $r = r(\mu,\mu_0,\mathbf{N}_0\cdot\mathbf{N}_{\rm ray})$. Here $\mu_0 = \mathbf{N}_0\cdot\mathbf{N}$ and $\mu = \mathbf{N}_{\rm ray}\cdot\mathbf{N}$ are directional cosines of the solar position and scattered light-ray direction with respect to the surface normal $\mathbf{N}$. It is also convenient to introduce local reference system with the z-direction along $\mathbf{N}$ and x-direction along

$$\mathbf{M} = \frac{\mathbf{N}_0 - \mu_0\mathbf{N}}{\sqrt{1-\mu_0^2}}. \tag{4}$$

With that choice, and spherical coordinates $(\theta,\phi)(\mu = \cos\theta)$, we can write

$$\mathbf{N}_0 = \begin{pmatrix} \sqrt{1-\mu_0^2} \\ 0 \\ \mu_0 \end{pmatrix} \tag{5}$$

and

$$\mathbf{N}_{\rm ray} = \begin{pmatrix} \sqrt{1-\mu^2}\cos\phi \\ \sqrt{1-\mu^2}\sin\phi \\ \mu \end{pmatrix} \tag{6}$$

In this way, we have

$$\cos\alpha = \mathbf{N}_0\cdot\mathbf{N}_{\rm ray} = \mu\mu_0 + \sqrt{1-\mu^2}\sqrt{1-\mu_0^2}\cos\phi \tag{7}$$

for the cosine of mutual angle α between $\mathbf{N}_0$ and $\mathbf{N}_{\rm ray}$.

Many studies of the sunlight reflection on the solid surfaces in the Solar System used Hapke's class of models. Since we do not need the highest accuracy in our work, we adopt Hapke's bidirectional reflectance function in a single-scattering approximation (e.g., Hapke, 1981, 2002)

$$r(\mu,\mu_0,\phi) = \frac{w}{4\pi}\frac{\mu_0}{\mu+\mu_0}[(1+B_0B_s(\alpha))P(\alpha) + H(\mu)H(\mu_0) - 1], \tag{8}$$

where $B_s(\alpha)$ is the backscatter function which describes the opposition effect of the surface

$$B_s(\alpha) = [1 + (1/h_s)\tan(\alpha/2)]^{-1}, \tag{9}$$

$H(x)$ is the Chandrasekhar's H-function, approximated in our computations with $(\gamma = \sqrt{1-w})$

$$H(x) = \frac{1+2x}{1+2\gamma x}, \tag{10}$$

and $P(\alpha)$ describes angular scattering properties of a single (average) surface particle. Here we consider the case of Henyey–Greenstein function

$$P(\alpha) = \frac{1-g^2}{(1+2g\cos\alpha+g^2)^{3/2}}, \tag{11}$$

with an anisotropy parameter g. We note that such a simplified Hapke model involves the following free parameters: (i) w the average single-scattering albedo, (ii) B_0 the opposition surge amplitude parameter, (iii) h_s characterizes the width of opposition surge, and (iv) g the asymmetry factor of a single-particle phase function (Henyey–Greenstein parameter). A number of authors derived their values from a high-quality photometry of individual asteroids and/or derived mean values for a given spectroscopic class (e.g., Helfenstein and Veverka, 1989). We shall use this general information, since the Apophis photometry is not prolific enough to derive specific value of (w,B_0,h_s,g) parameters for this object.

Before dealing with the recoil acceleration due to the scattered sunlight, we discuss a couple of useful parameters related to the scattering law described above. Most importantly we mention various definitions of "albedo" parameter. The hemispheric albedo A_h defines how the incident sunlight energy is partitioned between the reflection in optical wavelengths and thermal diffusion into the body. It is given by

$$A_h(\mu_0) = \frac{1}{\mu_0}\int_{\Omega_+} d\Omega\mu r(\mu,\mu_0,\phi), \tag{12}$$

where Ω_+ denotes the upper hemisphere on a unit sphere such that the integration in (12) goes as $\int_{\Omega_+} d\Omega = \int_0^1 d\mu\int_0^{2\pi} d\phi$. With $A_h(\mu_0)$ defined as above, the $F\mu_0A_h(\mu_0)$ amount of radiation energy is directly scattered and $F\mu_0[1-A_h(\mu_0)]$ amount of radiation energy is thermally reprocessed. The second concept is that of geometric (or physical) albedo A_g which gives the ratio of brightness of a sphere observed at zero phase to the brightness of a Lambert disk. We have

$$A_g = 2\pi\int_0^1 \mu_0 r(\mu_0,\mu_0,0)d\mu_0, \tag{13}$$

which for the above given Hapke's model (8) yields

$$A_g = \frac{1}{2}r_0\left(1+\frac{1}{3}r_0\right) + \frac{w}{8}[(1+B_0)P(0) - 1], \tag{14}$$

with $r_0 = (1-\gamma)/(1+\gamma)$ (e.g., Hapke, 1981). Photometric observations of Delbò et al. (2007) yield $A_g = 0.33 \pm 0.04$ for (99942) Apophis. Eq. (14) thus provides a correlated constraint on the Hapke parameters of the Apophis surface reflectivity. Finally, we have Bond's albedo A_B, given by

$$A_B = 2\int_0^1 \mu_0 A_h(\mu_0)d\mu_0, \tag{15}$$

which is the total amount of energy scattered by a spherical object in all directions to the energy of the incident sunlight. Still more involved definitions of the "albedo values" may be needed for the analytic radiation force computation: for instance a second-order moment of the hemispheric albedo is the required quantity when dealing with radiation diffusion on a sphere (e.g., Vokrouhlický and Bottke, 2001).

Turning now to the dynamical effect of the reflected sunlight, we note that the infinitesimal recoil acceleration exerted on the surface facet dS is given by (e.g., Mihalas, 1978)

$$d\mathbf{f}_{\rm sca} = -\Sigma\frac{dS}{mc}\int_{\Omega_+} d\Omega\mu\mathbf{N}_{\rm ray}I(\mathbf{N}_0,\mathbf{N}_{\rm ray}) \tag{16}$$

(recall Σ is the shadow function from Eq. (2)). With Hapke's model introduced above, we have

$$d\mathbf{f}_{\rm sca} = -\Sigma\frac{F}{mc}(K_1\mathbf{N} + K_2\mathbf{M})dS, \tag{17}$$

where

$$K_1(\mu_0) = \int_{\Omega_+} d\Omega\mu^2 r(\mu,\mu_0,\phi), \tag{18}$$

$$K_2(\mu_0) = \int_{\Omega_+} d\Omega\mu\sqrt{1-\mu^2}\cos\phi r(\mu,\mu_0,\phi). \tag{19}$$

Note that both K_1 and K_2 coefficients depend on the cosine μ_0 of the local solar zenith angle and should be evaluated at each integration timestep for each facet. We prevented too large computer time requirements by precomputing K_1 and K_2 for a sufficiently dense grid of μ_0-values and then used linear interpolation for evaluation of the infinitesimal recoil contributions (17). An example of the K_1 and K_2 function dependence on μ_0 is shown in Fig. 2.

Author's personal copy

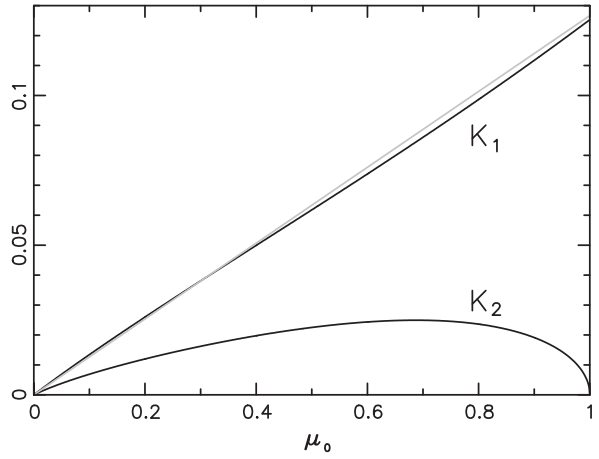

Fig. 2. $K_1(\mu_0)$ and $K_2(\mu_0)$ functions computed for Hapke parameters $w = 0.5$, $g = -0.35$, $h_s = 0.02$ and $B_0 = 0.97$ used in Section 4. Note the $K_1(\mu_0)$ function is well approximated with 2 $A_B\mu_0/3$ shown by the grey line ($A_B \simeq 0.2$ is the Bond albedo from Eq. (15)).

The total recoil acceleration of the asteroid is formally given by integrating (17) over the illuminated surface S_0:

$$\mathbf{f}_{\rm sca} = \int_{S_0} d\mathbf{f}_{\rm sca}. \tag{20}$$

In practice though, we use a discrete model of the asteroid shape consisting of a finite number of surface facets (usually several thousands). Integration in (20) is then replaced with summation over the model facets.

For sake of comparison with previous work we also note that the case of Lambertian diffusion on the surface is characterized with

$$r(\mu, \mu_0, \phi) = \frac{\mu_0}{\pi} A, \tag{21}$$

where A is a single "albedo" parameter in this model, equal to its hemispheric and Bond values. From (18) and (19) we easily obtain $K_1 = \frac{2}{3} A\mu_0$ and $K_2 = 0$ in this case.

2.3. Rubincam's hemispheric model

While we resort to an entirely numerical approach below, see Sections 3 and 4, we find it interesting to comment on the model presented in Rubincam (2007). Rubincam performed analytical computation of the radiation recoil force due to isotropically scattered sunlight on a body of particularly simple shape, namely a hemisphere. Inserting this effect into Gauss equations, Rubincam obtained an estimate of the time-averaged perturbation of orbital elements and from there he drew conclusions about the magnitude of the effect of radiation pressure on the Apophis trajectory. He correctly focused on secular effects in the semimajor axis value $\overline{(da/dt)}$, which have a potential to produce the most significant in-orbit displacement, and noted that only the scattered sunlight yields $\overline{(da/dt)} \neq 0$. Estimating its value for the assumed parameters of Apophis, Rubincam concluded that the radiation pressure may contribute in an important way to the orbit uncertainty budget during the 2029 encounter, noting in particular that it can be comparable to the effects due to the thermal forces (the Yarkovsky effect).

While this work represents an interesting attempt, we show here that its conclusion is incorrect for three separate reasons. First, the assumed hemispheric shape in Rubincam (2007) stretches the effect too much as already guessed by Giorgini et al. (2008). In a more detailed approach (Section 4), when we use a set of reasonable asteroid shapes in our numerical implementation, we obtain an effect order of magnitude smaller than predicted with the hemispheric model. Second, Rubincam's analytic calculation contains a small mistake that makes the effect apparently larger than it actually is. Finally, we should also point out that Rubincam's estimate has a conceptual flaw of folding the thermal (Yarkovsky) part of the perturbation into the reflected radiation budget (by using an albedo equal to unity). In fact, when properly modeled the orbital effect of the thermal forces with a non-zero value of the surface thermal inertia may be quite larger than the corresponding effect of the reflected radiation. As a result, one has to carefully distinguish the radiative orbital effects in optical and thermal in a proportion given by the albedo value.

Leaving the numerical experiments to Section 4, we now comment on the analytic results in Rubincam (2007). Basically all of them are performed carefully, but the final result suffers a small omission. Using the notation in that paper, the orbit-averaged semimajor axis drift in Eq. (33) of Rubincam (2007) should have read

$$\overline{\frac{da}{dt}} = -\frac{2(3\pi - 8)}{3\pi^2 n} \frac{F_{\rm E}}{c\rho R_{\rm A}} \frac{e}{1-e^2} \left(\frac{a_0}{a}\right)^2 \sin\beta. \tag{22}$$

Note the factor π^2 in the denominator, rather than π in Rubincam's result. Inserting the orbital parameters of Apophis we obtain $\overline{da/dt} \simeq -35 \sin\beta$ m/y, three times smaller than Rubincam's estimate (Eq. (36); where β is the angle between the hemisphere axis and direction to the apocentre in Rubincam's model). As a result, the maximum along-track displacement due to the radiation pressure in Rubincam's model becomes $\sim\pm 80$ km.

However, in the next sections we demonstrate that at all likelihood the true effect of the radiation pressure is yet another order of magnitude smaller than this estimate. In this respect one has to note that the large effect in Rubincam's model is a direct result of an extreme north–south shape asymmetry in the hemisphere model. Any more symmetric model would provide smaller effect; for instance, a spheroidal model evaluated also using analytic means by Vokrouhlický and Milani (2000) yields basically zero effect.

3. Numerical model and simulations

We implemented computation of the radiation pressure acceleration $\mathbf{f}_{\rm SRP} = \mathbf{f}_{\rm inc} + \mathbf{f}_{\rm sca}$ into the orbit determination software `OrbFit` provided by the University of Pisa dynamical group.[3] An arbitrary shape model is assumed and represented by a polyhedron with a large number of surface facets. Radar imaging and lightcurve analysis has not resulted in a shape model and pole orientation for (99942) Apophis yet; very likely, both will be obtained during its close approach to Earth in January 2013 (e.g., Giorgini et al., 2008). In this situation, the best we can do is to consider known shape models for near-Earth asteroids as a possible template of the Apophis shape and test the orbital effects due to the radiation pressure using these models. Since these are still not numerous enough, we also use a sample of artificial shape models known as Gaussian random spheres whose parameters have been calibrated by the shape models of the main belt asteroids (see Muinonen, 1998; Muinonen and Lagerros, 1998; Vokrouhlický and Čapek, 2002). The pole position is considered random in space, and the parameters of the bidirectional

[3] The `OrbFit` software can be downloaded from http://adams.dm.unipi.it/~orbmaint/orbfit/. We used a high-accuracy 15th order Radau-Everhart integrator included in this package to propagate orbit of Apophis and do not integrate past the very close 2029 Earth encounter. This way, accumulation of the integrator errors should not play an important role (see Giorgini et al., 2008). We should point out that our work is not a part of general distribution of `OrbFit` but may be requested from the authors.

Author's personal copy

reflectivity function (or just the albedo value in Lambertian approximation) are assumed in accord with the known geometric albedo value $A_g = 0.33 \pm 0.04$. Apophis rotation period has been constrained, though not accurately determined as yet, by the lightcurve observations. We take the ∼30.5 h value by Behrend et al. (2005).

With the lack of detailed information (such as the shape, pole and reflectivity parameters) we cannot compute the radiation pressure orbital displacement for Apophis accurately. Our approach is to compute it for a large sample of shape, pole and reflectivity-parameters possibilities and characterize the results in a statistical way using a mean/median value and a standard deviation. This defines a given computer run. In each individual simulation of a run, i.e. particular choice of the shape, pole and reflectivity parameters, we first perform an orbit determination for Apophis using all available observations, both sky-plane and radar astrometry (Fig. 1). The best-fit orbit is numerically propagated to the close approach in April 2029, and the geocentric state vector compared to the prediction of the nominal, conservative model where the effects of the radiation forces were not included.[4] The nominal model contains all relevant perturbations necessary for an accurate orbit determination, namely all planetary perturbations (including lunar effects) and the relativistic effects. None of the seven radar observations is rejected, and only four out of 1399 optical observations are rejected and considered as outliers. The root mean square of the residuals is only ∼0.26 arcsec for all models in the run. In particular, because the available observations cover a short interval of time, from March 2004 till January 2008, the quality of the fit using the nominal model and the extended model by the radiation forces is the same.[5]

4. Results

In this section we perform a number of simulations with the goal to reliably estimate the importance of the radiation pressure effects for the foreseeable Apophis' ephemerides, focusing on the orbital displacement during the very close approach in April 2029. We progress step-by-step starting with simpler cases and proceed to more complicated ones later.

4.1. Spherical model

At first, we considered the simplest shape model of the asteroid, namely a sphere. Sunlight scattering is modeled using the Lambertian model. In this case, we used two possibilities to implement the solar radiation pressure effects: (i) direct evaluation of the radiation pressure acceleration $\mathbf{f}_{\rm SRP} = -(FS_\perp/mc)(1+\frac{4}{9}A)\mathbf{n}_0$ with the cross-section $S_\perp = \pi D^2/4$ (e.g., Vokrouhlický and Milani, 2000) and (ii) we represented the sphere with a polyhedron model of 7200 surface facets and used methods from Section 2. Both methods provided identical results which conveniently validates our general method implementation in the `OrbFit` software. We used $D = 270$ m, bulk density[6] 2 g/cm^3 and albedo[7] $A = 0.2$. We find that the closest-approach distance[8] in April 13, 2029 has been shifted by about 4 km with respect to the nominal value 38046.825 km. This result is in a good agreement with a similar test reported by Giorgini et al. (2008). Moreover, it shows the effect of direct radiation pressure $\mathbf{f}_{\rm inc}$ is fairly small compared to the Yarkovsky effect, contrary to the finding of Rubincam.

4.2. Rubincam's hemispheric model

Next, we numerically verified conclusions from the analytic model of Rubincam (2007) and, at the same time, further tested implementation of the radiation forces in the `OrbFit` software. We constructed a hemispheric model using 7200 triangular surface facets. We oriented the pole position of the hemisphere in the orbital plane of Apophis with an arbitrary tilt β from the direction to pericenter and ran several simulations. In order to directly compare our results with those of Rubincam, we considered the reflected component of the radiation only using the Lambertian sunlight reflection and set the albedo equal to unity. The diameter of the hemisphere was 270 m and the bulk density 2.8 g/cm^3 in this case. Extreme differences with respect to the nominal model were observed for $\beta = 0^\circ$ and $\beta = 90^\circ$. In the first case the effect was basically zero and in the second case the distance of the closest approach in April 13, 2029 has been shifted by 88 km with respect to its nominal value (maximum over all β values). This is in a very good agreement with the analytic estimate obtained in Section 2.3. Adding the direct (incident) radiation pressure increases the effect by only ∼4 km, in agreement with the previous test. If this were the true radiation effect it would be very significant after the assumed orbital improvements in 2013. While this effect seems large, we must recall that in reality the effect of radiation pressure may be only one-fifth to one-fourth of this maximum value, depending on the real albedo. A larger portion has to be moved to the thermal budget and can produce still larger orbital effect when a non-zero thermal inertia is taken into account.

4.3. Gaussian random spheres used

The hemispheric shape model used in Rubincam (2007) is clearly a gross idealization of real asteroid shapes. A much better statistical representation is provided by a sample of Gaussian random spheres with properly chosen parameters (see, e.g., Muinonen, 1998; Muinonen and Lagerros, 1998). In the next set of simulations we thus used 200 Gaussian random spheres constructed by Vokrouhlický and Čapek (2002) and Čapek and Vokrouhlický (2004).[9] For each of the spheres, we considered 10 random pole orientations in space giving us 2000 individual simulations in a run. We used bulk density of 2 g/cm^3 and scaled all shape models such that their volume was equal to a sphere with a diameter of 270 m. Note that the diameter of Apophis is uncertain at the ∼20% level and its density is unmeasured. However, due to the inversely proportional effect of these parameters, our results may be scaled as necessary to allow for this. While performing our tests with the values given above, size and density uncertainty may eventually be accounted for by assuming an additional ≃40–50% uncertainty. We used two representative assumptions about the sunlight scattering on the surface: (i) the Lambertian model with albedo $A = 0.2$ and (ii) a Hapke model with the following set of parameters: $w = 0.5$, $g = -0.35$, $h_s = 0.02$ and $B_0 = 0.97$, yielding the geometric albedo $A_g = 0.34$. Obviously, the choice of the individual Hapke parameters

[4] We thus evaluate the fit-continuous model in the terminology of Giorgini et al. (2008).

[5] For instance, the current uncertainty in the semimajor axis determination is about an order of magnitude larger than the corresponding change due to radiation pressure (e.g., Dermott et al., 2001).

[6] Note the bulk density for Apophis is unknown. We choose this value by considering an analogy with (25143) Itokawa (e.g., Abe et al., 2006), which is an object of similar spectral type and about the same size as Apophis. Should another value of the bulk density apply, one may use a simple inverse proportional scaling of our result with this parameter.

[7] The effective albedo in the bracket of the radiation pressure formula $\mathbf{f}_{\rm SRP}$ for a sphere is given by $A = \frac{9}{2}\int_0^1 d\mu_0[\mu_0 K_1(\mu_0) + \sqrt{1-\mu_0^2}K_2(\mu_0)]$ for a general scattering law. Because $K_1(\mu_0)$ is reasonably well approximated by $\frac{2}{3}\mu_0 A_B$ and is larger than $K_2(\mu_0)$ (see Fig. 2), we obtain $A \simeq A_B \simeq 0.2$ where this value of Bond albedo holds for the Hapke parameters chosen later in this section.

[8] Note that for Apophis the close approach distance uncertainty coincides very well with the 3D along-track orbital uncertainty (S. Chesley, personal communication).

[9] The full sample of the 200 Gaussian random spheres used in this work was described and shown in Čapek (2007), available through http://sirrah.troja.mff.cuni.cz/∼davok/.

Author's personal copy

is not unique and the one mentioned above corresponds to somewhat larger value of the G parameter in the IAU H–G system (see Verbiscer and Veverka (1995) for the transformation between the IAU A_g and H–G photometric parameters and the Hapke parameters). With a more typical $G \simeq 0.15$ value we would have: $w = 0.34$, $g = -0.27$, $h_s = 0.05$ and $B_0 = 1.98$, yielding approximately the same geometric albedo value. We have checked that this choice of the Hapke parameters provide about the same statistical results as the first set and in general the freedom in the choice of Hapke parameters does not change our conclusions.

Statistical results for displacement of the close approach distance in April 13, 2029, referred to its nominal value, are summarized in Figs. 3 and 4. The upper panels – (a) – in both figures show the composite effect of the incident and reflected radiation components, while the lower panels – (b) – show the effect of the reflected part only. We note that the overall orbit displacement due to the radiation pressure is small, in particular significantly smaller if compared to its maximum value derived for the hemispheric shape model. Clearly, the typically much higher symmetry between the north and south hemispheres in the Gaussian shapes, and we also believe in real asteroids, diminishes the possible orbital effect (see Vokrouhlický and Milani (2000) for the proof of the null effect in the case of the rotational spheroids).

For sake of interest, we point out that the ∼(1–2) km standard deviation from the ≃4 km mean due to the radiation pressure is actually comparable to the perturbation due to the Poynting–Robertson (PR) component (e.g., Vokrouhlický and Milani, 2000). Indeed, the estimated secular change of the semimajor axis due to

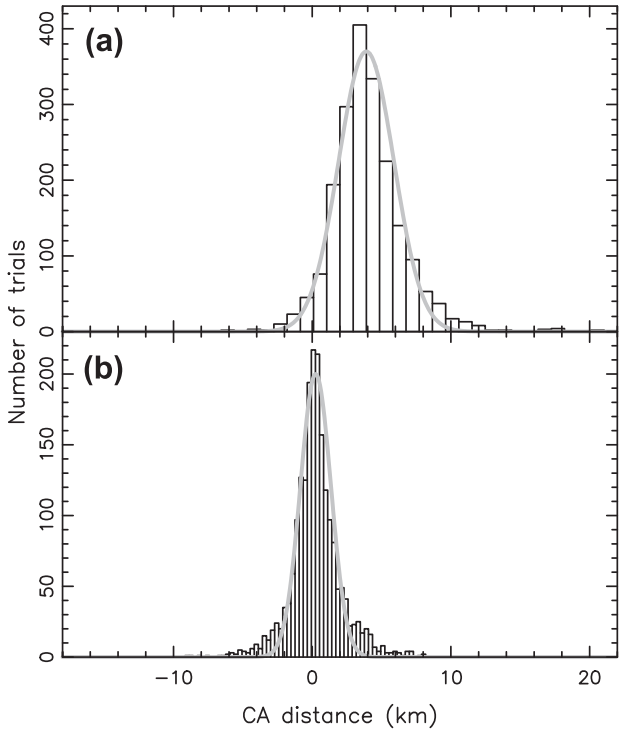

Fig. 3. Distribution of the close approach (CA) distance in April 2029 for 2000 trial simulations (200 different shapes modeled with Gaussian random spheres, each of which is given 10 different and random pole orientations) with the radiation forces. The close approach distance is referred to a nominal value 38046.825 km obtained in a simulation where radiation forces were excluded. Number of trials on the ordinate, close approach distance at the abscissa grouped into bins of 0.95 km (top) and 0.4 km (bottom) width. The top panel includes dynamical effects of the incident sunlight ($\mathbf{f}_{\rm inc}$) together with those of the reflected sunlight ($\mathbf{f}_{\rm sca}$). We assume Lambertian model for the scattering with an albedo of 0.2, effective size $D = 270$ m and bulk density 2 g/cm^3. The bottom panel shows effects of the reflected sunlight only. The grey Gaussian curves in both panels serve for a comparison only: the mean value at the top panel is ∼4 km, corresponding to the effect of the incident radiation, and the standard deviations are ∼2 km (top) and ∼1.1 km (bottom).

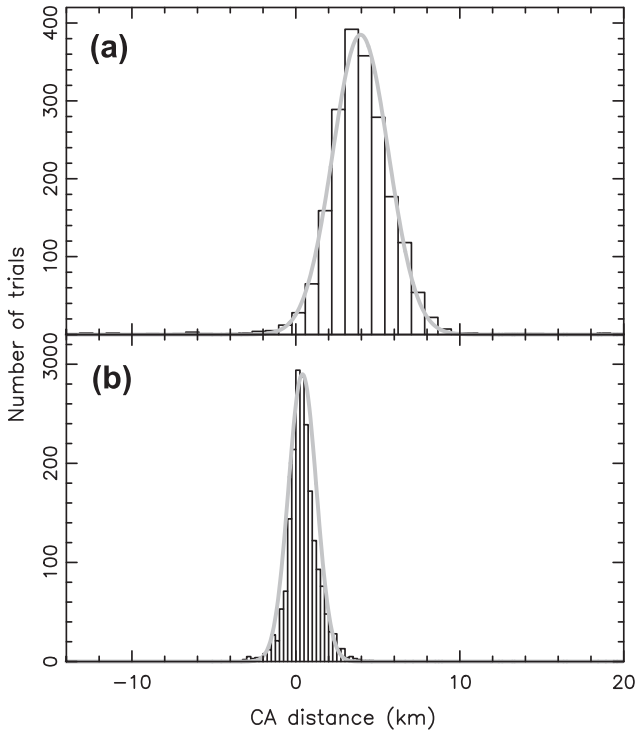

Fig. 4. The same as in Fig. 3, but now the reflected sunlight is modeled using the Hapke's bidirectional reflectance function (Section 2.2). The Hapke parameters are: $w = 0.5$, $g = -0.35$, $h_s = 0.02$ and $B_0 = 0.97$, yielding geometric albedo $A_g = 0.34$. The grey Gaussian curves in both panels serve for a comparison only: the mean value at the top panel is ∼4 km, corresponding to the effect of the incident radiation, and the standard deviations are ∼1.7 km (top) and ∼0.9 km (bottom).

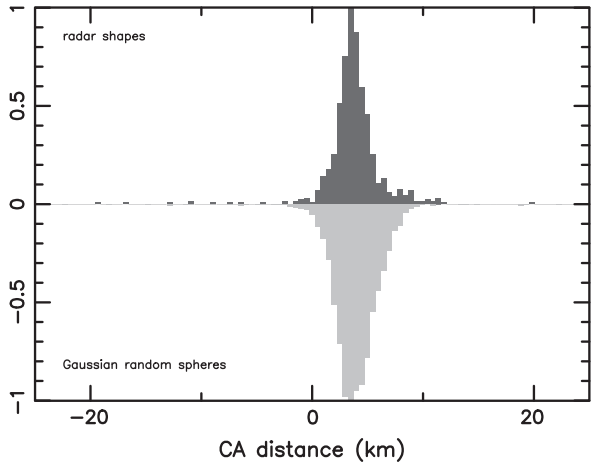

Fig. 5. Upper part: distribution of the close approach distance in April 2029 for 800 trial simulations (16 different radar-derived asteroid shapes, each of which is given 50 different and random pole orientations) with the radiation forces (ordinate values are arbitrarily normalized to unity in the maximum-occupied bin). The close approach distance is referred to a nominal value 38046.825 km obtained in a simulation where radiation forces were excluded. The sunlight reflected on the surface is modeled using the Hapke bidirectional function with parameters as in Fig. 4. Lower part (and inverted): normalized distribution of the close approach distance in April 2029 from the top panel (a) in Fig. 4 for comparison. Statistical properties of both distributions are basically identical: the difference in mean values is insignificant, while the standard deviation of the upper distribution ∼1.3 km is slightly smaller than that of the bottom distribution ∼1.7 km.

Author's personal copy

the PR effect for Apophis is $(da/dt)_{PR} \sim 3 \times 10^{-6}$ AU/Myr, about a factor 100–500 smaller than the corresponding value due to the Yarkovsky forces. Including the PR acceleration into the `OrbFit` integrator we obtained 1 km displacement of the close approach distance in April 13, 2029.

4.4. Radar shape models used

While we believe the Gaussian random sphere shapes represent the true asteroid models rather well, we finally tested this assumption. For that purpose we downloaded 16 shape models of the near-Earth asteroids determined using the radar ranging and available from http://echo.jpl.nasa.gov/links.html. We used these shape models of real asteroids and re-ran our simulation choosing each time 50 possible and random pole orientation in space. We scaled all models to the Apophis' 270 m effective size, used 2 g/cm^3 bulk density and assumed Hapke model of the sunlight reflection with the above given set parameters.

Statistical results for the 2029 close-approach displacement, as referred to the nominal orbit, are shown in Fig. 5, where a comparison with the same simulation but Gaussian random sphere shape models is also shown. As expected, there is no fundamental difference between results for the Gaussian shapes and those where we used the real asteroid shapes.

5. Conclusions

Results from our work show that the orbital perturbation of Apophis due to the solar radiation pressure, as propagated to this asteroids' very close approach in April 2029 (critical for the further evolution of its orbit), is more then order of magnitude smaller than the perturbation due to the Yarkovsky effect.[10] On the other hand, the few-kilometer size perturbation on the target plane position of the 2029 close approach of Apophis means the radiation pressure is a significant effect in absolute terms. This is because it can bring the true trajectory of Apophis close to or away from identified hundred-meter size (and smaller) keyholes associated with Earth-impacts in 2030s and later (see Chesley, 2006; Chesley et al., 2009). So two implications arise from our work.

First, until the Yarkovky effect for Apophis becomes constrained, the direct radiation pressure perturbation represents an addition to the orbital model that does not significantly improve its quality. Still, it can be included at low computer-time expense using the spherical model.

Second, things will change when the Yarkovsky effect is known for Apophis. Luckily, its close approach in January 2013 will at all likelihood provide a wealth of information: (i) not only physical parameters needed to the thermal force characterization will likely be constrained (such as the asteroid's shape, pole or thermal inertia), but (ii) the Yarkovsky effect could possibly also be directly measured using the precise orbital position as of 2013. Moreover, things may still further improve if high-quality astrometry data and physical parameter observations are taken in March 2021, during Apophis' next close approach to the Earth. At that moment, the Yarkovsky effect might be constrained to a significant-enough level that a more sophisticated model for direct solar radiation pressure might be included in the Apophis' orbital prediction. We believe this paper provides a suitable approach.

[10] The strength of the Yarkovsky effect on Apophis is not known yet. Our claim is based on statistically typical value expected for a body of its size and orbit (see Chesley, 2006), and for the pole position distribution among near-Earth asteroids (e.g., Kryszczyńska et al., 2007).

Acknowledgments

This work has been partly supported by the Grant Agency of the Czech Republic (Grant 205/08/0064) and the Research Program MSM0021620860 of the Czech Ministry of Education. We thank Andrea Milani and an anonymous reviewer for important suggestions that helped to significantly improve the final version of the paper.

References

Abe, S., and 16 colleagues, 2006. Mass and local topography measurements of Itokawa by Hayabusa. Science 312, 1344–1349.
Behrend, R., Damerdji, Y., Reddy, V.V., Gary, B.L., Correia, H., 2005. (99942) 2004 MN4 combined light-curve. <http://obswww.unige.ch/%7Ebehrend/r099942a.png>.
Bottke, W.F., Vokrouhlický, D., Rubincam, D.P., Brož, M., 2002. Dynamical evolution of asteroids and meteoroids using the Yarkovsky effect. In: Bottke, W.F., Cellino, A., Paolicchi, P., Binzel, R.P. (Eds.), Asteroids, vol. III. Arizona University Press, Tucson, pp. 395–408.
Bottke, W.F., Vokrouhlický, D., Rubincam, D.P., Nesvorný, D., 2006. The Yarkovsky and YORP effects: Implications for asteroid dynamics. Annu. Rev. Earth Planet. Sci. 34, 157–191.
Čapek, D., 2007. Thermal Effects in Physics and Dynamics of Small Bodies of the Solar System. PhD Thesis, Charles University, Prague.
Čapek, D., Vokrouhlický, D., 2004. The YORP effect with finite thermal conductivity. Icarus 172, 526–536.
Chapman, C.R., 2004. The hazard of near-Earth asteroid impacts on Earth. Earth Planet. Sci. Lett. 222, 1–15.
Chesley, S.R., 2006. Potential impact detection for near-Earth asteroids: The case of 99942 Apophis (2004 MN$_4$). In: Lazzaro, D., Ferraz-Mello, S., Fernández, J. (Eds.), Asteroids, Comets, Meteors. Cambridge University Press, Cambridge, pp. 215–228.
Chesley, S.R., Chodas, P.W., Milani, A., Valsecchi, G.B., Yeomans, D.K., 2002. Quantifying the risk posed by potential Earth impacts. Icarus 159, 423–432.
Chesley, S.R., Ostro, S.J., Vokrouhlický, D., Čapek, D., Giorgini, J.D., Nolan, M.C., Margot, J.-L., Hine, A.A., Benner, L.A.M., Chamberlin, A.B., 2003. Direct detection of the Yarkovsky effect by radar ranging to Asteroid 6489 Golevka. Science 302, 1739–1742.
Chesley, S.R., Vokrouhlický, D., Ostro, S.J., Benner, L.A.M., Margot, J.-L., Matson, R.L., Nolan, M.C., Shepard, M.K., 2008. Direct Estimation of Yarkovsky Accelerations on Near-Earth asteroids, Asteroids, Comets, Meteors 2008, Baltimore, Maryland, Contribution No. 1405, Paper Id. 8330.
Chesley, S.R., Milani, A., Tholen, D., Bernardi, F., Chodas, P., Micheli, M., 2009. An Updated Assessment of the Impact Threat from 99942 Apophis. DPS Meeting 41, # 43.06.
Delbò, M., Cellino, A., Tedesco, E.F., 2007. Albedo and size determination of potentially hazardous Asteroids: (99942) Apophis. Icarus 188, 266–269.
Dermott, S.F., Grogan, K., Durda, D.D., Jayaraman, S., Kehoe, T.J.J., Kortenkamp, S.J., Wyatt, M.C., 2001. Orbital evolution of interplanetary dust. In: Grn, E., Gustafson, B.S., Dermott, S., Fechtig, H. (Eds.), Interplanetary Dust. Springer-Verlag, Berlin, pp. 569–640.
Giorgini, J.D., and 13 colleagues, 2002. Asteroid 1950 DA's encounter with Earth in 2880: Physical limits of collision probability prediction. Science 296, 132–136.
Giorgini, J.D., Benner, L.A.M., Ostro, S.J., Nolan, M.C., Busch, M.W., 2008. Predicting the Earth encounters of (99942) Apophis. Icarus 193, 1–19.
Hapke, B., 1981. Bidirectional reflectance spectroscopy. 1. Theory. J. Geophys. Res. 86, 3039–3054.
Hapke, B., 2002. Bidirectional reflectance spectroscopy. 5. The coherent backscatter opposition effect and anisotropic scattering. Icarus 157, 523–534.
Helfenstein, P., Veverka, J., 1989. Physical characterization of asteroid surfaces from photometric analysis. In: Matthews, M.S., Binzel, R.P., Gehrels, T. (Eds.), Asteroids, vol. II. Arizona University Press, Tucson, pp. 557–593.
Kryszczyńska, A., La Spina, A., Paolicchi, P., Harris, A.W., Breiter, S., Pravec, P., 2007. New findings on asteroid spin-vector distributions. Icarus 192, 223–237.
Mihalas, D., 1978. Stellar Atmospheres. W.H. Freeman and Co., San Francisco.
Milani, A., Chesley, S.R., Sansaturio, M.E., Bernardi, F., Valsecchi, G.B., Arratia, O., 2009. Long term impact risk for (101955) 1999 RQ. Icarus 203, 460–471.
Muinonen, K., 1998. Introducing the Gaussian shape hypothesis for asteroids and comets. Astron. Astrophys. 332, 1087–1098.
Muinonen, K., Lagerros, J.S.V., 1998. Inversion of shape statistics for small Solar System bodies. Astron. Astrophys. 333, 753–761.
Rubincam, D.P., 2007. Orbital YORP and asteroid orbit evolution, with application to Apophis. Icarus 192, 460–468.
Verbiscer, A.J., Veverka, J., 1995. Interpretation of the IAU two-parameter magnitude system for asteroids in terms of Hapke photometric theory. Icarus 115, 369–373.
Vokrouhlický, D., Bottke, W.F., 2001. The Yarkovsky thermal force on small asteroids and their fragments. Choosing the right albedo. Astron. Astrophys. 371, 350–353.
Vokrouhlický, D., Čapek, D., 2002. YORP-induced long-term evolution of the spin state of small asteroids and meteoroids. Rubincam's approximation. Icarus 159, 449–467.

Author's personal copy

Vokrouhlický, D., Milani, A., 2000. Direct solar radiation pressure on the orbits of small near-Earth asteroids: Observable effects? Astron. Astrophys. 362, 746–755.

Vokrouhlický, D., Milani, A., Chesley, S.R., 2000. Yarkovsky effect on near-Earth asteroids: Mathematical formulation and examples. Icarus 148, 118–138.

Vokrouhlický, D., Chesley, S.R., Matson, R.D., 2008. Orbital identification for Asteroid 152563 (1992 Bf) through the Yarkovsky effect. Astron. J. 135, 2336–2340.

Paper 2

WDS'11 Proceedings of Contributed Papers, Part III, 19–24, 2011. *ISBN 978-80-7378-186-6 © MATFYZPRESS*

Modified Method of Asteroid Pairs Convergence

J. Žižka and D. Vokrouhlický

Institute of Astronomy, Charles University, V Holešovičkách 2, 18000 Prague 8, Czech Republic.

Abstract. Analysis of astronomical catalogs has recently revealed existence of a small population of asteroid couples (pairs) which reside on basically the same heliocentric orbit. While a different value of the mean anomaly implies they are two different objects, a common thinking is that they separated very recently from a parent asteroid sharing the same orbit. Indeed, backward integration of the orbits of the asteroids in pairs reveals very close encounters within the past tens to hundreds of kys. In this paper we first improve efficiency of these past encounters detection by computing relative state vectors of asteroid clones of the primary/secondary in the pair with respect to an arbitrary position on orbits of the clones of the secondary/primary in the same pair. In terms of a number of convergent configurations we typically gain several orders of magnitude as compared to the plain comparison of the clone positions and velocities used so far. Next, we apply our new method to the analysis of convergent configurations of asteroid pairs with similar-size components. [*Pravec et al.*, 2010] argue such pairs should not exist, provided their suggested mechanism of rotational fission is correct. We found 7 asteroid pairs which indicate fairly good convergence within the past 500 ky. We propose these bodies should be prime candidates for accurate photometric observations with the goal to determine their absolute magnitudes.

Introduction

Asteroid pairs are couples of asteroids which share basically the same heliocentric orbit. While today they are at different locations of their orbit, the tiny difference in their semimajor axis value implies their mean motion is slightly different and thus the two bodies could approach very closely in the past. Indeed, backward orbital tracking of components in the pairs reveals such very close encounters within the past tens to hundreds of kys for most cases. Examining mutual configuration of the two components at their separation, [*Vokrouhlický and Nesvorný*, 2008, 2009] proposed several possibilities of the processes that lead to formation of the pairs: (i) catastrophic collision, (ii) rotational fission, and (iii) binary system instability. [*Pravec et al.*, 2010] conducted an observational campaign determining rotation period P_1 of the primary component in numerous pairs. They found P_1 is correlated with the estimated mass ratio of the two components in the pair and concluded this finding strongly favorizes the rotational fission hypothesis.[1] One of the implications of the formation model promoted by [*Pravec et al.*, 2010] is that pairs should not have similar-size components. More quantitatively, assuming the same albedo value, difference in the absolute magnitude H values of the components in the pairs should always be larger than one magnitude. Yet, there are several candidate pairs which violate this rule. In this paper we re-examine these particularly interesting cases. First, using the most up-to-date asteroid catalog we anew identify candidates of pairs with closely similar-size components violating the standard model of [*Pravec et al.*, 2010]. Second, we numerically propagate their orbits to the past to confirm their convergence, henceforth strengthening their case as a real pair of asteroids of a common origin. In order to perform this second task as efficiently as possible, we also improve the convergence technique. We finally end-up with a list of seven confirmed asteroid pairs with similar-size components. We propose these asteroids should be carefully observed with the goal to determine their absolute magnitude as accurately as possible.

[1] [*Vokrouhlický and Nesvorný*, 2008] proposed the Yarkovsky-O'Keefe-Radzievskii-Paddack (YORP) effect (see, e.g., [*Bottke et al.*, 2006]) is the primary physical mechanism that is capable to efficiently bring small asteroids to the rotational fission limit.

Table 1. Convergent pairs with $\Delta H < 1$ mag. Absolute magnitudes H_1, H_2 and their differences ΔH are shown. $D_{\rm M}$ is the distance in the space of mean orbital elements and $D_{\rm P}$ the distance in proper element space. $T_{\rm conv}$ represents the age of each pair.

Asteroid pair		H_1 [mag]	H_2 [mag]	ΔH [mag]	$D_{\rm M}$ [m/s]	$D_{\rm P}$ [m/s]	$T_{\rm conv}$ [ky]
180906	217266	17.4	17.4	0.0	0.21	0.30	28-63
195479	2008 WK70	16.3	17.1	0.8	0.23	0.00	>37
165389	2001 VN61	16.3	16.8	0.5	0.48	0.09	>55
60677	142131	15.7	16.0	0.3	0.66	0.09	>97
2005 OS5	268305	16.9	16.7	0.1	0.90	0.54	>174
10484	44645	13.7	14.6	0.9	2.51	0.28	>212
80218	213471	16.5	16.6	0.1	4.14	1.41	>108

Selection of candidate pairs

Discovery of an asteroid pair proceeds in two steps: (i) first, its preliminary identification is based on proximity of the two orbits in the five dimensional space of orbital elements, and (ii) second, its confirmation is based on detailed orbital tracking of the two asteroid orbits backward in time. Note that (ii) is needed to justify a candidate couple to be a real pair, because random fluctuations in the asteroid distribution in the orbital space may also result in two very similar orbits. In this section we only briefly comment on the step (i), while a novel technique for (ii) is discussed in the next Section.

In order to quantitatively define proximity of two orbits in the space of orbital elements [*Vokrouhlický and Nesvorný*, 2008] introduced a metric $D_{\rm M}$

$$\left(\frac{D_{\rm M}}{na}\right)^2 = k_a \left(\frac{\delta a}{a}\right)^2 + k_e(\delta e)^2 + k_i(\delta \sin i)^2 + k_\Omega(\delta\Omega)^2 + k_\varpi(\delta\varpi)^2 \,, \qquad (1)$$

where $(\delta a, \delta e, \delta \sin i, \delta\varpi, \delta\Omega)$ is the difference vector of Keplerian orbital elements (semimajor axis a, eccentricity e, inclination i, longitude of node Ω and pericenter ϖ), n is the mean motion and k are numerical coefficients. Our choice of the first three elements, $k_a = 5/4$, $k_e = k_i = 2$ is based on the classical work of [*Zappalà et al.*, 1990]. Following [*Vokrouhlický and Nesvorný*, 2008], we choose $k_\Omega = k_\varpi = 10^{-4}$ for the relative weight factors of the secular angles in the metric $D_{\rm M}$. However, unlike [*Vokrouhlický and Nesvorný*, 2008], we use mean orbital elements rather than osculating elements of a given epoch. This is based on discussion of [*Rożek et al.*, 2011], who found that short-period perturbations in the osculating elements produce large oscillations in $D_{\rm M}$ and thus could obscure selection of the real pairs. The choice of mean orbital elements provides a more stable set of orbital parameters and it can serve to detect asteroid pairs with age up to My.

We used metrics (1) to search for asteroid pairs in the most recent catalog of mean orbital elements of asteroids as of April 2011. Given the motivation outlined in Section 1, our pool of candidates had to satisfy: (i) $D_{\rm M} < 10$ m/s (which sets the quantitative threshold of orbital proximity of our pairs; see [*Rożek et al.*, 2011]), and (ii) difference ΔH in absolute magnitudes of the secondary H_2 and primary H_1 components in the pair be $\Delta H < 1$ magnitude. We obtained about 15 candidate cases, out of which only some passed a more severe criterion of true orbital convergence discussed in the next Section. Basic parameters of those which successfully passed both criteria are given in Table 1. The absolute magnitudes H_1 and H_2 were taken from the `AstDyS`[2] catalog. These values may have an uncertainty up to $\simeq 0.5$ magnitude (e.g., [*Galád*, 2010]). We also complement the information of the distance $D_{\rm M}$ in the five dimensional space of mean orbital elements with a more traditional distance $D_{\rm P}$ in the three dimensional proper element space (e.g., [*Zappalà et al.*, 1990]). In this case we used analytic proper elements also provided by the `AstDyS` site. The last column gives information of the age of the pair $T_{\rm conv}$ as determined by orbital convergence in Section 4.

Backward numerical integrations and convergence conditions

In order to verify that a selected pair of asteroids is real, as opposed to a random fluke in the background population, we perform backward numerical integration of their orbit seeking conditions of their very close approach in Cartesian space. Details of this technique have been given in [*Vokrouhlický and Nesvorný*, 2008] or Supplementary information of [*Pravec et al.*, 2010]. In what follows we thus only

[2] http://hamilton.dm.unipi.it/astdys2

briefly recall basic steps and dwell on one improvement of identification of the convergent configurations developed in this paper.

Finite accuracy of astrometric observations implies the current orbits of asteroids in pairs, as given in catalogs, have some degree of uncertainty. This is typically expressed with a covariance matrix $\mathbf{\Sigma}$ of the orbital element $\mathbf{E}$ solution, determining probability distribution $p(\mathbf{E}) \sim \exp\left[-\frac{1}{2}\Delta\mathbf{E}\cdot\mathbf{\Sigma}\cdot\Delta\mathbf{E}\right]$ with $\Delta\mathbf{E} = \mathbf{E}-\mathbf{E}^\star$ and $\mathbf{E}^\star$ the best-fit orbital values. Any solution with high-enough $p(\mathbf{E})$ value are statistically equivalent and may represent true orbit of the body. With this perspective, we need to consider multiple realizations of the past orbital histories of a given asteroid, all starting from an initial data region with high $p(\mathbf{E})$ (typically a six dimensional ellipsoid). While these variants of the orbital evolution –that we call "geometrical clones"– are usually very close each other at current epoch, they rapidly diverge in the past. [*Vokrouhlický and Nesvorný*, 2008] also recognized, that the standard dynamical model which uses only planetary gravitational perturbations for the orbital evolution is not accurate enough for the purpose of convergence study of asteroids in pairs. Namely, the role of thermal accelerations, known as the Yarkovsky effect (e.g., [*Bottke et al.*, 2006]), is important. This is because the Yarkovsky effect may secularly change the value of semimajor axis over the timescale of the pair age by a value larger than the initial uncertainty of this element for the two orbits. Since the strength and sign of the Yarkovsky effect depends on apriori unknown parameters, such as surface thermal conductivity or rotation pole position, we must consider all possible values of the Yarkovsky effect. In practice, we assign to each geometrical clone a spectrum of expected Yarkovsky-effect values (modeled as an along-track acceleration producing semimajor axis change with a rate in an estimated interval of values $\langle (da/dt)_{\rm min}, (da/dt)_{\rm max}\rangle$; e.g., [*Vokrouhlický*, 1999]). We speak about the "Yarkovsky clones" to denote these variants of geometrical clones with different values of the Yarkovsky effect. In all examples given below we used 30 geometric clones and 40 Yarkovsky clones for each asteroid, thus altogether 1200 different variants of the possible past orbital evolutions for each body. Our integrations were performed using `SWIFT` software package [*Levison and Duncan*, 1994], where we included the effects of thermal accelerations. We used a fixed timestep of 5 d and performed integrations to 500 ky in the past.

A standard procedure for identification of convergent configurations of the numerically propagated clones of the two asteroids in the pair is as follows. At every timestep we compare heliocentric state vectors of all clones of the primary with all clones of the secondary component in the pair. In particular, let $(\mathbf{r}_1, \mathbf{v}_1)$ and $(\mathbf{r}_2, \mathbf{v}_2)$ are those state vectors, we compute (i) Cartesian distance $D_{\rm rel} = |\mathbf{r}_1 - \mathbf{r}_2|$, and (ii) relative velocity $V_{\rm rel} = |\mathbf{v}_1 - \mathbf{v}_2|$. We consider the configuration convergent, when both $D_{\rm rel}$ and $V_{\rm rel}$ are smaller than some quantitative threshold. In the case of distance, we require $D_{\rm rel} \le R_{\rm Hill}$, where $R_{\rm Hill} = r_1 \left(\frac{M_{\rm bin}}{3M_{\rm Sun}}\right)^{1/3}$, $M_{\rm bin}$ is the total estimated mass of the asteroids in the pair, $M_{\rm Sun}$ is the solar mass and r_1 is the heliocentric distance of the primary component in the pair. Recall that $R_{\rm Hill}$ is a measure of distance between the two asteroids when their mutual gravitational interaction becomes more important than the gravitational attraction by the Sun. In the case of velocity, we require $V_{\rm rel} \le V_{\rm esc}$, where $V_{\rm esc}$ is the estimated escape velocity from a spherical body of mass $M_{\rm bin}$. For reference, we note that $R_{\rm Hill}$ is typically of the order of several hundreds to thousands of km, while $V_{\rm esc}$ is typically few m/s.

An improved method for clone convergence

A major drawback of the convergence criterion outlined above is that the uncertainty ellipsoids occupied by the geometrical and Yarkovsky clones rapidly expand as the time increases to the past. So while their sampling is satisfactory at the current epoch, they become quickly under-sampled by the clones some tens to hundreds of thousands years ago. To solve the problem, we would need to use orders of magnitude more clones, which is not possible due to the CPU limitations. In this paper, we propose a compromise solution. Put in simple words, our strategy is as follows. When the clones of primary and secondary are close enough, we evaluate distance of a first chosen clone *to the orbit* of the second clone and vice-versa (see Fig. 1). This approach assumes the closest point on the orbit to a given clone of the first asteroid would have been occupied with a hypothetical clone of the second asteroid, were we able to consider a huge number of them. In the same time, this approach is computationally more efficient than determination of the orbital MOID (The Minimum Orbit Intersection Distance) for the two clone orbits (e.g., [*Gronchi*, 2000]).

Put in more quantitative terms we proceed as follows. At a given timestep of our numerical propagation of clones for the primary and secondary components in the pair we compute their mutual distances (as in the classical approach outlined above). When the distance $D_{\rm rel}$ of two particular clones is less than a specified threshold $D_{\rm tresh}$, $\simeq 0.003$ AU in our case, we switch to a mode which computes distance of

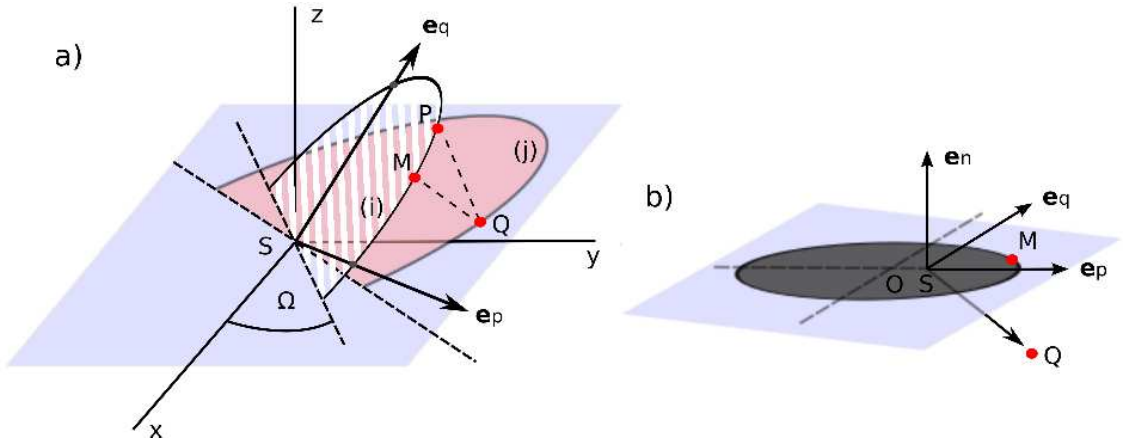

Figure 1. Geometrical insight into the new convergence method. a) The ellipses (i) and (j) are the osculating trajectories of the i-th clone of the primary and j-th clone of the secondary components in the pair. Points P and Q indicate their position at a given time as provided by direct numerical integration. Taking the clone Q as a reference, we seek point M on the osculating orbit of the clone P which has the minimum distance to Q. b) Q transformed into the reference frame $(\mathbf{e}_p, \mathbf{e}_q, \mathbf{e}_n)$ and clone P osculating orbit.

a clone to the orbit of its counterpart clone. For instance, let $(\mathbf{r}_1, \mathbf{v}_1)$ be the heliocentric state vector of the first clone (primary, say) and $(\mathbf{r}_2, \mathbf{v}_2)$ be the heliocentric state vector of the second clone (secondary, say), we

- first determine orbital elements of the second clone and from them we compute the orbit-attached orthonormal basis $(\mathbf{e}_p, \mathbf{e}_q, \mathbf{e}_n)$ such that $\mathbf{e}_p$ is directed to the osculating pericenter, $\mathbf{e}_n$ is directed along the osculating angular momentum vector and $\mathbf{e}_q = \mathbf{e}_n \times \mathbf{e}_p$;
- we determine the transformation matrix $\mathbf{T}$ from the heliocentric coordinate system used in our orbital propagator to the $(\mathbf{e}_p, \mathbf{e}_q, \mathbf{e}_n)$ frame, and transform the state vector of the first clone using $\mathbf{r}_1 \to \mathbf{R}_1 = \mathbf{T} \cdot \mathbf{r}_1$ and $\mathbf{v}_1 \to \mathbf{V}_1 = \mathbf{T} \cdot \mathbf{v}_1$;
- the elliptical orbit of the second clone obviously reads $\mathbf{R}_2(E) = (X_2(E), Y_2(E), 0)^{\mathrm{T}}$ in the $(\mathbf{e}_p, \mathbf{e}_q, \mathbf{e}_n)$ frame, such that $X_2(E) = a_2\,(\cos E + e_2)$ and $Y_2(E) = a_2\sqrt{1-e_2^2}\,\sin E$, where a_2 and e_2 are semimajor axis and eccentricity, and $E \in \langle 0, 2\pi \rangle$ is the eccentric anomaly;
- week the point $\mathbf{R}_2(E^\star)$ which minimizes $D^2 = (\mathbf{R}_1 - \mathbf{R}_2) \cdot (\mathbf{R}_1 - \mathbf{R}_2)$ by iteratively solving $E^\star$ from $(\mathbf{R}_1 = (X_1, Y_1, Z_1)^{\mathrm{T}})$

$$Y_1\sqrt{1-e_2^2}\cos E^\star + a_2 e_2^2\,\sin E^\star \cos E^\star - (X_1 + a_2 e_2)\sin E^\star = 0 \tag{2}$$

  (obviously, we make sure to determine global minimum of the distance function $D(E)$);
- the relative velocity of the first clone to the closest point on the orbit of the second clone is then given by $V_\star = V(E^\star) = |\mathbf{V}_1 - \mathbf{V}(E^\star)|$ with

$$\mathbf{V}(E^\star) = \sqrt{\frac{GM_{\mathrm{Sun}}}{a_2}}\left(\frac{-\sin E^\star}{1-e_2\cos E^\star}, \frac{\sqrt{1-e_2^2}\cos E^\star}{1-e_2\cos E^\star}, 0\right) . \tag{3}$$

We repeat the procedure twice, each time choosing one of the two clones as a reference point and the latter represented by its orbit. The resulting minimum distance and velocity values $(D_\star = D(E^\star), V_\star)$ are used in the statistical considerations instead of the plain values $(D_{\mathrm{rel}}, V_{\mathrm{rel}})$. While improving previous results by detecting more encounter configurations, our new method is obviously only approximate. Most importantly, it is not optimized to analyze clones convergence for pairs older than couple of hundreds of kys. This is because, when clones for either primary or secondary components spread over the whole heliocentric orbit, our criterion of determining $(D_\star, V_\star)$ only when $D_{\mathrm{rel}} \le D_{\mathrm{tresh}}$ is too restrictive. We plan to improve this issue in the forthcoming work.

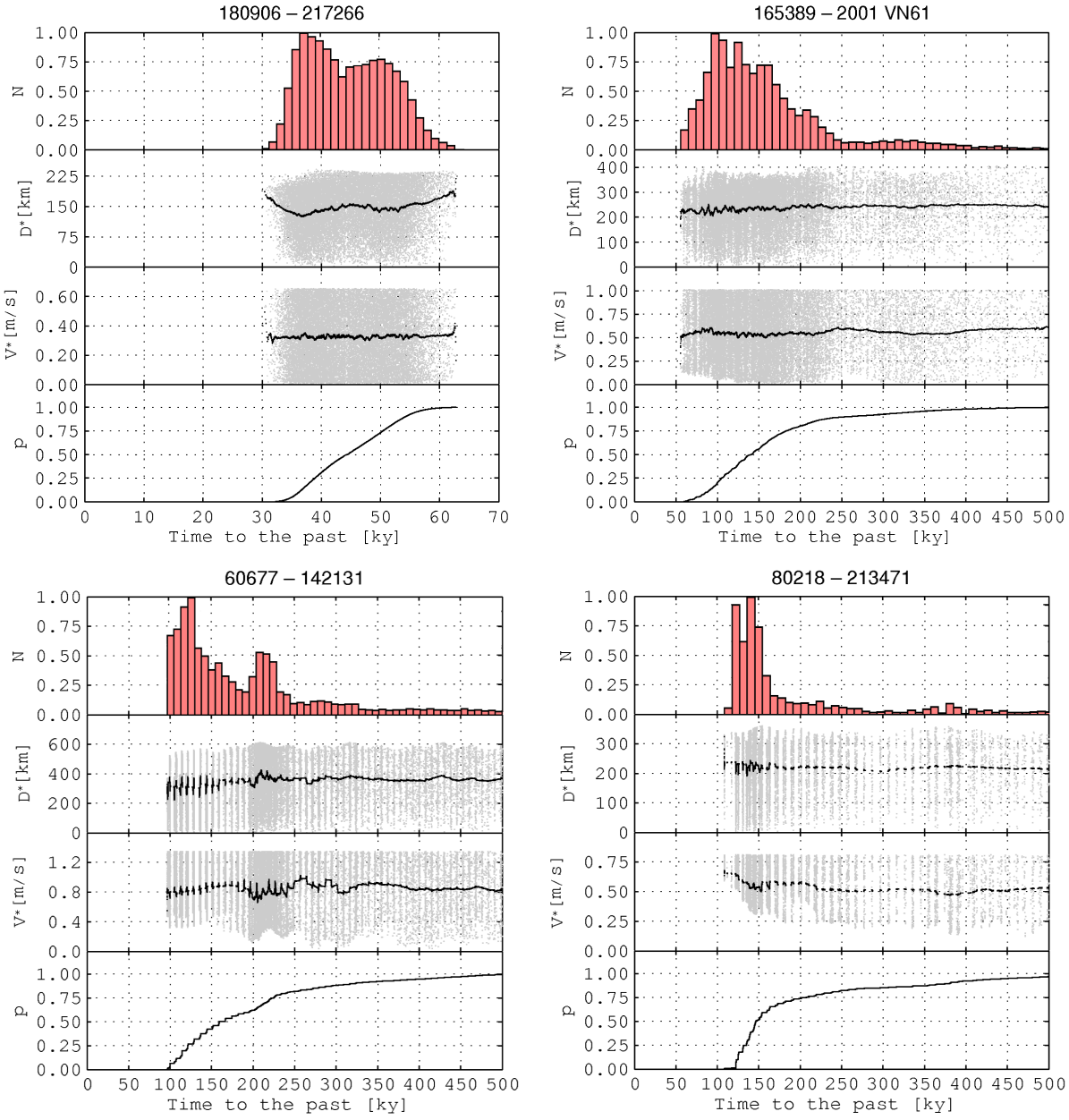

Figure 2. Results of convergence efforts for clones in the candidate pairs: 180906-217266 (top and left), 165389-2001 VN61 (top and right), 60677-142131 (bottom and left) and 80218-213471 (bottom and right). The abscissa is time to the past in ky. Upper panel shows distribution of number of convergent solutions binned in 1.5 ky to 10 ky intervals of time, henceforth providing statistical information about the age of the pair (the distribution has been normalized to unity at the most occupied bin). The bottom panel shows the same information but in cumulative form. The second and the third panels show $(D_\star, V_\star)$ values for converging clones; the black line is an average computed over a 10 y running window.

Asteroid pairs with $\Delta H < 1$: a brief analysis

We applied the above mentioned method to backward tracking of components in the selected candidates of similar-size asteroid pairs ($\Delta H < 1$ mag). Out of these, only 7 revealed solid convergence of clones and age less than 500 ky. Figures 2 and 3 show fundamental properties of these successful solutions. The first-shown pair, 180906-217266, is somewhat exceptional because of its young and well-defined age. The only caveat is that these bodies are rather small, we estimate their size to ~ 1.5 km only, such that their observation will require a middle-class telescope (1.5 m mirror size and more).

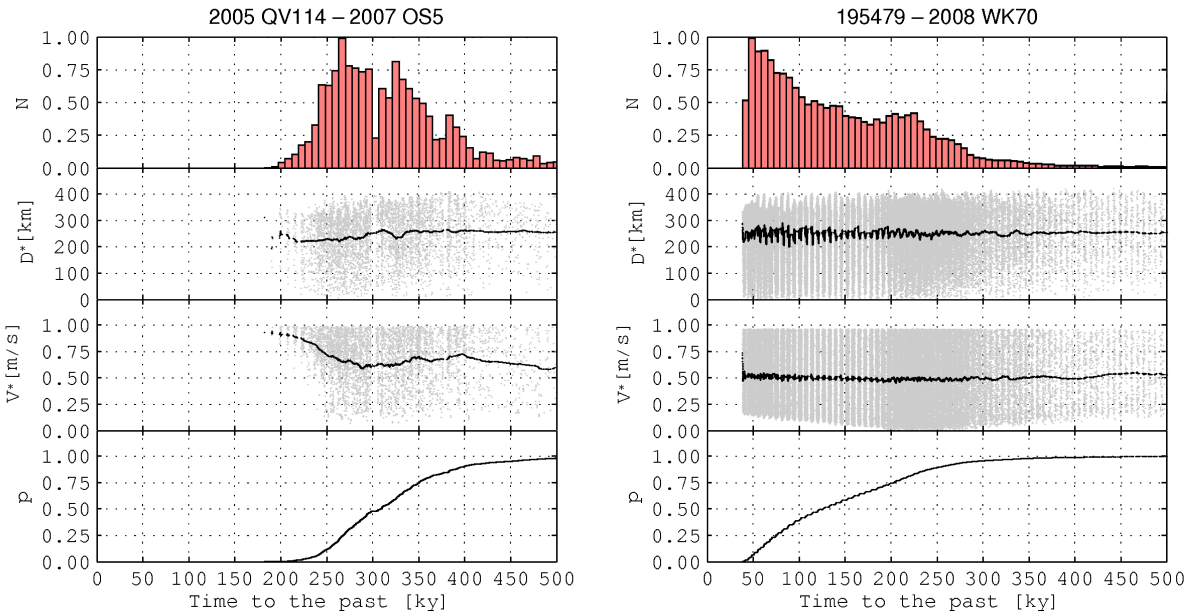

Figure 3. The same as in Fig. 2 but for candidate pairs: 268305-2007 OS5 (left) and 195479-2008 WK70 (right).

Conclusions

We found 7 asteroid pairs which indicate a solid convergence within the past 500 ky and which have formally similar-size components (as derived from their absolute magnitude values). This is apparently in contradiction with the currently standard model of their separation as individual bodies (cf. [*Pravec et al.*, 2010]). There are two possibilities of solution: (i) either the absolute magnitudes of the two components in these pairs were not determined accurately enough, or (ii) the formation scenario of the pairs needs modifications. Obviously the second possibility is more interesting, but we need first to rule out the first possibility. For that reason we propose the pairs identified in this paper need to be carefully observed with the goal to determine their absolute magnitude values with an uncertainty of $\simeq 0.05$ mag.

References

Bottke, W. F., Vokrouhlický, D., Rubincam, D. P., and Nesvorný, D., The Yarkovsky and YORP effects: Implications for asteroid dynamics, *Ann. Rev. Earth Planet. Sci.*, 34, 157–191, 2006.

Galád, A., Accuracy of calibrated data from the SDSS moving object catalog, absolute magnitudes, and probable lightcurves for several asteroids, *Astron. & Astrophys.*, 514, A55, 2010.

Gronchi, G., An algebraic method to compute the critical points of the distance function between two Keplerian orbits, *Cel. Mech. Dyn. Ast.*, 93, 295–329, 2005.

Levison, H. F., and Duncan, M. J., The long-term dynamical behavior of short-period comets, *Icarus*, 108, 18–36, 1994.

Pravec, P., and 25 colleagues, Formation of asteroid pairs by rotational fission, *Nature*, 466, 1085–1088, 2010.

Rożek, A., Breiter, S., and Jopek, T. J., Orbital similarity functions application to asteroid pairs, *Mon. Not. Roy. Astron. Soc.*, 412, 987–994, 2011.

Vokrouhlický, D., A complete linear model for the Yarkovsky thermal force on spherical asteroid fragments, *Astron. & Astrophys.*, 344, 362–366, 1999.

Vokrouhlický, D., and Nesvorný, D., Pairs of asteroids probably of a common origin, *Astron. J.*, 136, 280–290, 2008.

Vokrouhlický, D., and Nesvorný, D., The common roots of asteroids (6070) Rheinland and (54827) 2001 NQ8, *Astron. J.*, 137, 111–117, 2009.

Zappalà, V., Cellino, A., Farinella, P., and Knežević, Z., Asteroid families. I. Identification by hierarchical clustering and reliability assessment, *Astron. J.*, 100, 2030–2046, 1990.

Paper 3

A&A 595, A20 (2016)
DOI: 10.1051/0004-6361/201629290
c ESO 2016

Astronomy & Astrophysics

Asteroids 87887 – 415992: the youngest known asteroid pair?

J. Žižka[1], A. Galád[2], D. Vokrouhlický[1], P. Pravec[3], P. Kušnirák[3], and K. Hornoch[3]

[1] Institute of Astronomy, Faculty of Mathematics and Physics, Charles University, V Holešovičkách 2, 18000 Prague, Czech Republic
e-mail: jinziz@centrum.cz, vokrouhl@cesnet.cz
[2] FMFI, Comenius University, Mlynská dolina F1, 842 48 Bratislava, Slovakia
[3] Astronomical Institute, Czech Academy of Sciences, Fričova 298, 25165 Ondřejov, Czech Republic

Received 11 July 2016 / Accepted 27 August 2016

ABSTRACT

Context. Pairs of asteroids, that is, couples of single bodies on tightly similar heliocentric orbits, were recently postulated as a new category of objects in the solar system. They are believed to be close twins to binary and multiple systems.
Aims. Ages of the known pairs range from about 15 kyr to nearly a million years. Beyond the upper limit, the pairs disperse in the background population of asteroids and become difficult to detect. Below the lower limit, the pairs should be easily recognizable if they exist and are discovered by surveys. Using the available data, we analyze the possible existence of very young asteroid pairs with clearly proven ages ≤10 kyr.
Methods. We searched for candidate very young asteroid pairs in the current catalog of asteroid orbits. After a preliminary analysis, we selected the most promising case of the small asteroids (87887) 2000 SS286 and (415992) 2002 AT49. We collected photometric observations to determine their rotation periods and absolute magnitudes.
Results. The rotation period of (87887) 2000 SS286 is 5.7773 ± 0.0004 h. Analysis of the data for (415992) 2002 AT49 indicates as the most probable period 2.6366 ± 0.0003 h, but other solutions are still possible. The composite light curves of the two asteroids have very low amplitudes, 0.22 and 0.12 mag, suggesting roundish shapes. Our observations also allow us to determine the absolute magnitude in R band H_R = 14.99 ± 0.04 and H_R = 16.24 ± 0.03 for the primary and secondary components. A transformation to the visible band provides H = 15.44 ± 0.05 and H = 16.69 ± 0.04. These two asteroids experienced a very close encounter, probably a formation event, some 7.4 ± 0.3 kyr ago. The formal extension of our numerical runs backward in time reveal that these close encounters may have continued, starting from 45 kyr ago. However, based on tests using synthetic fission events, we argue that the older age solutions might be the true solution only at (10–15)% level, assuming their low initial separation velocity is of between 10–20 cm s^{-1}. This means that 87887–415992 probably is the youngest known asteroid pair in our dataset with a reliable determined age.

Key words. celestial mechanics – minor planets, asteroids: general

1. Introduction

Vokrouhlický & Nesvorný (2008) discovered a population of asteroid pairs that share very similar heliocentric orbits. After they checked that the proximity of the orbits of these pairs was well above a statistical false-positive level, the authors dubbed them asteroid pairs. Noting the anomalously low separation velocities of the two components in the pair at the proposed moment of their origin, Vokrouhlický & Nesvorný (2008) also speculated about the formation mechanisms. They proposed that either (i) the parent body of the pair underwent a rotational fission that directly sent the fragments onto separate heliocentric orbits, or that (ii) a binary or multiple asteroid system became unstable, which caused a satellite to switch from bound to unbound orbit about a primary. Some subsequent studies focused on analysing individual pairs, especially the cases where astronomical observations allowed the best physical characterization. For instance, the very well constrained orbits of (6070) Rheinland and (54827) 2001 NQ8 allowed tracing their mutual configuration back to a near-contact system (e.g., Vokrouhlický & Nesvorný 2009). The conveniently large size of the primary component in this pair allowed obtaining enough photometric observations to solve for the pole orientation of this asteroid (Vokrouhlický et al. 2011); a more detailed analysis of the past convergence conditions of the two asteroids then allowed predicting that the primary and secondary components in this pair had the same rotation sense. Photometric observations of other pairs allowed addressing this problem directly, which proved that in the first case for which complete information is available, (2110) Moore-Sitterly and (44612) 1999 RP27, the pole orientations are indeed similar (Polishook 2014). The relationship of the two components in the asteroid pairs has been confirmed using spectroscopic observations that revealed a close similarity of their color indexes or spectra (e.g., Moskovitz 2012; Polishook et al. 2014a,b; Duddy et al. 2012, 2013; Wolters et al. 2014). Slight differences, in particular redder spectra of the primary component in some pairs, have been interpreted as a possible dust settling on the larger asteroid during the formation of the pair. Finally, the relationship between pairs and binaries received a new twist when it was reported that the primary component in some pairs is a binary, or even multiple, system (e.g., Vokrouhlický 2009; Pravec et al. 2013, 2016).

The most convincing hint about the origin of asteroid pairs was provided by observations of Pravec et al. (2010). These authors analyzed the correlation between the rotation period of the primary (larger) asteroid in the pair and the estimated size ratio

of the two asteroids in the pair. They found that the correlation was most easily explained with a model in which the parent body of the pair underwent rotational fission, with prompt ejection of the smaller component onto an unbound orbit.

The next step in unraveling the circumstances of the asteroid pair origin is to determine which process (or processes) caused the fission in the parent object. Vokrouhlický & Nesvorný (2008) speculated that the parent asteroids were spun up by the Yarkovsky-O'Keefe-Radzievski-Paddack (YORP) effect (e.g., Vokrouhlický et al. 2015). This seems to be the only universal process that affects the rotation rate of asteroids smaller than $\lesssim$20−30 km strongly enough to bring them close to the fission limit within an astronomically relevant timescale. One possibility to confirm the YORP effect as the most likely candidate for the underlying process of asteroid pair formation would be to determine the exact statistics of pair formation in time and compare it with the prediction of the YORP theory. This goal is, however, well beyond the scope of the current paper. Ideally, it would imply selecting a size category of asteroid pairs and determine a complete sample of asteroid pairs that formed in the main belt, for example, within the past one hundred thousand years. However, there are strong selection and observation-incompleteness effects that prevent us from obtaining this information. Deciphering the respective bias correction is a complicated task that is yet to be done. In addition to finding the pairs, we would need to determine when precisely they formed. This is also difficult and uncertain. Previous studies have demonstrated that the uncertainty in the orbit propagation model, which is mainly due to unconstrained thermal accelerations, often results in a wide range of possible age solutions of the given pair. Moreover, in Sect. 4 we describe yet another level of uncertainty in determining the age of a given pair that has to do with the synodic cycles of their mutual heliocentric motion.

A simpler, but still interesting task, is to determine the youngest age of the asteroid pairs that belong to a given size category. This still faces the problem that the asteroid population is observationally not completely known, but at least it is less dependent on our ability of recognizing an asteroid pair among the population of unrelated asteroids (if both components in the pair are currently known in our catalogs). The reason is that when the asteroid pair is formed by a gentle separation that is characterized by a relative velocity of a fraction of a meter per second (see, e.g., Vokrouhlický & Nesvorný 2008, 2009), the heliocentric orbits of the two components are even more similar than is typical of older pairs. We recall that the asteroid pairs have been searched in the five-dimensional space of osculating orbital elements $(a, e, I, \Omega, \varpi)$, where a is the semimajor axis, e the eccentricity, I the inclination, Ω the longitude of node, and ϖ the longitude of pericenter (alternatively, the mean orbital elements might be used instead of the osculating ones, e.g., Rożek et al. 2011). For asteroid pairs that are several tens of kyr old, the value of the osculating mean longitude in orbit λ is unrelated because of Keplerian shear and differential Yarkovsky effects in their orbits. In principle, extremely young pairs may also have similar values of λ. A naive calculation shows that simple Keplerian shear would produce $|\Delta\lambda| \simeq 10°$−$20°$ in less than 10 kyr for orbits that have a semimajor axis difference of $|\Delta a| \simeq 10^{-5}$ au. This is because the third Kepler law provides a difference $\Delta\lambda$ in mean longitudes of two confocal Keplerian orbits with a slightly different values Δa of semimajor axis: $|\Delta\lambda|/360° \simeq 1.5\,(|\Delta a|/a)\,(T/P)$. Here, P is the orbital period and T is the time elapsed. Plugging in typical values for the orbits in the inner main belt and $T = 10$ kyr, we obtain the above-mentioned estimate. Even though planetary perturbations make the age determination more complex, numerical tests indicate that this estimate is roughly correct.

However, there is one more fundamental problem that indicates that a similarity of λ values is a necessary, but not sufficient, condition for the young age of the asteroid pair. This problem has been pointed out by Vokrouhlický & Nesvorný (2008), who studied the very close relative configuration of asteroids (1270) Datura and (215619) 2003 SQ168, which currently have $|\Delta\lambda| \simeq 1.6°$ and $|\Delta a| \simeq 3 \times 10^{-5}$ au in osculating elements. Vokrouhlický & Nesvorný (2008; see their Fig. 6) showed that this configuration repeats in time in a cycle of more than 100 kyr. While this pair might be very young, it might also be several hundreds of kyr old. In fact, because it is a member of the Datura family, its age is probably more than 500 kyr (e.g., Nesvorný et al. 2006; Vokrouhlický et al. 2009). This effect has been interpreted in terms of synodic cycles of the relative motion of the pair components about the Sun. At each completion of the synodic cycle, the two asteroids approach each other very closely, mimicking the initial conditions, until orbital perturbations from planets and the Yarkovsky effect do not move the orbits away from each other. Depending on the asteroid pair, this timescale may be longer than one Myr. All of the tightest pairs originally discovered by Vokrouhlický & Nesvorný (2008) belong to this older category, as has been shown in subsequent numerical tests.

With these results, we conclude that the youngest currently known asteroid pairs are $\simeq$15 kyr old. This is also the case of the above-mentioned well-studied pair of asteroids (6070) Rheinland and (54827) 2001 NQ8, for which Vokrouhlický et al. (2011) determined an age of 17.0 ± 0.2 kyr (see also Galád 2012, who additionally took into account gravitational effects of the dwarf planet Ceres and the largest asteroids, and obtained slightly younger age for this pair). There are two more cases, mentioned in Table 1 of Pravec et al. (2010), that might be of a comparable age. The question now is whether these are the youngest asteroid pairs among the currently known population. We here examine this question and consider 10 kyr as an order-of-magnitude limit for a young age.

The plan of our paper is as follows. We first sift the data in the current catalog of asteroid orbits and search for very tight asteroid pairs with similar longitudes in orbit (Sect. 2). As explained above, asteroid pairs with potentially youngest ages are expected to be contained in this sample. After eliminating false or very uncertain cases, we select the best candidate containing asteroids (87887) 2000 SS286 and (415992) 2002 AT49. Fortunately, these two objects were included in our observational efforts of determining the physical parameters of the components in asteroid pairs. We therefore report the currently available data and provide an estimate of the rotation periods and absolute magnitudes for the two asteroids in the selected pair (Sect. 3.2). Next, we analyze in detail a suite of numerical integrations of the two orbits backward in time, with the goal of determining the age of the 87887–415992 asteroid pair in Sect. 4. We pay particular attention to discerning the true age from false solutions that tend to repeat with the synodic period of the orbital revolution of these asteroids about the Sun. Implications and conclusions are collected in Sect. 5.

2. Candidate search

We conducted a new search for very close asteroid pairs in the updated catalog of the Minor Planet Center, which contained approximately 713 000 objects as of April 15, 2016. Of these

objects some 130 000 resided on single-opposition orbits that we discarded because their elements are typically quite uncertain. As described above, we sought not only for tight pairs in the five-dimensional space of $(a, e, I, \Omega, \varpi)$ osculating elements, but we considered the difference in the mean longitude in orbit λ of the two orbits. Based on the discussion at the end of Sect. 1, we selected only the pairs with $|\Delta\lambda| \leq 15°$. To ensure that we considered potential asteroid pairs, we also required cases with distance $d \leq 15$ m s^{-1}, using metrics defined in the space of osculating orbital elements (see Eq. (1) and Figs. 1 and 2 in Vokrouhlický & Nesvorný 2008).

With this procedure we obtained 23 potential candidates for very young pairs. We eliminated situations when the "pair" was a member of a known compact and very young asteroid family, such as (1270) Datura and (215619) 2003 SQ168. These situations arise from the incidental orbital proximity of two fragments that are launched at nearly the same relative velocity with respect to the parent body of the family. After performing this first-level trimming, we were left with 16 candidates that were not in any obvious young asteroid family.

Some of these remaining pairs have been analyzed in previous publications, where we demonstrated their convergence beyond the limit of 10 kyr. This was the case of

- (21436) Chaoyichi and (334916) 2003 YK39;
- (23998) 1999 RP29 and (205383) 2001 BV47;
- (56232) 1999 JM31 and (115978) 2003 WQ56;
- (63440) 2001 MD and (331933) 2004 TV14; and
- (76111) 2000 DK106 and (354652) 2005 JY103;

all reported in Pravec et al. (2010). As a consequence, these pairs were eliminated from our further considerations.

We numerically integrated nominal orbits of the remaining candidates and found that some of them did not converge in their formation configuration within the past 10 kyr. This was the case of

- (70208) 1999 RX33 and 2013 GZ99;
- (74096) 1998 QD15 and (224857) 2006 YE45;
- (188577) 2005 GM1 and (420756) 2013 EW4;
- (267333) 2001 UZ193 and 2007 DY95; and
- (320025) 2007 DT76 and 2007 DP16.

We estimated the greatest Yarkovsky effect in each of these cases and ensured that including this perturbation in our calculation did not change our conclusions.

At this stage, we were left with the following six last cases (sorted here according to increasing difference $|\Delta\lambda|$ of the mean longitude in orbit):

- (229401) 2005 SU152 and 2005 UY97 ($|\Delta\lambda| \simeq 1.1°$);
- (17198) Gorjup and (229056) 2004 FC126 ($|\Delta\lambda| \simeq 1.1°$);
- (355258) 2007 LY4 and (404118) 2013 AF40 ($|\Delta\lambda| \simeq 4.7°$);
- (87887) 2000 SS286 and (415992) 2002 AT49 ($|\Delta\lambda| \simeq 5.3°$);
- (356713) 2011 UK160 and 2014 QX220 ($|\Delta\lambda| \simeq 9.8°$); and
- (99052) 2001 ET15 and (291788) 2006 KM53 ($|\Delta\lambda| \simeq 10.5°$).

Again, some of these cases have been analyzed in the past. For instance, Fig. 4 in the supplementary materials of Pravec et al. (2010) shows the distribution of the past converging solutions for the tightest pair (229401) 2005 SU152 and 2005 UY97. While convergence may have been achieved as early as ≃3 kyr ago, many more solutions converge far beyond the 10 kyr limit, some up to 100 kyr ago. This huge spread is mainly caused by the small size of these asteroids and by the still rather poorly constrained orbit of the smaller component 2005 UY97. The former implies that Yarkovsky forces are potentially strong, and different clone variants for the asteroids in this pair therefore have a chance to closely approach at a widely spread time interval in the past. At the moment, we therefore exclude this pair from our analysis. A similar situation occurs for (355258) 2007 LY4 and (404118) 2013 AF40, and (356713) 2011 UK160 and 2014 QX220. In both cases, we have some solutions converging within the past 10 kyr, but most indicate a far older age. In all likelihood, these pairs will be found to be older than 10 kyr when their orbits are improved and physical parameters are determined that allow constraining the thermal accelerations.

The pairs (17198) Gorjup and (229056) 2004 FC126, and (99052) 2001 ET15 and (291788) 2006 KM53 present a slightly different story. In both cases we performed a detailed backward integration of a large number of clone variants of the two asteroids in the pair (some of which also sampled different possible strengths of the Yarkovsky forces). For the tighter pair (17198) Gorjup and (229056) 2004 FC126 we found that the clone clouds of the two components closely approached some 230 yr ago, but they missed each other at a minimum distance ≃50 000 km and at a minimum relative velocity ≃3 m s^{-1}. These values exceed our criteria of convergence (e.g., Vokrouhlický & Nesvorný 2008; Pravec et al. 2010), namely an encounter distance of about a Hill radius of the parent body of the pair (some 750 km) and a relative velocity on the order of the escape velocity from the parent body (some 1.5 m s^{-1}). Continuing the integration backward in time, we found that these conditions become eventually satisfied starting from 100 kyr ago. We conclude that this pair is older than 100 kyr and recently repeated their close initial configuration after completing a synodic cycle of their relative motion about the Sun. We found that a similar situation also occurred for the pair (99052) 2001 ET15 and (291788) 2006 KM53. Clone variants of the two asteroids have a chance to encounter some 5 kyr ago at a minimum distance of ≃10 000 km and with a minimum relative velocity of ≃1.5 m s^{-1}. While the velocity limit barely approaches the required level of the escape velocity from the parent body of the pair, the recorded minimum distance is about 15 times larger than the required threshold. This again indicates that the two asteroids recently completed a synodic cycle of their relative motion, and the true age of this pair is at least 100 kyr.

Finally, our candidate list shrunk to the pair consisting of asteroids (87887) 2000 SS286 and (415992) 2002 AT49. A preliminary orbital integration backward in time indicated a fair possibility of a very close encounter of these bodies some 7 kyr ago that would match our criteria for the common origin of the two bodies in a fission of their parent asteroid. However, we also have to revert the argument: is our finding indicative of a true age of this pair, or are there possible and statistically likely solutions preceding the young one? The analysis of this problem is the core of our paper, and we focus on this in Sect. 4. Before we address these aspects, we recall what is known about these two small main belt asteroids. In particular, we report the photometric observations that allowed us to determine their rotation periods and improve their size estimate.

3. Asteroid pair 87887 – 415992

3.1. What we know so far

The orbital elements and their uncertainty for 87887 and 415992 are listed in the Table 1. We note (i) a similar value of the longitude in orbit λ for the two asteroids (≃5.3° difference in this

Table 1. Equinoctial orbital elements and their uncertainty as of epoch MJD 57 400.0.

Asteroid		a [au]	h	k	p	q	λ [deg]	H [mag]
87887	2000 SS286	2.75480910	0.11083546	–0.02636157	–0.06375451	0.03574610	132.305893	15.44
415992	2002 AT49	2.75496372	0.11110586	–0.02644782	–0.06375849	0.03575475	137.633071	16.69
Uncertainty		δa	δh	δk	δp	δq	$\delta\lambda$	δH
87887	2000 SS286	1.9e-8	6.2e-8	8.0e-8	6.1e-8	6.5e-8	6.4e-6	0.05
415992	2002 AT49	2.4e-8	8.2e-8	2.1e-7	8.5e-8	1.0e-7	1.3e-5	0.04

Notes. a is semimajor axis, $(h,k) = e\,(\sin\varpi, \cos\varpi)$ where e is the eccentricity and ϖ is the longitude of perihelion, $(p,q) = \tan(i/2)\,(\sin\Omega, \cos\Omega)$ where i is the inclination and Ω is the longitude of node, and $\lambda = \varpi + M$ is the mean longitude in orbit (M is the mean anomaly). The default reference system is that of the mean ecliptic J2000. The orbital solution, together with the formal one-sigma uncertainties, is taken from the `AstDyS` catalog as of April 2016 (e.g., Knežević et al. 2002). The absolute magnitude values H are from our observations reported in Sect. 3.2.

case), and (ii) the associated anomalously small difference in the osculating semimajor axis a value ($\simeq 1.5 \times 10^{-4}$ au difference in this case). The typical amplitude of short-period oscillations of the osculating semimajor axis for the orbits of 87887 and 415992 is $\simeq 6 \times 10^{-3}$ au, somewhat enhanced by the resonant effects mentioned below. This is 40 times larger than the current difference of the semimajor axis values of the two asteroids in the pair. This proximity of the a and λ values suggests that this might be a very recently formed pair.

The semimajor axis value $\simeq$2.755 au locates the pair in the central part of the belt, just below the major mean motion resonance J5/2 with Jupiter. A closer look at the location of the pair reveals that it belongs to the Gefion family (see Nesvorný et al. 2015, and NASA PDS site Nesvorný asteroid families[1]). We note that Milani et al. (2014) associated this family with the largest member (93) Minerva. This large asteroid family has formed $\simeq$480–490 Myr ago, when a huge number of meteorites rained onto Earth after only a short cosmic travel from their site of origin, as evidenced by data of fossil micrometeorites discovered in Swedish limestone quarries (e.g., Schmitz et al. 1997, 2001; Heck et al. 2004). This also constitutes the suggested link of the Gefion family and the source zone of L chondrite meteorites (Nesvorný et al. 2009). Observations of the WISE spacecraft of numerous larger Gefion members allowed determining the mean geometric albedo $p_V = 0.27 \pm 0.06$ for Gefion members (e.g., Masiero et al. 2015). However, we suspect that this result may be overestimated because they used the biased asteroid absolute magnitudes (see Pravec et al. 2012). As a result, we conservatively adopted the mean albedo for the S-type asteroids, $p_V = 0.20 \pm 0.05$, in our work. The mean principal components of Sloan Digital Sky Survey (SDSS) spectra for the Gefion-family members read $PC_1 = 0.10 \pm 0.06$ and $PC_2 = -0.02 \pm 0.07$, and they qualify this family to belong to the complex of S-type families (e.g., Nesvorný et al. 2015; Masiero et al. 2015). SDSS observations allowed determining $PC_1 = 0.03 \pm 0.02$ and $PC_2 = -0.05 \pm 0.05$ for (87887) 2000 SS286, which are compatible with the Gefion values and confirm its membership in this family.

An instructive exercise is to formally compute the distance $v_{\rm prop}$ of the two asteroids in the 87887–415992 pair in the space of proper orbital elements. Obviously, in usual circumstances we would expect $v_{\rm prop}$ to be very small, perhaps on the order of m s^{-1}. However, using the synthetic proper elements of the two components given by the `AstDyS` website[2], and using standard metric in the proper elements space (e.g., Zappalà et al. 1990), we obtain $v_{\rm prop} \simeq 32$ m s^{-1}. This is a surprisingly high value. A closer inspection reveals that $v_{\rm prop}$ is dominated (97% of its total value) by a contribution from slightly offset proper eccentricity values of the two asteroids. The difference in nominal proper eccentricity values is $\simeq 1.25 \times 10^{-3}$, but both have an uncertainty $\simeq 1.7 \times 10^{-3}$. A brief numerical integration of the nominal orbits of the two asteroids proved that they are located very close to the three-body (3, −1, −1) mean motion resonance (e.g., Table 1 and Figs. 2 and 4 in Nesvorný & Morbidelli 1998). This produces a slow diffusion in eccentricity that affects the accuracy with which the proper elements could be determined (e.g., Knežević & Milani 2000). However, if the pair 87887–415992 is $\simeq$7 kyr young (Sect. 4), then the distance $v_{\rm prop}$ in proper element space is much less relevant and a less useful parameter than in the case of larger and older structures in the main belt. We note that the synthetic proper elements are typically determined by numerical integration and data analysis for a 2 Myr interval of time (e.g., Knežević & Milani 2000; Knežević et al. 2002). This is far longer than the age of this pair.

3.2. Our photometric observations

We conducted photometric observations of the two asteroids with the 1.54 m Danish telescope at La Silla, Chile, on two apparitions each. The individual nightly runs, together with their geometric circumstances, are listed in Tables 2 and 3. They include the mid-time (UTC) of the run rounded to the nearest tenth of a day, the asteroid distances from the Sun r and Earth Δ, the solar phase angle α, and the geocentric ecliptic coordinates of the asteroid (λ, β). All the observations were taken with the Bessell R filter with supplementary observations in the V filter on October 30, 2014 for asteroid 87887. They were calibrated in the Johnson-Cousins photometric system using Landolt (1992) standard stars. The telescope was tracked at half-apparent rate of the asteroid, providing star and asteroid images of the same profile in one frame. The exposure times were 180 s. There occurred several gaps in the coverage on individual nights because we combined the observations with quasi-simultaneous runs on our other asteroid targets, and a few runs were shortened because of less-than-ideal sky conditions on the given nights. We processed and reduced the data with our custom-made aperture photometry software Aphot32.

[1] http://sbn.psi.edu/pds/resource/nesvornyfam.html

[2] http://hamilton.dm.unipi.it/astdys/

Table 2. Aspect data for observations of (87887) 2000 SS286.

Date	r [au]	Δ [au]	α [deg]	λ [deg]	β [deg]
2014 10 30.2	2.657	1.712	8.2	18.0	13.0
2014 10 31.1	2.656	1.715	8.5	17.9	13.0
2014 11 15.1	2.639	1.793	13.6	15.5	12.4
2014 11 19.1	2.634	1.823	14.8	15.0	12.1
2016 02 01.3	2.504	1.561	8.3	152.3	–5.7
2016 02 13.1	2.514	1.534	3.5	149.7	–6.5
2016 03 16.1	2.542	1.651	12.4	143.3	–7.6

Notes. Asteroid distances from the Sun r and Earth Δ, the solar phase angle α, and the geocentric ecliptic coordinates of the asteroid (λ, β). All observations were carried out using the Danish 1.54 m telescope located at La Silla observatory, Chile.

Table 3. Aspect data for observations of (415992) 2002 AT49.

Date	r [au]	Δ [au]	α [deg]	λ [deg]	β [deg]
2014 10 25.3	2.634	1.658	5.2	28.25	13.4
2014 10 26.3	2.633	1.658	5.3	28.02	13.4
2014 10 30.2	2.629	1.660	6.1	27.13	13.3
2014 10 31.2	2.628	1.662	6.3	26.90	13.3
2016 02 08.3	2.531	1.594	8.9	160.88	–7.3
2016 02 09.3	2.531	1.590	8.5	160.69	–7.4
2016 02 14.1	2.536	1.575	6.5	159.71	–7.7
2016 03 03.3	2.553	1.574	4.4	155.55	–8.6
2016 03 05.2	2.555	1.579	5.0	155.12	–8.7
2016 03 09.1	2.559	1.592	6.5	154.28	–8.8

Notes. Asteroid distances from the Sun r and Earth Δ, the solar phase angle α, and the geocentric ecliptic coordinates of the asteroid (λ, β). All observations were carried out using the Danish 1.54 m telescope located at La Silla observatory, Chile.

We analyzed the obtained photometric data using the standard Fourier series method (e.g., Harris et al. 1989; Pravec et al. 1996, 2000).

3.2.1. (87887) 2000 SS286

The primary rotation period has been uniquely determined as $P = 5.7773 \pm 0.0004$ h. This is the weighted average of our period determinations from the two apparitions in 2014 and 2016. The quoted uncertainty accounts for the transformation between the sidereal and synodic rotation periods. The composite light curves from the two apparitions are shown in Figs. 1 and 2. The mean light-curve amplitude was 0.22 mag, suggesting that the asteroid has an only moderately elongated shape. We determined the color index $V - R = 0.45 \pm 0.02$, which is consistent with an S classification of the asteroid. The mean absolute magnitude in the Cousins R band is $H_R = 14.99 \pm 0.04$, converted into the Johnson V band to $H = 15.44 \pm 0.05$. The phase relation slope parameter is $G = 0.21 \pm 0.05$. Assuming the mean geometric albedo for S-type asteroids $p_V = 0.20 \pm 0.05$ (Pravec et al. 2012), we obtain a size estimate $D_1 = 2.43 \pm 0.32$ km for the primary in our pair.

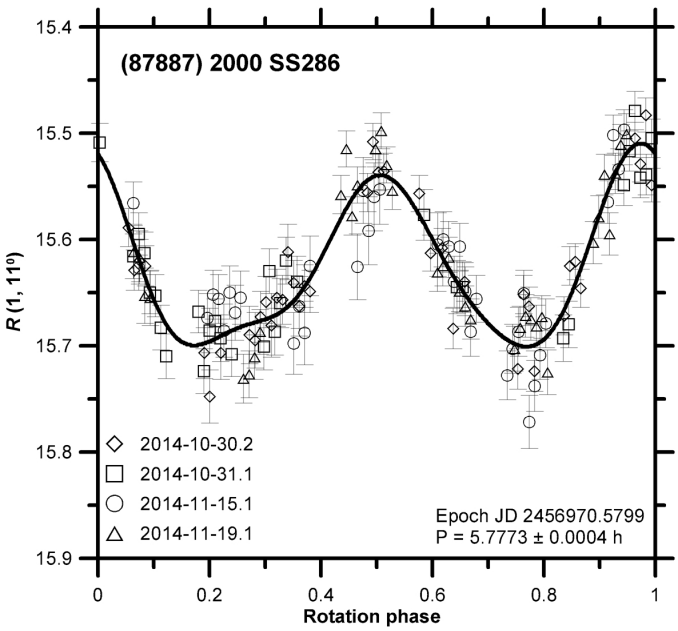

Fig. 1. Composite light curve of asteroid (87887) 2000 SS286 from observations in 2014.

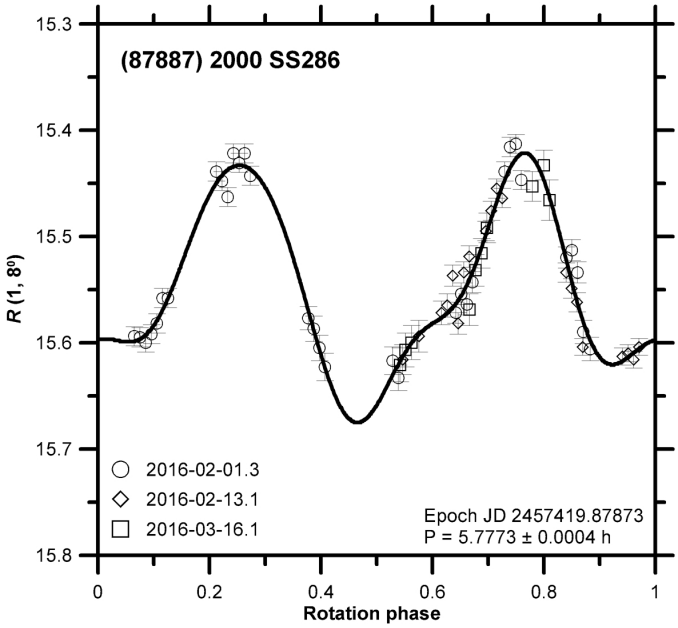

Fig. 2. Composite light curve of asteroid (87887) 2000 SS286 from observations in 2016.

We note that the photometric data of (87887) 2000 SS286 do not indicate any obvious signs of tumbling (if any, it should correspond to a small angle between the body axis and the angular rotation vector). The canonical theory for damping of the tumbling state (e.g., Harris 1994), however, would predict a timescale of ≃700 kyr, one hundred times longer than the proposed age of the pair. This implies that the pair-formation mechanism in this case should have been rather "gentle", leaving the primary to rotate about the principal axis of the inertia tensor.

3.2.2. (415992) 2002 AT49

Because of its low light-curve amplitude and the relatively low apparent brightness during our observations, we were unable

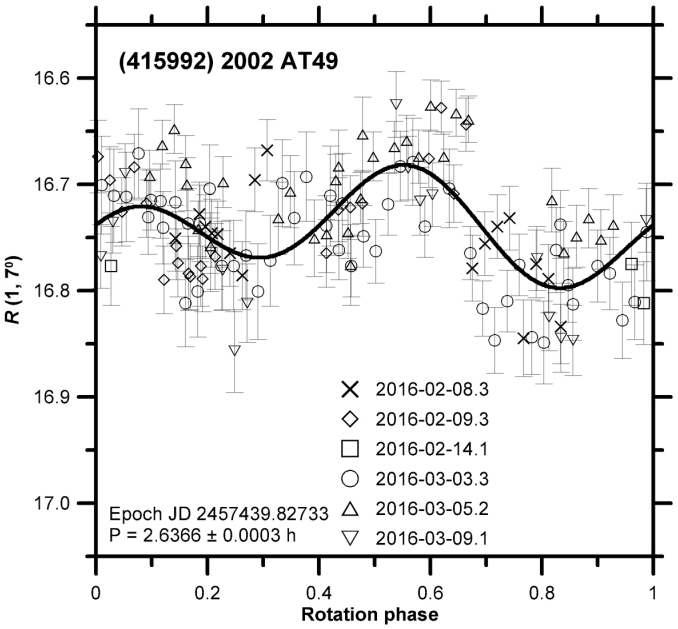

Fig. 3. Composite light curve of asteroid (415992) 2002 AT49 from observations in 2016.

to determine the rotation period of the secondary member of the asteroid pair uniquely. The formal best-fit solution from the 2016 data provides a period of $P = 2.6366 \pm 0.0003$ h with a light-curve amplitude of 0.12 mag (Fig. 3), but other values are also possible. This is because with such a limited dataset the Fourier fit has a characteristic broad χ^2 minimum, punctuated by sharp and separated minima. We report the formally best of them above, but other minima still have statistically admissible χ^2 values. We estimate that the realistic range of the synodic rotation periods for this asteroid is $\simeq$2.5 h to $\simeq$6 h. Clearly, more observations are needed to constrain it better.

Assuming the asteroid has the same G and $V - R$ values as the primary 87887, we obtained $H_R = 16.24 \pm 0.03$ and $H = 16.69 \pm 0.04$. The 2014 data, although of a lower quality and even lower light-curve amplitude ($\lesssim$0.1 mag), gave nearly the same $H_R = 16.25 \pm 0.03$. Assuming the mean geometric albedo for S-type asteroids $p_V = 0.20 \pm 0.05$, we obtain a size estimate $D_2 = 1.36 \pm 0.18$ km for the secondary in our pair.

Combining the sizes D_1 and D_2, we estimate the size of the parent body of this pair to be $D_{\rm par} \simeq 2.56 \pm 0.34$ km. Adopting a bulk density between 2 and 2.7 g cm^{-3}, which is appropriate for S-type asteroids (e.g., Carry 2012), we estimate the escape velocity from the parent body of the pair to be $\simeq 1.5 \pm 0.1$ m s^{-1} (see, e.g., supplementary materials of Pravec et al. 2010). Similarly, we estimate that the characteristic radius of the Hill sphere of the parent body was $\simeq 600^{+35}_{-50}$ km. For the sake of simplicity we use 1.5 m s^{-1} and 600 km.

4. Estimated age for the asteroid pair 87887 – 415992

4.1. Clones and backward orbit integration

The recent origin of recognizable asteroid pairs allows estimating their age, that is, the time since their formation, using backward orbit propagation of the two asteroids (e.g., Vokrouhlický & Nesvorný 2008). Here we briefly recall the standard approach. In the next section, we substantiate the traditional methods using a more in-depth analysis, allowing us to eliminate the simulated age solutions related to the near-repetition of the asteroid configuration with the synodic periodicity.

In an ideal world, where (i) the state vectors of the two asteroids in the pair would be known exactly at a given epoch; and (ii) our orbit-propagation model would be complete and absolutely precise, we would propagate nominal asteroid orbits backward in time until they would reach a moment that reflected their separation conditions from the common parent body. Unfortunately, this is not possible and we need to correct for both factors (i) and (ii), at least in approximate way.

For problem (i), the orbit determination procedure incorporates the necessary statistical tools. In particular, for a given initial epoch T_0 it provides not only the nominal (best-fit) orbital solution $\boldsymbol{e}^\star$, but also the covariance matrix Σ, under the assumption of a locally normal distribution of orbital solutions $\boldsymbol{e}$ around $\boldsymbol{e}^\star$ (e.g., Milani & Gronchi 2010). In our case, we used information provided by the `AstDyS` website for MJD epoch 57 400.0, and $\boldsymbol{e} = (a, k, h, q, p, \lambda)$ is a vector of equinoctical orbital elements (see Table 1). An infinitesimal probability $\mathrm{d}N(\boldsymbol{e})$ of finding the correct orbit solution in a volume $\mathrm{d}^6\boldsymbol{e}$ around $\boldsymbol{e}$ is therefore given by $\mathrm{d}N(\boldsymbol{e}) = p(\boldsymbol{e})\,\mathrm{d}^6\boldsymbol{e}$, where the probability density $p(\boldsymbol{e})$ reads

$$p(\boldsymbol{e}) = \frac{1}{(2\pi)^3 \Sigma^{\frac{1}{2}}} \exp\left[-\frac{1}{2}\left(\boldsymbol{e}-\boldsymbol{e}^\star\right)^{\mathrm{T}} \Sigma^{-1} \left(\boldsymbol{e}-\boldsymbol{e}^\star\right)\right]. \quad (1)$$

While the nominal solution $\boldsymbol{e}^\star$ is the most likely representation of the truth, some of the close-by solutions $\boldsymbol{e}$ may also have nearly the same weight. Only those solutions $\boldsymbol{e}$ that deviate too much from $\boldsymbol{e}^\star$ should be rejected.

When searching for the asteroid pair origin by numerical propagation of their orbits backward in time, we therefore need to consider a multitude of possible initial conditions at T_0. We use the word "clones" for these different realizations of each of the two asteroids. The clone distribution in the orbital elements space $\boldsymbol{e}$ must be consistent with the distribution in (1). This is achieved by generating the clone elements $\boldsymbol{e}$ using

$$\boldsymbol{e} = \mathsf{T}^{\mathrm{T}}\, \boldsymbol{z} + \boldsymbol{e}^\star, \quad (2)$$

with a six-dimensional vector $\boldsymbol{z}$ whose components are random deviates of the standard normal distribution, and T is a matrix satisfying $\mathsf{T}^{\mathrm{T}}\,\mathsf{T} = \Sigma$. We used a Cholesky decomposition to determine T from Σ (e.g., Gentle 2003; Press et al. 2007).

For problem (ii), that is, for the accuracy of the orbit propagator, we note that our code takes into account gravitational perturbations from planets and the most massive main belt objects (Ceres, Vesta and Pallas). We considered nominal masses for each of these perturbers, and variations due to their uncertainty were deemed negligible on the required propagation timescale $\lesssim$1 Myr. Moreover, the motion of both asteroids in the pair is affected by thermal accelerations known as the Yarkovsky effect (e.g., Bottke et al. 2006; Vokrouhlický et al. 2015). The Yarkovsky effect is a subtle non-gravitational acceleration due to recoil of photons that are thermally reradiated by the surface of the asteroid. This effect depends on a number of physical parameters such as the asteroid size, rotation period and pole orientation, surface thermal inertia, and bulk density, to mention only the most important. Unfortunately, except for rotation periods and a rough estimate of the size (Sect. 3.2), we do not have this information for either of the two components in the 87887–415992 pair. In this situation, it would be too difficult to use somewhat sophisticated formulations of the thermal accelerations (see, e.g., Vokrouhlický et al. 2000). We instead simplified the approach and empirically retained only the principal

orbital perturbation that is due to the Yarkovsky effect, which is the secular change $\mathrm{d}a/\mathrm{d}t$ in the semimajor axis (and the related advance in longitude in orbit, as described by Vokrouhlický et al. 2000). This was accomplished by mimicking the Yarkovsky effect with a transverse acceleration described in Farnocchia et al. (2013) (an older implementation of the same idea is provided by Vokrouhlický & Nesvorný 2008). With this approximation we did not include in our computation the off-plane component of the thermal acceleration and the related perturbations or the exact nature of short-period Yarkovsky effects. The magnitude of the empiric transverse acceleration was chosen to (i) have $\propto 1/r^2$ heliocentric dependence, and (ii) resulting in the expected $\mathrm{d}a/\mathrm{d}t$ value (e.g., Farnocchia et al. 2013). At the heliocentric distance of the 87887–415992 pair, the maximum semimajor axis drift value for a kilometer-sized asteroid is approximately $(\mathrm{d}a/\mathrm{d}t)_{\max} \simeq 2 \times 10^{-4}$ au Myr^{-1} (see, e.g., Fig. 2 in Bottke et al. 2006). Assuming a common value of the surface thermal inertia, the exact semimajor axis drift-rate for either the 87887 or 415992 asteroid reads $\mathrm{d}a/\mathrm{d}t = (\mathrm{d}a/\mathrm{d}t)_{\max} \cos\gamma/D$, where γ is the rotation pole obliquity and D is the size in kilometers. For D, we used the values estimated in Sect. 3.2, but γ are not available to us at this moment. In principle, we must assume all admissible values and test the sensitivity of the results on their choice. For simplicity, we assumed an isotropic distribution of the spin axis orientation for both asteroids, which implies that $\cos\gamma$ in the formula for $\mathrm{d}a/\mathrm{d}t$ is a random quantity with a uniform probability density distribution in the interval $(-1, 1)$. Therefore, individual realizations for $\mathrm{d}a/\mathrm{d}t$ may have equally likely positive or negative values, depending on whether the asteroid rotates in a prograde or retrograde sense.

Combining the two aspects (i) and (ii) from above in this way, we propagated in our model a certain number of clone realizations for each of the asteroids in the pair. Their initial conditions were constructed by Eq. (2), and each of the clones was assumed to have a randomly chosen Yarkovsky value of $\mathrm{d}a/\mathrm{d}t$. The initial state vectors of the planets at $T_0 = 57\,400.0$ MJD epoch were taken from the JPL ephemerides file, and the state vectors of the three massive main belt objects, Ceres, Vesta, and Pallas, from the `AstDyS` solution. We used the well-tested computer code `swift`[3], extended by our subroutines to account for the thermal accelerations. We used a three-day propagation time step, and typically let the integration extend to 1–3 Myr maximum backward in time when exploring the origin of the 87887–412992 pair. We complemented the basic version of the `swift` software with analysis subroutines specific to the asteroid pairs, such as computation of distance and relative velocity for a selected couple of clones. The time step should be short enough to avoid missing the close encounters: anticipating a relative velocity of about $\simeq$1 m s^{-1}, the bodies move by $\simeq$260 km in one time step. This is less than the estimated Hill radius of the parent body of this pair, and also less than the expected accuracy of our propagation model.

4.2. Results: clone convergence in the past

To illustrate the effect of near-periodic repetition of close-by configurations of the two asteroids in the pair, we first numerically integrated the nominal orbits of 87887 and 412992 without the thermal accelerations. At every three-day time step, we computed the mutual distance and relative velocities of the two asteroids. Figure 4 shows the result. The first, deep encounter is recorded $\simeq$7.42 kyr ago, reaching a minimum mutual distance

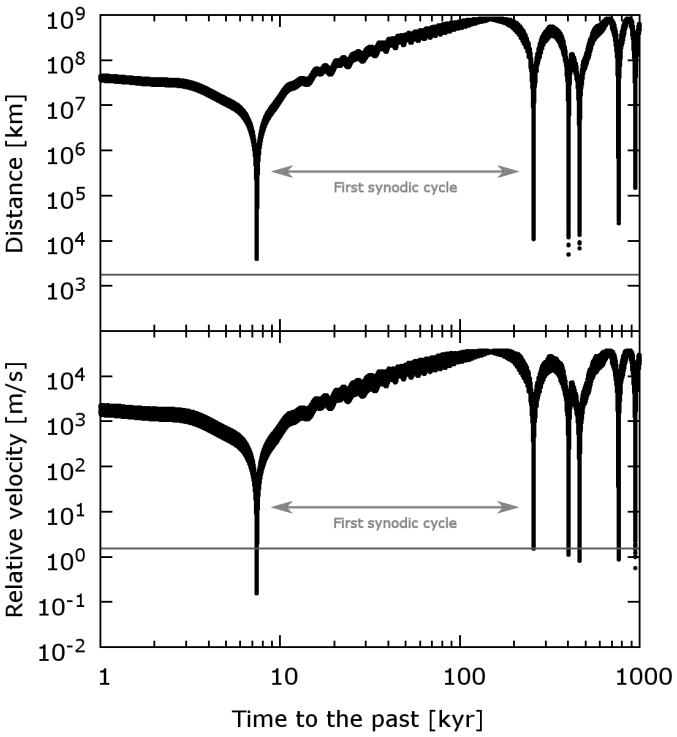

Fig. 4. Repetition of the geometric configuration of the nominal orbits for (87887) 2000 SS286 and (415992) 2002 AT49 (no thermal accelerations included in this run; note the logarithmic scale of the abscissa). The *top panel* shows the mutual distance of the two asteroids, the *bottom panel* shows their relative velocity. Both functions have deep minima at conjunctions. The first occurs ~7.42 kyr ago, followed by the second at $\simeq$257 kyr after completing one synodic cycle of their relative motion. The gray level line at the top shows a distance of $3\,R_{\mathrm{Hill}}$, while that at the bottom shows V_{esc} of the parent body.

of $\simeq$3900 km and a relative velocity of $\simeq$0.14 m s^{-1}. This was the event that classified this pair to be considered as a candidate for a very young pair mentioned in Sect. 2. When the propagation is continued backward in time, the asteroids separate in space for nearly 250 kyr before experiencing another close encounter at $\simeq$257 kyr. This time the minimum recorded distance was $\simeq$11 000 km and relative velocity $\simeq$1.52 m s^{-1}. The situation is then repeated typically four more times in the last 1 Myr.

The same pattern would obviously be repeated when various clones of the two asteroids were used instead of their nominal realizations (with now the thermal effects included as well). We found that the characteristics of the first deep minimum at $\simeq$7.4 kyr remain approximately the same for all possible clone combinations, those of the earlier encounters start to differ significantly. Already the epoch of the second encounter in the past is not always near $\simeq$257 kyr, but depending on the strength of the Yarkovsky effect, it could take part any time between $\simeq$45 kyr and $\simeq$500 kyr. This is illustrated at Fig. 5. In this simulation we considered 1000 clones of each of the asteroids in the pair. The clones sampled the uncertainty hyper-ellipsoid of the initial data $\boldsymbol{e}$ at T_0 and each having assigned some random value of the Yarkovsky effect. At every time step, that is, at every three-day interval, we checked the mutual distance of all 10^6 possible combinations of the clones. We monitored the deep close encounters illustrated in Fig. 4, and for each of them we recorded the relative velocity of the clones.

By focusing on the first deep encounter between the clones, we note that it occurred in a rather short time interval

[3] http://www.boulder.swri.edu/~hal/swift.html

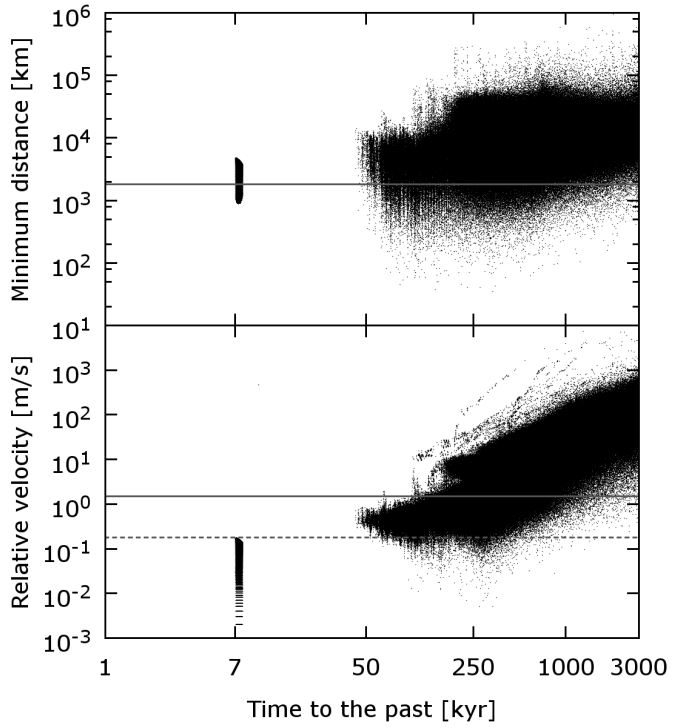

Fig. 5. *Top*: minimum distance between clones of (87887) 2000 SS286 and (415992) 2002 AT49 during different synodic cycles in the past (each of the asteroids was represented by 1000 clones, and we considered all possible combinations between them). The first deep encounter is well localized at some 7.4 kyr ago, but the subsequent encounters of different combinations of clones are spread in time starting from ≃45 kyr ago. *Bottom*: relative velocity of the clones at the moment of their nearest encounter from the top panel. Importantly, all possible clone combinations have an extremely low relative velocity ($\lesssim$0.18 m s^{-1}) during their first encounter in the past. The gray solid line at the top shows a distance of 3 $R_{\rm Hill}$, while that at the bottom shows $V_{\rm esc}$ of the parent body. The gray dashed line at the bottom indicates that the 0.18 m s^{-1} value is not exceeded by any of the clone pairs during their first encounter.

between 7.1 and 7.8 kyr ago. The relative youth of this event implies that all 10^6 clone combinations have a very similar minimum distance and relative velocity with only a minor spread. All minimum relative velocities are extremely low, with a floor limit of 0.18 m s^{-1}. Some may reach a mm s^{-1} level. These values are typically an order of magnitude lower than the estimated escape velocity ≃1.5 m s^{-1} from the parent body of the pair. The minimum recorded distances between the clones range from ≃900 km to ≃4800 km. These values are slightly higher than the estimated radius of the Hill sphere $R_{\rm Hill}$ of the parent body, namely ≃600 km. However, we should allow some tolerance in missing the ideal convergence. This is because our propagation model is not perfect, and incorrectly modeled effects at the level of ≃3 $R_{\rm Hill}$ may easily originate from (i) representing the complete model of the Yarkovsky effect with only the transverse acceleration, or (ii) a mismatch in modeling the short-periodic variations using the `swift` symplectic code that incorporates the Wisdom-Holman mapping algorithm (Wisdom & Holman 1991). Additionally, at such a close distance we need to take the mutual gravitational interaction of the two asteroids in the pair into account, which would help to bring them closer to each other. Empirically, we considered the ≃ 3 $R_{\rm Hill}$ level tolerable for the success in convergence of the clones. We thus find that about half of the clone combinations satisfy this liberal condition for the minimum distance.

Examining the second, and further, deep encounters in the past, we note that some may occur as early as ≃45 kyr ago. Since this is much earlier than seen for the nominal orbits (Fig. 4), for this to occur we need clones with strong Yarkovsky accelerations, especially for the smaller secondary component. Because we sampled all possible clone combinations, there are many different possibilities and the distance minima occur for basically any epoch beyond the 45 kyr time. However, many are quite distant ($\gtrsim$20 000 km) and/or occur very swiftly at relative speed of tens or even hundreds of meters per second. These cases should be considered as false. Nevertheless, close encounters are possible with distances well shorter than $R_{\rm Hill}$, in our simulation some as close as ≃50 km that are associated with a relative velocity lower than $V_{\rm esc}$. These solutions should be considered as valid. In terms of a fraction of tested clones, there are increasingly fewer of these successful solutions in the past. However, this is mainly an expression of the dilution of the spreading clone clouds by Keplerian shear, gravitational and non-gravitational perturbations. We recall that we used a fixed number of clones.

To conclude, both young (≃7.4 kyr) and old ($\gtrsim$50 kyr) solutions are possible in principle. Unless we can determine more arguments and tests, we cannot a priori decide which one is correct.

4.3. More results: lessons from integration of synthetic pairs

In an attempt to solve the true-age problem, we conducted the following numerical experiment. In brief, the main and severe constraint we used is the extremely low encounter velocity $\lesssim$0.18 m s^{-1} of all possible clone combinations during the first deep encounter ≃7.4 kyr ago. As a result, it must have occurred with 100% likelihood. Any solution that would postulate an older age for this pair would need to satisfy the ≃7.4 kyr velocity constraint during the subsequent deepest encounter. In what follows, we show that it is very difficult to meet this requirement.

To shed a more quantitative light on this problem, we performed a numerical simulation of 240 000 synthetic secondaries ejected from the primary at T_0 = 57 400.0 MJD epoch. We assumed that the synthetic secondaries (representing 415 992) were separated from the primary (representing 87 887) in a random direction in space and with a relative velocity $v_{\rm ej}$ in some interval of values $(0, V_{\rm max})$. We nominally took $V_{\rm max} = V_{\rm esc}$, where $V_{\rm esc} \simeq 1.5$ m s^{-1} is the escape velocity from the parent asteroid of the pair, but for the sake for probing our results in more detail, we also considered lower $V_{\rm max}$ values. With this procedure we created 240 000 synthetic pairs and additionally gave the primary and secondary components random values of the Yarkovsky drift-rate $\mathrm{d}a/\mathrm{d}t$ within the respective interval of values. The pairs were numerically propagated to the future for 3 Myr, and we monitored their relative configuration, focusing particularly on minima of distance during the synodic cycles. We recorded the absolute minimum of the relative velocity $v_{\rm enc}$ at which the two clones encountered and the time t when it occurred. Most often, this was already during the first encounter, but in some cases it also occurred during the subsequent encounters.

These results allowed us to characterize the probability $\mathrm{d}P$ that the two asteroids in the pair will encounter with relative velocity $(v_{\rm enc}, v_{\rm enc} + \mathrm{d}v_{\rm enc})$ in time $(t, t + \mathrm{d}t)$ after their separation with relative velocity $(v_{\rm ej}, v_{\rm ej} + \mathrm{d}v_{\rm ej})$:

$$\mathrm{d}P = \rho(v_{\rm ej}; v_{\rm enc}, t)\, \mathrm{d}v_{\rm ej}\, \mathrm{d}v_{\rm enc}\, \mathrm{d}t. \quad (3)$$

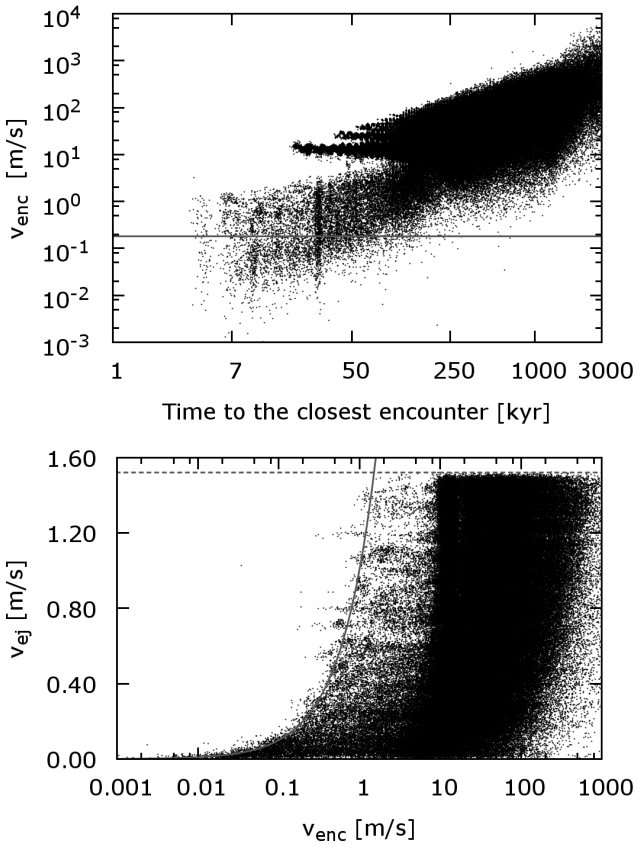

Fig. 6. Results from our numerical experiment with 240 000 synthetic pairs 87887–415992 separated at T_0 = 57 400.0 epoch by a low relative velocity v_{ej}. We numerically propagate their orbits until their configuration was repeated in a deepest close encounter at time t at which the relative velocity of the two asteroids is v_{enc} (we recall that the integration time span was 3 Myr in which the deepest encounter was sought). The *top panel* shows v_{enc} vs. t. The *bottom panel* shows v_{ej} vs. v_{enc}.

Here $\rho(v_{ej}; v_{enc}, t)$ is the associated probability density. We imposed the normalization

$$\int_0^{V_{max}} \int_0^{\infty} \int_0^{\infty} \rho(v_{ej}; v_{enc}, t)\, \mathrm{d}v_{ej}\, \mathrm{d}v_{enc}\, \mathrm{d}t = 1, \quad (4)$$

where in practice we replaced infinity in the integral bounds by some high values attained in our simulation. Obviously, we can only approximate the formally infinitesimal quantities with their finite realizations, such as

$$\Delta P_{ijk} \simeq \frac{N'_{ijk}(\Delta v_{ej}, \Delta v_{enc}, \Delta t)}{N}, \quad (5)$$

where $N'_{ijk}(\Delta v_{ej}, \Delta v_{enc}, \Delta t)$ is the number of recorded events in the finite intervals $(v_{ej\,i}, v_{ej\,i}+\Delta v_{ej})$, $(v_{enc\,j}, v_{enc\,j}+\Delta v_{enc})$ and $(t_k, t_k+\Delta t)$, and N being number of all events. We had $\Delta v_{ej} = \Delta v_{enc} = 0.04$ m s^{-1} and $\Delta t = 10$ kyr. The indexes i, j, and k span positive numbers until the parameter (velocities or time) fills the necessary interval of values with Δ steps.

Figure 6 shows our raw data: (i) the top panel shows v_{enc} as a function of t, and (ii) the bottom panel shows v_{enc} as a function of v_{ej}. There are two clear trends. First, v_{enc} generally increases with t because of the cumulative effect of gravitational and non-gravitational perturbations in the orbits of the two components in the synthetic pairs. Second, v_{enc} is nearly always higher than v_{ej}, only in very rare cases is the opposite true. This is again an expression of orbital perturbations. We added these data into our procedure to estimate the probability ΔP_{ijk} from Eq. (5), and used it to evaluate the following hypothesis: what is the probability that upon separation of the two components with v_{ej} in the interval $(0, V_{max})$ they encounter each other at any time in the future with a relative velocity v_{enc} in the interval $(0, V_{cut})$. We set $V_{cut} = 0.18$ m s^{-1} because this is the hard limit of the encounter velocity of 87887–415912 during their approach ≃7.4 kyr ago (see Sect. 4.2). We tested both $V_{max} = V_{esc}$, for which we have

$$P_{old} = \int_0^{V_{max}} \int_0^{V_{cut}} \int_0^{\infty} \rho(v_{ej}; v_{enc}, t)\, \mathrm{d}v_{ej}\, \mathrm{d}v_{enc}\, \mathrm{d}t \simeq 0.02, \quad (6)$$

and also strengthened the case $V_{max} = 0.18$ m s^{-1}, for which we have

$$P'_{old} = \int_0^{V_{max}} \int_0^{V_{cut}} \int_0^{\infty} \rho(v_{ej}; v_{enc}, t)\, \mathrm{d}v_{ej}\, \mathrm{d}v_{enc}\, \mathrm{d}t \simeq 0.13. \quad (7)$$

We note that in both cases, we recalculated the proper normalization of the probability density $\rho(v_{ej}; v_{enc}, t)$ using Eq. (4).

As a sanity check, we now pushed the procedure and determined the V_{max} value at which the probability of the old solution P_{old} from Eq. (6) increases to 50%. We ran this test and found that V_{max} would need to be as low as ≃0.02 m s^{-1}. While not impossible, this value is about an order of magnitude lower than statistically expected from the separation of the two components in pairs (see, e.g., Jacobson & Scheeres 2011).

Our results in Eqs. (6) and (7) may be expressed in simple words: separating the asteroids by a low relative velocity, orbit perturbations typically act to increase it significantly during the next closest encounter after completing one (or sometimes more) synodic cycle. There is only a ≃2% chance of meeting at 0.18 m s^{-1} when the initial separation extended to V_{esc}, and this chance increases to only ≃13% at 0.18 m s^{-1} when the initial separation was smaller or equal to this value. Additionally, we note that we did not use the fact that the older age solutions of the 87887–415992 pair preceded the young age by at least 37 kyr (Fig. 5). If this constraint is used, then the probability of the older age would decrease even more.

Therefore, we may conclude that it is very unlikely that the asteroid pair 87887–415992 has an age ≳10 kyr and the two components underwent only a close fly-by with an extremely slow relative velocity ≃7.4 kyr ago. Instead, this nearest encounter in the past is their true moment of origin.

4.4. More results: analysis of the young-age solution

We now return to our simulations of 87887–415912 past convergence and investigate the encounter conditions at ≃7.4 kyr. In particular, we use the information about the given Yarkovsky drift-rate in semimajor axis $\mathrm{d}a/\mathrm{d}t$ to each of the clones. We recall that $\mathrm{d}a/\mathrm{d}t \propto \cos\gamma$, where γ is the obliquity of the spin axis. Thus the positive or negative sign of $\mathrm{d}a/\mathrm{d}t$ unambiguously implies either prograde or retrograde sense of rotation of the clone. Therefore, it is interesting to consider the statistics of successfully converging solutions in terms of this parameter because it could tell us about expected rotation state of the asteroid. We note, for instance, that this method has led Vokrouhlický et al. (2011) to predict that the smaller component in the 6070−54827 pair should rotate in a retrograde sense.

We note that all 10^6 clone combinations converged within ≃8 R_{Hill} ≃ 4800 km distance. Using this largest set of the converging cases, we find no preference between the four combinations of prograde and retrograde modes of the clones of

Table 4. Dependence of the age of the (87887) 2000 SS286 and (415992) 2002 AT49 asteroid pair on obliquities γ_1 and γ_2 of the primary and secondary component.

$[\cos\gamma_1, \cos\gamma_2]$	T_{age} [kyr]	δT_{age} [kyr]	$P = N_{conv}/N_{tot}$
$\cos\gamma_1 > 0, \cos\gamma_2 > 0$	7.37	0.09	0.25
$\cos\gamma_1 < 0, \cos\gamma_2 > 0$	7.26	0.08	0.25
$\cos\gamma_1 > 0, \cos\gamma_2 < 0$	7.62	0.10	0.25
$\cos\gamma_1 < 0, \cos\gamma_2 < 0$	7.49	0.10	0.25

Notes. Statistical parameters of solutions for which clones of (87887) 2000 SS286 and (415992) 2002 AT49 converged at a relative distance of $8\,R_{Hill} \simeq 4\,800$ km (all 10^6 possibilities in our numerical experiment). T_{age} and δT_{age} is the mean value of the age and its formal uncertainty in kyr. The results are sorted into four cases according to the assumption about the rotation sense of the clones: $\cos\gamma_1$ and $\cos\gamma_2$ are cosines of obliquity of the the clones of the primary and secondary in the pair. P is the fraction of solutions in each of the cases.

87887 vs. 415992, however. We only note that solutions for prograde-rotating clones of 415992 occur slightly earlier (by about 0.3 kyr) than those for retrograde-rotating clones of 415992. The results are summarized in Table 4 and Fig. 7.

We also analyzed smaller subsets of the convergence cases that approached to a closer distance. For instance, considering only those that approached at $\simeq 3\,R_{Hill} \simeq 1800$ km, little more than one tenth of the cases, or even less, such as $\simeq 2\,R_{Hill} \simeq 1200$ km. Unfortunately, no preference in spin axis orientation for the primary or secondary clones was detected. There was always an about equal chance for all four combinations. We assume that this negative result, as compared to that for the 6070−54827 pair, is due to the quite smaller size of the asteroids constituting the pair.

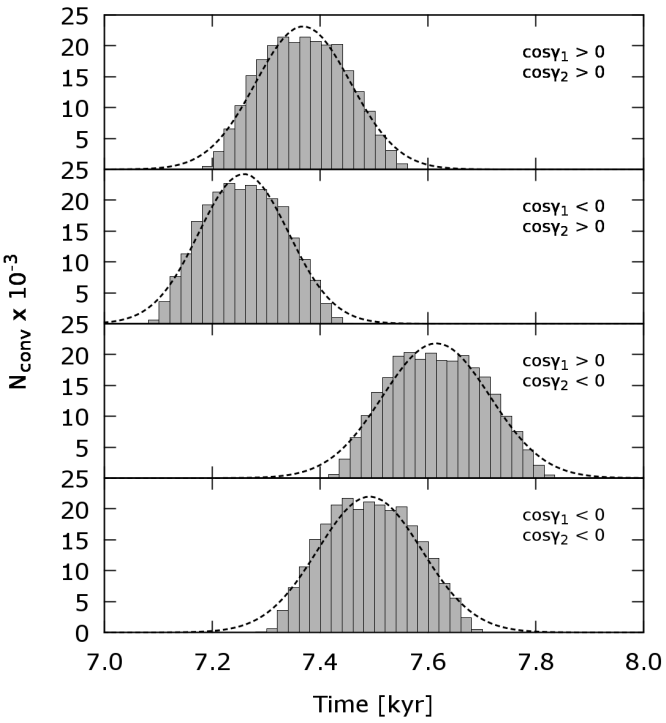

Fig. 7. Statistical distribution of (87887) 2000 SS286 and (415992) 2002 AT49 solutions converging within the past 10 kyr. We select all $N_{tot} = 10^6$ possible clone combinations that approached less than $\simeq 8\,R_{Hill} \simeq 4800$ km. The abscissa is the time in kyr, the ordinate gives the number of converging solutions grouped in 20 yr bins. The solutions are grouped into four cases of possible combinations of rotation sense of the clones for each of the components in the pair. The sign of $\cos\gamma$ (γ is the obliquity) serves as a indicator of the rotation sense (see the text). The *upper two panels* are for secondary clones that rotate in a prograde sense ($\cos\gamma_2 > 0$), the *lower two panels* show the reverse.

5. Discussion and conclusions

We have shown that determining the age of an asteroid pair might not be as straightforward as it looks and in principle might need detailed considerations. In most of the cases for which our message is irrelevant, the orbit uncertainty of the two components is too large and a continuum of ages from some epoch in the past is possible (see, e.g., the case of asteroids (21436) Chaoyichi and (334916) 2003 YK39 in Fig. 2 of the supplementary materials of Pravec et al. 2010). However, there are cases of more accurate orbits where the age solutions might be localized in time into separate intervals reflecting the synodic cycles of the relative motion of the two asteroids in the pair. These situations require careful analysis to distinguish between the different possibilities. Previously reported age solutions for the pairs did not pay close attention to this aspect, and some of them perhaps need to be verified or reanalyzed (including the most famous case of (6070) Rheinland and (54827) 2001 NQ24).

The second implication of our work is relevant to the general picture of asteroid pair formation. In particular, does the relative rarity of known asteroid pairs with ages younger than 10 kyr fit the general idea of their formation by rotational fission (Pravec et al. 2010)? We addressed this question using approximate arguments in two steps.

First, we checked that a collisional origin is not a likely model for a very recent origin of the 87887−415992 pair. Bottke et al. (2005) developed a model that described the collisional evolution of the asteroid main belt. One of the results that could be inferred from their approach, is a statistically mean timescale T_{disr} for a disruption of a body with size D among the current population of asteroids in the belt. As we were interested in the origin of the 87887–415992 pair, we chose $D \simeq 2.5$ km and found that $T_{disr} \simeq 15$ kyr. We note that the $H \simeq 15.3$ mag population of asteroids in the inner main belt may be close to completeness, but this is not the case in the outer main belt where the majority of asteroids reside. Therefore we cannot assume that we know all events that have led to the origin of our studied pairs, since a number of them may still have been missed. By comparing the known population of $H \simeq 15.3$ in the MPC catalog to their expected number by Bottke et al. (2005) (assuming a global mean geometric albedo of $\simeq 0.125$), we note a factor of $\simeq 2$ incompleteness. This means that instead of recording every event, we statistically expect detection of every second event, with a frequency of $\simeq 30$ kyr, for example. Our pair 87887–415992 would have been anomalously young in this model.

We now try to determine how well the formation of the 87887–415992 pair in the last 10 kyr fits within the rotational fission model (Pravec et al. 2010). We should point out that we currently do not have a rigorous procedure or model that would include all participating factors and biases. Our computation should therefore be considered more as an estimate.

We start with the results in Pravec et al. (2008), who analyzed the rotation-rate f distribution $N(f)$ of small asteroids in the main belt and Hungaria regions. They found that $N(f)$ is basically flat, except for an excess of slow rotators with $f \leq 1$ cycle per day, where they found about twice as many objects compared

to bins corresponding to $f \geq 1$ cycle per day frequencies. We estimate that on a timescale over which the YORP effect doubles f, about one-fourth of the population may reach the critical fission limit. However, about half of the asteroids in these bins may decelerate, rather than accelerate their rotation in the model of Pravec et al. (2008). This decreases the fraction to about one-eighth. We should also consider that reaching the estimated fission frequency may not yet be enough, but still a certain time may be needed to mechanically break the body. We do not have a quantitative estimate in this respect, therefore we assume another factor of 2−5 in the population. We thus estimate that about one in 16 to 40 of objects in the asteroid population at small sizes is prone to rotationally fission within the estimated doubling timescale by the YORP effect.

Next, we considered results from Čapek & Vokrouhlický (2004), who computed the strength of the YORP effect for a large sample of asteroids of various shapes. Taking their results for high surface inertia ≃130 [SI units], which is appropriate for small asteroids (e.g., Delbò et al. 2007), we concluded that a characteristic doubling timescale for $D \simeq 2.5$ km asteroids in the main belt is ≃20 Myr. Finally, we turned again to the results of Bottke et al. (2005), who showed there are about 120 thousands main belt bodies in their 2.45 km size bin. We found above that about 1/40 to 1/16 of them may be prone to rotationally fission, which is ≃3−7.5 thousand. As a result, one such event is statistically expected every ≃2.5−6.5 kyr (if evenly distributed). As we expect an observational incompleteness of a factor ≃4−9 for these events, however, we estimated that our records should include about one event $\simeq(4-9)\times(2.5-6.5)/2 \simeq 5-30$ kyr old (we note that above we mentioned a population incompleteness of ≃2 for 2−2.5 km bodies across the main belt; in pairs, we must find both components, hence the incompleteness factor squares, and the secondary may be slightly smaller than the primary, which leads to a higher incompleteness factor in the population). This is close to the age we determined for the 87887–415992 pair and also because we are currently not aware of more events of that young age. We note that if some of the pairs mentioned in Sect. 2 were to be younger than 10 kyr, which we deem unlikely, the overall conclusions from our study would not be changed. We may therefore conclude that the ≃7 kyr age of the youngest known asteroid pair in the belt with a parent body of ≃2.5 km size agrees well with the fission model "powered" by the YORP effect.

We finally note that several cases of asteroid activity, such as dust-tail formation or a split into a number of small fragments, were reported over the past decade (e.g., Jewitt et al. 2015, and references therein). It is possible that some of these events were triggered by rotational fission, but by their nature they seem to differ from the generic population of asteroid pairs discussed in this paper. More likely, they correspond to a sudden activation of primitive, cometary-like bodies. In contrast, asteroid pairs are found equally well in all spectral groups of asteroids, and typically produce several near-equal size components.

Acknowledgements. We thank the referee, whose comments helped us to improve the original version of this paper. This work was supported by the Czech Science Foundation (grant P209-12-0229). The work at Modra was supported by the Slovak Grant Agency for Science VEGA (Grant 1/0670/13).

References

Bottke, W. F., Durda, D. D., Nesvorný, D., et al. 2005, Icarus, 179, 63
Bottke, W. F., Vokrouhlický, D., Rubincam, D. P., & Nesvorný, D. 2006, Ann. Rev. Earth Planet. Sci., 34, 157
Čapek, D., & Vokrouhlický, D. 2004, Icarus, 172, 526
Carry, B. 2012, Planet. Space Sci., 73, 98
Delbò, M., dell'Oro, A., Harris, A. W., Mottola, S., & Mueller, M. 2007, Icarus, 190, 236
Duddy, S. R., Lowry, S. C., Wolters, S. D., et al. 2012, A&A, 539, A36
Duddy, S. R., Lowry, S. C., Christou, A., et al. 2013, MNRAS, 429, 63
Farnocchia, D., Chesley, S. R., Vokrouhlický, D., et al. 2013, Icarus, 224, 1
Galád, A. 2012, A&A, 548, A25
Gentle, J. E. 2003, Random Number Generation and Monte Carlo Methods (New York: Springer)
Harris, A. W. 1994, Icarus, 107, 209
Harris, A. W., Young, J. W., Bowell, E., et al. 1989, Icarus, 77, 171
Heck, P. R., Schmitz, B., Baur, H., Halliday, A. N., & Wieler, R. 2004, Nature, 430, 323
Jacobson, S. A., & Scheeres, D. J. 2011, Icarus, 214, 161
Jewitt, D., Hsieh, H., & Agarwal, J. 2015, in Asteroids IV, eds. P. Michel, F. E. DeMeo, & W. F. Bottke, 221
Knežević, Z., & Milani, A. 2000, Celest. Mech. Dyn. Astron., 78, 17
Knežević, Z., Lemaître, A., & Milani, A. 2002, in Asteroids III, eds. W. F. Bottke, A. Cellino, P. Paolicchi, & R. P. Binzel, 603
Landolt, A. U. 1992, AJ, 104, 340
Masiero, J. R., DeMeo, F. E., Kasuga, T., & Parker, A. H. 2015, in Asteroids IV, eds. P. Michel, F. E. DeMeo, & W. F. Bottke, 323
Milani, A., & Gronchi, G. F. 2010, Theory of Orbital Determination (Cambridge: Cambridge University Press)
Milani, A., Cellino, A., Knežević, Z., et al. 2014, Icarus, 239, 46
Moskovitz, N. A. 2012, Icarus, 221, 63
Nesvorný, D., & Morbidelli, A. 1998, AJ, 116, 3029
Nesvorný, D., Vokrouhlický, D., & Bottke, W. F. 2006, Science, 312, 1490
Nesvorný, D., Vokrouhlický, D., Morbidelli, A., & Bottke, W. F. 2009, Icarus, 200, 698
Nesvorný, D., Brož, M., & Carruba, V. 2015, in Asteroids IV, eds. P. Michel, F. E. DeMeo, & W. F. Bottke, 297
Polishook, D. 2014, Icarus, 241, 79
Polishook, D., Moskovitz, N., Binzel, R. P., et al. 2014a, Icarus, 233, 9
Polishook, D., Moskovitz, N., DeMeo, F. E., & Binzel, R. P. 2014b, Icarus, 243, 222
Pravec, P., Šarounová, L., & Wolf, M. 1996, Icarus, 124, 471
Pravec, P., Hergenrother, C., Whiteley, R., et al. 2000, Icarus, 147, 477
Pravec, P., Harris, A. W., Vokrouhlický, D., et al. 2008, Icarus, 197, 497
Pravec, P., Vokrouhlický, D., Polishook, D., et al. 2010, Nature, 466, 1085
Pravec, P., Harris, A. W., Kušnirák, P., Galád, A., & Hornoch, K. 2012, Icarus, 221, 365
Pravec, P., Kušnirák, P., Hornoch, K., et al. 2013, IAU Circ., 9268
Pravec, P., Scheirich, P., Kušnirák, P., et al. 2016, Icarus, 267, 267
Press, W. H., Teukolsky, S. A., Vetterling, W. T., & Flannery, B. P. 2007, Numerical Recipes: The Art of Scientific Computing (Cambridge: Cambridge University Press)
Rożek, A., Breiter, S., & Jopek, T. J. 2011, MNRAS, 412, 987
Schmitz, B., Peucker-Ehrenbrink, B., Lindström, M., & Tassinari, M. 1997, Science, 278, 88
Schmitz, B., Tassinari, M., & Peucker-Ehrenbrink, B. 2001, Earth and Planetary Science Letters, 194, 1
Vokrouhlický, D. 2009, ApJ, 706, L37
Vokrouhlický, D., & Nesvorný, D. 2008, AJ, 136, 280
Vokrouhlický, D., & Nesvorný, D. 2009, AJ, 137, 111
Vokrouhlický, D., Milani, A., & Chesley, S. R. 2000, Icarus, 148, 118
Vokrouhlický, D., Ďurech, J., Michałowski, T., et al. 2009, A&A, 507, 495
Vokrouhlický, D., Ďurech, J., Polishook, D., et al. 2011, AJ, 142, 159
Vokrouhlický, D., Bottke, W. F., Chesley, S. R., Scheeres, D. J., & Statler, T. S. 2015, in Asteroids IV, eds. P. Michel, F. E. DeMeo, & W. F. Bottke, 509
Wisdom, J., & Holman, M. 1991, AJ, 102, 1528
Wolters, S. D., Weissman, P. R., Christou, A., Duddy, S. R., & Lowry, S. C. 2014, MNRAS, 439, 3085
Zappalà, V., Cellino, A., Farinella, P., & Knežević, Z. 1990, AJ, 100, 2030

B. History of understanding the Solar System

The dynamics and orbital characteristics of the Solar System along with the attempts to provide information about its orbital history are a very complex and rapidly developing part of celestial mechanics. It has been a long and arduous journey to obtain the current knowledge, undertaken by many individuals, some well-known, some whose names have faded from popular memory. The aim of this chapter is to outline the key points of this journey and the main concepts that have influenced the current view of the structure of the Solar System.

B.1 The Period until the Renaissance

The attempts to explain celestial movements are as old as mankind. People have always been looking up at the sky, with a desire to make sense of the movements of the celestial bodies they observed. The success of such an enquiry went hand in hand with the quality of the observational data and the technical capacity of the given epoch. The primary knowledge of the processes taking place in the universe was merely descriptive and falls within the period before the Renaissance. It was not until the Renaissance when the door was opened to new discoveries, as well as the interpretation of already known, empirically described processes.

B.1.1 Pre-Antiquity astronomy

The beginnings of astronomy date back to about 6,000 years ago. People's interest in the movement of celestial bodies was conditioned by the purely practical needs of the civilizations. Thanks to the constellation of objects on the celestial sphere, they were able to predict, solely based on their experience, the period of floods, solstice, and other important events. The study of the movements of the Sun, the Moon and the planets also found a significant application in the introduction of the first chronometric instruments and calendars. Astronomy began to thrive in Mesopotamia about 3,000 BC with the rise of the Chaldean civilization. The people of this civilization built large cities with ziggurats - astronomical observatories, which were very advanced for their time. Chaldean astronomers mostly concentrated on the observations of the Moon and the Sun, and later began studying the planets as well. Moon observations led to the creation of a lunar calendar, and one synodic period served as a benchmark for determining the length of one year, which they determined as a period of ≈ 354 days. A similar result was achieved by Chinese astronomers at that time.

Somewhat later, around the 5^{th} century BC, Chaldean astronomers already knew the approximate orbital periods of the brightest planets, as well as their retrograde and looping motion as observed in relation to the stars in the background.

Egyptian astronomy also achieved significant results in observation. The Egyptians were extremely proficient in predicting the flooding of the Nile, which

was vital to them. The duration of the Egyptian year was 365 days, divided into 12 months with 30 days each. Furthermore, they developed the method of approximate determination of the angular diameter of the Sun, based on the measurement of the period starting from the first appearance of the Sun above the horizon until its complete emergence in relation to the total duration of its movement from the east to the west. Numerically, this ratio was 1/750, which is $28'50''$.

Chinese astronomy was developing relatively independently and its origins can be traced back to the 3$^{\text{rd}}$ millennium BC. Chinese astronomers used gnomon in their observations - a vertical rod mounted in the ground. By analysing the shadow cast by the rod, they determined the angular height of the Sun over the horizon. They also successfully calculated the obliquity of the ecliptic $\epsilon = \frac{H-h}{2}$, where H is the height of the Sun at noon during the summer solstice and h is the height at winter solstice. They calculated it as $\epsilon = 23°54'$. Around the 8$^{\text{th}}$ century BC, Chinese astronomers were able to measure that the ecliptic longitude of the stars was shifting by 1° in 83 years, which is $45''$ a year. Today's value of the annual precession is about $50.26''$.

However, other civilizations did not fall behind. Europe had its Stonehenge observatory for determining the dates of the solstice and equinox. On Yucatan peninsula, there was Mayan astronomy, in the Peruvian Andes the astronomy of the Incas, and there were others.

In the period before the antiquity, astronomers naturally focused mainly on observing the Sun and the Moon, using their findings to create calendars and chronometric devices. They also observed bright stars, whose movement they explained as the sky's rotation around the Earth. On the other hand, the movements of the planets were still problematic. Ancient astronomers also used simple observation devices and achieved accuracy relative to their equipment. However, it is important to note that astronomical research in the pre-antiquity era was purely descriptive and based on empirical results of observations. Astronomers were not concerned with the origin of the observed facts, nor did they discuss the possible forces behind the phenomena they could observe in the sky.

B.1.2 Ancient Greek astronomy

Ancient Greek astronomy, which began around the 6$^{\text{th}}$ century BC can be considered as the beginning of scientific astronomy as such. Great progress was achieved largely thanks to excellent knowledge of geometry and mathematics. Greek astronomers tried to make sense of the phenomena that they observed and they advanced from merely recording periodically recurring events to the first attempts to interpret them by means of generally applicable laws.

The main representative was **Thales of Miletus** (624 – 548 BC), who perceived mathematics and geometry as the cornerstones of astronomy. Moreover, the Pythagorean school, founded by **Pythagoras of Samos** (570 – 510 BC), believed in the general laws of nature. The most comprehensive interpretation of the origin of celestial movements in this period comes from **Plato** (427 – 347 BC) and **Aristotle** (384 – 322 BC).

Plato claimed that the stars and even the Earth rotated evenly around their axes. He also ordered the bodies of our Solar System according to their distance

from the Earth in the following order: Moon, Sun, Venus, Mercury, Mars, Jupiter and Saturn. Aristotle, on the other hand, devised a complicated model of the planets residing in principal and auxiliary spheres moving around the Earth. The cause of the movement of these spheres was supposed to be an indeterminate rotating sphere located beyond the sphere of the stars. In his system, Aristotle correctly placed the planets beyond the Moon and the Sun, but his view was still geocentric.

The first known proponent of the heliocentric model was **Aristarchus of Samos** (310 – 250 BC), who came up with two basic principles - (i) all planets orbit around the Sun, (ii) their motion is uniform. Unfortunately, the measurements were not accurate enough yet to reveal an uneven motion of the planets and due to conflicts with the astrological ideas of the time, Aristarchus's heliocentric model was not further developed. It is important to note that what led Aristarchus to the notion of heliocentrism were his results determining celestial body dimensions $R_{\odot} \approx 7R_{♁}$, $R_{☾} \approx (7/19)R_{♁}$ and mutual distances $r_{♁☾} \approx 19R_{♁}$ and $r_{♁\odot} \approx 19r_{♁☾}$ (Heath, 1913).

The person who is considered to be the father of scientific astronomy is **Hipparchus** (190 – 120 BC). Hipparchus combined various mathematical and geometrical constructs with the results of the astronomical observations of his time and attempted to quantitatively describe the movements of the Moon, the Sun, and the planets. In addition to measuring star positions and compiling a catalogue of the stars, he also studied the differences between the sidereal and tropical years and determined their length.

The last significant Alexandrian astronomer was **Claudius Ptolemy** (90 – 165), who is known for his *Almagest*, a work which is considered to be a summary of ancient astronomy. This extensive work is devoted to practically all the then-known astronomical issues. He developed a model that, with an accuracy corresponding to his time, captured the anomalies of the motion of the planets. The key idea was based on the fact that Ptolemy replaced the irregular movements of planets by a superposition of several simple uniform circular movements (Fig. B.1). In Almagest, Ptolemy also kinematically describes the inequalities in the Moon's movement, especially evection, first observed by Hipparchus. The evection is caused by periodic perturbations in the Moon's motion due to the solar attraction. The eccentricity of the Moon's orbit varies with a 31.8-day period and it leads to a periodical change of the Moon's ecliptic longitude of approximately 1° 17', corresponding to Ptolemy's estimate of two full moons. Ptolemy was also somewhat reserved concerning astrology, which he did not consider to be comparable to scientific astronomy. Nevertheless, he did not deny its certain, albeit debatable, findings.

He was concerned with a variety of issues – for instance, it is worth mentioning his views of the effect of celestial bodies. To the theory of the then-known Solar System, he added that the active power of the Sun is in its heating and drying, which is most apparent when the Sun is at its zenith. The Moon, according to Ptolemy, has an effect on irrigation, most likely due to the fact that it is closest to the Earth. He believed that the Moon has an influence on the changes in the water levels of rivers. Just like ancient navigators, he knew the relationship between the ebb and flow, and the moonrise and moonset. He also attributed a certain active force to the planets.

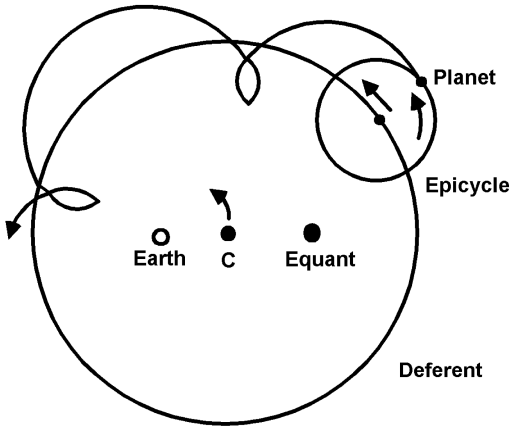

Figure B.1: A schematic representation of the Ptolemaic model. Each of the planets is orbiting evenly along a smaller circle - epicycle, whose center is moving at a constant angular velocity along a larger circle - deferent. Point C is the center of the deferent. By choosing an appropriate distance of the Earth from the deferent center, the ratio of the epicycle size to the deferent, and appropriately determined angular velocities, Ptolemy managed to obtain values corresponding well with real observations. He presented a unique model for his time, accounting for the characteristic retrograde loops of the planets.

After antiquity, the greatest advances in astronomy took place in the Islamic world. Arabic science adopted the Ptolemaic system and refined the theories of solar and lunar motion. One of the iconic figures of Arabic astronomy of that time was the Persian astronomer **Al-Biruni** (973 – 1048), who expressed doubts about the validity of the geocentric system and studied the conversion formulas between individual calendars. **Ulugh Beg** (1394 – 1449), an Uzbek astronomer from the famous Samarkand observatory, also achieved outstanding observational results.

Even though this historical period marked the beginning of a truly scientific approach to astronomy, the causes of the movements of the celestial bodies were still shrouded in mystery. Ancient astronomy was rather empirical and descriptive. Any discussion of the causes and consequences of the movements of the celestial bodies was predominantly based on astrological dogmas.

B.2 The Middle Ages and the Renaissance

Up until the Middle Ages, the Ptolemaic geocentric model of the universe was generally accepted and respected. His successors then gradually added more epicycles and deferents for an even better agreement with observations.

The roots of the modern view of the Solar System, however, go back to **Nicolaus Copernicus** (1473 – 1543), who reflected on the complexity of the Ptolemaic model as such, but also considered the persisting differences between theory and observations. Copernicus mainly tried to explain why the planets move in a direction opposite to that of the fixed stars. He gradually came to the conclusion that the answer to this question was a more elegant system, in which the Sun

was the center of the universe, and the planets, located in spheres, were orbiting around it. He understood the movements in the celestial sphere as the result of a superposition of the Earth's circular motion around the Sun, which was located near the center of a circular orbit, and the rotation of Earth itself. Later he added the precession as well.

Copernicus supported all his claims with mathematical proofs and astronomical observations. In the ninth chapter of the first book of his work *De Revolutionibus*, he formulated his views on mutual attraction. Gravity, according to him, was a certain natural inclination of objects to be attracted to the Sun, Earth, Moon, and planets. These reflections, however, did not lead Copernicus to the notion of universal gravitation.

Copernicus measured our Solar System quite accurately. He was able to determine the relative radii of the planets' orbits compared to the radius of the Earth's orbit with unusual precision. The relative error as opposed to today's values was less than $\leq 1\%$ for planets except Saturn, for which it was $\leq 4\%$. Note, however, that the value of the Astronomical Unit was still quite different from the actual value. It was established as 1 au $\approx 1200 R_{\oplus} \approx 7.5 \times 10^6$ km. Copernican heliocentrism increased the accuracy of the calculations of the ephemerides of astronomical objects and it was used, for instance, by the German mathematician and astronomer **Erasmus Reinhold** (1511 – 1553) in his work *Tabulae prutenicae*, which became the basis for the reform of the Gregorian calendar.

Copernicus's views of the structure of the universe were surpassed by the Italian philosopher and astronomer **Giordano Bruno** (1548 – 1600). As a result of his revolutionary idea of the infinity of time and space, the Earth and the Sun lost their privileged position in the universe. Giordano Bruno predicted the existence of other planets in the Solar System and he also believed in the existence of planets around other stars. Unfortunately, he could not support his claims with astronomical observations or mathematical proofs.

Shortly after Nicolaus Copernicus's death, the world's most accurate naked-eye astronomer, **Tycho Brahe** (1546 – 1601), was born. In Denmark, on November 11, 1572, he observed a bright new star in the constellation of Cassiopeia and recorded its angular distances from the nearby stars. As the supernova (now SN 1572) was not moving in relation to the other stars, he correctly categorized it as a fixed star. By measuring the daily parallax of comet *C/1577 V1*, he also correctly revealed that it must be located beyond the Moon's orbit, where the planets are. Thanks to his observations of the comet, he concluded that the then-established spheres could be an obstacle in its movement. At the same time, he challenged the respected Aristotelian notion that comets were formed in the upper layers of the Earth's atmosphere.

Brahe rejected Copernicus's heliocentric theory; nevertheless, he appreciated its benefits regarding the calculations of planet ephemerides. The reason was that, due to an insufficient accuracy of the observations of his time, he could not measure a non-zero annual stellar parallax. He went on to build his own model of the universe - a compromise between the geocentric and heliocentric theory, placing the Earth in the centre, with the Sun orbiting around the Earth, while the other planets orbited around the Sun. Over time, already during Tycho's life, there were increasing inaccuracies in the predicted planetary positions. For

corrective purposes, this brilliant Danish astronomer gathered the observations of planets over a period of 20 years. Especially the observations of Mars were exceptional, covering almost 10 of its revolutions around the Sun, with $\approx 2'$ precision. They later became the basis for **Johannes Kepler** (1571 – 1630) in his efforts to find the kinematic laws of planetary motion.

Johannes Kepler was searching for a mathematical expression of Mars's trajectory around the Sun. As a supporter of the heliocentric theory, his first step was to define the trajectory of the Earth with a greater precision. Unfortunately, the accuracy of astronomical observations of the time did not allow for a distinction between a circular and an elliptical orbit. However, the Earth's non-zero orbital eccentricity manifested itself in another way – an uneven motion of the Sun along the ecliptic. Kepler subsequently came to the result that the Earth moved faster in the perihelion than in the aphelion. In 1601, he began studying the trajectory of Mars.

Out of a large sample of Tycho Brahe's measurements, he chose and specified the positions of twelve Mars oppositions from the years 1580-1604 (Kepler, 1609). In principle, Kepler used 2 rays for the determination of the shape of the Mars trajectory. The first ray p_1 always corresponded to a Mars opposition and started in the Sun, passing through the Earth and Mars. For the construction of the second ray p_2, it was necessary to wait one Mars year (687 days), when Mars occupied the same position in relation to the stars, whereas the Earth was in another place (on its way toward completing a second orbit). With the knowledge of the heliocentric longitude θ of the Earth and the geocentric longitude ϕ of Mars, it was possible to construct the second ray p_2 starting out at the center of the Earth, diverging from the vernal equinox by the angle ϕ. The intersection of rays p_1 and p_2 then determined the actual position of Mars in the given opposition.

By analyzing the results, Kepler found that the trajectory was an elongated circle with the closest and farthest points to the Sun called perihelion and aphelion, respectively. Eventually, in 1605, he described the motion of Mars using his well-known equation and determined that the trajectory of Mars was an ellipse with the Sun in its focus. Kepler, in his work *Astronomia Nova*, also discussed weight and gravitation. He believed that the power that causes the motion of planets originates in the Sun and is of a magnetic nature. Kepler's Third Law was published in *Harmonices mundi libri* in 1619. The results of Kepler's work fundamentally simplified and refined the calculation of planet ephemerides, which Kepler summarized and published in the *Rudolphine Tables* in 1627.

The Italian physicist and astronomer **Galileo Galilei** (1564 – 1642) was of fundamental importance for the confirmation of the heliocentric system and for the entire observational astronomy. In 1609, he constructed the first simple refractor, which he soon turned toward the sky.

He discovered that the surface of the Moon was irregular, with craters and mountains, comparing the nature of its surface to that of the Earth. He also focused on the planet Jupiter, around which he discovered four of the now-called Galilean moons. However, in the case of his observation of Saturn, he did not distinguish its rings due to an unfavorable orientation towards the Earth. In his telescope, he perceived the planet as a triple star. His observations of the phases of Venus and the changes in brightness depending on Venus's distance from Earth provided him with a compelling argument in favor of heliocentric theory.

Galileo naturally also pointed the telescope to the Sun, where he observed the emergence, evolution and disappearance of sunspots. He attributed the movement of sunspots to the rotation of the Sun around its axis and estimated the time of one synodic period of its rotation. The sunspots did not escape the attention of other astronomers, such as **Thomas Harriot** (1560 – 1621) or **Johann Fabricius** (1587 – 1617), who first published the discovery in 1611.

Descriptive geometric research of the Solar System also required an accurate determination of the Earth's radius and the length of the astronomical unit. The first astronomer who was able to accurately determine the Earth's radius was **Jean Picard** (1620 – 1682). According to the methodology of the Italian mathematician **Francesco Maurolico** (1494 – 1575) and the Dutch mathematician and astronomer **Willebrord Snellius** (1580 – 1626), Picard and his team used the triangulation method to measure the distance along the local meridian between Paris and Sourdon near the French town of Amiens. The result of their calculations was that 1° in latitude corresponds to 57060 toises (a French unit of measurement) (Picard, 1671). After the conversion of 1 toise ≈ 1.949 m, Earth's radius equalled 6372 km, assuming a perfectly spherical shape of the Earth.

Later, the Cassini family made their own independent measurements, which showed that the Earth was flattened along its equator. This was in contradiction with the law of universal gravitation written by Isaac Newton (1643 – 1727). Newton and his followers, on the contrary, argued that the Earth was flattened at its poles. The dispute was resolved when two more geodetic surveys funded by the French Academy of Sciences confirmed the flattening of the Earth at its poles (e.g. Smith, 1996; Murdin, 2009).

Investigator	**Approx. Date**	**1/4 Meridian Arc Length [m]**	**F**[a]
Eratosthenes	200BC	11 562 500	—
Willebrord Snellius	1615	9 660 000	—
Jean Picard	1670	10 009 081	—
Cassini Brothers	1700	10 042 652	-1:66
French Academy of Science	1750	10 000 157	1:310.3
Delambre and Méchain	1800	10 000 000	1:334

Note: [a] Flattening.

Table B.1: An overview of the major protagonists involved in the research of Earth's geometric properties. Adapted from Brinker and Minnick (1987).

A greater precision in the calculation of Earth's radius naturally affected the length of the astronomical unit as well.

From the observations of the great opposition of Mars from Cayenne and Paris, in 1672, a French astronomer **Jean Richer** (1630 – 1696) and a French astronomer of Italian origin **Giovanni Domenico Cassini** (1625 – 1712) derived the value of Mars's horizontal parallax as $p_M = 25\,\frac{1}{3}''$. The horizontal parallax of the Sun is expressed as $p_S/p_M \approx a'/a$, where a' and a are the semi-major axes of Mars and Earth. The ratio a'/a can be determined from Kepler's third law. Based on the calculated value $p_S = 9.5\,\frac{1}{5}''$, they then determined the length of the astronomical unit as $\approx 1.38 \times 10^{11}$m (e.g. Olmsted, 1942).

A further refinement of the value of the astronomical unit was based on the work of the *New Method of Determining the Parallax of the Sun*, written by an

English astronomer and mathematician **Edmond Halley** (1656 – 1742). Later, a French astronomer **Jérôme Lalande** (1732 – 1807) applied Halley's method to the results of his observations of Venus's transits across the Sun from 1761 and 1769. He calculated the value of the astronomical unit as $\approx 1.53 \times 10^{11}$m.

In the last third of the 17th century, it was finally possible to settle the age-old debate about whether the speed of light is finite or infinite. The first adequate estimate of the speed of light comes from the Danish astronomer **Ole Christensen Rømer** (1644 – 1710), who systematically observed the onsets and end times of the eclipses of Jupiter's moon Io. He discovered that the interval between the two occultations is shorter when the Earth approaches Jupiter and longer when it moves away. The Dutch astronomer **Christiaan Huygens** (1629 – 1695) determined the speed of light as 220,000 km s^{-1} based on Rømer's observations (Huygens, 1690).

B.3 The modern era

The entire period of Renaissance astronomy was a cornucopia of discoveries. The end of the Renaissance also witnessed a rise in the field of stellar, galactic, and extragalactic astronomy, cosmology, and others. Astronomy, the oldest scientific discipline, was beginning to fragment into partially overlapping sub-fields. Astronomers armed with increasingly more sophisticated telescopes were revealing the near as well as the distant universe at a growing pace. The ever-increasing astrometric accuracy of observations led to discoveries of hitherto unknown phenomena, both in stellar astronomy and in planetary movements, or the dynamic behavior of the Moon.

The English astronomer **John Flamsteed** (1646 – 1719), the first British royal astronomer and founder of the Royal Greenwich Observatory, increased the accuracy of the measurements of the positions of the celestial bodies by using a reticle in his telescope. He also used micro-metric screws for a more accurate positioning of the telescope. Flamsteed's measurements of the star positions were very precise. He compiled the *Historia Coelestis Britannica* – in his time the most accurate catalogue of nearly 3,000 stars and their positions with a mean error of[1] $\approx 10''$.

An even greater astrometric accuracy of $5''$ was later achieved by the English astronomer **James Bradley** (1693 – 1762), the discoverer of the aberration of light and the nutation of the Earth's axis. The discovery of nutation was brought on by his astrometric measurements of the changes in star positions that could not be explained by either the precession of the Earth's axis or aberration.

Precise astrometric observations allowed **Edmond Halley** (1656 – 1742) to discover proper motion of certain stars. By comparing the stars' current positions with those recorded in Ptolemy's *Almagest*, he revealed proper motion of Arcturus, Sirius and Aldebaran. In the case of the first two, Halley's conclusions correspond to today's values. In the case of Aldebaran's movement, the results differ – probably due to a mistake in Halley's calculations (see Brandt, 2010). Halley also speculated that the difference between observed and expected positions of

[1]Flamsteed unknowingly became the first known observer of the planet Uranus, which he recorded in his catalogue under the name '34 Tauri'.

Jupiter and Saturn may be rooted in their mutual gravitational interaction. After the discovery of Jupiter's first four moons by Galileo and Saturn's five moons by Huygens and Cassini, the moons were studied in greater detail. With regard to the observation accuracy of the time, astronomers were not able to reveal the elliptical character of the moons' orbits and assumed a circular motion.

Up until then, it was still possible to think of the Solar System research as geometrically descriptive without a quantitative explication of the causes of the dynamic behavior of known objects. A theoretical basis for the dynamics of the Solar System and celestial mechanics in general is the work of **Isaac Newton** (1643 – 1727) entitled *Philosophiae Naturalis Principia Mathematica*, published in 1687. This extensive work is divided into three books dealing with the mechanics of point mass and rigid bodies, hydrodynamics, and lastly, gravitation and celestial mechanics.

Newton proved that if a body moves around the Sun in an elliptical orbit, the gravitational force acting on the body decreases inversely proportional to the square of distance[2]. Newton also showed that if the body moves around a certain centre, then the force that deflects this body from its motion along the tangent of the trajectory must necessarily be directed toward this centre. He concluded that the motion of the planets is therefore the result of the Sun's gravity. Newton further expanded this conclusion to the movement of comets and moons, which gave rise to his law of universal gravitation. From the gravitation law, he derived Kepler's third law in its exact form, which he applied to the system Jupiter-Callisto and calculated Jupiter's mass, thus opening the door to the first method of determining the mass of celestial bodies. He also provided a theoretical basis for the 2-body problem, which was applied to the movement of comets, moons and later asteroids or physical binary stars.

Newton devised a method of determining the orbital parameters of celestial bodies from three observations and used it on the spectacular occurrence of the Kirch[3] comet in 1680. His results were in perfect agreement with the observations and confirmed the success of this method. It was soon extensively used by Edmond Halley, who, in his *Synopsis of the Astronomy of Comets* (1705), published calculations of 24 comet orbits. Based on comet observations by **Peter Apian** (1495 – 1552) in 1531, Johannes Kepler and **Christen Longomontanus** (1562 – 1647) in 1607, and his own observations from 1682, Halley concluded that there were not three different comets, but one comet[4] returning periodically every 75-78 years. Edmond Halley also recognized the elliptical character of the orbit, which was approaching a parabolic profile in the perihelion and he predicted the return of the comet between 1758 and 1759. A more specific period of April 1759 was then calculated by the French astronomer **Alexis Clairaut** (1713 – 1765). Although the comet actually occurred a month earlier, it was bulletproof evidence

[2]The general formula relating the form of the central force to the shape of the trajectory is described by Binet's equation – a non-linear differential equation of the second order derived by the French astronomer **Jacques Binet** (1786 – 1856).

The formula is $f(u^{-1}) = h^2u^2(u + d^2u/d\theta^2)$, where f is the acceleration of the particle in the central force field, h is the specific angular momentum and $u \triangleq 1/r$, where $r(\vartheta)$ is the polar equation of the trajectory (e.g. Moulton, 2012). Newton thus solved the inverse Kepler problem $u(r(\vartheta)) \to f(r)$.

[3]C/1680 V1

[4]1P/Halley

of the validity of Newton's gravitation theory. The comet was also observed by the French astronomer **Charles Messier** (1730 – 1817) - an excellent observer, the discoverer of 14 new comets, and the author of the *Catalogue of Nebulae and Star Clusters* (1781).

Figure B.2: Comet from 1680 above Rotterdam. Author: Lieve Verschuier.

B.3.1 Theories of lunar motion

Although astronomers had already known about the main perturbations of the Moon's orbit before Newton's theory, the publication of Newton's *Principia* marked the beginning of the stage of quantitative description of lunar motion. Newton showed that the irregularities in lunar motion were a result of perturbations caused mainly by the Sun.

It was problematic for him, however, to solve the problem of the pericenter precession. Newton supposed a near-circular motion of the Moon, and in his calculations, he reached the conclusion that the perigee is shifting by $1°32'28''$ over one revolution around the Earth, which is roughly half the current value (see Taton et al., 2003, for further details). From other lunar perturbations, Newton qualitatively explained the precession of lunar nodes, perturbations in inclination, evection and variation[5] (Gutzwiller, 1998). Note that the comprehensive perturbation theory of lunar motion is a relatively complicated branch of celestial mechanics, and the mathematical tools for its final elaboration were not yet available in Newton's time.

[5]The $\frac{15}{4}me\sin(2D-M)$ term with a $2D-M$ argument in equation (B.2) is called evection and the value of coefficient $\frac{15}{4}me$ is $52'56''$. If higher order terms are taken into account, the value will converge to $\approx 1°16'26''$. The period of the evection term is $\frac{2\pi}{2n-2n'-cn} = \frac{2\pi}{n(2-2m-c)} = \frac{T}{2-2m-c} \approx 31.8$ days. The variation term $\frac{11}{8}m^2\sin 2D$ has a period of 14.8 days. If solar eccentricity were to be considered, another term $-3me'\sin M'$ would appear, M' being the Sun's mean anomaly. This term is called annual equation, with an amplitude of $772''$ over a one year period.

The lunar orbit is predominantly perturbed by the Sun. The perturbation forces vary depending on the distance of the Moon while orbiting the Earth, but also in the course of the year due to the non-zero eccentricity of the Earth's orbit. There are, of course, other sources of perturbations such as tidal forces, which participate in the whole 3-body system. Newton, however, identified the main perturbations in the longitude and latitude.

Let us consider a geocentric system where the reference plane is the plane of the apparent orbital motion of the Sun around the Earth, while the primary direction is the direction towards the vernal equinox. In this system, we study the motion of the Moon, whose apparent orbit on the celestial sphere intersects the ecliptic in the ascending node Ω. Its orbit is also inclined to the ecliptic ($i \approx 5.15°$). If v is the mean longitude of the Moon, assuming undisturbed motion, it holds that (e.g. Brown, 1896)

$$v \approx nt + \epsilon + 2e \sin M + \frac{5}{4}e^2 \sin 2M - \frac{1}{4}\gamma^2 \sin 2F, \tag{B.1}$$

where n is the mean motion of the Moon, e is eccentricity, $\gamma = \tan i \approx i$ is the tangent of the inclination of the lunar orbit, ϵ is the mean longitude at epoch, $M = nt + \epsilon - \varpi$ is the mean anomaly and $F = nt + \epsilon - \Omega$ is the mean argument of latitude, which is the angular distance between the mean Moon and the ascending node. Note that the terms in this equation are purely Keplerian.

According to the results of the modern theory of lunar motion, in an approximation to the 2$^{\text{nd}}$ order, we have (e.g. Brown, 1896)

$$v \approx nt + \epsilon + 2e \sin M + \frac{5}{4}e^2 \sin 2M - \frac{1}{4}\gamma^2 \sin 2F + \frac{11}{8}m^2 \sin 2D + \frac{15}{4}me \sin(2D - M), \tag{B.2}$$

where $m = \frac{n'}{n} \approx 0.0748$ is the ratio of the mean motion of the Sun and the mean motion of the Moon, and

$$D = t(n - n') + \epsilon - \epsilon' \tag{B.3}$$

is the mean elongation of the Moon. The secular perturbations of the longitude of pericenter ϖ and the longitude of ascending node Ω can be calculated by using constants c and g so that (see Brouwer and Clemence, 1961)

$$\varpi = (1 - c)nt + \varpi_0, \qquad \Omega = (1 - g)nt + \Omega_0. \tag{B.4}$$

The constants c and g were first introduced by the French mathematician **Alexis Claude Clairaut** (1713 – 1765), who modeled the perturbation of the lunar motion by a rotating ellipse. The results of his calculations were published in his monograph entitled *Tables de la lune*, which summarizes the calculated lunar positions, which differ from the actual values by approximately $1.5'$. The constants introduced by Clairaut can be expressed in the form of a power series in the variable m as follows (Brown, 1896):

$$c = 1 - \frac{3}{4}m^2 - \frac{225}{32}m^3 + \ldots \qquad g = 1 + \frac{3}{4}m^2 - \frac{9}{32}m^3 + \ldots. \tag{B.5}$$

Finally, it is necessary to substitute the original variables in the equation (B.2) by using the following equations:

$$M \to M = cnt + \epsilon - \varpi_0, \qquad F \to F = gnt + \epsilon - \Omega_0. \tag{B.6}$$

The French mathematician **Jean Baptiste d'Alambert** (1717 – 1783) introduced the term $\frac{225}{32}m^3$ in the equation (B.5), which was also done by Clairaut. This clearly helped to reduce the difference between the theory and observations. Note that the $\frac{3}{4}m^2$ term alone contributes to a shift of the pericenter during one revolution approximately by the value estimated by Newton $(\frac{3}{4}m^2)\cdot 360^\circ \approx 1.5^\circ$, whereas $(\frac{3}{4}m^2 + \frac{225}{32}m^3)\cdot 360^\circ \approx 2.6^\circ$, which is roughly the current value.

Another significant advance in the theory of lunar motion was the work published in 1753 entitled *Theoria motus Lunae exhibens omnes eius inaequalitates* by the Swiss mathematician **Leonhard Euler** (1707 – 1783). Later, between 1753 and 1771, he introduced the so-called second lunar theory, which included tables of calculated positions of the Moon as well as some corrections of existing series.

Leonhard Euler's work can be classified as a classical analytical method, where the time evolution of orbital elements is determined by solving the equations of motion. Not only did he find expressions for the time derivatives of the semi-major axis, eccentricity, and the longitude of perigee, but he also considered the non-zero eccentricity of the Earth's orbit. In addition, he examined the lunar motion in a co-rotating reference frame, where the coordinate axes x and y rotate at the angular velocity n in the plane of the ecliptic, with the z axis pointing to its north pole. Euler derived 3 differential equations of the second order and solved them by using the method of variation of constants. Due to his failing eyesight, he concluded his work with the help of his son **Johann Euler** (1734 – 1800), the German astronomer **Wolfgang Kracke** (1743 – 1814) and the Russian astronomer **Andrew Lexell** (1740 – 1784).

One of the many issues at hand was also the effect of secular acceleration of the longitude of the Moon. The French mathematician and astronomer **Pierre Simon de Laplace** (1749 – 1827) attributed Moon acceleration to small yet continual changes in the eccentricity e' of the Earth's orbit caused by perturbations of the planets. This effect is evident when higher order terms in the disturbing function of the Moon are taken into account, which also results in new terms[6] on the right side of the equation (B.2).

Later, at the beginning of the 19th century, the French astronomer **Charles Delaunay** (1816 – 1872) developed an even more general theory with new canonical variables, providing the most extensive algebraic solution of lunar motion before the rise of modern information technologies. His results, including terms up to the eighth, or even ninth and tenth order, were summarized in *The Theory of Lunar Motion* between 1860 and 1867.

Delaunay's expansions were refined and extended by the Belgian astronomer **André Deprit** (1926 – 2006). Deprit utilized the powerful force of computers, especially the symbolic algebraic manipulators, and expanded the original series by adding more terms. He also found some numerical inaccuracies that Delaunay omitted, thus revising his theory (see Deprit et al., 1971).

[6]Secular acceleration gives rise to a slow increase in the mean motion n of the Moon. The longitude of the Moon is then $v = nt+\epsilon+\frac{3}{2}mn'e'_0\alpha t^2+$ *periodic terms*, where e'_0 is the eccentricity of the Earth's path for a given epoch and $e' \approx e'_0 - \alpha t$ (e.g. Brown, 1896). Numerically we get $\frac{3}{2}mn'e'_0\alpha t^2 \approx 10''(\frac{t}{100})^2$, which corresponds to secular acceleration of approximately $10''$ per century. An even more detailed analysis of the higher-order terms, which was conducted by the British astronomer and mathematician **John Adams** (1819 – 1892), converged closer to the current value of $\approx 6''$ per century (Adams, 1853).

In England 1857, the Danish astronomer **Peter Andreas Hansen** (1795 – 1874) published some equally detailed tables of lunar positions in his works entitled *Fundamenta nova investigationis* and *Tables of the Moon*. The deviations in comparison to the actual Moon positions were not more than $1'' - 2''$ over a period of 100 years.

At the beginning of the 20th century, the theory of lunar motion was further elaborated, largely thanks to **George William Hill** (1838 – 1914), an employee of the US Naval Observatory, then run by the Canadian astronomer **Simon Newcomb** (1835 – 1909). George Hill made an impact in many sub-fields of astrodynamics. Among other issues, he was dealing with the three-body problem, and he also refined and further developed the theory of Jupiter's and Saturn's motion.

Hill's work was expanded by the English mathematician and astronomer **Ernest William Brown** (1866 – 1938), whose tables for calculating the positions of the Moon in 1923 practically replaced those made by Peter Hansen, which had been used until then. Ernest Brown's series included up to 1,500 terms and were expanded later in 1966 by numerical methods of **Wallace Eckert** and **Harry Smith**, their number growing to 6,000 (Eckert and Smith, 1966b,a).

At the beginning of the 1990s, an extensive semi-analytical theory of lunar motion - ELP 2000-82 (Chapront-Touze and Chapront, 1983) was presented based on the knowledge of a whole spectrum of various perturbations of the system Moon – Earth - Sun including tidal, relativistic as well as planetary perturbations. The theory comprises all the tiny effects that affect lunar motion and includes tens of thousands of terms. It also provides an impressive accuracy in the determination of lunar coordinates within centimeters. The ELP 2000-82 is written in the Fortran language and contains dozens of data files that include terms corresponding to the particular perturbations[7].

At present, the most accurate geocentric coordinates of the Moon are stated by the JPL DEXXX Series[8], based on the numerical models of the Solar System developed in the Pasadena Jet Propulsion Laboratory, originally for the purpose of astronavigation. The ephemerides are determined from a numerical integration of the equations of motion, considering both the shape of the bodies of the Solar System and relativistic corrections. Initial conditions are based on a large number of observations, including accurate radar observations of planets or analysis of reflected laser beams from corner reflectors on the surface of the Moon. These were placed during the US Apollo 11, 14 and 15 missions and the Russian robotic missions Lunokhod 1 and Lunokhod 2 between 1969 and 1977. Nowadays, the Moon-Earth distance can be determined with millimeter accuracy.

B.3.2 Planetary theory

In the time of Tycho Brahe and Johannes Kepler, astronomers were unable to detect small perturbations in the planetary motion. However, since the 17th century, there was a growing accuracy in determining their positions, mainly thanks to the use of telescopes and more accurate measurements of time. Astronomers soon discovered small deviations to the elliptic orbits.

[7] See the VizieR catalogue: `ftp://cdsarc.u-strasbg.fr/pub/cats/VI/79/`.

[8] `http://ssd.jpl.nasa.gov/?ephemerides`

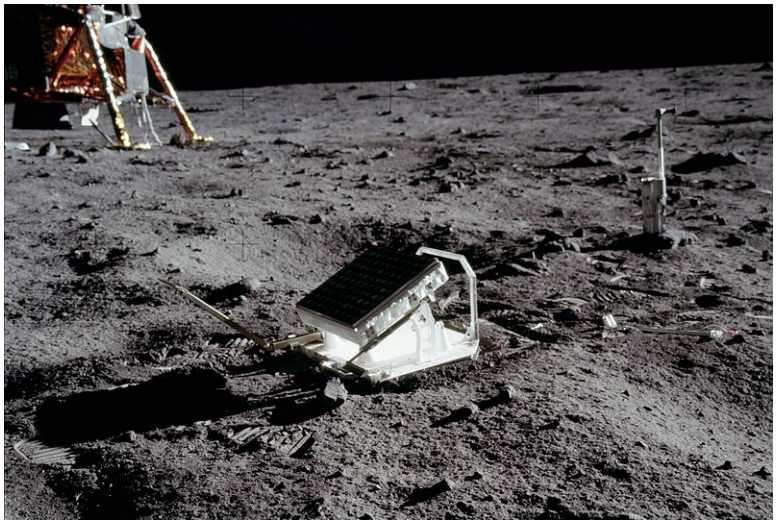

Figure B.3: Corner reflector placed during the Apollo 11 mission. Source: NASA Apollo Archive.

Even though it is not difficult to solve the two body problem, in a system of three or more bodies, analytical solutions either do not exist or they do but only in special cases. Generally, a system of N bodies can be described by $6N$ first order differential equations with $6N$ initial conditions. For a complete solution of the three body problem, we would require 18 integrations, while there are only 10 classical integrals of motion. A rectilinear and uniform motion of the center of mass $\mathbf{T}$ of a three-body system with masses M_i and total mass M can be expressed as

$$\mathbf{T} = \frac{1}{M}\sum_{i=1}^{3} M_i \mathbf{R}_i = \mathbf{C}_1 t + \mathbf{C}_2, \tag{B.7}$$

where $\mathbf{C}_1$ and $\mathbf{C}_2$ are constant vectors representing 6 integrals of motion. The other 4 integrals are the components of the total angular momentum $\mathbf{L}$, where

$$\mathbf{L} = \sum_{i=1}^{3} M_i \mathbf{R}_i \times \frac{d\mathbf{R}_i}{dt} = \mathbf{C}_3, \tag{B.8}$$

and the total energy of the system $E_{\text{tot}} = E_{\text{kin}} + E_{\text{pot}} = C_4$. In a special case of the restricted three body problem, there is another integral of motion - the Jacobi integral, which can be expressed in the co-rotating reference frame with the center in the barycenter as

$$C_J = n^2(x^2 + y^2) + 2\left(\frac{GM_1}{R_1} + \frac{GM_2}{R_2}\right) - (\dot{x}^2 + \dot{y}^2 + \dot{z}^2), \tag{B.9}$$

where (x, y, z) are the Cartesian coordinates of the test particle and $n = 2\pi/T$.

The absence of a complete analytical solution of the N-body problem led to the development of perturbation theory. The main principle here is that the motion of bodies in the Solar System is predominantly governed by the Sun, while the gravitational interactions with planets only cause small deviations from the Keplerian motion.

The main protagonists of the development of the perturbation theory and modern celestial mechanics of the 18th century were **Leonhard Euler** (1707 – 1783), **Alexis Claude Clairaut** (1713 – 1765), **Jean Le Rond d'Alembert** (1717 – 1783), **Joseph Louis de Lagrange** (1736 – 1813) and **Pierre Simon de Laplace** (1749 – 1827).

Planetary perturbation theory was first elaborated by Euler. His work on mutual perturbation of Jupiter and Saturn earned him a recognition of the French Academy of Sciences in 1748 and 1752. Not only was he the first who presented the method of the variation of constants - a general method to solve inhomogeneous linear ordinary differential equations, but he also derived the first form of the disturbing function.

Lagrange wrote his treatise on Jupiter's and Saturn's motion around 1766 and followed up on Euler's method of the variation of constants. The definitive version was completed in 1782. Lagrange's work entitled *Méchanique analytique* published in 1788 is a summary of his research and includes the Lagrange planetary equations as well as the Lagrange brackets or his form of disturbing function. Lagrange's planetary equations are the fundamental equations describing perturbations of orbital elements and are included in every major publication on celestial mechanics. The following is one of the many variants of these equations (Murray and Dermott, 1999):

$$\frac{da}{dt} = \frac{2}{na}\frac{\partial \mathcal{R}}{\partial \epsilon}, \tag{B.10}$$

$$\frac{de}{dt} = -\frac{\sqrt{1-e^2}}{na^2 e}(1-\sqrt{1-e^2})\frac{\partial \mathcal{R}}{\partial \epsilon} - \frac{\sqrt{1-e^2}}{na^2 e}\frac{\partial \mathcal{R}}{\partial \varpi}, \tag{B.11}$$

$$\frac{d\epsilon}{dt} = -\frac{2}{na}\frac{\partial \mathcal{R}}{\partial a} + \frac{\sqrt{1-e^2}(1-\sqrt{1-e^2})}{na^2 e}\frac{\partial \mathcal{R}}{\partial e} + \frac{\tan\frac{1}{2}I}{na^2\sqrt{1-e^2}}\frac{\partial \mathcal{R}}{\partial I}, \tag{B.12}$$

$$\frac{d\Omega}{dt} = \frac{1}{na^2\sqrt{1-e^2}\sin I}\frac{\partial \mathcal{R}}{\partial I}, \tag{B.13}$$

$$\frac{d\varpi}{dt} = \frac{\sqrt{1-e^2}}{na^2 e}\frac{\partial \mathcal{R}}{\partial e} + \frac{\tan\frac{1}{2}I}{na^2\sqrt{1-e^2}}\frac{\partial \mathcal{R}}{\partial I}, \tag{B.14}$$

$$\frac{dI}{dt} = -\frac{\tan\frac{1}{2}I}{na^2\sqrt{1-e^2}}\left(\frac{\partial \mathcal{R}}{\partial \epsilon} + \frac{\partial \mathcal{R}}{\partial \varpi}\right) - \frac{1}{na^2\sqrt{1-e^2}\sin I}\frac{\partial \mathcal{R}}{\partial \Omega}, \tag{B.15}$$

where $\mathcal{R}$ is the disturbing function and $\lambda = M + \varpi = n(t-T) + \varpi = nt + \epsilon$, where ϵ is the mean longitude at epoch. If we consider a system of three bodies - a dominant body of mass m_c and two orbiting bodies with masses m_i and m_j, then the equations of motion are:

$$\ddot{\mathbf{r}}_i = \nabla_i(U_i + \mathcal{R}_i) \qquad \ddot{\mathbf{r}}_j = \nabla_j(U_j + \mathcal{R}_j), \tag{B.16}$$

where

$$U_i = G\frac{m_c + m_i}{r_i} \qquad U_j = G\frac{m_c + m_j}{r_j}, \tag{B.17}$$

$$\mathcal{R}_i = \frac{Gm_j}{r_{ij}} - Gm_j\frac{\mathbf{r}_i\mathbf{r}_j}{r_j^3} \qquad \mathcal{R}_j = \frac{Gm_i}{r_{ij}} - Gm_i\frac{\mathbf{r}_i\mathbf{r}_j}{r_i^3}, \tag{B.18}$$

while $\mathbf{r}_i$ and $\mathbf{r}_j$ are position vectors with respect to the central body. As there are partial derivations with respect to orbital elements in equations (B.10) – (B.15),

the disturbing functions $\mathcal{R}_i, \mathcal{R}_j$ need to be transformed. Let us use a prime to mark the orbital elements of the outer planet to distinguish them from the orbital elements of the inner planet. Because the derivation of the following desired transformation

$$\mathcal{R}(x, x', y, y', z, z') \rightarrow \mathcal{R}(a, a', e, e', I, I', \lambda, \lambda', \varpi, \varpi', \Omega, \Omega')$$

is beyond the scope of this chapter, we present the main result of the theory, which is that the disturbing function $\mathcal{R}$ can be expressed in the form of a Fourier series (e.g. Murray and Dermott, 1999)

$$\mathcal{R} = \sum C \cos D, \tag{B.19}$$

where functions $C = C(a, a', e, e', I, I')$. General form of the argument D is

$$D = j_1\lambda' + j_2\lambda + j_3\varpi' + j_4\varpi + j_5\Omega' + j_6\Omega, \tag{B.20}$$

while $\sum_{i=1}^{6} j_i = 0$ (D'Alembert principle). Note that in the two-body problem, the mean longitude is a linearly increasing function of time and the other angles (Ω, ϖ) remain constant. Terms $C \cos D$ in the disturbing function are of two types: (i) short-period terms ($j_1 \neq 0 \wedge j_2 \neq 0$) and (ii) secular terms with $j_1 = 0 \wedge j_2 = 0$. Thus, the short-period terms predominantly lead to small and fast changes of the osculating elements, whereas the secular terms act for a much longer time.

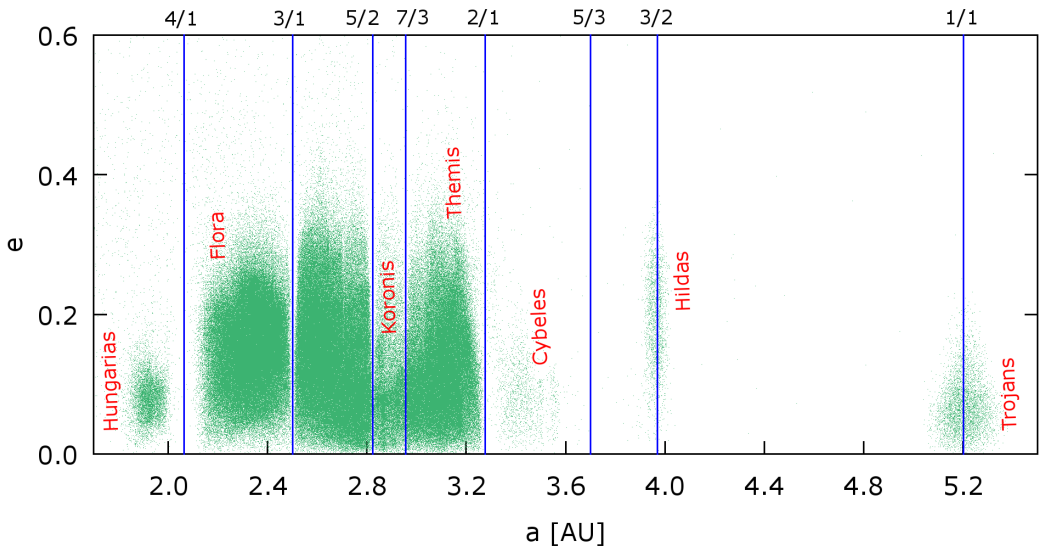

Figure B.4: The non-uniform distribution of known asteroids in the (a, e) space. The blue lines mark the mean motion resonances with Jupiter and also the so-called Kirkwood gaps, which were first discovered in the second half of the 19th century (Kirkwood, 1867). Kirkwood gaps are located in the most prominent mean-motion resonances J4/1, J3/1, J5/2 and J2/1 with Jupiter. Some resonances, on the other hand, are stable and are occupied by asteroid families such as Hilda (J3/2) or the Jupiter trojans (J1/1).

Let's discuss the value of $j_1\lambda' + j_2\lambda \approx (j_1 n' + j_2 n)t + const$ in equation (B.20). If $(j_1 n' + j_2 n) \approx 0$, then the period of the corresponding argument D is longer than any of the two orbital periods. The previous relation is fulfilled for certain combinations of the mean motions n, n' and coefficients j_1 and j_2. We call these arguments resonance terms and they also contribute to the secular evolution of planetary orbits[9]. The constant $k = |j_1 + j_2|$ is termed the order of resonance.

Aside from the mean-motion resonances, the secular evolution of a system is also affected by secular resonances, which occur when two bodies have a synchronous precession either of the pericenter, the ascending node, or both[10]. For more information on resonances see Murray and Dermott (1999).

In the second half of the 18th century, Joseph Lagrange and Pierre Laplace also dealt with the problem of stability of our Solar System. By analyzing the secular terms and solving Lagrange equations, they proved that the semi-major axes of planets do not exhibit secular changes and fluctuate around certain mean values. It is thus not possible for the planets to pass from an elliptical to a parabolic orbit and leave our Solar System.

It must be noted, however, that the Lagrange-Laplace secular theory for N planets, which provided Laplace with evidence of the stability of the Solar System was based on certain simplifying assumptions, such as small values of eccentricity and inclination, or neglecting mean-motion resonances and short-period terms. Particularly, the disregard of mean-motion resonances is not an entirely appropriate assumption, because Jupiter and Saturn are near 5/2 resonance. Moreover, in Lagrange and Laplace's time, Uranus, Neptune, and Pluto had not yet been discovered, as well as other resonances in the Solar System. Taking into account the presence of secular resonances would also further complicate the whole problem.

The conclusions of the Lagrange-Laplace secular theory in connection with the problem of stability of the Solar System imply that if the planets are orbiting in the same sense, their masses are of the same order, the eccentricities and inclinations are small, then the semi-major axes are subject only to small changes and the eccentricities and inclinations remain small as well[11].

The very laborious expansions of the disturbing function to higher order terms were made during the 19th century by **Benjamin Peirce** (1809 – 1880), **Urbain Jean Joseph Le Verrier** (1811 – 1877) and **Felix Boquet** (1852 – 1929). Peirce developed the disturbing function to the sixth order in eccentricities and inclinations (Peirce, 1849), Le Verrier an order higher (Le Verrier, 1855), and terms of the eighth order were published by Boquet in 1889 (Boquet, 1889). Developments in mutual inclinations and node longitudes up to the seventh order were made by Newcomb in 1895 (Newcomb, 1895).

[9]The 2/1 resonance corresponds to condition $2n' \approx n$ and argument $2\lambda' - \lambda$.

[10]Let g and s denote the frequencies of precession of the pericenter and ascending node of an asteroid. Then, for example, $\nu_6 = g - g_6 \approx 0$ corresponds to the secular resonance between the asteroid and Saturn.

[11]The condition of the long-term stability of the semi-major axis is necessary, but not sufficient. For example, if the eccentricity increases to 1, then the pericenter distance $q = a(1 - e)$ is zero, which leads to a collision with the Sun.

Discoveries of new bodies

Motivated by the Titius-Bode rule, astronomers at the turn of the 18th and 19th century focused on finding another planet at a distance of 2.8 au. The Founder of the Palermo Observatory, **Giuseppe Piazzi** (1746 – 1826), during his observations on 1 January 1801 assumed he had discovered a new star, with a brightness comparable to a star of eighth magnitude. The next day he noticed its movement and continued in his observations until February 11. Piazzi originally attributed a cometary character to this body. Unfortunately, the news of the existence of a new object reached the astronomical community too late, at a time when it was no longer possible to observe. It was sighted again a year later by **F. X. von Zach** (1754 – 1832), who used Piazzi's observations and applied the new Gauss's method of orbit determination from 3 observations. The new star, as supposed by Piazzi, was named Ceres Ferdinandea as a tribute to King Ferdinand IV. In 1802, Ceres was also observed by the German physicist and astronomer **Heinrich Wilhelm Matthias Olbers** (1758 – 1840), who later discovered Pallas and Vesta. The English astronomer with German roots **William Herschel** (1738 – 1822) proposed that these new bodies would be called asteroids.

In the late 18th century, immense success was achieved by the already mentioned William Herschel. Herschel spent nine years systematically watching the sky, especially double stars. He was an excellent telescope maker, and the resolving power of his instruments allowed him to discover that some nebulae in the Messier catalog are actually clusters of stars. He also published a catalogue of nebulae and star clusters, listing thousands of objects. In connection with the theme of celestial mechanics, however, his discovery of the planet Uranus on 13 March 1781 is certainly crucial. At first, Herschel thought that he had discovered a new comet, as the new object was moving at a speed of $\approx 2.5''$/hour that night. He then corrected his initial error and declared it was a discovery of a new planet of our Solar System[12].

The theoretical methods of celestial mechanics were also successful in discovering Neptune. After the discovery of Uranus, the measurements of its ecliptic longitude did not correspond to expected values - it seemed that Uranus was slowing down in longitude. This gave rise to the notion that the discrepancy could be a consequence of the existence of another planet.

On the appeal of the director of Paris Observatory, **François Jean Dominique Arago** (1786 – 1853), Le Verrier calculated the expected position of the hypothetical planet. Then he immediately informed the German astronomer **Johann Gottfried Galle** (1812 – 1910) who at the night of 23-24 September 1846, together with **Heinrich Louis d'Arrest** (1822 – 1875) found Neptune $52''$ from the predicted position[13].

Note that after systematic observations of Neptune, astronomers noticed small deviations in its path, which were probably caused by inaccurately determined

[12]Under extremely favorable conditions, Uranus can be seen by the naked eye and it had been observed in the past, mistaken for a star. Among the historically documented observers of Uranus, there were the royal astronomers John Flamsteed, James Bradley, the French astronomer Pierre Charles Le Monnier and the German astronomer Johann Tobias Mayer.

[13]The English astronomer **John Couch Adams** (1819 – 1892) determined the position of Neptune with an accuracy of 2°. However, after lengthy disputes, Le Verrier was considered to be the first.

masses of Uranus and Neptune. However, this led to the idea of the existence of another body. Searching for Planet X was undertaken at the Lowell Observatory in Flagstaff in Arizona in 1909 by its founder, the American mathematician **Percival Lowell** (1855 – 1916). Even though he determined the area where the Planet X was to be found, Pluto was discovered after his death by **Clyde Tombaugh** (1906 – 1997), who used brute force and checked positions of thousands of stars. Clyde Tombaugh found Pluto on 13 March 1930, 150 years after the discovery of Uranus by William Herschel.

B.3.3 The Solar System in the late 19th and in the 20th century

The promising results of the Lagrange-Laplace secular theory led Laplace to the notion of a long-term stability of the Solar System. He was also convinced that the systems described by this theory were deterministic, meaning that the state of the system can be determined for any given time if the initial conditions of the corresponding equations of motion are known.

At the end of the 19th century, **Jules Henri Poincaré** (1854 – 1912), a great French scientist, mathematician, physicist, and astronomer, began to deal with the three body problem. In his three-part work *Les Méthodes Nouvelles de la Mécanique Céleste* he showed that even in the restricted three body problem, there are cases in which infinitesimally close paths at time t_0 move away from one another as the exponential function of time t (Poincaré, 1892, 1899). This basically laid the foundations of deterministic chaos.

The extent of chaoticity with regard to the stability of nonlinear dynamic systems was studied by the Russian mathematician and physicist **Aleksandr Mikhailovich Lyapunov** (1859 – 1924). Lyapunov introduced an excellent tool for identifying chaotic motion - now known as the Lyapunov characteristic exponent. Let us consider a dynamic system described by N differential equations in the form

$$\frac{dz_i}{dt} = f_i(\mathbf{z}) \qquad i = 1..N \tag{B.21}$$

with initial conditions $\mathbf{z}_0(0)$ and a solution $\mathbf{z}(t)$. Let vectors $\delta\mathbf{z}(0)$ and $\delta\mathbf{z}(t)$ represent the infinitesimal change in the initial conditions $\mathbf{z}_0(0)$ and the corresponding deviation of the solution at time t. For a general initial perturbation, the largest Lyapunov exponent is defined by

$$\lambda = \lim_{t\to\infty} \lim_{|\delta\mathbf{z}(0)|\to 0} \frac{1}{t} \ln \frac{|\delta\mathbf{z}(t)|}{|\delta\mathbf{z}(0)|}. \tag{B.22}$$

The trajectory is chaotic if $\delta\mathbf{z}(t) = \delta\mathbf{z}(t_0)\mathrm{e}^{\lambda(t-t_0)}$ provided that $\lambda > 0$.

With the development of computer technology, it was possible to perform numerical integrations of equations of motion for times gradually approaching the age of the Solar System. Due to the choice of the time step and the low performance of computers, the first numerical simulations included only the giant planets and Pluto.

The first backward integration to 120,000 years provided some insight into the resonance between Neptune and Pluto (Cohen and Hubbard, 1965). An even longer integration covering a period of 5 Myr was conducted by Kinoshita and

Nakai in 1984 (Kinoshita and Nakai, 1984). They pointed to Pluto's unstable orbit, which was a result of close encounters between Pluto and Neptune. The chaoticity of Pluto's orbit was proved four years later (Sussman and Wisdom, 1988).

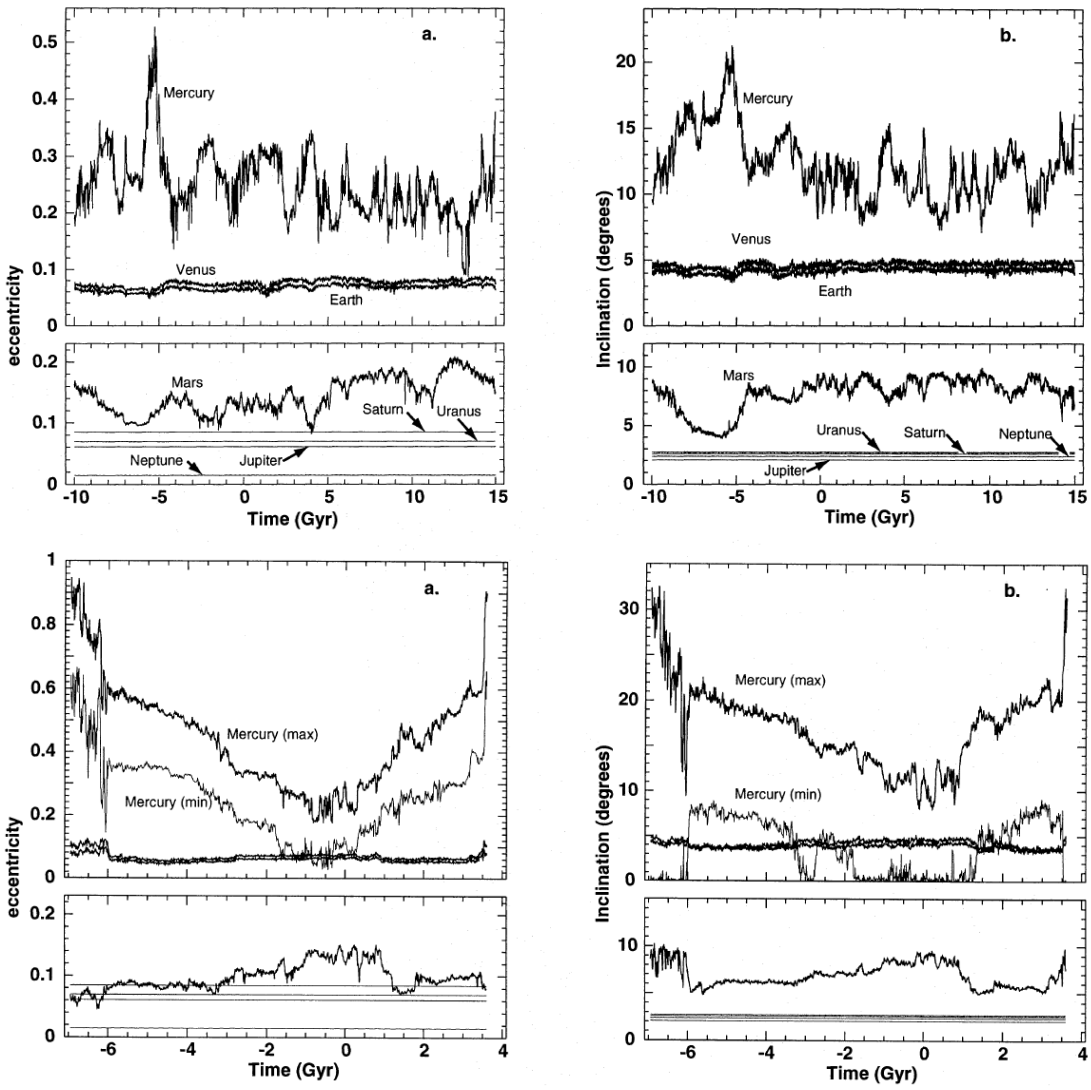

Figure B.5: Numerical propagation of the Solar System in the time interval of $[-10, 15] \times 10^9$ years according to Laskar (1994). The orbits of the outer planets are clearly stable in the time scale of 10^9 years as opposed to the chaotic behavior of the inner planets. The bottom pair of images shows possible solutions with the maximal and minimal values of Mercury's eccentricity between -6.6×10^9 and 3.5×10^9 years.

Sussman and Wisdom numerically propagated the orbit of Pluto back to 845 Myr and determined the value of maximum Lyapunov exponent $\lambda \approx 10^{-7.3}$ y^{-1} corresponding to Lyapunov time[14] of approximately 20 Myr. Another work on long-term integration of the Solar System regarding its stability is, for example, the LONGSTOP project (Roy et al., 1988).

[14]Lyapunov time is the e-folding time $\tau_e = 1/\lambda$ of the system.

Laskar (1988) carried out backward numerical simulation to 10 Myr including all 8 planets and found out that the orbits of the inner planets have a chaotic character – he determined $\lambda \approx 10^{-6.7}$ y^{-1} and the Lyapunov time of ≈ 5 Myr.

In a more recent study Laskar and Gastineau (2009), the Solar System was propagated 5 billion years into the future. The result of the 2,500 various propagations within the uncertainty of initial conditions is that, similarly to Laskar (1994), up to 1% of the solutions lead to an increase in Mercury's eccentricity and then to a significant change of its trajectory to a nearly hyperbolic path. Moreover, some of these solutions can even result in a collision between Mercury, Mars, Venus and Earth.

The view of the structure of the Solar System was of course fundamentally influenced by the development of spacecraft exploration. Data from numerous space probes and sky surveys also significantly contributed to the current knowledge. Some of the important interplanetary probes were Pioneer 10 & 11, Voyager 1 & 2, Galileo, Cassini-Huygens, New Horizons, and Juno. Smaller bodies in the Solar System were studied in greater detail thanks to the probes such as Dawn (Ceres, Vesta), Rosetta (67P/Churyumov-Gerasimenko), Stardust (9P/Tempel) and others. In 2006, the American planetary probe called New Horizons was launched and after nine years, reached Pluto and acquired its very first detailed photograph.

There are also geodesic satellites on regular orbits around the Earth, such as LAGEOS 1 and LAGEOS 2, which, apart from researching the movement of tectonic plates and the shape of the Earth, were also used to test the general theory of relativity. In 2011, the Italian satellite called LARES was launched with a similar aim. The complete list of missions unfortunately exceeds the scope of this chapter. For more details, see for example Kruse (2011).

B.3.4 Early 21$^{\text{st}}$ century

Already during the 20th century, relatively soon after Pluto's discovery, astronomers raised hypotheses about the existence of other bodies beyond the orbit of Neptune. The first public hypotheses on the existence of such objects were published by the Irish astronomer **Kenneth Essex Edgeworth** (1880 – 1972) (Edgeworth, 1943) and later in 1951 by the American astronomer **Gerard Peter Kuiper** (1905 – 1973) (Kuiper, 1951). Although the first body entitled 1992 QB1 had to wait almost half a century for its discovery, there were other small bodies discovered in the meantime - the Centaurs that orbit between Jupiter and Neptune. The first one, (2060) Chiron, was discovered in 1977 (Kowal et al., 1979). The discovery of the first transneptunian object[15] (15760) 1992 QB1, however, was made more than a decade later (Jewitt and Luu, 1993). We currently know of more than $\approx$ 2,500 TNOs, which belong to the Kuiper Belt, Scattered disc or to a resonant population.

Objects of the Kuiper Belt (KBOs), which is formally located in the region of [30,50] au, are divided into three types: a) classical KBOs ($\approx 50\%$) where $e < 0.2$ and $r \in [42, 48]$ au, b) Plutinos ($\approx 10\%$) in the 2/3 mean-motion resonance with Neptune, c) scattered KBOs ($\approx 40\%$) on very eccentric orbits, some extending to approximately ≈ 1000 au from the Sun (Trujillo, 2003).

[15]We use the abbreviation TNO.

The KBOs are further divided into a cold population ($e < 0.1, I < 5^\circ$) and a hot population with $I > 5^\circ$, which differ in their composition and possibly their origin. It is generally believed that the hot population probably originated near Neptune's original orbit, and during the migration of the giant planets was scattered to the remote parts of the Solar System, while the cold population probably appeared near its current location closer to the Sun, and was moved to the current location due to Neptune's migration. However, some studies imply that the cold population originated in situ during a rapid accretion when the size of planetesimals was less than 10-100 km (Parker et al., 2011).

Although the Kuiper Belt is currently the subject of intensive research, its detailed dynamic structure and origin are still an open question. One of the unresolved issues is the existence of a relatively sharp edge of the Kuiper Belt at a distance of 48 au (1/2 resonance with Neptune), beyond which there is a significant decrease in the number of KBOs and, moreover, none of them exhibit near-circular paths. Other KBOs occur further from the Sun - some near the 2/5 resonance (55 au) with Neptune, some near more distant resonances.

The now classical studies explain the distribution of the orbital elements of KBOs by Neptune's migration away from the Sun. As Neptune migrated, the bodies of the primordial Kuiper Belt with nearly circular orbits, could have been captured by the 1/2 or 2/3 resonance (similar to Pluto today), which subsequently increased their eccentricities (Malhotra, 1993, 1995). More recent papers (e.g. Levison and Morbidelli, 2003) have shown that the current dynamically cold KBOs probably originated at a distance of $\approx$ 35 au and were then expelled outward by the 1/2 resonance with Neptune in the final phase of its migration. However, it should be noted that there is still no general consensus regarding the origin and orbital evolution of the cold population.

Nesvorný (2015) simulated the formation of the Kuiper Belt by placing Neptune into distances 20-30 au along with a set of 10^6 particles of the dynamically cold disc. At the time t_0, these particles were initially scattered between the Neptune's orbit and the distance of 30 au. Neptune's migration time scale was chosen from the interval $1 \leq \tau \leq 100$ Myr. The result of the simulations was a fairly good match in the current distribution of inclinations in the Kuiper belt when selecting $\tau \geq 10$ Myr and the starting distance of Neptune ≤ 25 au. This indicates that the migration is relatively slow compared to models with $\tau \leq 10$ Myr.

The Scattered disc, which seems to be the reservoir of most of the observed periodic comets, including the Centaurs - likely transient, yet long-lived reservoir in the migration from this disc, is also a hot area of research.

The notion of the existence of a population at very large distances was addressed by the Dutch astronomer **Jan Hendrik Oort** (1900 – 1992). Today, this hypothetical part of the Solar System, reaching distances of up to 200,000 au, is called the Oort cloud[16]. Duncan et al. (1987) simulated the formation of a cometary cloud and its orbital evolution on a time scale corresponding to 4.5×10^9 years. They found that it probably originated thanks to the planetesimal interactions with the giant planets and the tidal forces of the Galaxy. Duncan et al. (1987) provided an estimation of the position of the inner boundary of the Oort cloud to $\approx$ 3000 au.

[16]Or Öpik-Oort cloud, according to similar notions of its existence expressed by the Estonian astronomer **Ernst Öpik** (1893 – 1985) in 1932.

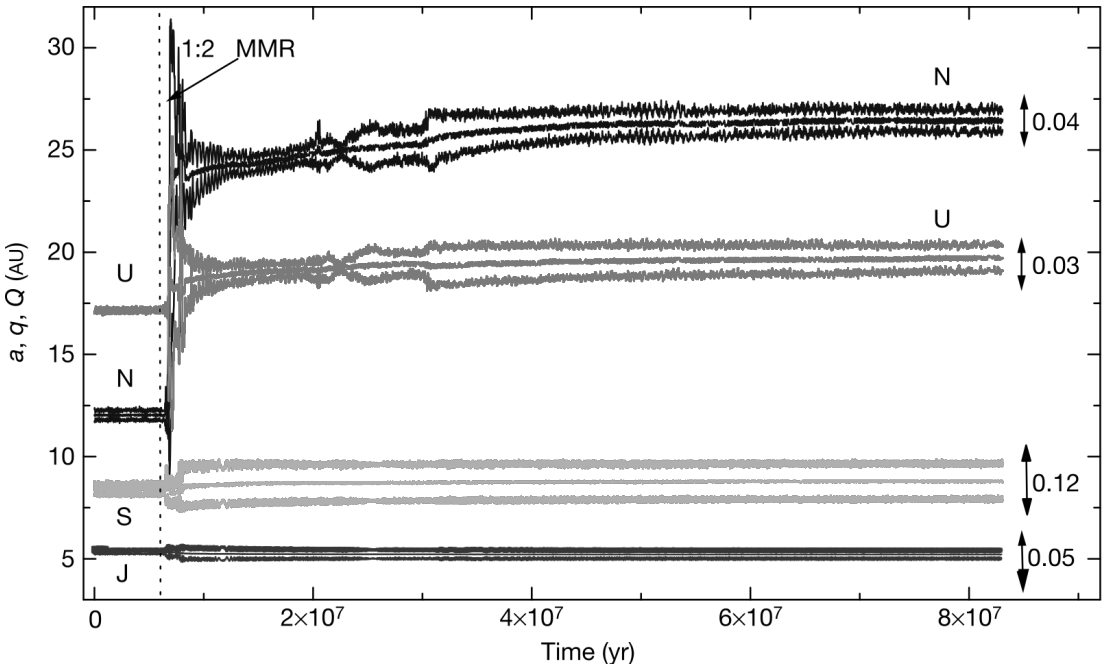

Figure B.6: Orbital evolution of the giant planets according to the Nice model, with the semi-major axis a, distance of the pericentre q and the apocentre Q. It shows the initial, slow migration caused by the interaction of the planets with the planetesimal disc. A major change occured when Jupiter and Saturn were in 1/2 mutual resonance. Planetary orbits became chaotic and started overlapping. Uranus and Neptune were gradually pushed toward the planetesimal disc, whose inner edge, at time t_0, was located beyond Neptune's orbit and the outer edge at a distance of 35 au (Tsiganis et al., 2005). Source: Tsiganis et al. (2005).

Many simulations today rely on modern concepts of formation and evolution of the Solar System, which are currently best described by the Nice model. The Nice model is a set of significant theories supported by N-particle simulations that describe the evolution of the whole Solar System in an effort to explain the dynamic processes leading to its current state (Tsiganis et al., 2005; Morbidelli et al., 2005; Gomes et al., 2005). The model is widely recognized and, in contrast to the previous ones, it assumes that after the elimination of the protoplanetary disc, giant planets substantially migrated from their original paths. This phenomenon can explain the period of the Late Heavy Bombardment, the origin of the Oort cloud and Jupiter's and Neptune's trojans, and partially also the structure and distribution of TNOs.

However, not even this model is without problems, for example concerning the origin and number of irregular moons. Although the Nice model is now able to explain the origin of the populations in the Kuiper belt, it predicts somewhat higher eccentricities for the bodies that are currently observed. Therefore, its further development and refinement is to be expected.

Recent research has also started focusing on extra solar systems. In 1992, astronomers Aleksander Wolszczan and Dale Frail announced the discovery of two planets orbiting the pulsar PSR B1257+12 (Wolszczan and Frail, 1992) and, three years later, Michael Mayor and Didier Queloz discovered the first exoplanet moving around a star of the main sequence, 51 Pegasi (Mayor and Queloz, 1995).

To date (Feb. 2018), about 3700 exoplanets have already been confirmed. Some of the extra solar systems show a completely different orbital structure than the Solar System. An example could be the existence of hot Jupiters on orbits very close to the parent star. Numerical simulations have pointed to their possible dual origin: (a) migration from the cold regions of their origin towards the star (D'Angelo and Lubow, 2008) and b) formation in situ near the star (D'Angelo and Bodenheimer, 2016). Methods of detecting exoplanets, such as the radial velocity method, transit methods, and others, are also rapidly developing.

Particularly irregularities in transit times may point to the presence of another perturbing planet. The TTV method (Transit Timing Variations) can detect planets of an even smaller mass. It is basically an inverse method of looking for a perturbing planet with such orbital characteristics that best fit the observed irregularities in transit times (Agol et al., 2005; Holman and Murray, 2005; Nesvorný and Morbidelli, 2008).

Note that in the evolution of the Solar System, non-gravitational perturbations also play a significant role (see Chapter 1). Relatively new is also the discovery of young populations in the Solar System - the young asteroid pairs, families and binary systems (see Chapter 3)..